Development of Novel Electrocatalysts for Hydrogen Evolution Reaction



Jiaying (Iris) Mo

Inorganic Chemistry Laboratory

Department of Chemistry

Wolfson College

A thesis submitted for the degree of Doctor of Philosophy

Michaelmas Term 2021

Declaration

All research works reported in this thesis have not previously been accepted in substance for any degree and is not being concurrently submitted in candidature for any degree. This thesis is conducted by the author unless stated otherwise. All materials from other sources has been properly and fully acknowledged.

Jiaying Mo

Acknowledgements

Firstly, I would like to express my deepest gratitude to my supervisor Prof. Edman Tsang for his guidance and support during the past four years. I am also blessed that Prof. Tsang can serve as the witness of my wedding during the pandemic.

Thanks is also given to all members of the Tsang group for friendly discussions on academic works and out-of-lab community activities. Particularly, I would like to thank Dr. Tugce Ayvali, Bruce Li, Tommy Sun, Dr. Tim Sudmeier, Dr. Jianwei Zheng, Dr Tianyi Chen and Dr. Pu Zhao for their friendship.

Throughout my DPhil studies, I have received numerous supports from my research collaborators, Tsang group members, and administrative staffs from the Department of Chemistry. For this, I would like to express my appreciation to:

Dr. Tim Sudmeier, Dr. Thomas Lau, Yifei Wang, Dr. Lingling Zhai, Dr. Ivana Lin, Dr Jake Yang, Dr Ian McPherson, Dr Bozhidar Stefanov, Dr. Weiran Zheng and Dr Eduardo Barbosa for the insightful discussions on electrochemistry;

Dr. Simson Wu, Dr. Molly Li, Dr. Tai-sing Wu (NSRRC, Taiwan) and Prof. Yun-liang Soo (NSRRC, Taiwan) in acquiring the XAS data and discussions on XAS analysis;

Prof. Xue-Qing Gong and Dr. Zhiqiang Wang (East China University of Science and Technology, China), Prof. Tiffany Chen (National Tsing Hua University, Taiwan) and her colleagues, Ted Tseng, Dr. Xin-ping Duan and Lu Chen (University of Science and Technology, China) for DFT calculations and model discussions;

Prof. Tong Li and Weikai Xiang (Ruhr-Universität Bochum, Germany) for acquiring APT data and discussions;

Prof. Kazu Suenaga, Ryuichi Kato (AIST Japan), Dr. Tianyi Chen, Dr. Huihuang Fang, Baron Ho, Dr. Alex Robertson, Shengda Pu, Dr. Winson Kuo (Texas A&M University, USA) for acquiring the stunning TEM, STEM-EELS and EDX images and discussions in electron microscopy;

Dr. Tiago V. Alves (Universidade Federal da Bahia, Brazil) and Prof. Pedro H. C. Camargo (University of Helsinki, Finland) in the DDA modelling and discussions;

Dr. Molly Li, Dr. Georg Held (Diamond Light Source, UK), Dr. Simson Wu in acquiring XPS data and discussions on peak analysis.

Dr. Lingling Zhai, Dr. Ben Lo and Prof. Shu Ping Lau (PolyU, Hong Kong), Prof. Chiu Tang and Dr. Sarah Day (Diamond Light Source, UK) for their technical supports in SXRD measurements and interesting discussions;

Dr. Eduardo Barbosa for the discussions in nanoparticle synthesis methods and Tommy Sun for the collaborations in the core-shell materials, Bruce Li for the fruitful discussions in the PEC systems, and Dr. Bozhidar Stefanov and Dr. Jianwei Zheng for the supports in building the on-bench set-up and equipment;

Dr. Robert Jacob, Dr. Simson Wu and Dr. Will Peng for the technical supports in BET analysis;

Dr. Weiran Zheng (PolyU, Hong Kong) for acquiring the SEM images and discussions;

Dr. Tugce Ayvali, Dr. Simson Wu, Dr. Ivana Lin, Dr. Jake Yang, Dr. Heyao Shi and Tommy Sun for proofreading my thesis and offering constructive advice to improve it.

Outside the lab, I would like to thank my best friend, also my bridesmaid, Zhining who keeps me bright and cheerful during all this times. I would also like to thank Ivana, Candy, Jake, Bruce, Hayley and Grant for our awesome gatherings. Thanks are given to TomTom, Shiki, and Dakki for their fluffy love. Special thanks also go to my church buddies Pat, Nadia, Toby, Karis, Karen, Kelly, Auntie Iris, Jane, Yao, Talia and Elena for witness of my spiritual growth under God.

Last but certainly not least, this thesis is dedicated to my family for their continuous and unparalleled love, help and supports all these years. They always encourage me to explore new directions in life and seek my own destiny. I am grateful to my brother John for always being supportive and encouraged no matter when I need help.

Finally, I would like to thank my husband Simson for his unfaltering love and patience on me, which is my biggest driving force to complete the degree. To my dear Simson, this journey would not have been possible without your love, commitment and encouragement, and I dedicate this milestone to you.

Abstract

Development of Novel Electrocatalysts for Hydrogen Evolution Reaction

A thesis submitted for the degree of Doctor of Philosophy

Jiaying (Iris) Mo, Wolfson College, Michaelmas 2021

This thesis explores the activities of novel electrocatalytic systems for the hydrogen evolution reaction (HER) from both the material and methodology aspects. Furthermore, a library of ex-situ and in-situ spectroscopic, imaging, and electrochemical techniques are employed to elucidate the working mechanism behind each of the electrocatalytic system studied in this thesis.

Replacing the expensive and scarce platinum-based catalysts and minimizing the overall energy inputs remain the principal challenges for the HER, especially considering green hydrogen production for electrolyser applications in practice. To that end, a series of alternative metal groups are screened for the HER and it is found that Ag possesses comparable activities as Pt at high overpotentials. The activities are correlated to the surface energies of the metals that ultimately affect the hydrogen adsorption strengths as suggested by first principal calculations. As a result, the morphologies of Ag nanoparticles, dictated by the combinations of exposed facets (and hence different surface energies) of the metals, are investigated. Electrochemical testing reveals that Ag nanocubes can outperform commercial Pt at -2.5 V and it is suggested computationally that the weaker hydrogen adsorption strengths on the Ag surface can lead to a change of the rate-determining step from Volmer to Tafel step.

In an attempt to lower the overpotentials required by the Ag nanoparticles, solar energy is exploited as an additional energy source to drive the reactions. Using a sonochemical approach, the Ag nanoparticles are combined with Au, with excellent plasmonic absorptions of solar

radiation, to form bimetallic core-shell nanomaterials. The 3D frameworks and elemental distributions are reconstructed via atom probe tomography to reveal an atomic-layered shell with precisely controlled Ag to Au ratio. STEM-EELS, XAS, and DDA simulations suggest the hot electrons excited by LSPR are transferred from Au to the higher energy excited states of Ag for proton reduction under visible light, which gives a significant enhancement in current densities when compared with the light-off conditions.

The second part of the thesis identifies polar metal oxides as electrocatalyst supports to promote the HER activities. An electrochemical activated magnesium hydroxide material, which is generated from the polar MgO (111) faceted nanocrystals, is found to exhibit exceptional HER activities due to its high proton affinity. A combination of in-situ synchrotron XRD technique and ex-situ TEM, SAED and XPS analysis is employed to study the activation process, and it is found that the Ru-MgO (111) interface is electrochemically and topotactically hydrolysed to Ru-$Mg(OH)_2$ (001) under acidic medium. The extensive hydroxyl layers stemmed from the topotactic transitions of the polar magnesium oxide phases provide Grotthuss-like channeled pathways for protons to hop across. This allows efficient diffusion of protons on the surface and makes available active sites for proton reduction to take place.

List of Abbreviations

APT	Atom Probe Tomography
BET	Brunauer–Emmett–Teller
CE	Counter Electrode
DDA	Discrete dipole approximation
DFT	Density Functional Theory
DI	Deionized
ECSA	Electrochemically Active Surface Area
EELS	Electron Energy Loss Spectroscopy
EG	Ethylene Glycol
EXAFS	Extended X-ray Absorption Fine Structure
FCC	Face-Centered Cubic
FFT	Fast Fourier Transform
FTO	Fluorine-Doped Tin Oxide
FWHM	Full Width Half Maximum
GC	Gas Chromatography
HAADF	High-Angle Annular Dark Field
HE	Hot Electron
HER	Hydrogen Evolution Reactions
HRTEM	High-Resolution Transmission Electron Microscopy
ICP-MS	Inductively Coupled Plasma Mass Spectrometry
LSV	Linear Sweep Voltammetry
LSPR	Localized Surface Plasmon Resonance
MEA	Membrane-Electrode Assemblies
MgO (111)	Magnesium oxide with preferentially exposed (111) facets
NPs	Nanoparticles
PEM	Proton Exchange Membrane
Pt/C	Platinum supported on Vulcan carbon
PVP	Polyvinylpyrrolidone

RDS	Rate Determining Step
RE	Reference Electrode
RHE	Reversible Hydrogen Electrode
Ru/MgO(111)	Ruthenium supported on Magnesium oxide with preferentially exposed (111} facets
SAED	Selected Area Electron Diffraction
SCE	Saturated Calomel Electrode
SMSI	Strong Metal–Support Interactions
SPR	Surface Plasmon Resonance
STEM	Scanning Transmission Electron Microscopy
SXRD	Synchrotron X-Ray Diffraction
TCD	ThermoConductivity Detectors
TEM	Transmission Electron Microscopy
TOF	Turnover Frequency
UV-Vis	UV-Visible Spectroscopy
WE	Working Electrode
XANES	X-ray Absorption Near Edge Structure
XAS	X-ray Absorption Spectroscopy
XPS	X-ray Photoelectron Spectroscopy
XRD	X-ray Diffraction

List of Publications:

[1] J. Mo, E.C.M. Barbosa, S. Wu, Y. Li, Y. Sun, W. Xiang, T. Li, S. Pu, A. Robertson, T. sing Wu, Y. liang Soo, T. V. Alves, P.H.C. Camargo, W. Kuo, S.C.E. Tsang, Atomic-Precision Tailoring of Au–Ag Core–Shell Composite Nanoparticles for Direct Electrochemical-Plasmonic Hydrogen Evolution in Water Splitting, Adv. Funct. Mater. 31 (2021) 1–11. https://doi.org/10.1002/adfm.202102517.

[2] J. Mo, S. Wu, T.H.M. Lau, R. Kato, K. Suenaga, T.S. Wu, Y.L. Soo, J.S. Foord, S.C.E. Tsang, Transition metal atom–doped monolayer MoS2 in a proton-exchange membrane electrolyzer, Mater. Today Adv. 6 (2020) 0–6. https://doi.org/10.1016/j.mtadv.2019.100020.

[3] J. Mo, B.I. Stefanov, T.H.M. Lau, T. Chen, S. Wu, Z. Wang, X.Q. Gong, I. Wilkinson, G. Schmid, S.C.E. Tsang, Superior Performance of Ag over Pt for Hydrogen Evolution Reaction in Water Electrolysis under High Overpotentials, ACS Appl. Energy Mater. 2 (2019) 1221–1228. https://doi.org/10.1021/acsaem.8b01777.

[4] S. Wu, K.Y. Tseng, R. Kato, T.S. Wu, A. Large, Y.K. Peng, W. Xiang, H. Fang, J. Mo, I. Wilkinson, Y.L. Soo, G. Held, K. Suenaga, T. Li, H.Y.T. Chen, S.C.E. Tsang, Rapid Interchangeable Hydrogen, Hydride, and Proton Species at the Interface of Transition Metal Atom on Oxide Surface, J. Am. Chem. Soc. 143 (2021) 9105–9112. https://doi.org/10.1021/jacs.1c02859.

[5] S. Wu, Y.-K.K. Peng, T.-Y.Y. Chen, J. Mo, A. Large, I. McPherson, H.-L.L. Chou, I. Wilkinson, F. Venturini, D. Grinter, P. Ferrer Escorihuela, G. Held, S.C.E. Tsang, Removal of Hydrogen Poisoning by Electrostatically Polar MgO Support for Low-Pressure NH3 Synthesis at a High Rate over the Ru Catalyst, ACS Catal. 10 (2020) 5614–5622. https://doi.org/10.1021/acscatal.0c00954.

[6] L. Zhai, T. Woon, B. Lo, Z. Xu, J. Potter, J. Mo, X. Guo, C.C. Tang, S. Chi, E. Tsang, S.P. Lau, In Situ Phase Transformation on Nickel-Based Selenides for Enhanced Hydrogen Evolution Reaction in Alkaline Medium, ACS Energy Lett. 5 (2020) 2483–2491. https://doi.org/10.1021/acsenergylett.0c01385.

[7] H.W. Man, C.S. Tsang, M.M.J. Li, J. Mo, B. Huang, L.Y.S. Lee, Y. chung Leung, K.Y. Wong, S.C.E. Tsang, Transition metal-doped nickel phosphide nanoparticles as electro- and photocatalysts for hydrogen generation reactions, Appl. Catal. B Environ. 242 (2019) 186–193. https://doi.org/10.1016/j.apcatb.2018.09.103.

[8] T.H.M. Lau, S. Wu, R. Kato, T.S. Wu, J. Kulhavý, J. Mo, J. Zheng, J.S. Foord, Y.L. Soo, K. Suenaga, M.T. Darby, S.C.E. Tsang, Engineering Monolayer 1T-MoS2 into a Bifunctional Electrocatalyst via Sonochemical Doping of Isolated Transition Metal Atoms, ACS Catal. 9 (2019) 7527–7534. https://doi.org/10.1021/acscatal.9b01503.

[9] H.W. Man, C.S. Tsang, M.M.J. Li, J. Mo, B. Huang, L.Y.S. Lee, Y. chung Leung, K.Y. Wong, S.C.E. Tsang, Tailored transition metal-doped nickel phosphide nanoparticles for the electrochemical oxygen evolution reaction (OER), Chem. Commun. 54 (2018) 8630–8633. https://doi.org/10.1039/c8cc03870h.

Table of Contents

Declaration i
Acknowledgements ii
Abstract iv
List of Abbreviations vi
List of Publications viii
Table of Contents ix
Chapter 1 Introduction 1
1.1 Background 2
1.1.1 Hydrogen - A Potential Energy Vector 2
1.1.2 Electrochemical Catalysis 4
1.1.3 Photoelectrochemical Catalysis 14
1.2 Electrochemical HER 16
1.2.1 Electrochemical Water Splitting Fundamentals 17
1.2.2 HER Reaction Mechanism 19
1.2.3 HER Activity Descriptor 21
1.2.4 HER Activity Parameters 23
1.3 Photoelectrochemical HER 26
1.3.1 Reaction Mechanism 27
1.3.2 PEC Cell Performance Descriptors 29
1.4 Catalyst Development for HER 30
1.4.1 Morphology-controlled Metal NPs 34
1.4.2 Bimetallic Core-shell Materials 38
1.4.3 Metal Oxide Supports 41
1.5 Aims and Objectives 44
1.6 Thesis Overview 45
1.7 References 47
Chapter 2 Analytical Techniques 60
2.1 Introduction 61
2.2 X-Ray Diffractions (XRD) 61
2.3 Synchrotron XRD (SXRD) 66
2.4 Transmission Electron Microscopy (TEM) 67
2.5 Scanning Transmission Electron Microscopy (STEM) 70
2.6 X-Ray Photoelectron Spectroscopy (XPS) 72
2.7 UV-Visible Spectroscopy (UV-Vis) 75

2.8 Atom Probe Tomography (APT) 77
2.9 X-Ray Absorption Spectroscopy (XAS) 79
2.10 Brunauer–Emmett–Teller (BET) Theory 82
2.11 Electrochemical Techniques 84
2.12 References 86
Chapter 3 Experimental Methods 90
3.1 Characterizations 91
3.1.1 XRD 91
3.1.2 Titan STEM and Super-X EDS 91
3.1.3 STEM-EELS 91
3.1.4 SEM 92
3.1.5 TGA 92
3.1.6 APT 92
3.1.7 XPS 93
3.2 HER Catalytic Testing 93
3.2.1 PEM Water Electrolyser 93
3.2.2 Three-electrode Aqueous Medium Systems 96
3.2.3 Operando Electrochemical SXRD 100
3.3 Computational Modelling and Calculations 102
3.3.1 DFT Calculations on Hydrogen Adsorption Energies 102
3.3.2 DDA Analysis of Au-Ag Core-shell Materials 102
3.3.3 DFT Modelling on MgO Supports 103
3.4 References 104
Chapter 4 Hydrogen Evolution in PEM Water Electrolyser 106
4.1 Background 108
4.2 Materials 109
4.3 Synthesis 110
4.3.1 Synthesis of Silver Cubes 110
4.3.2 Synthesis of Silver Spheres 111
4.3.3 Synthesis of Silver Wires 111
4.3.4 Synthesis of Metal Supported on Vulcan Carbon 112
4.4 Characterizations 113
4.4.1 X-Ray Diffractions (XRD) 113
4.4.2 Thermogravimetric Analysis (TGA) 115
4.4.3 Transmission Electron Microscopy (TEM) 116
4.4.4 Energy-dispersive X-Ray Spectroscopy (EDX) 119

4.4.5 UV-Visible Spectroscopy (UV-Vis) 120
4.5 Hydrogen Evolution Reactions in Water Electrolysis 122
4.5.1 Experimental Methods 122
4.5.2 Catalytic Performance 123
4.5.3 Structure-Activity Correlations in PEM Electrolyser 125
4.5.4 The Surface Electrochemistry of Morphology-controlled Ag NPs 131
4.5.5 Post-reaction Analysis and Stability 136
4.6 Conclusions 139
4.7 References 139
Chapter 5 Hydrogen Evolution in Direct Electrochemical-Plasmonic water electrolysis 142
5.1 Background 144
5.2 Materials 145
5.3 Synthesis 145
5.3.1 Synthesis of Au Nanoparticles 146
5.3.2 Synthesis of Ag Nanoparticles 146
5.3.3 Synthesis of Au-Ag core-shell NPs 147
5.4 Characterizations 148
5.4.1 Transmission Electron Microscopy (TEM) 148
5.4.2 Energy Dispersive X-Ray Spectroscopy (EDX) 151
5.4.3 Atom Probe Tomography (APT) 154
5.4.4 UV-Visible Spectroscopy (UV-Vis) 159
5.4.5 X-Ray Absorption Spectroscopy (XAS) 160
5.5 Surface Plasmon Analysis 167
5.6 Direct Electrochemical-Localized Surface Plasmon Resonance (EC-LSPR) 173
5.6.1 Experimental Methods 173
5.6.2 Direct Plasmonic Chronoamperometry 176
5.6.3 Stability Test and Control Experiments 186
5.6.4 Plasmonic Chronoamperometry with Solar Simulator 189
5.6.5 Linear Sweep Voltammetry (LSV) Analysis 191
5.7 Discrete Dipole Approximation (DDA) 193
5.8 Conclusions 195
5.9 References 196
Chapter 6 Enhanced Hydrogen Evolution Reactions on Polar MgO Supports 199
6.1 Background 201
6.2 Materials 204
6.3 Synthesis 204

6.3.1 MgO Support Preparations 205
6.3.2 Ru-loading MgO Catalysts 206
6.4 Characterizations 206
6.4.1 X-Ray Diffraction (XRD) 206
6.4.2 Transmission Electron Microscopy (TEM) 208
6.4.3 Brunauer–Emmett–Teller (BET) Analysis 210
6.4.4 ICP-MS Analysis 210
6.5 Catalytic Performance in HER 211
6.5.1 Experimental Methods 211
6.5.2 Results and Discussions 212
6.6 Structure-Activity Correlations on MgO Supports 216
6.6.1 XPS Analysis 216
6.6.2 Operando SXRD Measurements 219
6.6.3 Electron Microscopy (EM) Analysis 226
6.6.4 DFT Modelling and Calculations 230
6.7 Conclusions 236
6.8 References 237
Chapter 7 Conclusions and Outlook 240
7.1 Conclusions 240
7.2 Outlook 242
7.3 Reference 243

Chapter 1 Introduction

Table of Contents

Chapter 1 Introduction 1

1.1 Background 2

1.1.1 Hydrogen - A Potential Energy Vector 2

1.1.2 Electrochemical Catalysis 4

1.1.3 Photoelectrochemical Catalysis 14

1.2 Electrochemical HER 16

1.2.1 Electrochemical Water Splitting Fundamentals 17

1.2.2 HER Reaction Mechanism 19

1.2.3 HER Activity Descriptor 21

1.2.4 HER Activity Parameters 23

1.3 Photoelectrochemical HER 26

1.3.1 Reaction Mechanism 27

1.3.2 PEC Cell Performance Descriptors 29

1.4 Catalyst Development for HER 30

1.4.1 Morphology-controlled Metal NPs 34

1.4.2 Bimetallic Core-shell Materials 38

1.4.3 Metal Oxide Supports 41

1.5 Aims and Objectives 44

1.6 Thesis Overview 45

1.7 References 47

1.1 Background

The hydrogen economy is crucial to the decarbonization landscape where it serves as a decentralised energy vector that connects upstream renewable energy supplies and downstream zero-emissions power demands. Despite various research efforts into green hydrogen generation, only 4% of the global hydrogen stream is from renewable energy, particularly from water electrolysis.[1] Along with the increasing attention placed on the topic, such as COP26, optimising the hydrogen evolution reaction has become an important research area. In the following sections, green hydrogen production by water electrolysis and photoelectrochemical processes will be further discussed.

1.1.1 Hydrogen - A Potential Energy Vector

The development of alternative power sources to fossil fuel combustion is imperative due to imminent global warming as well as drastic climate changes in recent years.[2] Among all renewable energies, solar, wind and tidal wave appear to be prominent choices, especially for residential purposes, thanks to the easy installation of these set-ups in terms of space occupation and efficiency.[3] Nonetheless, the transient nature of these renewables has limited their use as a continuous power source. As a result, the excess energy produced during peak-hours needs to be stored and subsequently be converted back to electrical energy during the off-peak timeframe.[4] Meanwhile, hydrogen is regarded as an ideal chemical vector for renewable power storage by virtue of its superior energy density (142 MJ/kg) and carbon-free emission.[5–9] It is worthwhile to mention that hydrogen can be used as fuel for fuel cells to convert its chemical energy into electricity at high efficiencies of around 40-60% which is widely commercialized nowadays for the new generation of carbon-free transport, such as hydrogen fuel cell cars (Figure 1.1).

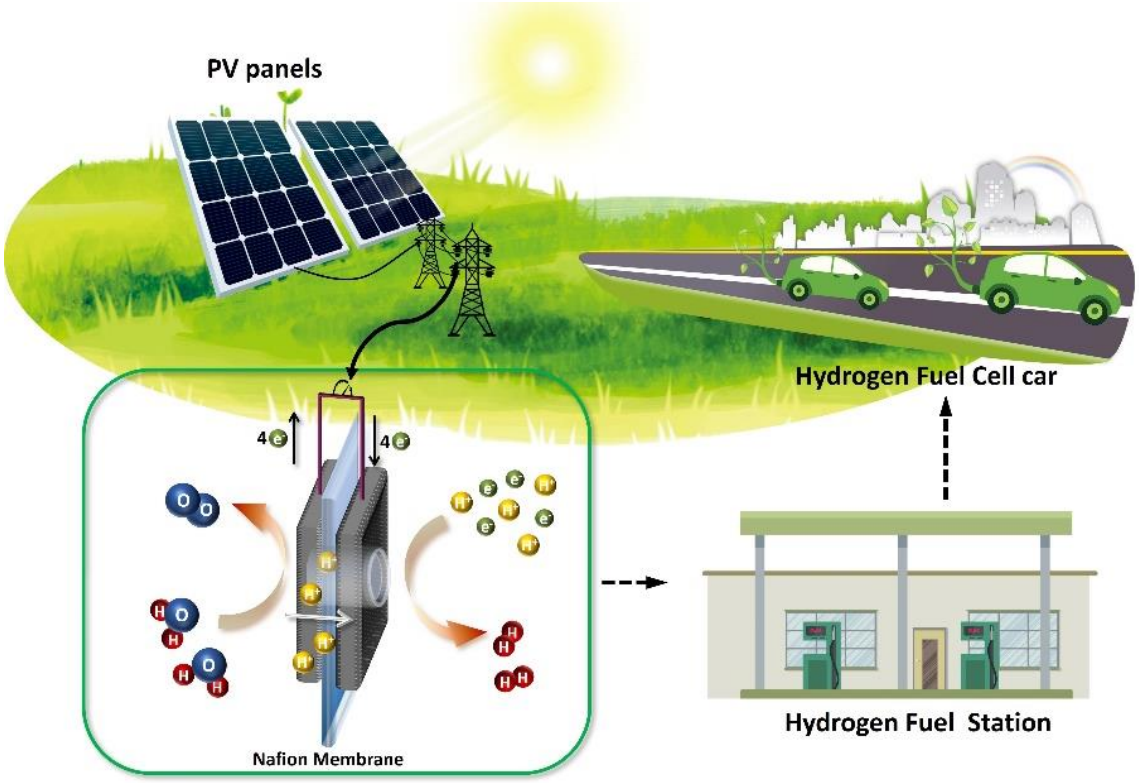


Figure 1.1 Schematic of renewable hydrogen cycle featuring solar panels, electrolysers, hydrogen fuel stations and hydrogen fuel cell vehicles.

The typical generation of hydrogen from water can be achieved via electrolysis,[10–12] photolysis[13–15] or thermal means.[16–19] Globally, around three-quarters of all hydrogen production is from steam methane reforming (SMR) due to economic cost factors ($1/kg vs $4-5/kg green hydrogen, where green means hydrogen is produced from water electrolysis with electricity input from renewable sources).[20] During SMR, methane first reacts with water to form dihydrogen and carbon monoxide at a high temperature of 800 ^{o}C.[21] Subsequently, the carbon monoxide further reacts with water molecules to form dihydrogen and carbon dioxide via the water-gas shift reaction. As a result, the production of "grey hydrogen" from SMR contributes to tremendous emissions of carbon dioxide and is regarded as a significant culprits of global warming since the industrial revolution.[22]

On the other hand, an alternative option to produce green and high-quality hydrogen is through water electrolysis, where water is dissociated to dihydrogen and dioxygen by appropriately applied potential with the use of different electrocatalysts. To date, proton-exchange membrane

(PEM) electrolysers are widely commercialized and installed globally with a more competitive capital expenditure cost (more of which discussed in section 1.2.1), which provides an attractive concept to convert renewable electrical energy into pure hydrogen without carbon emission.[23] Additionally, solar energy has drawn more and more attention to be utilized in the water electrolysis system to reduce the electrical power consumption by tailoring catalysts with bifunctional ability to utilize the electrical and photo energy at the same time to further suppress cost for the production of green hydrogen.[24] There are two general routes available to convert the solar energy into chemical fuel (H_2) through water splitting: a) Indirect solar-to-hydrogen production (make use of the conventional solar panels to provide renewable electricity to run the commercial electrolysers) and b) Direct solar-to-hydrogen production (using a single device for both light absorption and water splitting process). The indirect and direct solar-to-hydrogen production routes are employed in chapter 4 and chapter 5 respectively.

The platinum group metal (PGM)-based catalysts are widely used in industry for electrochemical HER because of their intrinsic electrocatalytic activity and chemical stability.[25,26] Due to the scarcity and thus limited supply of platinum with high cost, the deployment of green hydrogen is slow and only contributes to 4% of the global hydrogen supply at present. The work presented in this thesis aims to tackle this issue by discovering alternative earth-abundant metal groups as electrocatalysts. Specifically, this research focuses on identifying various means to lower activation barriers, and hence energy inputs, for hydrogen evolution reactions.

1.1.2 Electrochemical Catalysis

1.1.2.1 Background

Electrochemical catalytic processes involve oxidation and reduction reactions through the direct transfer of electrons with the help of electrocatalysts to lower the overpotentials of the reactions.[27,28] Specifically, electrocatalyst provides active surface sites to stabilize the

intermediates via surface adsorption, offering an alternative pathway with lower activation energy for the electrochemical reaction.[28] On the most basic level, an electrochemical system consists of at least two electrodes, namely anode and cathode, which are connected electrically by a metal wire and are dipped into a conductive medium. The electrolyte can be classified into two broad categories, the first being the liquid electrolyte containing dissolved ions, and the other being the solid electrolyte with ion conductivity. The electrocatalysis process takes place at the electrode-electrolyte interface, in which the catalyst-casted electrode plays the role of electron donor/acceptor.[29] In this thesis, we will investigate the catalytic processes at the electrode/electrolyte interface in a three-electrode system immersed in an aqueous solution with conductive ions. The rate of such an electrochemical reaction is determined by several different steps including mass transport, adsorption, electrochemical redox reaction, as well as the rate of charge transfer.

1.1.2.2 Charge Transfer

1.1.2.2.1 Electrochemical Equilibrium and Nernst Equation

In a general context, electrochemistry describes chemical phenomena that involve charge separations in solution. The separation of charge is pertinent to charge transfer that can take place either homogeneously (between different chemical species in solution), or heterogeneously (between the working electrode and chemical species in solution at the interface).[30,31] A general one-electron reduction process at the interface between a metallic working electrode (m) and a solution phase (aq) can be described as:

$$Ox_{(aq)}{}^{c} + e^{-}{}_{(m)} \rightleftharpoons Red_{(aq)}{}^{c-1} \qquad (Equation\ 1.1)$$

where the $Ox_{(aq)}$ and $Re_{(aq)}$ are the oxidant and reductant species in solution; $e^{-}{}_{(m)}$ refers to the source of electrons that resides on the metal electrode. In contrast to chemical equilibrium that is mainly controlled by the individual chemical potentials of reactants and products,

electrochemical equilibrium is concerned with the balance between the chemical and electrical potentials. This is because the electrochemical equilibrium involves the charge transfer between two different phases, the solution (s) and the electrode (m), which leads to two different electrical potentials ϕ_s and ϕ_m. The electrochemical potential ($\overline{\mu_j}$) of species j is introduced to describe both the chemical and electrical components of the process:

$$\overline{\mu}_j = \mu_j + Z_j F\phi \qquad (Equation\ 1.2)$$

where u_j is the chemical potential; $Z_jF\phi$ is the electrical energy, where Z_j is the charge on molecule j; F is the Faraday constant and ϕ is the potential of the particular phase of the species j. According to equation 1.1 for a one-electron reduction process at electrochemical equilibrium,

$$\overline{\mu}_{ox} + \overline{\mu}_{e^-} = \overline{\mu}_{red} \qquad (Equation\ 1.3)$$

By substituting Equation 1.2 to Equation 1.3, we can obtain

$$\mu_{ox} + cF\phi_s + (\mu_{e^-} - F\phi_m) = \mu_{red} + (c-1)F\phi_s \qquad (Equation\ 1.4)$$

which can be rearranged to obtain the Nernst equation:[31]

$$\phi_m - \phi_s = \frac{\Delta\mu^0}{F} + \frac{RT}{F}\ln\left(\frac{\alpha_{ox}}{\alpha_{red}}\right) \qquad (Equation\ 1.5)$$

where $\Delta\mu^0 = \mu_{ox}^0 - \mu_{red}^0 + \mu_{e-}$, representing the standard chemical potentials of the oxidant, reductant species and the electron, respectively; ϕ_s and ϕ_m are the electrical potential (V) of the electrolyte solution and electrode material, respectively; R is the gas constant (8.314 J K^{-1} mol^{-1}); T is the absolute temperature (K); F is the Faraday constant (96485 C mol^{-1}); α_{ox} and α_{red} are the activities of the reduced and oxidised species at the electrode interface (mol kg^{-1}), respectively.

Practically, the absolute value of the electrode potential difference (ϕ_m - ϕ_s) is not possible to measure directly with only one electrode-solution interface. As a result, at least two electrode-

solution interfaces are needed for a complete circuit, in which the reference electrode is introduced. The potential applied (E) between the working electrode and reference electrode can be described as:

$$(\phi_m - \phi_s)_{working} - (\phi_m - \phi_s)_{reference} = E^0 + \frac{RT}{F}\ln\left(\frac{\alpha_{ox}}{\alpha_{red}}\right) \quad (Equation\ 1.6)$$

where E^0 is the standard electrode potential (V) when the reference electrode is a standard hydrogen electrode (SHE). Due to the non-ideality of the solution, the concentration c_i is not the same as the activity (α_i), and the relation between α_i and c_i can be described as:

$$\alpha_i = \gamma_i\ c_i \quad (Equation\ 1.7)$$

where γ_i is the activity coefficient of species i, and c_i is the concentration of specie i (mol cm^{-3}). The Nernst equation (Equation 1.6) can combine with Equation 1.7 and be rearranged to:

$$E = E_f^0 + \frac{RT}{F}\ln\left(\frac{c_{ox}}{c_{red}}\right) \quad (Equation\ 1.8)$$

with

$$E_f^0 = E^0 + \frac{RT}{F}\ln\left(\frac{\gamma_{ox}}{\gamma_{red}}\right) \quad (Equation\ 1.9)$$

where E_f^0 is the formal potential (V). Here γ_i is taken as a constant assuming that the activity coefficient of the analyte is invariant to its concentration when the electrolyte concentration is sufficient. Eventually, the Nernst equation correlating to the species concentrations at equilibrium conditions can be established. During electrochemical experiments, an additional potential will be applied on the working electrode that may disturb the electrochemical equilibrium and thus result in a Faradaic or non-Faradaic process.

1.1.2.2.2 Faradaic Process

In a typical Faradaic process, charged particles are transferred across the electrode/solution interface, from one bulk phase to another during the electrochemical redox reaction. The

Faraday's laws of electrolysis describe the relationship between the mass (m) of elements deposited at an electrode and charge (Q).[31–33] In a typical case of constant current electrolysis:

$$m = \frac{QM}{F\upsilon} \qquad (Equation\ 1.10)$$

with

$$Q = I\ t \qquad (Equation\ 1.11)$$

where m is the mass of species on the electrode (g); M is the molar mass (g mol^{-1}); F is the Faraday constant (96485 C mol^{-1}); υ is the valence; I is the current flow (A); t is time (s).

1.1.2.2.2.1 Butler-Volmer Equation and Tafel Plot

During electrochemical experiments, the applied potential may disturb the equilibrium and the electron transfer will cause a Faradaic current flow (I) through the working electrode.

Taking the reaction (Equation 1.12) as an example:

$$Ox_{(aq)}{}^{c} + e^{-}{}_{(m)} \underset{k_{ox}}{\overset{k_{red}}{\rightleftarrows}} Red_{(aq)}{}^{c-1} \qquad (Equation\ 1.12)$$

The arrows are used in Equation 1.12 instead of harpoons as shown in Equation 1.1, which indicates the absence of equilibrium.

The total current passing through an electrode can be determined with:

$$I = I_{red} + I_{ox} = A\ F\ J \qquad (Equation\ 1.13)$$

According to first-order heterogeneous rate law:

$$J = J_{red} + J_{ox} = k_{red}[ox]_0 - k_{ox}[red]_0 \qquad (Equation\ 1.14)$$

The I_{ox} and I_{red} are the current flows of oxidation and reduction (A); A is the electrode area (cm^2); F is the Faraday constant (96485 C mol^{-1}); J is the heterogeneous reaction flux at the electrode/solution interface (mol m^{-2} s^{-1}); k_{ox} and k_{red} are the electron transfer rate constants

for oxidation and reduction, respectively. $[ox]_0$ and $[red]_0$ are the surface concentrations of the oxidant and reductant species in solution (mol cm^{-3}).

Combining the heterogeneous reaction flux with the Gibbs energy, the Butler-Volmer equation is introduced:[31]

$$J = [ox]_0 k^o e^{-\frac{\alpha F}{RT}\eta} - [Red]_0 k^o e^{\frac{(1-\alpha)F}{RT}\eta} \qquad (Equation\ 1.15)$$

with

$$k_{red} = k^o e^{-\frac{\alpha F}{RT}\eta} \qquad (Equation\ 1.16)$$

$$k_{ox} = k^o e^{\frac{(1-\alpha)F}{RT}\eta} \qquad (Equation\ 1.17)$$

where k^o is the standard electrochemical rate constant (cm s^{-1}); η is the overpotential (V) applied to working electrode where $\eta = E - E_f^0$; and E (V) is the potential of the working electrode; E_f^0 (V) is the formal potential; T is temperature (K); α is the transfer coefficient, which is an indication of whether the transition state of the electroactive species in solution is reactant-like (α =0) or product-like (α =1). The parameter α lies in the range 0 to 1 for an one-electron process. Experimentally, α is often found to be about 0.5.

As a result, the current and potential relationship according to the Butler-Volmer equation can be described as:

$$I = AFJ = AFk^o \left\{ e^{-\frac{\alpha F}{RT}\eta}[ox]_0 - e^{\frac{(1-\alpha)F}{RT}\eta}[red]_0 \right\} \qquad (Equation\ 1.18)$$

All the parameters have been defined above. The Tafel law can be derived from the Butler-Volmer equation under irreversible electron transfer kinetics. That is, an overpotential has to be applied to drive the reaction in either reductive or oxidative pathway. When the reduction process is dominating in the reaction with a much faster rate, the oxidation process becomes negligible such that the current can be expressed as:

$$I_{red} = AFJ_{red} = AFk^o \left\{ e^{-\frac{\alpha F}{RT}\eta} [ox]_0 \right\} \qquad (Equation\ 1.19)$$

Assuming the concentration of oxidant species $[ox]_0$ does not deviate significantly from its bulk value, the logarithm of equation 1.19 is:[33]

$$\ln|I_{red}| = -\frac{\alpha FE}{RT} + constant \qquad (Equation\ 1.20)$$

Similarly, when the oxidation process dominates with a much faster rate compared with the reduction process, the reduction will be negligible.

$$I_{ox} = AFJ_{ox} = AFk^o \left\{ e^{\frac{(1-\alpha)F}{RT}\eta} [red]_0 \right\} \qquad (Equation\ 1.21)$$

$$\ln|I_{ox}| = \frac{(1-\alpha)FE}{RT} + constant \qquad (Equation\ 1.22)$$

By plotting the ln $|I_{red}|$ or ln $|I_{ox}|$ against E, the Tafel slope $-\frac{\alpha F}{RT}$ or $\frac{(1-\alpha)F}{RT}$ can be obtained, which can be used to determine the transfer coefficient α of the redox couple. With the help of the Tafel slope, the rate-determining step of the overall HER reaction can be identified by comparing with the typical values of the classified HER steps.[34,35] Additionally, the Tafel slope is an important parameter to compare activities of different electrocatalysts for the HER, further discussed in section 1.2.4.

1.1.2.2.3 Non-Faradaic Process

In a non-Faradaic process, charge is progressively stored instead of transferring across the electrode/solution interface, resulting in double layer capacitance. A high concentration supporting electrolyte can be added to the solution to minimize the effect of the non-Faradaic process. In theory, as potential is applied at the electrode, the charges at the surface of the electrode accumulate. Electrostatic attraction will then lead to the accumulation of oppositely charged ions in the solution adjacent to the electrode. The electrode/solution interface is acting as a capacitor, and the two sheets of ions with opposite charges are called the electrical double

layer (EDL). There are several sophisticated models describing the gradual change of the ion arrangements at the electrode-solution interface between the charged electrode surface and the bulk solution.[32]

In the Helmholtz double-layer model, the solvated ions arrange themselves along the surface of the charged electrode. The model is similar to a two-plate conventional capacitor with two layers of opposite charge (named as outer Helmholtz plane and inner Helmholtz plane) form at the electrode/solution interface and are separated by an atomic distance.[36] In Figure 1.2a, the electric potential varies linearly as a function of distance from the electrode surface according to the Helmholtz model. The capacitive current, or non-Faradaic current, can be determined by:

$$I = \frac{dQ}{dt} = C_{dl}\, A\, \frac{dE}{dt} = C_{dl}\, A\, \upsilon \qquad (Equation\ 1.23)$$

where C_{dl} is the double layer capacitance per area ($\mu F\ cm^{-2}$); A is the electrode area (cm^2); υ is the scan rate ($V\ s^{-1}$). In order to analyse the electrochemical mechanism more straightforward, the non-Faradaic current will be minimized via a slower scan rate or smaller electrode area during the experiment.

However, the Helmholtz model does not account for the disrupting effect of thermal motion of the solvated molecules. The Gouy-Chapman model is developed to take into account the disordering effect of thermal motion. Figure 1.2b shows the continuous distribution of electrolyte ions (cations and anions) in the electrolyte solution described by the Gouy-Chapman model. The ions of opposite charge accumulated close to the electrode surface while the ions of the same charge are repelled from the electrode. The Helmholtz model overemphasized the rigidity of the bulk solution and the Gouy-Chapman model overestimate the EDL capacitance, therefore the Stern Model was developed to combine these two models. In the Stern model as shown in Figure 1.2c, the distributions of ions are separated into two parts, the ions closest to the electrode are constrained and strongly absorbed to form the compact/Stern layer while the

ions outside the compact layer are dispersed as the diffuse layer as shown in the Gouy-Chapman model.[32,36]

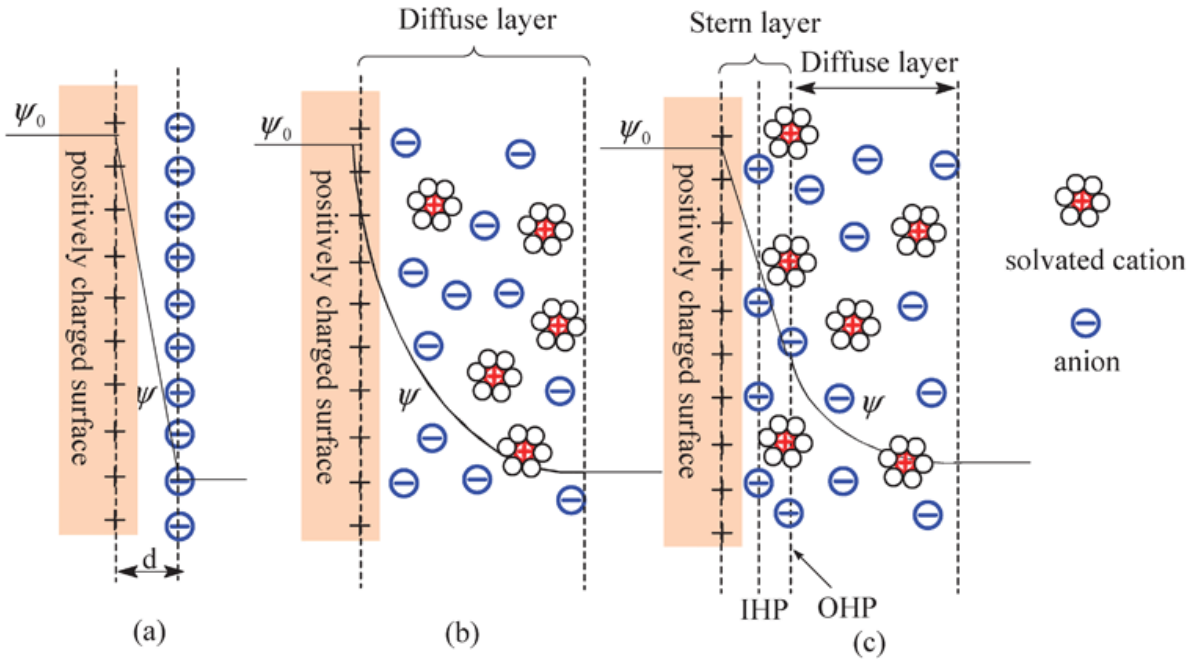


Figure 1.2 Models of the electrical double layer (EDL) with a positively charged surface in **a)** the Helmholtz model; **b)** the Gouy-Chapman model and **c)** the Stern model. Figure reproduced from ref.[36]

1.1.2.3 Mass Transport

Mass transport describes the movement of substances in solution, which occurs via three main mechanisms: diffusion, migration and convection.[31] Diffusion is defined as the spontaneous movement of the species down the concentration gradient while migration refers to the movement of charged species caused by the gradient of the electrical potential across the solution.[28] Convection is caused by the movement of solution via natural or forced process.[28] The natural process depends on the thermal or density gradients while the forced process is related to the mechanical stirring, bubbling or pumping of the solution. Forced convection could be enhanced deliberately via different mechanical methods such as rotating disk to minimize the effect of the unpredictable natural convection to allow the well-defined quantitative analysis and boost the electrochemical signal by providing more fresh electroactive species to the interface.

In general, to facilitate the probing of the electrochemical reactions taking place at the electrode surface, the effect of mass transport needs to be minimized to prevent it from being the rate-limiting step.[28] Different hydrodynamic techniques can be employed to ensure the sufficient transfer of reactants to and products away from the electrode, including rotating disk electrodes, wall jet electrodes and gas bubbling to the electrodes.[28] Another strategy to prevent mass transport limitations is to add a high concentration of supporting electrolyte that provides ample amount of reactant at any time. Protons in acidic electrolytes for hydrogen evolution reaction (HER) is a good example where reactants are present in the electrolyte in high concentrations.

1.1.2.4 Chemical Adsorption

For a chemical reaction to take place, adsorption of the reactant molecule onto the substrate is an essential step. Principally, adsorption can be classified into physisorption and chemisorption. The former is taken as the precursor state where molecules are lightly attached to the substrate surface by van der Waal's force (bond strength c.a. 13 - 42 kJ/mol); the latter, in contrast, refers to the formation of chemical bonds because of orbital overlap between the reactant and substrate in proximity (bond strength c.a. 84 - 418 kJ/mol).

The strength of chemisorption determines the rate of reaction. To accelerate the chemical reaction, catalysts can be added to lower the activation barrier by providing an alternative pathway. Paul Sabatier further discovered that the binding energy between the catalyst and the reactant should not be too strong or too weak in order to achieve greater catalytic performance.[37] Particularly, in electrochemical reactions, the principle explores the relationship between the exchange current density and the metal-hydrogen bond strength, which identifies the apex position at around 245 kJ/mol (Figure 1.3). Below 245 kJ/mol, the current density increases with the strength of the M-H bond so as to provide enough binding force for the hydrogen to anchor on the metal for the reaction to take place; beyond 245 kJ/mol, the trend is reversed as the binding force is too strong which refrains the hydrogen atom from

desorbing for the dihydrogen formation; thus eventually poisons the catalytic interface. Under the Sabatier principle, platinum, with a moderate M-H bond strength, is identified to be the metal that stays the closest to the apex position as shown in Figure 1.3.

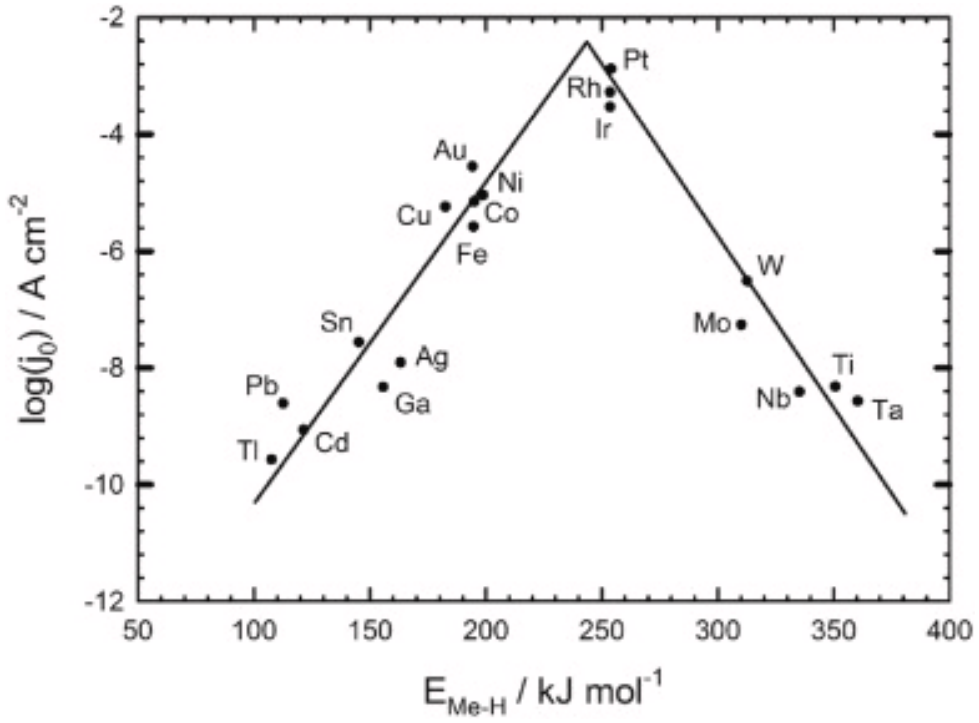


Figure 1.3 Volcano-type dependence between the exchange current density and Me-H bond strength. Figure reproduced from ref.[38]

1.1.3 Photoelectrochemical Catalysis

1.1.3.1 Background

Solar power is by far the most abundant and accessible source of renewable energy on Earth (~1.2×10^{14} kJ are received at the Earth's surface every second).[39,40] Thus, there is tremendous interest in coupling solar irradiation to electrochemical reactions to lower the activation barrier and energy consumption, which is called the photoelectrochemical (PEC) process. The photoactive nanostructures are able to convert the sunlight into a storable and distributable chemical fuel through the PEC process, which could be potentially achieved by PEC water splitting to generate hydrogen, carbon dioxide reduction to form hydrocarbon fuels (such as

methane, methanol and formic acid), nitrogen fixation to produce ammonia as the hydrogen carrier and so on.[41–47]

To date, plasmonic nanostructures are widely used as photoactive catalysts to drive the photoelectrochemical catalysis with the help of localized surface plasmon resonance (LSPR) excitation. The LSPR excited plasmons are capable of lowering the activation barrier, enhancing the chemical transformation rates and controlling the reaction selectivity. in the photoelectrochemical catalysis system.[24,48–53] The use of LSPR excitation to drive the photoelectrochemical catalysis can be divided into two different types: a) Indirect photoelectrochemical catalysis, where excitation of LSPR is used to transfer photon energy to nearby semiconductors and other photocatalysts to drive reaction remotely[48–50,52] and b) direct photoelectrochemical catalysis, where nanostructures are acting as both the light absorber and the catalytic active site.[24,53–55] In this thesis, we will focus on the direct photoelectrochemical catalysis on water splitting to make use of the LSPR excitation in lowering the activation barrier of the HER process and enhancing the reaction rate.

1.1.3.2 Localized Surface Plasmon Resonance (LSPR)

LSPR excitation occurs when the oscillation frequency of the free electron cloud in nanoparticles matches that of the incident photons (which are in fact electromagnetic waves with a pre-defined range of frequencies).[56] The oscillation frequency of the surface electron clouds depends critically on the nature of the material, for instance, electron density, nuclear mass, particle size. Taking these into account, only the coinage metals, such as silver and gold, can trigger LSPR massively under visible light.

Under illumination, the conduction electrons are excited, and a localized plasma cloud is formed, leaving behind a positively charged surface nuclei to form a dipole. Coulombic attraction will draw the electrons back, but as the sign of the electric field changes, a dipole in the opposite direction will be induced. When the oscillation frequency of the electron clouds

matches with the frequency of the incident photons, the resonance between the photons and the surface electrons will lead to LSPR excitation, which then builds up a strong electric field and high concentration of energetic electrons at nanoparticle surfaces.[56–58]

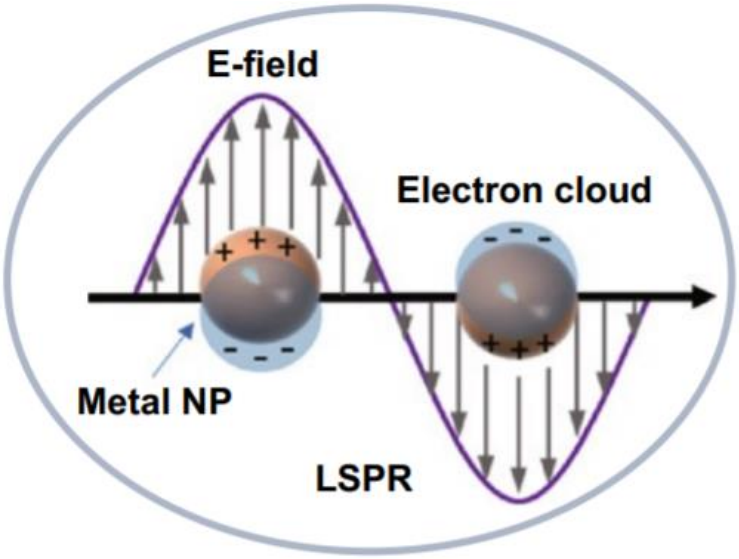


Figure 1.4 Schematic of localized surface plasmon resonance (LSPR) induced on the metal NPs by incident light. Figure reproduced from ref.[59]

1.2 Electrochemical HER

Water electrolysis is the process of splitting water into hydrogen and oxygen through external electrical inputs, where the first commercial demonstration can be dated back to the 19th century. Notwithstanding the concerted efforts in 100 years of research and development, only 4% of H_2 global supply is produced by the electrochemical water splitting given the high capital cost of the system (dominated by the limited supply hence costly platinum-based catalysts particularly).[60] In practice, the energy conversion efficiency of a commercial electrolyser system is about 60-80%,[1] allowing rooms for further development of earth-abundant and efficient electrocatalysts systems to raise the energy conversion efficiency and lower the capital cost.

1.2.1 Electrochemical Water Splitting Fundamentals

The water electrolysis process is composed of two separate reactions: oxygen evolution reaction (OER) at the anode and hydrogen evolution reaction (HER) at the cathode. The minimum theoretical thermodynamic voltage required to drive the OER and HER (to spilt water) is 1.23 V, based on a Gibbs free energy change of $\Delta G^0 = 237.2$ kJ mol^{-1} (298K and 1bar). However, additional energy (activation energy, Ea) is required to drive the reaction to proceed at an appreciable rate, which can be achieved by applying an additional potential bias (overpotential η) above the 1.23 V minimum to the water-splitting system. This overpotential can then be reduced by the use of different electrocatalysts.[40,61]

Alkaline water electrolysis and Proton Exchange Membrane (PEM) water electrolysis are widely employed for hydrogen production and being matured technologies at a commercial level worldwide.[61] In alkaline water electrolysis, the cathode and anode are immersed in a liquid alkaline electrolyte consisting of caustic potash solution (20% - 30% KOH). As shown in Figure 1.5a, the cathode and anode of the alkaline electrolysis system are separated by a diaphragm which only allow hydroxide ions and water molecules to get through, so that the product gases (O_2 and H_2) can be separated to maintain system efficiency and safety.

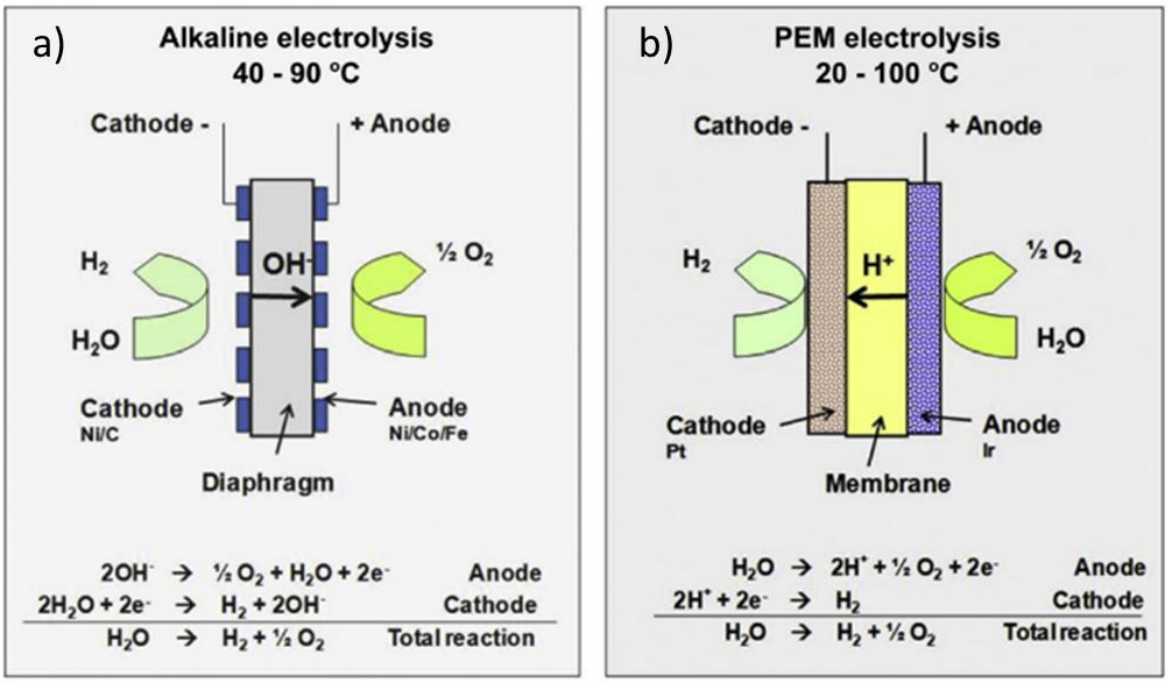


Figure 1.5 Schematic illustration of **a)** the alkaline water electrolysis system and **b)** PEM water electrolysis system with corresponding reaction steps. Figure reproduced from ref.[61]

However, alkaline electrolysers have three major issues, including gas crossover through the diaphragm, limited current densities and low operating pressure.[61] As the diaphragm cannot completely prevent the product gas from cross-diffusing through it, which may lead to an explosive hydrogen concentration level (lower explosion limit >4 mol% H_2) in the oxygen evolution chamber.[62] Additionally, the high ohmic losses across the liquid electrolyte and diaphragm resulting in the low achievable current density and the liquid phase of alkaline electrolyte makes it impossible to operate under high pressure.

On the other hand, the PEM electrolyser can greatly overcome the drawbacks of the alkaline electrolyser. The solid polymer electrolyte membrane (Nafion®) acts as both electrolyte and product gas separator in the system, which can provide high proton conductivity, low product gas permeability and achieve a compact cell design with high operating pressure. At the same time, the thin PEM membrane (~20-300 um thick) provides a good proton conductivity of 0.1± 0.02 S cm^{-1} at room temperature,[63] which enables to achieve a higher current density above 2 A cm^{-2}, reducing the operational and intrinsic cost of the electrolyser modules.

Moreover, the ability of the PEM membranes to operate at high pressures brings the advantage of delivering hydrogen at high pressure (also called electrochemical compression) to the end-users, thus requiring less energy to further compress and store the hydrogen.[64] As shown in Figure 1.5b, in PEM water electrolyser, water is oxidized to gaseous oxygen and protons at the anode, the protons subsequently diffuse through the PEM and are reduced to dihydrogen at the cathode. The rate of PEM water electrolysis strongly depends on the electrocatalysts utilized since the electrodes both activate the adsorption of reactant species and provide an active surface for the bond cleavage and formation processes.

Throughout the years, the electrocatalysts for hydrogen evolution reactions have evolved from platinum black to platinum on carbon, with current efforts focused on lowering the loading of the Pt and improving the stability of the carbon support.[65,66] To date, the costs of the cathode catalysts still contribute a large part to the water electrolysis process, and as such, the aim of this thesis is to identify earth-abundant yet high-efficient electrocatalysts for the HER process.

1.2.2 HER Reaction Mechanism

The hydrogen evolution reaction is taking place at the cathode side of the water electrolysis system, which involves the transfer of two electrons to reduce two protons forming dihydrogen.

$$2H^+ + 2e^- \rightarrow H_2 \qquad (Equation\ 1.31)$$

The HER reaction under an acidic medium comprises two possible reaction routes, known as the Volmer-Tafel and Volmer-Heyrovsky mechanisms.[67,68] The mechanism starts with a primary discharge step (Volmer reaction) where the reduction catalyst abstracts a hydrogen atom from a proton source (Equation 1.32).[69] Here "cat" represents a surface site on the catalyst.

$$H_3O^+ + e^- + cat \rightarrow cat - H + H_2O\ (discharge\ reaction) \qquad (Equation\ 1.32)$$

The adsorbed H atom will then either combine with another adsorbed H to produce H_2 in the Tafel reaction (Equation 1.33):

$$cat - H + cat - H \rightarrow 2\,cat + H_2 \text{ (recombination reaction)} \quad \text{(Equation 1.33)}$$

OR will abstract an H atom from a proton source in a single electron transfer process, the Heyrovsky reaction (Equation 1.34):

$$H_3O^+ + e^- + cat - H \rightarrow cat + H_2 + H_2O\ (ion + atom\ reaction) \quad (Equation\ 1.34)$$

The schematic illustrations of the two HER mechanisms are shown in Figure 1.6.

When the electroactive sites are rich at the surface, protons in the electrolyte can be electrochemically discharged and adsorbed on an active site readily in the Volmer step. In such case, adsorbed hydrogens are more likely to be adjacent to each other and result in the formation H_2 via the Tafel mechanism. On the other hand, when the availability of electroactive surface sites is limited, the distance between two adsorbed hydrogen atoms produced from the discharge reaction is much greater than its van der Waals radius, which makes the Heyrovsky mechanism more favouable.[70]

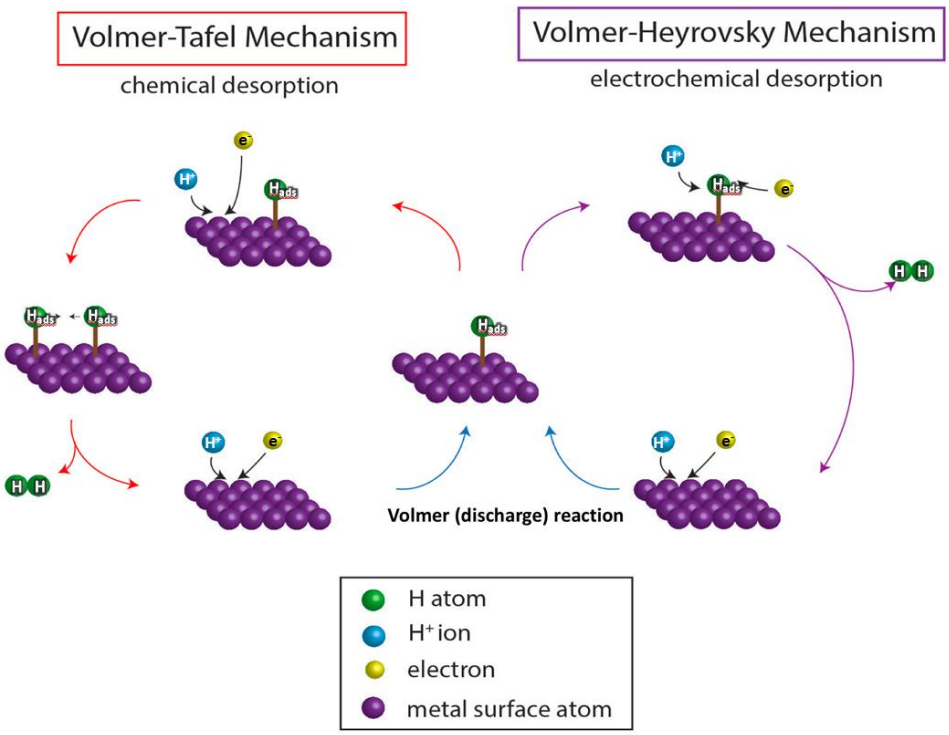


Figure 1.6 The mechanisms of hydrogen evolution on the surface of a metal catalyst under acidic conditions.

As mentioned in section 1.1.2.2.2, the Tafel slope is an important parameter to compare activities of different electrocatalysts for the HER, which can be obtained by plotting the logarithm of the magnitude of the current density versus overpotential η. Many researchers have reported that the magnitude of the Tafel slope is related to the rate-determining-step of the HER mechanism, which is associated with the binding energy between the metal catalyst surface and hydrogen atoms.[71,72] HER Tafel slopes of around 30, 40 and 120 mV dec^{-1} are suggested to be the evidence for the Tafel, Heyrovsky or Volmer limiting step respectively.[35,67] According to this, the Tafel slope is usually considered to be an important tool to gain initial insight into the reaction mechanism. On the other hand, the Tafel slope is also heavily dependent on the reaction conditions. For example, for 20 wt% Pt/C catalysts, the Tafel slope is at 30 mV/dec in 0.5 M H_2SO_4 in CV/LSV at a lower overpotential range, but changes to 120 mV/dec and 125 mV/dec with wider potential ranges when it is in PEM and 0.5 M NaOH conditions respectively. Furthermore, the validity of using only the Butler-Volmer equation to describe the electrocatalytic kinetics in the redox reaction is limited, the coverage terms of absorbed hydrogen should also be considered in the microkinetic model for mechanism analysis.[35]

1.2.3 HER Activity Descriptor

As mentioned in section 1.2.2, the HER is occurred via the Volmer-Tafel or Volmer-Heyrovsky mechanisms under an acidic medium. Both mechanisms involve the hydrogen absorption and hydrogen desorption process of the electrode catalyst surface, which are associated with the metal-hydrogen (M-H) bond strength as illustrated in Figure 1.3. Instead of M-H bond strength, the free energy of hydrogen adsorption (ΔG_H) is often used as an effective descriptor of activity.[73] A sufficient electrocatalyst that is active towards HER should bind the reaction intermediates neither too weakly nor too strongly according to the Sabatier principle. When the ΔG_H is strongly positive, implying weak absorption of hydrogen on the catalyst surface, leading

to a low coverage of reactants and the overall reaction rate is limited by the absorption step (Volmer limiting). On the other hand, if the ΔG_H is strongly negative with strong hydrogen absorption with the catalyst surface, the overall reaction rate is limited by the desorption step (Heyrovsky or Tafel limiting).[74] As a result, an optimal HER catalyst is expected to have a hydrogen absorption energy close to zero ($\Delta G_H \cong 0$), so that hydrogen binding energy will not be too weak or too strong.[71,75]

As shown in Figure 1.7, the experimentally determined HER current densities are plotted against the ΔG_H of different electrocatalyst materials, which shows a volcano-relationship that the catalyst with a hydrogen absorption energy close to zero results in a better HER catalytic performance. A critical step to develop the HER catalyst material is to control their binding energies to the active intermediate species during the reaction process. Pt electrocatalyst gives a hydrogen absorption energy slightly below zero, which sits at the top of the volcano curve and needs negligible overpotential to drive HER in acidic conditions. Nevertheless, the high cost and scarcity of platinum-based catalysts hinder their extensive use as electrodes. A series of non-Pt based electrocatalysts were developed,[12,76–78] and the volcano plot provides useful information regarding the catalyst design for HER. As a starting point, the electrocatalysts can be designed by using metals with a ΔG_H close to zero or changing the experimental conditions to facilitate the rate-determine step and hence the overall reaction rate. Detailed microkinetic analysis shows that the electrocatalytic activity is also strongly dependent on applied pH and potential which in turn on surface species coverage.[35] With different surface species coverages, the rate-determining step will be changed resulting in different accessibility of HER catalytic performance, which will be further discussed in chapter 4.

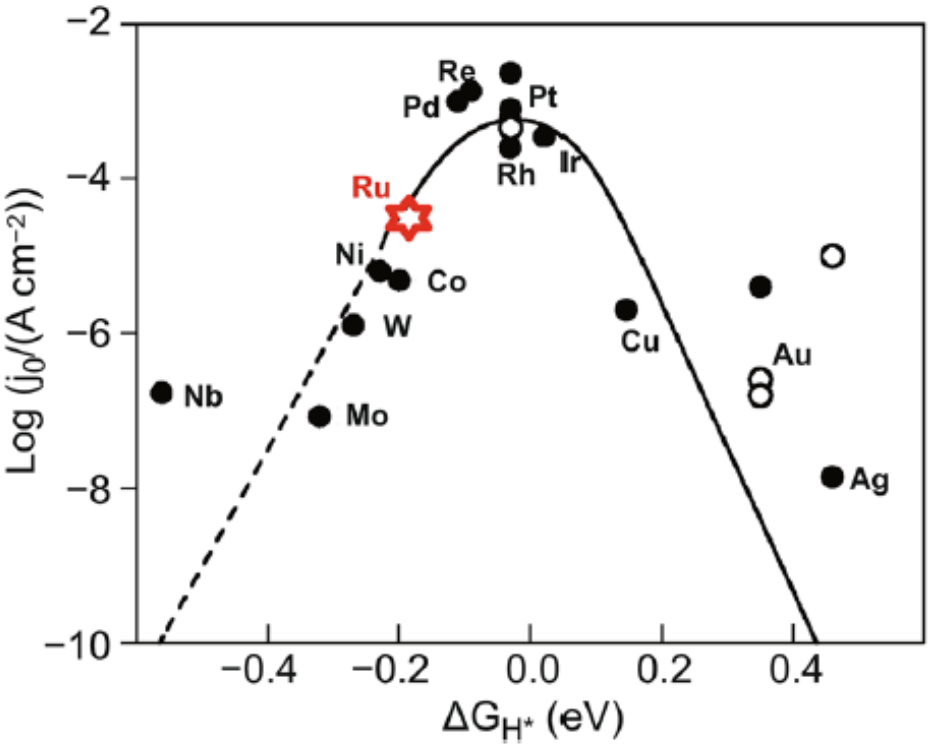


Figure 1.7 The logarithm of HER current density as a function of hydrogen absorption free energy (ΔG_H) for various catalysts materials. High H coverage of metals on the left side of the volcano, lower on the right side. Figure reproduced from ref.[79]

1.2.4 HER Activity Parameters

There are lots of methodologies employed for HER activity analysis in the literature for different electrocatalysts system comparisons. Onset potential, overpotential, Tafel slope measurements and turnover frequency (TOF) are usually employed to reveal the electrocatalytic activity for HER. LSV as one of the essential techniques to evaluate the HER activity is typically the first step in characterizing, in which the voltage is scanned from a lower limit to an upper limit at a constant scan rate to measure the catalytic current as shown in Figure 1.8a. The current is usually normalized to the superficial geometric electrode area enable the comparison of the catalytic activity in different electrocatalyst systems and experimental conditions.[80] The onset potential which indicates the potential at which the catalytic current is first occurred can be obtained by the LSV measurement. However, there are no standard criteria

for researchers to define the onset potential positions, which causes difficulties in comparing the catalytic activities between the electrocatalysts via the onset potential. As a result, comparing the overpotential required at the current density of 10 mA cm^{-2} has been accepted as the benchmark criteria in analysing the various electrocatalytic materials for HER and OER processes.[70] As 10 mA cm^{-2} is expected to be the current density corresponding to an efficiency of 12.3% for a solar-to-hydrogen device, which is suggested to be cost competitive with other hydrogen production methods.[80–83]

Along with the overpotential at 10 mA cm^{-2}, the Tafel slope measurement is also an important parameter to fulfil the mechanism analysis. As shown in Figure 1.8, electrocatalyst A (red) and electrocatalyst B (blue) show the same overpotential required for 10 m A cm^{-2}, but obviously, the HER mechanism is different for these two electrocatalysts according to their Tafel slopes as shown in Figure 1.8b. As mentioned in chapter 1, equation 1.22, the slope of the Tafel plot is inversely proportional to the charge transfer coefficient, which means the lower the Tafel slope, the faster the charge transfer across the electrocatalytic interface, resulting in better catalytic performance in HER. Electrocatalyst A with a lower Tafel slope will give a better catalytic performance for high current density devices such as PEM electrolysers in the range of current density > 10 mA cm^{-2} whereas electrocatalyst B has a lower onset potential and perform better at a lower current density range (< 10 mA cm^{-2}).[80] This will be further discussed in chapter 4 for Ag nanoparticles acting as cathode catalysts for HER in PEM water electrolysis. As a result, the overpotential required at specific current density as well as the Tafel slopes are important parameters to compare catalysts and analyse the mechanism, which both measure the total electrode activity.

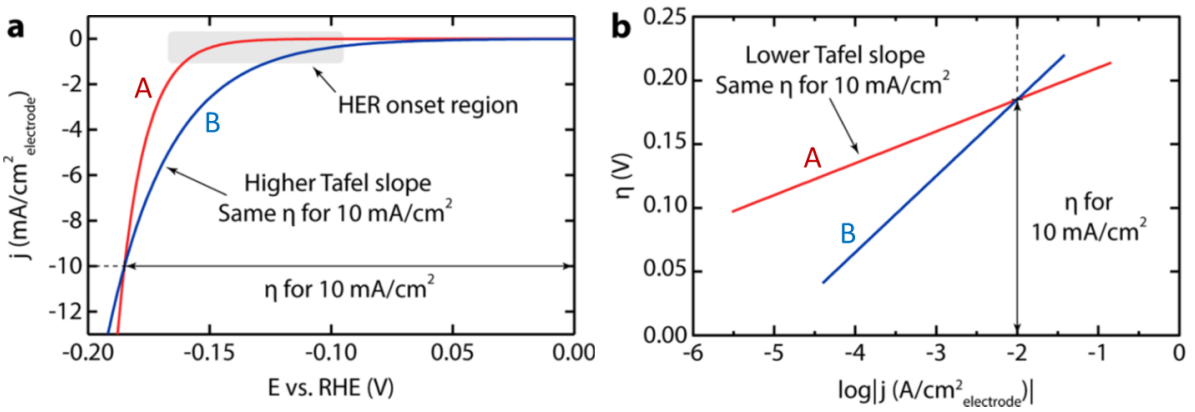


Figure 1.8 a) The LSV measurement of electrocatalyst A (red) and electrocatalyst B (blue) and their corresponding Tafel plot **(b)**. Figure reproduced from ref.[80]

On the other hand, the intrinsic activity measurement of each catalytic site can be determined by the turnover frequency (TOF, s^{-1}). In HER, TOF describes the number of H_2 gas molecules produced per active site per second, which can be used to evaluate how rapidly an electrocatalyst can catalyse the HER process.[70] In practice, the number of H_2 molecules produced can be measured by analytical equipment such as gas chromatography.

Measuring the electrochemically active surface area (ECSA) is one of the most common approaches to estimate the number of active sites in non-precious materials such as metal sulphides, metal selenides, metal carbides etc, which assumes every metal atom on the electrode is involved in the catalysis.[84–86] The ECSA is usually obtained by measuring the capacitive current in the non-Faradaic region at different scan rates.

$$ECSA = \frac{C_{dl}}{C_s} \qquad (Equation\ 1.36)$$

where C_{dl} is electrochemical double-layer capacitance; C_s is the specific capacitance. C_{dl} is half of the slope magnitude when the current density is plotted against the scan rate in the non-Faradaic region. C_s is the specific capacitance of a flat surface glassy carbon electrode with 1 cm^2 of surface area, which is assumed to be 40 µF cm^{-2}.[28,85,87]

The ECSA can be used to predict the activity trends of similar materials within the same studies, in most cases is in good agreement with the HER and OER activity trends of the catalytic materials.[70,88] However, the number of active sites does not scale directly with the overall surface area or ECSA, which hinders the accuracy of TOF estimation significantly in activity analysis. Due to the drawback of strong dependency on the active site density, TOF is therefore less useful as a primary activity parameter in evaluating electrocatalysts.[70,80]

At the same time, the catalytic performance is also dependent on the mass loading of the catalyst material (increase in metal loading will lead to inflated overheads and material costs), thus the activity per unit mass (or mass activity) is a critical metric to assess the feasibility of an electrocatalyst commercially.[89] In particular, for precious metal-based catalysts, the amount of catalyst used to achieve a required activity standard should be taken into account as the cost of the precious metal is a primary concern in practice.[90] In this thesis, the overpotentials, Tafel slope analysis and catalyst mass-normalized current density will be used in conjunction to compare the HER activities of different electrocatalyst systems.

1.3 Photoelectrochemical HER

The photoelectrochemical (PEC) hydrogen evolution reaction (HER) can be classified as the direct solar-to-hydrogen production regime where the PEC cell is responsible for both the light absorption and water splitting process. At the same time, it can also be considered as "artificial photosynthesis", whereby solar energy is captured and stored in the form of chemical fuel (H_2 in water splitting process).[91] As mentioned in section 1.2, the water splitting process is a thermodynamically uphill reaction (ΔG =237 kJ mol^{-1}) that requires an intensive electrical energy input of a minimum of 1.23 V at room temperature to drive the reaction.[83] By coupling with solar energy, a photoelectrochemical water splitting process requires a lower input bias to offset the overpotential for water oxidation and reduction. In other words, the oxygen evolution and hydrogen evolution step in a PEC water splitting process can take place at potentials below

1.23 V and above 0 V respectively when compared with the reversible hydrogen electrode (RHE).[43]

1.3.1 Reaction Mechanism

Photoelectrochemical cells convert water into hydrogen and oxygen with the help of solar energy in a two-electrode system, in which the photoactive nanostructures (such as plasmonic nanoparticles, semiconductors etc.) act as the working electrode and platinum wire (Pt) works as the counter electrode as shown in Figure 1.9. Additionally, reference electrode such as saturated calomel electrode (SCE) or Ag/AgCl electrode is employed in the system to investigate the half-reaction in the PEC cell in most measurements.[42]

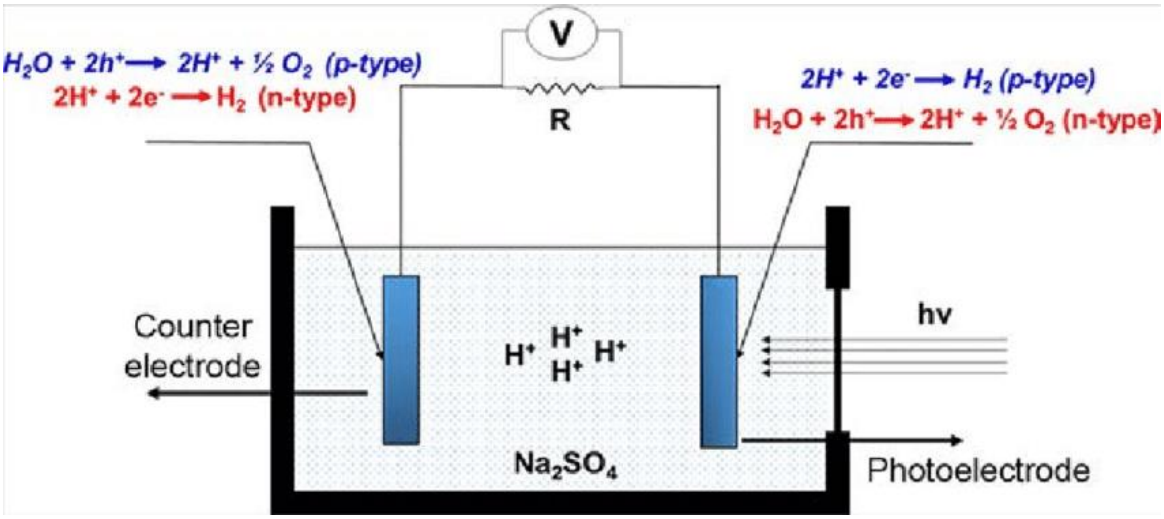


Figure 1.9 Schematic diagram of a photoelectrochemical cell for water splitting process using n-type or p-type semiconductor as the photoelectrodes. Figure reproduced from ref. [92]

In the PEC cell for water splitting process, the overall water splitting reaction is as follows:[93]

$$2H_2O \rightarrow 2H_2 + O_2 \qquad \Delta G = +237\ kJ\ mol^{-1} \quad (Equation\ 1.31)$$

When semiconductors are under illumination where photons are having higher energy than the bandgap (E_g), electron-hole pairs are generated. Similarly, when the resonance frequency of the oscillation of the surface electrons for plasmonic nanostructure matching with that of photons, LSPR excited hot electrons are generated.[42] Semiconductors that have a large number

of electrons in the conduction band is an n-type semiconductor, whereas in a p-type semiconductor, holes are the dominant carriers[93] (this is discussed in detail in section 1.4). When using n-type semiconductors as working electrodes, the excited electrons are collected in the photoanode and are subsequently transported to the counter electrode through an external circuit.[94,95] The photogenerated electrons are then consumed at the cathode (Pt counter electrode) to reduce H^+ into H_2, while the holes react with water molecules at the n-type semiconductor surface (photoanode) resulting in O_2 and H^+ formation as shown in Figure 1.10b. In contrast, when using a p-type semiconductor as the working electrode, photogenerated electrons are used to reduce H^+ into H_2, while in the counter electrode (Pt), water is oxidized to O_2 and H^+ as shown in Figure 1.10a. In other words, n-type semiconductors produce an anodic photocurrent for which holes are transferred to the electrolyte, while p-type semiconductors generate a cathodic photocurrent by transmitting electrons to the electrolyte.[95]

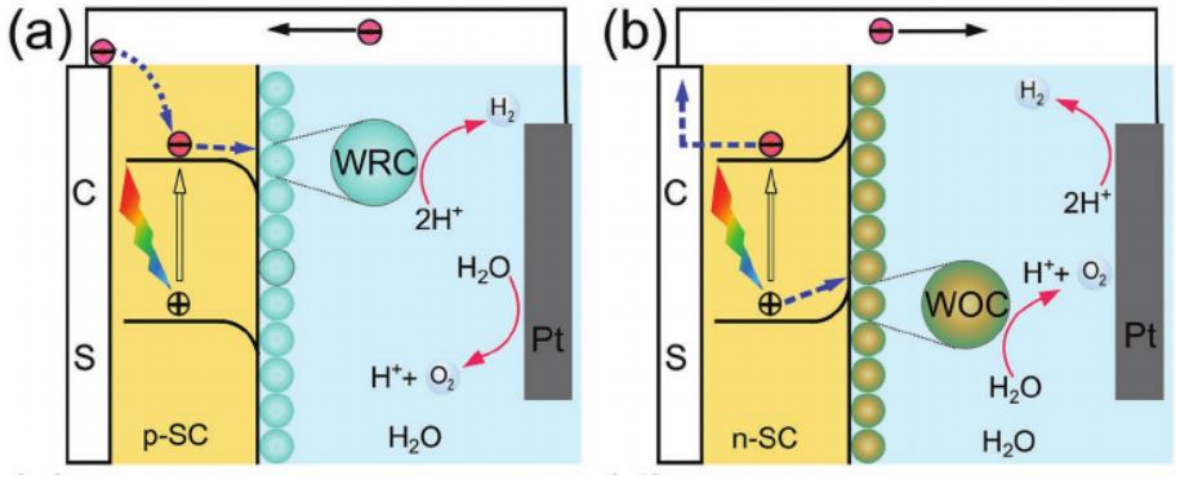


Figure 1.10 Photoelectrochemical water splitting process for **a)** p-type semiconductor and **b)** n-type semiconductor as the photoelectrode and Pt as the counter electrode. WRC: water reduction centre; WOC: water oxidation centre; CS: conducting substrate. Figure reproduced from ref.[96]

In the case of plasmonic nanostructures acting as the photoelectrodes, the PEC water splitting mechanism is similar to the p-type semiconductor system, in which the LSPR-excited hot electrons at the nanoparticle surface are used to reduce the H^+ into H_2 at the photocathode while

water is oxidized into O_2 and H^+ at the Pt counter electrode.[24] Plasmonic nanostructures acting as photoelectrodes to enhance the HER activity in the water-splitting system will be further discussed in chapter 5.

1.3.2 PEC Cell Performance Descriptors

The performance of the PEC cell can be evaluated by measuring its efficiencies such as apparent quantum efficiency (AQE), solar-to-hydrogen efficiency (STH) or applied bias photon-to-current efficiency (ABPE). It should be noted that the actual quantum efficiency is the internal quantum efficiency (IQE), which is calculated from the division of reacted electrons over the absorbed photons. However, it is hard to determine the number of photons absorbed by the specific PEC water splitting system due to light scattering and photon loss. As a result, the incident photons are detected and used to obtain the quantum efficiency at a specific monochromatic wavelength, known as apparent quantum efficiency (AQE).[97]

$$AQE(\%) = \frac{Number\ of\ reacted\ electrons}{Number\ of\ incident\ photons} \times 100\% \qquad (Equation\ 1.32)$$

$$= \frac{Number\ of\ evolved\ hydrogen\ molecules\ \times 2}{Number\ of\ incident\ photons} \times 100\% \quad (Equation\ 1.33)$$

The solar-to-hydrogen (STH) efficiency can be used as a practical standard to measure the performance of the photocatalysts that can be calculated as follows:

$$STH = \frac{Output\ energy\ as\ H_2\ gas}{Energy\ of\ incident\ solar\ light} = \frac{r_{H_2} \times \Delta G}{P_{sun} \times S} \times 100\% \quad (Equation\ 1.34)$$

where r_{H_2} is the rate of hydrogen production (mmol/s); ΔG is the gain in Gibbs free energy per mol of H_2 at room temperature ($237 * 10^3$ J mol^{-1}); P_{sun} is the energy flux of the sunlight (mW cm^{-2}) and S is the area of the working electrode (cm^2). Considering the ASTM-G173 AM 1.5 global tilt, the solar irradiation has an energy flux of 100 mW cm^{-2}.

The applied bias photon-to-current efficiency (ABPE) is the efficiency measured in the presence of an external applied bias. The external-applied bias and the generated photocurrent both take important roles in determining the ABPE of the PEC process as follows:

$$ABPE = \frac{|J_{ph}| \times (1.23 - |V_b|)}{P_{sun}} \times 100\% \qquad (Equation\ 1.35)$$

where J_{ph} (mA cm^{-2}) is the photocurrent density obtained under an applied bias V_b (V); P_{sun} is the energy flux of the sunlight (mW cm^{-2}). Considering the ASTM-G173 AM 1.5 global tilt, solar irradiation has an energy flux of 100 mW cm^{-2}.

According to a published report from the Department of Energy (DOE) in the U.S., the PEC technology needs to satisfy a series of requirements to attain a commercialization status: the photoanode materials need to achieve a STH conversion efficiency (>10%) at a constant photocurrent (10-15 mA cm^{-2}) with material stability of more than 2000 hours whilst maintaining cost-effectiveness.[42,98] To date, researchers have developed various catalytic systems for PEC water splitting applications, such as tandem systems composing of InGaP/GaAs that drives the STH efficiencies to 10-19%, but their high cost and poor stability hinder the technological translation into practical applications.[99–102] On the other hand, cost-effective photoelectrode materials such as WO_3 and Cu_2O possess high stability, but their STH conversion efficiencies are only in the range of 1-3%, which is below the DOE commercialization target.[41,103,104] As a result, the research of photoelectrode requires immense development before it can be deployed by the industry.

1.4 Catalyst Development for HER

Many experimental observations show that the HER activity is pH-dependent with a wide range of electrocatalysts.[105,106] Particularly, the experimental reaction rate of HER in alkaline solution is about two to three orders of magnitude lower than that in acidic solution, which has hindered the development in water splitting for high-purity hydrogen production.[107,108] Therefore, this

thesis focuses on developing the heterogeneous catalyst materials for hydrogen evolution in acidic media.

As mentioned in section 1.2.3, noble metal Pt-based materials are ideal HER electrocatalysts in terms of overpotentials. However, the high cost and scarcity of Pt widely hinder its commercial applications on large scales, and as a result, the development of earth-abundant metal catalysts is of crucial importance for HER process. Desirably, the electrocatalysts need to possess the following properties in order to replace Pt: highly active, cost-effective, stable over long-lifetime, and easily upscalable.[106,109] In recent decades, significant progress has been made in the search for non-platinum group metals (non-PGM) with the advent of transition metal chalcogenides,[82,84,110] metal nitrides,[111] bimetallic nanostructures,[112–114] single crystals[115,116] and metal nanoparticles (NPs) loaded on different supports,[117–119] which have comparable catalytic activities with Pt-based materials. Among the Pt alternative catalysts, metal NPs loaded on different supports are the catalysts that have the highest potential to scale up for commercialization. This is in contrast to 2D MoS_2-based materials that require time-consuming and hazardous n-Butyllithium exfoliations to obtain single/few layers in low yields[120] or metal nitrides that demand long synthesis time at high temperature settings with impurity concerns.[121] As a result, metal NPs loaded on various supports is the major electrocatalyst system used in this thesis, with focus on evaluating potential candidates for both the metal NPs and supports to maximize catalytic performance.

Compared with the commonly used platinum (Pt)-based catalysts, ruthenium (Ru) is expected to be a good alternative because of its similar metal-hydrogen bond strength (~65 kcal mol^{-1}), lower water decomposition barrier, and considerably lower price (only 4% cost of Pt).[79,122,123] Song *et al.*[124] reported the formation of Ru NPs on nitrogen-doped graphite carbon foam (Ru-NGC) exhibits a similar overpotential (25 vs. 29 mV) and Tafel slope (31 vs. 29 mV dec^{-1}) as

Pt/C at a current density of 10 mA cm^{-2} in 0.5 M H_2SO_4, indicating Ru-based catalysts are of great potential to be Pt alternatives.

Additionally, as HER is based on a series of surface processes, increasing the quantity of active sites by changing the electrocatalyst morphology plays a substantial role in enhancing the catalytic performance.[125] Great progress have been made to engineer metal nanoparticles at nanoscale leading to different size-and shape-dependent properties for various applications. Li *et al.*[126] successfully fabricated a pine-shaped Pt nanostructured electrode by facile electrodeposition techniques, showing an ultrahigh HER performance and fast current density enhancement of 3.85 mA mV^{-1}, which is 2.6 and 13.8 times higher than that of the Pt nanosphere and commercial Pt flat electrodes. Clark *et al.*[127] elucidated the strongly facet-dependent electrochemical reduction of CO_2 to CO is greatly promoted on the Ag (110) facets with superior CO evolution activity compared to the Ag (111) and Ag (100) facets due to large density of under-coordinated sites of Ag (110) facets. The morphology-controlled metal NPs will be further discussed in section 1.4.1 and morphology-controlled Ag NPs supported on carbon will be employed in chapter 4.

Introducing another metal into the lattice of a given metal is also an effective way to modify its electrochemical properties. For instance, a bimetallic surface can be fabricated for HER electrocatalysis, in which metal species with variant bond strengths with hydrogen can be introduced.[105] Thus, multi-functional active centres, including robust under-coordinated sites, can be created to optimize the ΔG_H of the electrocatalyst system for HER process. Lv *et al.*[128] have reported a new NiAu-Au core-shell nanoparticle that shows superior catalytic performance for HER in 0.5 M H_2SO_4, which is comparable to the benchmark Pt catalyst with a similar Tafel slope of 36 mV dec^{-1} (versus 30 mV dec^{-1} of Pt). It is suggested that the high activity arises from the formation of under-coordinated Au active sites around the shell, leading to a smaller ΔG_H (closer to zero) on the Au surface for HER. In this thesis, the bimetallic NPs

will be further discussed in Section 1.4.2 and Au-Ag core-shell nanoparticles are utilized for PEC hydrogen production in chapter 5.

On the other hand, efficient HER electrocatalysts should possess catalytic properties such as high electronic conductivity, active surface structure and large electrocatalytically active surface area, which can be achieved by incorporating conducting components into the electrocatalysts as catalyst supports for electrons/ protons transfer.[111] Carbon-based materials are widely used as supports for various catalysts owing to their low cost and excellent electron conductivity, which can greatly enhance the catalytic performance. This can be achieved by increasing the specific surface area to fully expose the metal active sites and prevent the aggregation of active sites during the reaction.[129] At the same time, metal oxides are also widely employed as supports for electrochemical catalysis due to their diverse structure, low cost and high abundance.[79,130] Compared with carbon, metal oxide supports tend to have stronger interactions with the metal NPs at the interface, which can enhance the activity and stability of the electrocatalyst systems.[79] Although the metal oxides generally suffer from lower electrical conductivity compared with the carbon supports, Wu *et al.*[131] discovered that the polar MgO (111) support would facilitate proton conducting by a network of hydroxyl groups on the polar surface, offering a great potential to utilize the polar MgO (111) materials as HER electrocatalyst supports to enhance the HER performance. In this thesis, polar magnesium oxide supports will be further analysed in section 1.4.3 and Ru NPs loaded on polar MgO (111) supports will be employed as the electrode catalyst for HER in chapter 6.

1.4.1 Morphology-controlled Metal NPs

It is generally believed that the properties of metal nanoparticles depend largely on the particle size, shape, composition, and crystallinity. In nanomaterials, the shape of the nanoparticles is determined by the different facet arrangements, and the resultant particle shape is expected to be a crucial factor that affects the electrochemical properties of a nanoparticle.[132] Both the reactivity and selectivity of a crystal can be tailored by controlling the shape of nanocrystals. For example, Wang and co-workers have employed Pt nanocubes (Pt (100) dominated), truncated cubes (Pt (100) dominated), and polyhedrons (Pt (111) dominated) as catalysts for the oxygen reduction reaction (ORR) in a H_2SO_4 medium.[133] It is reported that the current density of ORR for Pt nanocubes is four times that of the Pt polyhedrons, which can be attributed to the different binding strengths of sulphate ions on Pt (111) and Pt (100) facets. It is found that the strong adsorption of the sulphate ions on the Pt (111) facets hinders the ORR and causes the low activity of the Pt polyhedrons; whereas Pt nanocubes that are enclosed by Pt (100) facets have more active sites for ORR in H_2SO_4 medium that can give higher current density. As a result, enforcing refined control of particle morphology can tune the various electrochemical properties of the NPs.

It is well documented that surface energy dictates the formation of particle shape and the deviation from typical spherical geometry strongly affect the properties of the NPs.[132] The total surface energy is determined by the surface area and nature of the surface facets. To maintain a thermodynamically stable polyhedron shape with minimal energy, it can be achieved by enclosing the crystal with facets of the lowest possible surface energy as well as truncating appropriate facets to give the minimum possible surface area of a standard volume.[132] For the face centred cubic (FCC) structure, the surface energies of the low-index crystallographic facets is ascending in the order of $\gamma\{111\} < \gamma\{100\} < \gamma\{110\}$.[134] Based on the facet energy and surface area constraints, the minimum surface-energy requirement predicts that the FCC

crystal should be enclosed mainly by {111} facets in a truncated octahedron shape to maintain minimum surface area for a given volume, which achieves a nearly spherical shape.[132] A variety of methodologies are emerging for the synthesis of NPs in different morphologies such as temperature-dependent polyol synthesis, high-temperature reduction method, electrochemical synthesis and so on.[135]

In this thesis, the morphology-controlled NPs are mainly synthesized via polyol synthesis. The polyol process is widely used in commercial applications given its low cost, operational simplicity and scalability.[136] Principally, the polyol method is a versatile liquid-phase method utilizing both the high boiling point and reducing ability of polyol to produce the NPs, in which the polyol acts as both a reducing agent and a solvent.[136] The experimental process typically involves heating a suspension of metal precursors with a polymeric stabilizer dissolved in polyol at a temperature close to the refluxing point.[137]

Among various metals, silver has the highest electrical conductivity which is a crucial property for electrochemical reaction, and it is the most abundant and cost-effective metal compared with the other noble metals.[138] As a result, silver-based catalysts have drawn more and more attention in hydrogen evolution reactions. For example, Li *et al.*[138] adopted the laser ablation technique in liquid to generate Ag NPs with a high density of stacking faults (laser-generated Ag NPs, L-Ag NPs). According to their theoretical calculations, the production of stacking faults will lead to low coordination number and high tensile strain in L-Ag NPs, which can lower the ΔG_H remarkably (the ΔG_H closer to zero) and thus improve the hydrogen adsorption strength resulting in a superior catalytic performance in HER. The L-Ag NPs exhibits a lower overpotential (32 mV at 10 mA cm^{-2}) and Tafel slope (31 mV dec^{-1}) compared with that of the benchmark Pt/C (33 mV at 10 mA cm^{-2}, 35 mV dec^{-1}) with negligible degradation after 160 hours stability test.

In particular, silver-based catalysts with different morphologies (nanocubes, nanospheres, nanowires, etc.) have been widely applied in heterogeneous catalysis because of the tuneable surface active sites on the various dominant facets of the metal.[139] As mentioned above, the shape of the Ag NPs is determined by different facet arrangements. The Ag nanocubes are mainly enclosed by (100) facets; Ag nanowires are formed with (100) side facets and (111) facet ends; and the Ag nanosphere is mainly dominated by the thermodynamically stable (111) facets.[135] Silver crystal adopts an FCC structure and the atomic arrangement of close-packed Ag (111) and loose-packed Ag (100) are illustrated in Figure 1.11a.

The (100) surface can be obtained by cutting the FCC Ag crystal parallel to the front surface of the FCC cubic unit cell as shown in Figure 1.11b. On the (100) surface, each surface layer atom has a coordination number (CN) of 8, which consists of four nearest neighbours in the first layer and other four in the layer right below the surface layer. This is different from the CN of Ag metal atoms in the bulk which has a CN of 12 for FCC metals. The (100) surface offers various adsorption sites for molecules including atop sites, bridge sites between 2 atoms and hollow sites between 4 atoms. On the other hand, the (111) surface can be obtained by cutting the Ag FCC crystal by a surface plane that has the same x, y, z values as illustrated in Figure 1.11c. The (111) surface is adopting a hexagonal packing of the surface layer atoms, which is believed to be the most compact arrangement of atoms within a single layer, resulting in a close-packed Ag (111) surface. Additionally, the Ag (111) surface layer atoms have a CN of 9, including six nearest neighbours in the first layer and the other three in the layer right below the surface layer. All the surface atoms are equivalent and (111) surface offer adsorption sites of atop sites, bridge sites between 2 atoms, and hollow sites between 3 atoms.[140]

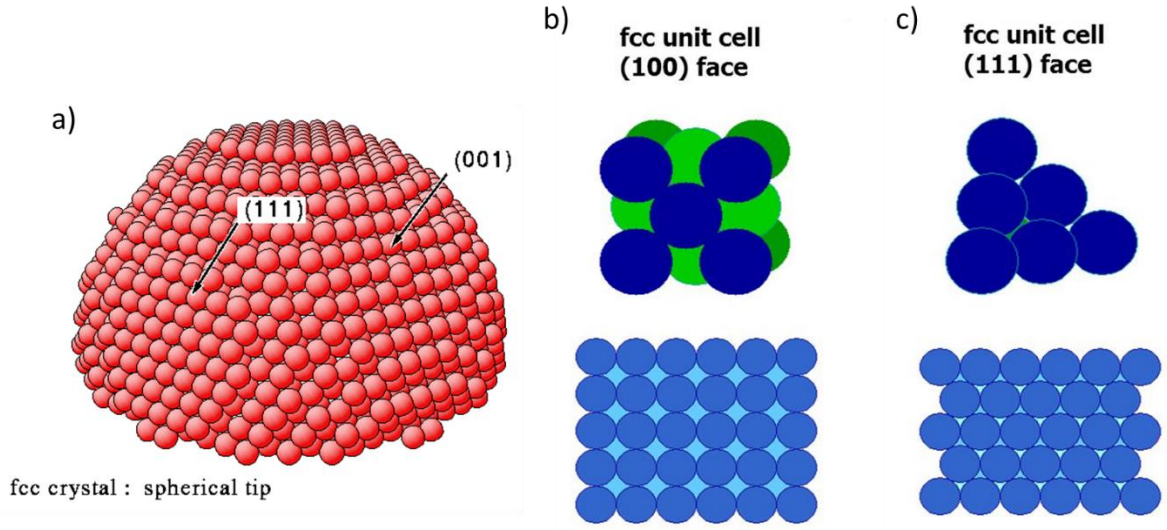


Figure 1.11 a) Schematic illustration of an FCC spherical crystal consists of (111) and (001) planes; **b)** FCC unit cell (100) face with the corresponding conventional birds-eye view of the (111) surface; **c)** FCC unit cell (111) face with the corresponding conventional birds-eye view of the (111) surface. Figure reproduced from ref.[141]

As pointed out above, the surface geometry, coordination number, adsorption sites and adsorption energy to molecules are different between the Ag (111) and Ag (100) surfaces. Both the reactivity and selectivity of Ag NPs can be tailored by controlling the mainly exposed surface of Ag nanocrystals. Additionally, the hydrogen adsorption energies as well as the M-H bond strengths are different between the Ag (100) and Ag (111) surfaces. Ferrin and co-workers[142] calculated that the surface H binding energy is more thermodynamically stable on the Ag (111) surface compared with the Ag (100) surface, resulting in different reactivity in HER process. Also, the surface H binding energy of Ag is much weaker than that of the Pt metals, such that the Ag NPs have a great potential to be a Pt alternative for HER under high surface species coverage where the M-H bond desorption (Tafel or Heyrovsky) is the rate limiting step. In this thesis, Ag NPs of different morphologies (nanocubes, nanowires and nanospheres) were synthesized via the polyol method and employed in PEM electrolyser as cathode electrocatalysts for hydrogen production; this is further discussed in chapter 4.

1.4.2 Bimetallic Core-shell Materials

Bimetallic nanoparticles (BNPs), by definition, are composed of two different constituent metals that can provide either multifunctionality or synergistic effect that is not otherwise possible with monometallic NPs. BNPs greatly depend on the identity of the constituent metal, the way the two metals are atomically arranged, as well as the particle sizes.[143] In other words, the activity of a less robust but low-cost metal for HER can be synergistically boosted by the other constituent metal, thereby reducing the need to use expensive metal groups. For example, Zhang and co-workers have prepared a Pd-Cu BNPs, namely $Pd_{71}Cu_{29}$/C NP, as electrocatalysts for HER, which outperforms the commercial monometallic Pd/C with an overpotential of 75 mV at 10 mA cm^{-2} and Tafel slope of 48 mV dec^{-1} (versus 182 mV at 10 mA cm^{-2} and 108 mV dec^{-1} of Pd/C) with high durability.[112] The superior activity of the bimetallic $Pd_{71}Cu_{29}$ NPs can be attributed to the modification of the electronic structure of Pd by electron transfer from Cu within the bimetallic NPs. As a result of the synergistic electronic effect between Cu and Pd, the duplex can approach the apex of the volcano curve as described by the Sabatier principle, and therefore the HER rate can be promoted significantly. It can thus be inferred that the catalytic properties of the resulting NPs can be improved to great extent via bimetallization, which may not be achieved by the use of monometallic catalysts, and more importantly, the consumption of precious materials can be reduced.[143]

The bimetallic NPs are usually prepared in different forms, such as alloys and core-shells. In particular, core-shell NPs are among the most studied nano-crystals, in which the properties can be modified by changing the constituting materials or the core to shell ratio.[144] Compared with alloys, core-shell nanostructures can be controlled precisely in particle size, core diameters, shell thickness, and morphologies of the core and shell.[145] The overall particle stability of the core can be increased by coating with layers of shell material, such that the reactivity of the core decreases and the thermal stability increases. Moreover, the shell coating

can offer additional properties to the core metal, particularly functional capabilities such as light capturing, dispersibility and stability.[145] Yang *et al.*[146] successfully synthesized uniform Ag-Au core-shell nanocubes particles, in which an ultrathin Au shell was deposited to protect the Ag core from the oxidative environment and resulted in improved chemical stability and surface-enhanced Raman scattering (SERS) activity compared with the pure Ag nanocubes.

The successive chemical reduction method is one of the most promising ways in synthesizing core-shell structured bimetallic NPs. It involves the deposition of metal on the pre-synthesized monometallic NPs of another metal, where the pre-synthesized monometallic NPs are chemically surrounded by the deposited metal atoms.[143] In this thesis, Au-Ag core-shell nanospheres were synthesized for HER catalytic reaction. To facilitate the crystallization of Ag as a shell on the Au core, Ag precursors underwent a controlled stepwise reduction in the presence of pre-synthesized Au nanospheres. Additionally, the sonochemical approach was also employed in the Au-Ag core-shell synthesis to improve the reaction rate, break down agglomerates and enhance the dispersion of particles in the solvent media.[145] As a result, the Au-Ag core-shell NPs have uniform shells and similar particle sizes.

Compared with other bimetallic nanocomposites, the lattice constants of Ag and Au are similar in magnitude (2.3 Å for Ag (111) and 2.4 Å for Au (111)) that allows versatile formation of a wide range of bimetallic nanostructures.[147] As plasmonic metals, Ag and Au both have excellent optical properties in the visible light region and outstanding electronic conductivity; this makes them good candidates for electrochemical and photoelectrochemical hydrogen production catalysts.[148] In particular, the surface plasmon resonance (SPR) absorption of Ag and Au features at different wavelength regimes (400 - 450 nm for Ag and 510 - 540 nm for Au for a particle size of 10 - 50 nm),[149,150] which can lead to a broader visible-light absorption range within the Ag-Au bimetallic NP compared with the monometallic cases. However, both elements have their own benefits and shortcomings. Au has a low interband transition energy

of 2.3 eV and it may thus lead to energy loss through such transitions; whereas the larger energy gap of Ag (3.7 eV) does not allow this interband transition and hence incident light energy can be utilized more efficiently for hot electron generation.[151] Additionally, Au is resistant in the oxidative environment compared with the Ag NPs. As a result, the fabrication of Ag and Au NPs into Au-Ag core-shell nanostructures can combine the advantages of these two metals into one single NP. In this case, Ag can enable the efficient use of incident light energy with lower interband transition loss in the visible light and near-infrared range; while Au can enhance the overall resistivity of the NPs to oxidative degradation.[152] Additionally, the optical features of Au-Ag core-shell NPs can be tuned and tailored to specific absorption regions for various applications by regulating the compositions, shell thickness and particle sizes.[153]

LSPR excitation in plasmonic Ag/Au NPs can be indirectly used to empower semiconductors in photocatalysis by acting as both light absorbers and electron mediators. This enables maximum utilization of the entire visible light region of the solar spectrum and promotes charge separation.[56,154–156] Patra *et al.*[147] deposited a Ag shell over an Au core supported on TiO_2 for solar water splitting to enhance H_2 production activity. The Au-Ag core-shell NPs are used to broaden the range of visible-light absorption between 400-650 nm that is conducive to hot electron formation. They pointed out the Au core binds to TiO_2 directly to form heterojunctions to promote charge seperation; whereas the deposited Ag shell enhances the electron transfer process. Upon visible light absorption, the Au-Ag core-shell NPs are triggered to form hot electrons that are subsequently transferred to the TiO_2 conduction band for hydrogen evolution. Meanwhile, Shi *et.al*. reported the use of a plasmonic Au-MoS_2 hybrid to greatly improve the HER by increasing the carrier density in MoS_2 through the injection of hot electrons from the Au nanorods.[157] In general, most of the reported methods rely on semiconductors to act as electron acceptors for hydrogen production so as to inject LSPR-excited hot electrons into the conduction band. However, the inevitable high impedance across

the bandgap and the low concentration of mobile electrons of the semiconductors have concomitantly limited their electronic conductivity, which causes a low solar-to-hydrogen (STH) efficiency.[158–160]

On the other hand, bifunctional Au-Ag core-shell NPs provide a great potential to directly harness solar energy without the use of bandgap materials for HER. Under visible light illumination, plasmonic hot electrons can be generated by Au-Ag cores-shell NPs for hydrogen formation on the polarized metallic surface. In this case, the silver shell provides higher energy (more positive) excited states as an avenue to allow LSPR-promoted hot electrons to carry out proton reduction and the low interband transition loss enables the efficient use of incident light energy. At the same time, the gold core is for plasmonic absorption to capture major solar radiation (major peak at ~530 nm)[161] and enhance the overall particle resistivity to oxidative degradation. Moreover, both Ag and Au are well-recognized active metal centres in electrochemical reactions due to their superior electrical conductivity and excellent stability.[138,162–164]

As a result, the Au-Ag core-shell NPs are great candidates for both electrochemical and photoelectrochemical hydrogen production. In this thesis, Au-Ag core-shell NPs with tunable mixed shell composition and shell thickness were employed as the electrocatalysts for HER in chapter 5.

1.4.3 Metal Oxide Supports

In industrial heterogeneous catalytic processes such as petroleum refinement and energy conversion, catalysts are usually composed of metal particles supported on metal oxides (MMO) with flexible tunability.[165–167] The wide adoption of MMO structures is due to the intrinsic strong metal-support interactions (SMSI), which can reduce the usage of costly precious metal by dispersing it across the support whilst maintaining a high surface area.[168,169] In addition, the

structural and electronic properties of the catalyst can be modified through SMSI to achieve favourable activity and durability.[170,171]

In the past, it was believed that metal oxides are inactive towards electrochemical reactions due to their insulating or semiconductor behaviour and hence limited electronic conductivity.[172] Nonetheless, in recent years, several advances have been made such that metal oxides are not only being widely used as catalytic supports for HER, but also allows the use of platinum-free active sites (such as nickel, cobalt, phosphide, ruthenium).[173–175] There are several widely-reported methods that can modify and activate the metal oxides, including oxygen vacancy control,[176] phase-structure engineering,[177] non-metal doping,[178,179] metal doping,[180,181] and morphology engineering.[182,183] For example, Li and co-workers have activated the molybdenum oxide surface with oxygen vacancies by introducing P dopants into the system.[179] The authors suggest that phosphorus, having a low electronegativity, can enhance proton adsorption and desorption that ultimately facilitates HER. Meanwhile, Luo *et al.*[182] have created large accessible pores on molybdenum oxides that can facilitate mass transport and charge transfer during HER.

In addition to the aforementioned methods, there is a surface cleavage strategy that can unleash the intrinsic potential of the metal oxides. By definition, this method truncates the less active surface of the metal oxides and leave behind the more active facets. As mentioned in previous sections, more active facets imply higher surface energies, which thus provides more active interfaces for catalytic reactions to take place. Among the metal oxides that can aptly undergo surface modifications, magnesium oxide has received numerous attentions in recent years due to ease of exposing its polar surface.[184–188] A typical polar MgO powder can be synthesized by the hydrothermal method using benzoic acid, which can effectively suppress the growth of the more stable (100) and (110) facets.[189] The (111) facet can thus become the dominant exposed surface. Furthermore, octopolar MgO (111), in which all the 8 exposed surfaces are (111) facet,

can be synthesized by progressive surface reconstructions from MgO nanocube to octahedron-shape for a prolonged period.[190–192]

Naturally, the most stable form of magnesium oxide is composed of Mg^{2+} and O^{2-} ions arranged alternately in a solid ionic lattice such that the charges are cancelled out against each other resulting in a net-zero dipole moment (Figure 1.12a).[193] The stability is given by the long-range Madelung potential where electrons are stabilized at oxide sites and destabilized at the Mg^{2+} sites. By preferentially exposing the MgO (111) facets, the Mg^{2+} and O^{2-} ions are arranged in alternate layers instead and generate a net dipole moment (Figure 1.12c). This will lower the vacant Mg^{2+} orbitals and raise the O^{2-} orbitals, and ultimately reduce the binding energies of the valence electrons in the occupied energy states. The less electrostatically bounded electrons give rise to high surface energy of the polar facets.[194]

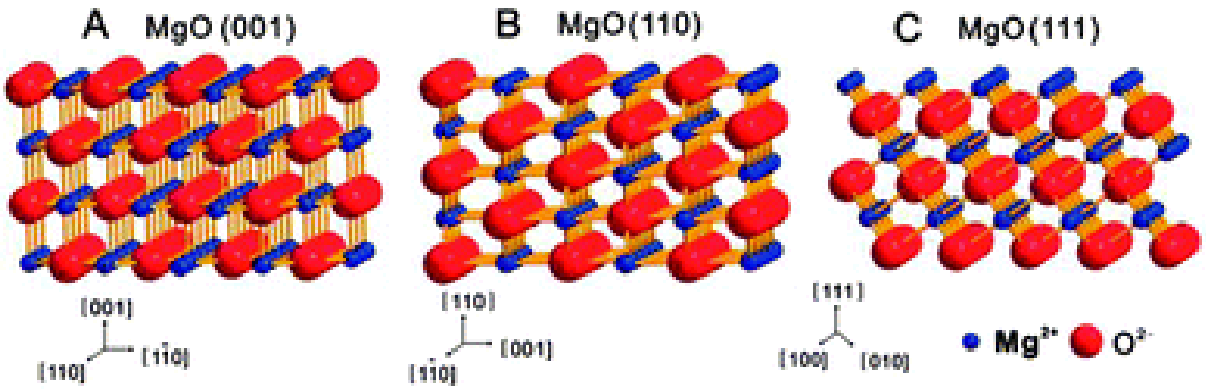


Figure 1.12 Atomic structure of MgO with predominant exposure of **a)** (001) facet; **b)** (110) facet; **c)** (111) facet. Figure reproduced from ref.[193]

Macroscopically, high-energy facets, caused by the net dipole moment on the polar surface, often result in electrostatic instability, which can be relaxed or cancelled by the introduction of compensating charges.[194] This can be achieved by modification of the surface electronic structure, such as surface reconstruction or redox change of framework species; or by a strong change in the surface stoichiometry such as adsorption of foreign molecules.[195] These processes can give rise to surface defects and alter the surface stoichiometry, allowing electronic structure

modifications that can catalyse surface reactions. For example, Liao and co-workers have previously reported a Cu/polar ZnO structure that exhibited a higher methanol selectivity (70%) than the non-polar ZnO counterpart (40%).[196] The authors attribute this to the formation of surface defects during the relaxation of the high-energy polar ZnO (002) facets, conferring the catalyst a strong electron trapping ability. Subsequently, the electrons of the polar ZnO at the conductive band could be transferred to the Cu Fermi level and facilitate the hydrogenation of CO_2 to methanol.

Unlike typical polar metal oxides that can relax through redox changes, such as from Ce^{4+} to Ce^{3+} for polar CeO_2, the rigid oxidation state of Mg^{2+} has rendered this solution not feasible.[197] Instead, a more energetically favourable solution is to allow the adsorption of protons or water molecules onto the highly energetic oxygen-terminated surface of MgO (111).[198] The compensation of charges can effectively reduce the surface energy. Additionally, by depositing metal species onto the polar surface, electron transfer can take place at the particle interface and provide extra stabilization.[199]

The resultant proton-covered surface of MgO (111) resembles the (001) facet of brucite $Mg(OH)_2$. This provides an extensive network of surface hydroxyl groups with a close interatomic distance that allows Grotthuss-like hydrogen-bonding movements and hence offers the platform of facile proton hopping.[188,200] In this thesis, MgO with preferentially exposed (111) facets is utilized as catalytic supports to host surface protonic movement and to provide the framework for phase change during the electrochemical hydrogen evolution reactions. More details will be explored in chapter 6.

1.5 Aims and Objectives

As discussed in the previous sections, the optimization of the hydrogen evolution reaction (HER) plays a crucial role in reducing the overall cost of water electrolysis and hence leaping

forward towards the carbon-free hydrogen economy. In this thesis, a series of novel electrocatalysts are synthesized and employed for electrochemical HER, along with utilizing photoelectrochemical means in lowering the overpotential for the reaction.

As illustrated previously, one of the directions towards the optimization of electrochemical HER is to replace the platinum-based catalysts with more abundant metal candidates at a lower cost. A detailed investigation has been undertaken to screen a multitude of metal species and it was discovered that the use of silver-based metal active centres can deliver higher catalytic performance than platinum but at a cost of higher overpotential. On the other hand, it is also proposed in the literature that lowering the required applied voltages at a given current density of the water electrolysis can significantly reduce the operational expenses incurred during the reaction. We therefore suggest the tactical introduction of visible light into the system in order to reduce the electrical energy input. With the help of LSPR-enabled core-shell materials, photons can be captured from the visible light region and HER can be promoted by the LSPR-excited hot electrons for more readily proton reductions via the bifunctional catalytic surface. A detailed mechanism has also been derived to explain the rationale.

In addition to the metal-groups, altering the catalytic supports can also strategically facilitate the proton reduction mechanisms that ultimately improves the HER rates. Electrostatically polar MgO (111) supports have been employed to study the proton-hopping effect on the catalytic supports. A variety of spectroscopic techniques have been carried out to investigate the proton migration mechanism on the catalytic surfaces and rationalize the structure-activity correlations on MgO supports.

1.6 Thesis Overview

This thesis contains seven chapters with chapters 4 to 6 systematically detailing the three electrochemical systems studied over the course of this DPhil degree.

Chapter 1 introduces the fundamental concepts used in this thesis, with the first sub-section outlining the general theories behind the electrochemical and photoelectrochemical catalytic processes. A library of equations has also been derived and explained in this sub-section. The next two sub-sections expand on the electrochemical and photoelectrochemical HER respectively, including the fundamental working mechanisms and the factors that affect the catalytic performance. The fourth sub-section in chapter 1 reviews the catalyst development for HER, specifically from the perspectives of three different systems, including morphology-controlled metal nanoparticles, bimetallic core-shell materials, and electrostatically polar metal oxide catalytic support.

Chapter 2 provides an overview and the principles behind various analytical techniques used in this thesis, which includes imaging, spectroscopy, and electrochemical methods.

Chapter 3 details the experimental protocols regarding the characterizations and catalytic performance evaluations described in the following experimental chapters.

Chapter 4 outlines the screening of a range of metal NPs on carbon catalysts, and silver is particularly selected due to its exceptional performance. The characterizations of a series of morphology-controlled silver NPs are then conducted, followed by electrochemical testing of the materials at a range of applied potentials. The structure-activity relationship is then explored where the hydrogen adsorption energies of different facets are correlated to the catalytic performance.

Chapter 5 details the protocol for applying visible light to lower the onset overpotentials of HER. A library of gold-silver core-shell NPs with different shell thicknesses is synthesized as the electrocatalysts and characterized to investigate the mechanisms of the LSPR-promoted HER.

Chapter 6 outlines the synthesis and characterizations of the electrostatically polar MgO (111) nanosheet and assess its potential as an electrocatalyst support in HER. In-situ synchrotron X-ray diffraction techniques are employed to discern the effect of the structural changes of the material on the enhanced electrochemical activity.

Chapter 7 summarizes the findings of the previous chapters and provides an outlook to future directions of relevant research.

1.7 References

1. Shiva Kumar, S. & Himabindu, V. Hydrogen production by PEM water electrolysis – A review. *Mater. Sci. Energy Technol.* **2**, 442–454 (2019).
2. King, L. C. & Van Den Bergh, J. C. J. M. Implications of net energy-return-on-investment for a low-carbon energy transition. *Nat. Energy* **3**, 334–340 (2018).
3. Pinaud, B. A. *et al.* Technical and economic feasibility of centralized facilities for solar hydrogen production via photocatalysis and photoelectrochemistry. *Energy Environ. Sci.* **6**, 1983–2002 (2013).
4. Creutzig, F. *et al.* The underestimated potential of solar energy to mitigate climate change. *Nat. Energy* **2**, 17140 (2017).
5. Ma, Y. *et al.* Titanium dioxide-based nanomaterials for photocatalytic fuel generations. *Chem. Rev.* **114**, 9987–10043 (2014).
6. Pu, Z. *et al.* A universal synthesis strategy for P-rich noble metal diphosphide-based electrocatalysts for the hydrogen evolution reaction. *Energy Environ. Sci.* **12**, 952–957 (2019).
7. Cabán-Acevedo, M. *et al.* Efficient hydrogen evolution catalysis using ternary pyrite-type cobalt phosphosulphide. *Nat. Mater.* **14**, 1245–1251 (2015).
8. Dincer, I. & Zamfirescu, C. *Sustainable Hydrogen Production*. *Sustainable Hydrogen Production* vol. 305 (Elsevier, 2016).
9. Tiwari, J. N. *et al.* Multicomponent electrocatalyst with ultralow Pt loading and high hydrogen evolution activity. *Nat. Energy* **3**, 773–782 (2018).
10. Niether, C. *et al.* Improved water electrolysis using magnetic heating of FeC-Ni core-shell nanoparticles. *Nat. Energy* **3**, 476–483 (2018).
11. Yu, L. *et al.* Non-noble metal-nitride based electrocatalysts for high-performance alkaline seawater electrolysis. *Nat. Commun.* **10**, 1–10 (2019).
12. Mo, J. *et al.* Superior Performance of Ag over Pt for Hydrogen Evolution Reaction in Water Electrolysis under High Overpotentials. *ACS Appl. Energy Mater.* **2**, 1221–1228 (2019).
13. Wang, Y. *et al.* Mimicking Natural Photosynthesis: Solar to Renewable H2 Fuel

Synthesis by Z-Scheme Water Splitting Systems. *Chem. Rev.* **118**, 5201–5241 (2018).

14. Mateo, D. *et al.* 111 Oriented Gold Nanoplatelets on Multilayer Graphene As Visible Light Photocatalyst for Overall Water Splitting. *Nat. Commun.* **7**, 1–8 (2016).

15. Zhao, Z. *et al.* Electronic structure basis for enhanced overall water splitting photocatalysis with aluminum doped SrTiO3 in natural sunlight. *Energy Environ. Sci.* **12**, 1385–1395 (2019).

16. Thompson, L. T., Schaidle, J. & Schweitzer, N. High activity carbide supported catalysts for water gas shift. *ACS Natl. Meet. B. Abstr.* 2378–2381 (2011).

17. Levalley, T. L., Richard, A. R. & Fan, M. The progress in water gas shift and steam reforming hydrogen production technologies - A review. *Int. J. Hydrogen Energy* **39**, 16983–17000 (2014).

18. Men, Y. & Yang, M. SMSI-like behavior and Ni promotion effect on NiZnAl catalysts in steam reforming of methanol. *Catal. Commun.* **22**, 68–73 (2012).

19. Roh, H. S., Eum, I. H. & Jeong, D. W. Low temperature steam reforming of methane over Ni-Ce (1-x)Zr (x)O2 catalysts under severe conditions. *Renew. Energy* **42**, 212–216 (2012).

20. Birol, F. *'The Future of Hydrogen: Seizing Today's Opportunities' Report prepared by the IEA for the G20*. (2019).

21. Simpson, A. P. & Lutz, A. E. Exergy analysis of hydrogen production via steam methane reforming. *Int. J. Hydrogen Energy* **32**, 4811–4820 (2007).

22. Howarth, R. W. & Jacobson, M. Z. How green is blue hydrogen? *Energy Sci. Eng.* **9**, 1676–1687 (2021).

23. IRENA International Renewable Energy Agency. *Green Hydrogen Cost Reduction Scaling Up Eletrolysers To Meet The 1.5oc Climate Goal*. (2020).

24. Mo, J. *et al.* Atomic-Precision Tailoring of Au–Ag Core–Shell Composite Nanoparticles for Direct Electrochemical-Plasmonic Hydrogen Evolution in Water Splitting. *Adv. Funct. Mater.* **31**, 1–11 (2021).

25. Rausch, B., Symes, M. D., Chisholm, G. & Cronin, L. Decoupled catalytic hydrogen evolution from a molecular metal oxide redox mediator in water splitting. *Science (80-.).* **345**, 1326–1330 (2014).

26. Li, M. *et al.* Single-atom tailoring of platinum nanocatalysts for high-performance multifunctional electrocatalysis. *Nat. Catal.* **2**, 495–503 (2019).

27. Watzele, S. A., Garlyyev, B., Gubanova, E. & Bandarenka, A. S. Structure-reactivity relations in electrocatalysis. in *Reference Module in Chemistry, Molecular Sciences and Chemical Engineering* (Elsevier, 2021).

28. Bard, A. J. & Faulkner, L. R. *ELECTROCHEMICAL METHODS Fundamentals and Applications*. (Wiley New York, 2001).

29. Léger, J. M. & Hahn, F. Chapter 3 - Contribution of In-situ Infrared Reflectance Spectroscopy in the Study of Nanostructured Fuel Cell Electrodes. in *In-situ Spectroscopic Studies of Adsorption at the Electrode and Electrocatalysis* 63–98 (Elsevier Science B.V., 2007).

30. Bard, A. J. & Faulkner, L. R. *Electrochemical Methods Fundamentals and Applications*. (John Wiley & Sons, Incorporated, 2000).

31. Compton, R. G. & Banks, C. E. *Understanding Voltammetry*. (Imperial College Press, 2011).

32. Atkins, P. & Paula, J. de. *Atkins' Physical Chemistry*. (OUP oxford, 2009).

33. Li, D., Lin, C., Batchelor-McAuley, C., Chen, L. & Compton, R. G. Tafel analysis in practice. *J. Electroanal. Chem.* **826**, 117–124 (2018).

34. Chen, J. Y., Jheng, S. Lou, Chan, C. Y. & Tuan, H. Y. Morphology controlled synthesis of Pd2Ge nanostructures and their shape-dependent catalytic properties for hydrogen evolution reaction. *Int. J. Hydrogen Energy* **44**, 12958–12970 (2019).

35. Shinagawa, T., Garcia-Esparza, A. T. & Takanabe, K. Insight on Tafel slopes from a microkinetic analysis of aqueous electrocatalysis for energy conversion. *Sci. Rep.* **5**, 1–21 (2015).

36. Zhang, L. & Zhao, X. S. Carbon-based materials as supercapacitor electrodes. *Chem. Soc. Rev.* **38**, 2520–2531 (2009).

37. Rothenberg, G. *Catalysis: Concepts and Green Applications*. (Wiley-VCH, 2008).

38. Durovi, M., Hn, J. & Bouzek, K. Electrocatalysts for the hydrogen evolution reaction in alkaline and neutral media. A comparative review. *J. Power Sources* **493**, 229708 (2021).

39. Blankenship, R. E. *et al.* Comparing photosynthetic and photovoltaic efficiencies and recognizing the potential for improvement. *Science (80-.).* **332**, 805–809 (2011).

40. Roger, I., Shipman, M. A. & Symes, M. D. Earth-abundant catalysts for electrochemical and photoelectrochemical water splitting. *Nat. Rev. Chem.* **1**, (2017).

41. Wu, H. *et al.* Photocatalytic and Photoelectrochemical Systems: Similarities and Differences. *Adv. Mater.* **32**, (2020).

42. Choudhary, S. *et al.* Nanostructured bilayered thin films in photoelectrochemical water splitting - A review. *Int. J. Hydrogen Energy* **37**, 18713–18730 (2012).

43. Marwat, M. A. *et al.* Advanced Catalysts for Photoelectrochemical Water Splitting. *ACS Appl. Energy Mater.* **4**, 12007–12031 (2021).

44. Li, J., Li, H., Zhan, G. & Zhang, L. Solar water splitting and nitrogen fixation with layered bismuth oxyhalides. *Acc. Chem. Res.* **50**, 112–121 (2017).

45. Tu, W., Zhou, Y. & Zou, Z. Photocatalytic conversion of CO2 into renewable hydrocarbon fuels: State-of-the-art accomplishment, challenges, and prospects. *Adv. Mater.* **26**, 4607–4626 (2014).

46. Liu, D. *et al.* Selective photoelectrochemical oxidation of glycerol to high value-added dihydroxyacetone. *Nat. Commun.* **10**, (2019).

47. Ali, M. *et al.* Nanostructured photoelectrochemical solar cell for nitrogen reduction using plasmon-enhanced black silicon. *Nat. Commun.* **7**, 1–5 (2016).

48. Li, Y. *et al.* Photocatalytic water splitting by N-TiO2 on MgO (111) with exceptional quantum efficiencies at elevated temperatures. *Nat. Commun.* **10**, 1–9 (2019).

49. Gogoi, D., Namdeo, A., Golder, A. K. & Peela, N. R. Ag-doped TiO2 photocatalysts with effective charge transfer for highly efficient hydrogen production through water splitting. *Int. J. Hydrogen Energy* **45**, 2729–2744 (2020).

50. Ingram, D. B. & Linic, S. Water Splitting on Composite Plasmonic Metal Semiconductor Photoelectrodes Evidence for Selective Plasmon-Induced Formation of Charge Carriers near the Semiconductor Surface. *J. Am. Chem. Soc.* **133**, 5202–5205 (2011).

51. Ke, X. *et al.* Tuning the reduction power of supported gold nanoparticle photocatalysts for selective reductions by manipulating the wavelength of visible light irradiation. *Chem. Commun.* **48**, 3509–3511 (2012).

52. Mubeen, S. *et al.* An autonomous photosynthetic device in which all charge carriers derive from surface plasmons. *Nat. Nanotechnol.* **8**, 247–251 (2013).

53. Chen, X., Zhu, H., Zhao, J., Zheng, Z. & Gao, X. Visible-Light-Driven Oxidation of Organic Contaminants in Air with Gold Nanoparticle Catalysts on Oxide Supports. *Angew. Chemie* **120**, 5433–5436 (2008).

54. Linic, S., Christopher, P., Xin, H. & Marimuthu, A. Catalytic and photocatalytic transformations on metal nanoparticles with targeted geometric and plasmonic properties. *Acc. Chem. Res.* **46**, 1890–1899 (2013).

55. Tian, B. *et al.* UV-driven overall water splitting using unsupported gold nanoparticles as photocatalysts. *Chem. Commun.* **54**, 1845–1848 (2018).

56. Kale, M. J., Avanesian, T. & Christopher, P. Direct photocatalysis by plasmonic nanostructures. *ACS Catal.* **4**, 116–128 (2014).

57. Brus, L. Noble metal nanocrystals: Plasmon electron transfer photochemistry and single-molecule raman spectroscopy. *Acc. Chem. Res.* **41**, 1742–1749 (2008).

58. Christopher, P., Xin, H., Marimuthu, A. & Linic, S. Singular characteristics and unique chemical bond activation mechanisms of photocatalytic reactions on plasmonic nanostructures. *Nat. Mater.* **11**, 1044–1050 (2012).

59. Kunwar, S., Pandit, S., Jeong, J. H. & Lee, J. Improved Photoresponse of UV Photodetectors by the Incorporation of Plasmonic Nanoparticles on GaN Through the Resonant Coupling of Localized Surface Plasmon Resonance. *Nano-Micro Lett.* **12**, 1–16 (2020).

60. Konieczny, A., Mondal, K., Wiltowski, T. & Dydo, P. Catalyst development for thermocatalytic decomposition of methane to hydrogen. *Int. J. Hydrogen Energy* **33**, 264–272 (2008).

61. Carmo, M., Fritz, D. L., Mergel, J. & Stolten, D. A comprehensive review on PEM water electrolysis. *Int. J. Hydrogen Energy* **38**, 4901–4934 (2013).

62. Schröder, V., Emonts, B., Janßen, H. & Schulze, H. P. Explosion limits of hydrogen/oxygen mixtures at initial pressures up to 200 bar. *Chem. Eng. Technol.* **27**, 847–851 (2004).

63. Shin, J., Kang, S. -a., Choi, J., Sohn, J.-Y. & Kim, C.-Y. Highly cross-linked poly(styrene sulfonic acid)-grafted poly(tetrafluoroethylene-co-perfluoropropyl vinyl ether) membranes with various thicknesses and their application to direct methanol

fuel cell. *High Perform. Polym.* **26**, 488–495 (2014).

64. Aouali, F. Z. *et al.* Modelling and experimental analysis of a PEM electrolyser powered by a solar photovoltaic panel. *Energy Procedia* **62**, 714–722 (2014).

65. Zhang, L., Doyle-Davis, K. & Sun, X. Pt-Based electrocatalysts with high atom utilization efficiency: From nanostructures to single atoms. *Energy Environ. Sci.* **12**, 492–517 (2019).

66. Li, C. & Baek, J. B. Recent Advances in Noble Metal (Pt, Ru, and Ir)-Based Electrocatalysts for Efficient Hydrogen Evolution Reaction. *ACS Omega* **5**, 31–40 (2020).

67. Li, Y. *et al.* MoS2 nanoparticles grown on graphene: An advanced catalyst for the hydrogen evolution reaction. *J. Am. Chem. Soc.* **133**, 7296–7299 (2011).

68. Conway, B. E. & Tilak, B. V. Interfacial processes involving electrocatalytic evolution and oxidation of H2 , and the role of chemisorbed H. *Electrochim. Acta* **47**, 3571–3594 (2002).

69. Bockris, J. O. Fiftieth Anniversary: A Brief Summary of Hydrogen Electrode Kinetics. *J. Electrochem. Soc.* **99**, 366C (1952).

70. Anantharaj, S. *et al.* Environmental Science Precision and correctness in the evaluation of electrocatalytic water splitting : revisiting activity parameters with a critical assessment. *Energy Environ. Sci.* **11**, 744–771 (2018).

71. Skúlason, E. & Tripkovic, V. Modeling the electrochemical hydrogen oxidation and evolution reactions on the basis of density functional theory calculations. *J. Phys. Chem. C* **114**, 18182–18197 (2010).

72. Nørskov, J. K., Bligaard, T., Rossmeisl, J. & Christensen, C. H. Towards the computational design of solid catalysts. *Nat. Chem.* **1**, 37–46 (2009).

73. Roger, P. The Rate Of Electrolytic Hydrogen Evolution And The Heat Of Adsorption Of Hydrogen. *Trans. Faraday Soc.* **54**, 1053–1063 (1958).

74. Narayanan, H., Viswanathan, B., Krishnamurthy, K. R. & Nair, H. Hydrogen from photo-electrocatalytic water splitting. in *Solar Hydrogen Production: Processes, Systems and Technologies* 419–486 (Academic Press, 2019). doi:10.1016/B978-0-12-814853-2.00012-6.

75. Greeley, J., Jaramillo, T. F., Bonde, J., Chorkendorff, I. & Nørskov, J. K. Computational high-throughput screening of electrocatalytic materials for hydrogen evolution. *Nat. Mater.* **5**, 909–913 (2006).

76. Lau, T. H. M. *et al.* Transition metal atom doping of the basal plane of MoS2 monolayer nanosheets for electrochemical hydrogen evolution. *Chem. Sci.* **9**, 4769–4776 (2018).

77. Mo, J. *et al.* Transition metal atom–doped monolayer MoS2 in a proton-exchange membrane electrolyzer. *Mater. Today Adv.* **6**, 100020 (2020).

78. Man, H. W. *et al.* Transition metal-doped nickel phosphide nanoparticles as electro- and photocatalysts for hydrogen generation reactions. *Appl. Catal. B Environ.* **242**, 186–193 (2019).

79. Yang, Y. *et al.* Engineering Ruthenium-Based Electrocatalysts for Effective Hydrogen Evolution Reaction. *Nano-Micro Lett.* **13**, 1–20 (2021).

80. Benck, J. D., Hellstern, T. R., Kibsgaard, J., Chakthranont, P. & Jaramillo, T. F. Catalyzing the Hydrogen Evolution Reaction (HER) with Molybdenum Sulfide Nanomaterials. *ACS Catal. Catal.* **4**, 3957–3971 (2014).

81. Seitz, L. C. *et al.* Modeling practical performance limits of photoelectrochemical water splitting based on the current state of materials research. *ChemSusChem* **7**, 1372–1385 (2014).

82. Chen, Z. *et al.* Core-shell MoO3 -MoS 2 Nanowires for Hydrogen Evolution : A Functional Design for Electrocatalytic Materials. *Nano Lett.* **11**, 4168–4175 (2011).

83. Walter, M. G. *et al.* Solar water splitting cells. *Chem. Rev.* **110**, 6446–6473 (2010).

84. Benck, J. D., Chen, Z., Kuritzky, L. Y., Forman, A. J. & Jaramillo, T. F. Amorphous molybdenum sulfide catalysts for electrochemical hydrogen production: Insights into the origin of their catalytic activity. *ACS Catal.* **2**, 1916–1923 (2012).

85. Wang, X. D. *et al.* Self-supported NiMoP2 nanowires on carbon cloth as an efficient and durable electrocatalyst for overall water splitting. *J. Mater. Chem. A* **5**, 7191–7199 (2017).

86. Lei, C. *et al.* Charge Engineering of Mo2C@Defect-Rich N-Doped Carbon Nanosheets for Efficient Electrocatalytic H2 Evolution. *Nano-Micro Lett.* **11**, 1–10 (2019).

87. Li, H. *et al.* Nickel Diselenide Ultrathin Nanowires Decorated with Amorphous Nickel Oxide Nanoparticles for Enhanced Water Splitting Electrocatalysis. *Small* **13**, 1–8 (2017).

88. Zhai, L. *et al.* In Situ Phase Transformation on Nickel-Based Selenides for Enhanced Hydrogen Evolution Reaction in Alkaline Medium. *ACS Energy Lett.* **5**, 2483–2491 (2020).

89. Hughes, J. P., Clipsham, J., Chavushoglu, H., Rowley-Neale, S. J. & Banks, C. E. Polymer electrolyte electrolysis: A review of the activity and stability of non-precious metal hydrogen evolution reaction and oxygen evolution reaction catalysts. *Renew. Sustain. Energy Rev.* **139**, 110709 (2021).

90. Gasteiger, H. A., Kocha, S. S., Sompalli, B. & Wagner, F. T. Activity benchmarks and requirements for Pt, Pt-alloy, and non-Pt oxygen reduction catalysts for PEMFCs. *Appl. Catal. B Environ.* **56**, 9–35 (2005).

91. Tachibana, Y., Vayssieres, L. & Durrant, J. R. Artificial photosynthesis for solar water-splitting. *Nat. Photonics* **6**, 511–518 (2012).

92. Narayanan, H., Viswanathan, B., Krishnamurthy, K. R. & Nair, H. *Hydrogen from photo-electrocatalytic water splitting*. *Acadamic press* (Elsevier Inc., 2019).

93. Seo, H.-W. & Kim, J.-S. Hydrogen Production by Photoelectrochemical Water Splitting. *Appl. Sci. Converg. Technol.* **27**, 61–64 (2018).

94. Minggu, L. J., Wan Daud, W. R. & Kassim, M. B. An overview of photocells and photoreactors for photoelectrochemical water splitting. *Int. J. Hydrogen Energy* **35**,

5233–5244 (2010).

95. Bajorowicz, B. *et al.* Application of metal oxide-based photocatalysis. in *Metal Oxide-Based Photocatalysis: Fundamentals and Prospects for Application* 211–340 (Elsevier, 2018).

96. Niu, F. *et al.* Hybrid Photoelectrochemical Water Splitting Systems: From Interface Design to System Assembly. *Adv. Energy Mater.* **10**, 1900399 (2020).

97. Li, R. & Li, C. Photocatalytic Water Splitting on Semiconductor-Based Photocatalysts. *Adv. Catal.* **60**, 1–57 (2017).

98. Department of Energy, U. S. *White Papers on Materials for Photoelectrochemical Water Splitting*. (2013).

99. Sun, K. *et al.* A Stabilized, Intrinsically Safe, 10% Efficient, Solar-Driven Water-Splitting Cell Incorporating Earth-Abundant Electrocatalysts with Steady-State pH Gradients and Product Separation Enabled by a Bipolar Membrane. *Adv. Energy Mater.* **6**, 1600379 (2016).

100. Ager, J. W., Shaner, M. R., Walczak, K. A., Sharp, I. D. & Ardo, S. Experimental demonstrations of spontaneous, solar-driven photoelectrochemical water splitting. *Energy Environ. Sci.* **8**, 2811–2824 (2015).

101. Cheng, W. H. *et al.* Monolithic Photoelectrochemical Device for Direct Water Splitting with 19% Efficiency. *ACS Energy Lett.* **3**, 1795–1800 (2018).

102. Varadhan, P., Fu, H. C., Kao, Y. C., Horng, R. H. & He, J. H. An efficient and stable photoelectrochemical system with 9% solar-to-hydrogen conversion efficiency via InGaP/GaAs double junction. *Nat. Commun.* **10**, 1–9 (2019).

103. Marsen, B., Miller, E. L., Paluselli, D. & Rocheleau, R. E. Progress in sputtered tungsten trioxide for photoelectrode applications. *Int. J. Hydrogen Energy* **32**, 1310–1315 (2007).

104. Pan, L. *et al.* Boosting the performance of Cu2O photocathodes for unassisted solar water splitting devices. *Nat. Catal.* **1**, 412–420 (2018).

105. Zheng, Y., Jiao, Y., Vasileff, A. & Qiao, S. The Hydrogen Evolution Reaction in Alkaline Solution : From Theory , Single Crystal Models , to Practical Electrocatalysts. *Angew. Chemie - Int. Ed.* **57**, 7568–7579 (2018).

106. Huang, X. *et al.* Vertical CoP Nanoarray Wrapped by N , P-Doped Carbon for Hydrogen Evolution Reaction in Both Acidic and Alkaline Conditions. *Adv. Energy Mater.* **9**, 1803970 (2019).

107. Herranz, J. & Gasteiger, H. A. Environmental Science oxidation and evolution reaction mechanism. *Energy Environ. Sci.* **7**, 2255–2260 (2014).

108. Rheinländer, P. J. *et al.* Kinetics of the Hydrogen Oxidation / Evolution Reaction on Polycrystalline Platinum in Alkaline Electrolyte Reaction Order with Respect to Hydrogen Pressure. *J. Electrochem. Soc.* **161**, F1448–F1457 (2014).

109. McKone, J. R., Marinescu, S. C., Brunschwig, B. S., Winkler, J. R. & Gray, H. B. Earth-abundant hydrogen evolution electrocatalysts. *Chem. Sci.* **5**, 865–878 (2014).

110. Laursen, A. B., Kegnæs, S., Dahl, S. & Chorkendorff, I. Molybdenum sulfides -

Efficient and viable materials for electro - And photoelectrocatalytic hydrogen evolution. *Energy Environ. Sci.* **5**, 5577–5591 (2012).

111. Theerthagiri, J., Lee, S. J., Murthy, A. P., Madhavan, J. & Choi, M. Y. Fundamental aspects and recent advances in transition metal nitrides as electrocatalysts for hydrogen evolution reaction: A review. *Curr. Opin. Solid State Mater. Sci.* **24**, 100805 (2020).

112. Zhang, X., Wu, D. & Cheng, D. Component-dependent electrocatalytic activity of PdCu bimetallic nanoparticles for hydrogen evolution reaction. *Electrochim. Acta* **246**, 572–579 (2017).

113. Liao, F. *et al.* Ir-Au Bimetallic Nanoparticle Modified Silicon Nanowires with Ultralow Content of Ir for Hydrogen Evolution Reaction. *ChemCatChem* **11**, 2126–2130 (2019).

114. Li, H. *et al.* Facile fabrication of activated NiFe bimetallic NPs anchored N-doped CNTs arrays as reliable self-standing electrocatalyst for HER and OER. *J. Solid State Chem.* **289**, 121498 (2020).

115. Owens-Baird, B. *et al.* Crystallographic facet selective HER catalysis: exemplified in FeP and NiP2single crystals. *Chem. Sci.* **11**, 5007–5016 (2020).

116. Strmcnik, D., Lopes, P. P., Genorio, B., Stamenkovic, V. R. & Markovic, N. M. Design principles for hydrogen evolution reaction catalyst materials. *Nano Energy* **29**, 29–36 (2016).

117. Shervedani, R. K. & Amini, A. Sulfur-doped graphene as a catalyst support: Influences of carbon black and ruthenium nanoparticles on the hydrogen evolution reaction performance. *Carbon N. Y.* **93**, 762–773 (2015).

118. Murthy, A. P., Madhavan, J. & Murugan, K. Recent advances in hydrogen evolution reaction catalysts on carbon/carbon-based supports in acid media. *J. Power Sources* **398**, 9–26 (2018).

119. Demir, E., Akbayrak, S., Önal, A. M. & Özkar, S. Nanoceria-Supported Ruthenium(0) Nanoparticles: Highly Active and Stable Catalysts for Hydrogen Evolution from Water. *ACS Appl. Mater. Interfaces* **10**, 6299–6308 (2018).

120. Krishnan, U., Kaur, M., Singh, K., Kumar, M. & Kumar, A. A synoptic review of MoS 2 : Synthesis to applications. *Superlattices Microstruct.* **128**, 274–297 (2019).

121. Tareen, A. K., Priyanga, G. S., Behara, S., Thomas, T. & Yang, M. Mixed ternary transition metal nitrides: A comprehensive review of synthesis, electronic structure, and properties of engineering relevance. *Prog. Solid State Chem.* **53**, 1–26 (2019).

122. Yu, J. *et al.* Recent Advances and Prospective in Ruthenium-Based Materials for Electrochemical Water Splitting. *ACS Catal.* **9**, 9973–10011 (2019).

123. Zheng, Y. *et al.* High Electrocatalytic Hydrogen Evolution Activity of an Anomalous Ruthenium Catalyst. *J. Am. Chem. Soc.* **138**, 16174–16181 (2016).

124. Song, Q. *et al.* Ruthenium@N-doped graphite carbon derived from carbon foam for efficient hydrogen evolution reaction. *Chem. Commun.* **55**, 965–968 (2019).

125. Eftekhari, A. Electrocatalysts for hydrogen evolution reaction. *Int. J. Hydrogen Energy* **42**, 11053–11077 (2017).

126. Li, Y. *et al.* Under-Water Superaerophobic Pine-Shaped Pt Nanoarray Electrode for Ultrahigh-Performance Hydrogen Evolution. *Adv. Funct. Mater.* **25**, 1737–1744 (2015).

127. Clark, E. L. *et al.* Influence of Atomic Surface Structure on the Activity of Ag for the Electrochemical Reduction of CO2 to CO. *ACS Catal.* **9**, 4006–4014 (2019).

128. Lv, H. *et al.* A New Core/Shell NiAu/Au Nanoparticle Catalyst with Pt-like Activity for Hydrogen Evolution Reaction. *J. Am. Chem. Soc.* **137**, 5859–5862 (2015).

129. Tian, W. *et al.* Porous Carbons : Structure-Oriented Design and Versatile Applications. *Adv. Funct. Mater.* **30**, 1909265 (2020).

130. Xue, Y., Sun, S., Wang, Q., Dong, Z. & Liu, Z. Transition metal oxide-based oxygen reduction reaction electrocatalysts for energy conversion systems with aqueous electrolytes. *J. Mater. Chem. A* **6**, 10596–10626 (2018).

131. Wu, S. *et al.* Rapid Interchangeable Hydrogen , Hydride , and Proton Species at the Interface of Transition Metal Atom on Oxide Surface. *J. Am. Chem. Soc.* **143**, 9105–9112 (2021).

132. Sau, B. T. K. & Rogach, A. L. Nonspherical Noble Metal Nanoparticles : Colloid-Chemical Synthesis and Morphology Control. *Adv. Mater.* **22**, 1781–1804 (2010).

133. Wang, C., Daimon, H., Onodera, T., Koda, T. & Sun, S. A General Approach to the Size- and Shape-Controlled Synthesis of Platinum Nanoparticles and Their Catalytic Reduction of Oxygen. *Angew. Chemie - Int. Ed.* **120**, 3644–3647 (2008).

134. Wang, Z. L. Transmission Electron Microscopy of Shape-Controlled Nanocrystals and Their Assemblies. *J. Phys. Chem. B* **104**, 1153–1175 (2000).

135. Xia, Y., Xiong, Y., Lim, B. & Skrabalak, S. E. Shape-Controlled Synthesis of Metal Nanocrystals : Simple Chemistry Meets Complex Physics ? *Angew. Chemie - Int. Ed.* **48**, 60–103 (2009).

136. Fievet, F. *et al.* The polyol process: a unique method for easy access to metal nanoparticles with tailored sizes, shapes and compositions. *Chem. Soc. Rev.* **47**, 5187–5233 (2018).

137. Ott, F. *et al.* Soft chemistry nanowires for permanent magnet fabrication. in *Magnetic Nano- and Microwires* 629–651 (Elsevier, 2015).

138. Li, Z. *et al.* A silver catalyst activated by stacking faults for the hydrogen evolution reaction. *Nat. Catal.* **2**, 1107–1114 (2019).

139. Wen, C., Yin, A. & Dai, W. L. Recent advances in silver-based heterogeneous catalysts for green chemistry processes. *Appl. Catal. B Environ.* **160**–**161**, 730–741 (2014).

140. Christopher Hammond. *The Basics of Crystallography and Diffraction*. (Oxford University Press, 2015).

141. Nix, R. Surface Structures- fcc Metals. *Chemistry LibreTexts* https://chem.libretexts.org/Bookshelves/Physical_and_Theoretical_Chemistry_Textbook_Maps/Book%3A_Surface_Science_(Nix)/01%3A_Structure_of_Solid_Surfaces/1.03%3A_Surface_Structures-_fcc_Metals (2021).

142. Ferrin, P., Kandoi, S., Nilekar, A. U. & Mavrikakis, M. Hydrogen adsorption, absorption and diffusion on and in transition metal surfaces: A DFT study. *Surf. Sci.* **606**, 679–689 (2012).

143. Sharma, G. *et al.* Novel development of nanoparticles to bimetallic nanoparticles and their composites: A review. *J. King Saud Univ. - Sci.* **31**, 257–269 (2019).

144. Oldenburg, S. J., Averitt, R. D., Westcott, S. L. & Halas, N. J. Nanoengineering of optical resonances. *Chem. Phys. Lett.* **288**, 243–247 (1998).

145. Chaudhuri, R. G. & Paria, S. Core/Shell Nanoparticles : Classes, Properties, Synthesis Mechanisms, Characterization, and Applications. *Chem. Rev.* **112**, 2373–2433 (2012).

146. Yang, Y., Liu, J., Fu, Z.-W. & Qin, D. Galvanic Replacement-Free Deposition of Au on Ag for Core–Shell Nanocubes with Enhanced Chemical Stability and SERS Activity. *J. Am. Chem. Soc.* **136**, 8153–8156 (2014).

147. Patra, K. K. & Gopinath, C. S. Bimetallic and Plasmonic Ag–Au on TiO2 for Solar Water Splitting: An Active Nanocomposite for Entire Visible-Light-Region Absorption. *ChemCatChem* **8**, 3294–3311 (2016).

148. West, P. R., Ishii, S., Naik, G. V, Emani, N. K. & Shalaev, V. M. Searching for better plasmonic materials. *Laser Photonic Rev.* **4**, 795–808 (2010).

149. NanoComposix. Silver Nanoparticles: Optical Properties. https://nanocomposix.com/pages/silver-nanoparticles-optical-properties.

150. NanoComposix. Gold Nanoparticles: Optical Properties. https://nanocomposix.com/pages/gold-nanoparticles-optical-properties.

151. Valenti, M. *et al.* Hot Carrier Generation and Extraction of Plasmonic Alloy Nanoparticles. *ACS Photonics* **4**, 1146–1152 (2017).

152. Borah, R. & Verbruggen, S. W. Silver − Gold Bimetallic Alloy versus Core − Shell Nanoparticles : Implications for Plasmonic Enhancement and Photothermal Applications. *J. Phys. Chem. C* **124**, 12081–12094 (2020).

153. Qiu, G., Ng, S. P. & Wu, C. M. L. Bimetallic Au-Ag alloy nanoislands for highly sensitive localized surface plasmon resonance biosensing. *Sensors Actuators, B Chem.* **265**, 459–467 (2018).

154. Liu, G. *et al.* Controllable Ag Migration To Form One-Dimensional Ag/Ag2S@ZnS for Bifunctional Catalysis. *ACS Appl. Energy Mater.* **3**, 6146–6154 (2020).

155. Li, X. *et al.* Au Multimer@MoS2 hybrid structures for efficient photocatalytical hydrogen production via strongly plasmonic coupling effect. *Nano Energy* **30**, 549–558 (2016).

156. Mukherjee, S. *et al.* Hot Electrons Do the Impossible: Plasmon-Induced Dissociation of H2 on Au. *Nano Lett.* **13**, 240–247 (2013).

157. Shi, Y. *et al.* Hot Electron of Au Nanorods Activates the Electrocatalysis of Hydrogen Evolution on MoS2 Nanosheets. *J. Am. Chem. Soc.* **137**, 7365–7370 (2015).

158. Shaner, M. R., Atwater, H. A., Lewis, N. S. & McFarland, E. W. A comparative technoeconomic analysis of renewable hydrogen production using solar energy. *Energy Environ. Sci.* **9**, 2354–2371 (2016).

159. Wang, Q. *et al.* Scalable water splitting on particulate photocatalyst sheets with a solar-to-hydrogen energy conversion efficiency exceeding 1%. *Nat. Mater.* **15**, 611–615 (2016).

160. Qiu, Y. *et al.* Efficient solar-driven water splitting by nanocone BiVO4-perovskite tandem cells. *Sci. Adv.* **2**, e1501764 (2016).

161. Marzo, A. *et al.* Standard or local solar spectrum? Implications for solar technologies studies in the Atacama desert. *Renew. Energy* **127**, 871–882 (2018).

162. Yaqoob, A. A., Umar, K. & Ibrahim, M. N. M. Silver nanoparticles: various methods of synthesis, size affecting factors and their potential applications–a review. *Appl. Nanosci.* **10**, 1369–1378 (2020).

163. Tran, T. D. *et al.* Gold nanoparticles as an outstanding catalyst for the hydrogen evolution reaction. *Chem. Commun.* **54**, 3363–3366 (2018).

164. Alba-Molina, D. *et al.* Tailoring the ORR and HER electrocatalytic performances of gold nanoparticles through metal-ligand interfaces. *J. Mater. Chem. A* **7**, 20425–20434 (2019).

165. Yan, L. *et al.* Recent advances in nanostructured Nb-based oxides for electrochemical energy storage. *Nanoscale* **8**, 8443–8465 (2016).

166. Gates, B. C. Supported Metal Clusters: Synthesis, Structure, and Catalysis. *Chem. Rev.* **95**, 511–522 (2002).

167. Dong, W. *et al.* Subnano Ruthenium Species Anchored on Tin Dioxide Surface for Efficient Alkaline Hydrogen Evolution Reaction. *Cell Reports Phys. Sci.* **1**, 100026 (2020).

168. Blizanac, B. B., Pylypenko, S., Olson, T. S., Konopka, D. & Atanassov, P. Functional DMFC Cathode Catalysts and Supports Based on Niobium Oxide Phase. *J. Electrochem. Soc.* **158**, B485 (2011).

169. Tauster, S. J., Fung, S. C. & Garten, R. L. Strong metal-support interactions. Group 8 noble metals supported on titanium dioxide. *J. Am. Chem. Soc.* **100**, 170–175 (2002).

170. Campbell, C. T. Electronic perturbations. *Nat. Chem.* **4**, 597–598 (2012).

171. van Deelen, T. W., Hernández Mejía, C. & de Jong, K. P. Control of metal-support interactions in heterogeneous catalysts to enhance activity and selectivity. *Nat. Catal.* **2**, 955–970 (2019).

172. Suen, N. T. *et al.* Electrocatalysis for the oxygen evolution reaction: recent development and future perspectives. *Chem. Soc. Rev.* **46**, 337–365 (2017).

173. Chen, Z., Duan, X., Wei, W., Wang, S. & Ni, B. J. Recent advances in transition metal-based electrocatalysts for alkaline hydrogen evolution. *J. Mater. Chem. A* **7**, 14971–15005 (2019).

174. Sun, H. *et al.* Self-Supported Transition-Metal-Based Electrocatalysts for Hydrogen and Oxygen Evolution. *Adv. Mater.* **32**, 1806326 (2020).

175. Yi, D. *et al.* Regulating Charge Transfer of Lattice Oxygen in Single-Atom-Doped Titania for Hydrogen Evolution. *Angew. Chemie - Int. Ed.* **59**, 15855–15859 (2020).

176. Chen, D., Chen, C., Baiyee, Z. M., Shao, Z. & Ciucci, F. Nonstoichiometric Oxides as Low-Cost and Highly-Efficient Oxygen Reduction/Evolution Catalysts for Low-Temperature Electrochemical Devices. *Chem. Rev.* **115**, 9869–9921 (2015).

177. Li, Y. *et al.* Electronic-reconstruction-enhanced hydrogen evolution catalysis in oxide polymorphs. *Nat. Commun.* **10**, 3149 (2019).

178. Geng, S., Liu, Y., Yu, Y. S., Yang, W. & Li, H. Engineering defects and adjusting electronic structure on S doped MoO2 nanosheets toward highly active hydrogen evolution reaction. *Nano Res.* **13**, 121–126 (2020).

179. Li, L., Zhang, T., Yan, J., Cai, X. & Liu, S. F. P Doped MoO3−x Nanosheets as Efficient and Stable Electrocatalysts for Hydrogen Evolution. *Small* **13**, 1700441 (2017).

180. Zeng, H. *et al.* Electron Density Modulation of Metallic MoO2by Ni Doping to Produce Excellent Hydrogen Evolution and Oxidation Activities in Acid. *ACS Energy Lett.* **5**, 1908–1915 (2020).

181. Zhong, X. *et al.* Mo Doping Induced More Active Sites in Urchin-Like W18O49 Nanostructure with Remarkably Enhanced Performance for Hydrogen Evolution Reaction. *Adv. Funct. Mater.* **26**, 5778–5786 (2016).

182. Luo, Z. *et al.* Mesoporous MoO3–x Material as an Efficient Electrocatalyst for Hydrogen Evolution Reactions. *Adv. Energy Mater.* **6**, 1600528 (2016).

183. Jin, Y. *et al.* Porous MoO2 Nanosheets as Non-noble Bifunctional Electrocatalysts for Overall Water Splitting. *Adv. Mater.* **28**, 3785–3790 (2016).

184. Zhu, K., Hu, J., Kübel, C. & Richards, R. Efficient preparation and catalytic activity of MgO(111) nanosheets. *Angew. Chemie - Int. Ed.* **45**, 7277–7281 (2006).

185. Wu, S. *et al.* Removal of Hydrogen Poisoning by Electrostatically Polar MgO Support for Low-Pressure NH 3 Synthesis at a High Rate over the Ru Catalyst. *ACS Catal.* **10**, 5614–5622 (2020).

186. Hu, J., Zhu, K., Chen, L., Kübel, C. & Richards, R. MgO(111) Nanosheets with Unusual Surface Activity. *J. Phys. Chem. C* **111**, 12038–12044 (2007).

187. Hu, J. *et al.* Adsorption Properties of MgO(111) Nanoplates for the Dye Pollutants from Wastewater. *J. Chem. Eng. Data* **55**, 3742–3748 (2010).

188. Wu, S. *et al.* Rapid Interchangeable Hydrogen, Hydride, and Proton Species at the Interface of Transition Metal Atom on Oxide Surface. *J. Am. Chem. Soc.* **143**, 9105–9112 (2021).

189. Wang, F., Ta, N. & Shen, W. MgO nanosheets, nanodisks, and nanofibers for the Meerwein–Ponndorf–Verley reaction. *Appl. Catal. A Gen.* **475**, 76–81 (2014).

190. Hacquart, R. & Jupille, J. Morphology of MgO smoke crystallites upon etching in wet environment. *J. Cryst. Growth* **311**, 4598–4604 (2009).

191. Hacquart, R. & Jupille, J. Hydrated MgO smoke crystals from cubes to octahedra. *Chem. Phys. Lett.* **439**, 91–94 (2007).

192. Geysermans, P., Finocchi, F., Goniakowski, J., Hacquart, R. & Jupille, J. Combination of (100), (110) and (111) facets in MgO crystals shapes from dry to wet environment.

Phys. Chem. Chem. Phys. **11**, 2228 (2009).

193. Li, Y. & Shen, W. Morphology-dependent nanocatalysts: Rod-shaped oxides. *Chem. Soc. Rev.* **43**, 1543–1574 (2014).

194. Li, Y., Chi, S. & Tsang, E. Unusual Catalytic Properties of High-Energetic-Facet Polar Metal Oxides. *Acc. Chem. Res.* **54**, 366–378 (2021).

195. Noguera, C. Polar oxide surfaces. *J. Phys. Condens. Matter* **12**, R367–R410 (2000).

196. Liao, F. *et al.* Morphology-dependent interactions of ZnO with Cu nanoparticles at the materials' interface in selective hydrogenation of CO2 to CH3OH. *Angew. Chemie - Int. Ed.* **50**, 2162–2165 (2011).

197. Ye, L. *et al.* Ceria Nanocrystals Supporting Pd for Formic Acid Electrocatalytic Oxidation: Prominent Polar Surface Metal Support Interactions. *ACS Catal.* **9**, 5171–5177 (2019).

198. Wu, S. *et al.* Removal of Hydrogen Poisoning by Electrostatically Polar MgO Support for Low-Pressure NH 3 Synthesis at a High Rate over the Ru Catalyst. *ACS Catal.* **10**, 5614–5622 (2020).

199. Goniakowski, J. & Noguera, C. Characteristics of Pd deposition on the MgO(111) surface. *Phys. Rev. B* **60**, 16120–16128 (1999).

200. Ciston, J., Subramanian, A. & Marks, L. D. Water-driven structural evolution of the polar MgO (111) surface: An integrated experimental and theoretical approach. *Phys. Rev. B* **79**, 085421 (2009).

Chapter 2 Analytical Techniques

Table of Contents

Chapter 2 Analytical Techniques 60
2.1 Introduction 61
2.2 X-Ray Diffractions (XRD) 61
2.3 Synchrotron XRD (SXRD) 66
2.4 Transmission Electron Microscopy (TEM) 67
2.5 Scanning Transmission Electron Microscopy (STEM) 70
2.6 X-Ray Photoelectron Spectroscopy (XPS) 72
2.7 UV-Visible Spectroscopy (UV-Vis) 75
2.8 Atom Probe Tomography (APT) 77
2.9 X-Ray Absorption Spectroscopy (XAS) 79
2.10 Brunauer–Emmett–Teller (BET) Theory 82
2.11 Electrochemical Techniques 84
2.12 References 86

2.1 Introduction

The crux in developing a robust catalytic material is to understand the structure-activity relationship and how different reaction conditions can impact the performance. Using modern microscopes, scientists can utilise different imaging techniques to examine the atomic arrangements and determine the morphologies. And the X-ray spectroscopic techniques can be used to probe the structure and extract information such as bond distance, bond angle, oxidation state etc. Macroscopically, bulk properties such as light absorption range and atomic composition can be obtained from various spectroscopic techniques; catalytic performances can be obtained through electrochemical parameters such as Tafel slopes and overpotentials etc.

The recent decade has seen vigorous development in improving the capabilities of characterization techniques. Thanks to the advancements in synchrotron facilities and the invention of in-situ cells, operando structural changes can be probed and monitored in real-time under working reaction conditions. This allows the discovery of intermediate phases that cannot be possibly obtained from ex-situ techniques or post-mortem analysis.

In a nutshell, the analytical techniques need to be used in conjunction with characterization methods to investigate the electronic and structural properties of the catalyst materials. In this chapter, the principle behind the various techniques will be explored and discussed.

2.2 X-Ray Diffractions (XRD)

Powder X-ray diffraction (XRD) is widely used as an essential analytical technique to elucidate the structure of crystalline solids and the physical properties of catalyst materials.[1] The incident X-ray radiation is formed of high-energy photons which undergoes elastic scattering by the electron density around nuclei when shine onto the samples.[2] As the atomic spacings in a crystal are similar to the incident X-Ray wavelengths in the Angstrom range, the incident X-rays can

diffract through the ordered crystallographic gratings and undergo constructive/destructive interference to generate different diffractograms.[2] Particularly, analysing the specific XRD diffractograms of the interest catalysts can help to determine the interlayer lattice spacing, unit cell parameters, dominant facets in the structure, and estimate the catalyst crystallinity and particle sizes.[2] The high energy and concentrated incident X-rays allow deep penetration into the sample materials with low interactions to atoms of the materials, which make it to be a bulk analytical technique.[3]

In a lab-based X-ray diffraction instrument, the sample is illuminated by X-ray beams emitted from the X-ray tube which moves in a synchronized motion with the detector. In principle, the X-ray tube with a tungsten filament is acting as a cathode that emits electrons. The emitted electrons are then accelerated by the electric field (caused by applied potentials) and bombard the target anode materials (copper or tungsten), which leads to the ejection of core electrons from the anode materials. Electrons from higher energy levels drop down to fill the hole (caused by the ejected electron) and release the energy in the form of X-rays that match the specific wavelengths of the target anode materials. The emitted X-rays are then monochromated and illuminated on the sample materials at different incidents angles by moving the X-ray source.[2]

With high crystallinity of sample materials, the elastic scattering interference will occur constructively or destructively based on the incident angles, interlayer spacing and emitted beam wavelengths, which can be correlated with Bragg's Law (Equation 2.1) and generate fingerprint diffractograms for the sample materials.

$$n\lambda = 2d \sin\theta \qquad (Equation\ 2.1)$$

where n is a positive integer corresponding to order of reflection; λ is X-ray beam wavelength; d is the interlayer spacing; and θ is the incident angle between X-ray and scattering plane.

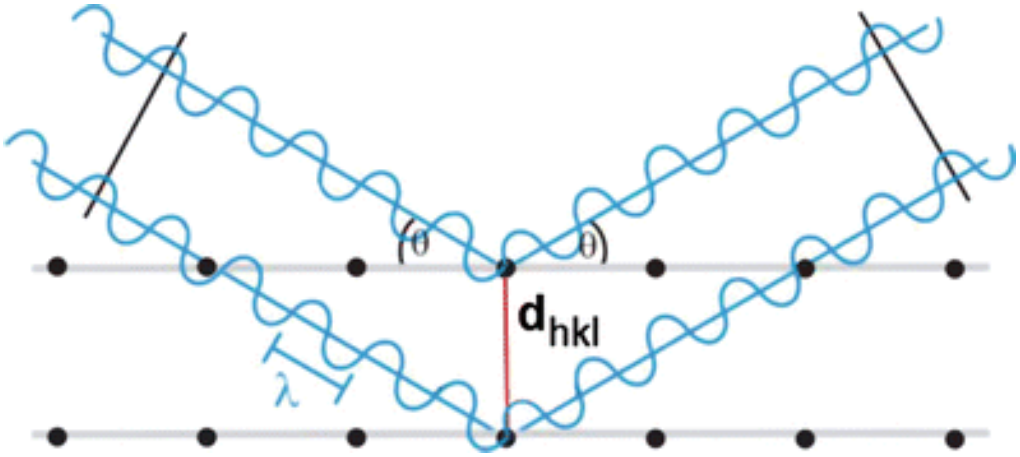


Figure 2.1 Working principles of Bragg's Law explaining the interference pattern of X-rays scattered by crystal materials. Figure reproduced from ref.[4]

With the obtained interlayer lattice spacing, it is possible to calculate the lattice parameters and specify the directions and planes in the lattice using the Miller indices. In the case of simple cubic structure (e.g., Au, Ag, MgO), the lattice vectors are orthogonal and of equal length, the relationship between interlayer lattice spacing and Miller indices is determined to be:

$$\frac{1}{d^2} = \frac{h^2 + k^2 + l^2}{a^2} \qquad (Equation\ 2.2)$$

where d is the interlayer spacing; h, k and l are Miller indices; a is the lattice parameter.

In the case of hexagonal crystal structure (e.g., Ru, $Mg(OH)_2$), the interlayer lattice spacing, and Miller indices are correlated to be:

$$\frac{1}{d^2} = \frac{4}{3}\left(\frac{h^2 + hk + k^2}{a^2}\right) + \frac{l^2}{c^2} \qquad (Equation\ 2.3)$$

where d is the interlayer spacing; h, k and l are Miller indices; a and c are the lattice parameter.

In order to figure out the planes responsible for each reflection, it requires to index the reflections and assign the h, k, l in the diffractograms. Among the simple cubic structure, the primitive lattice, body-centred lattice and face-centred lattice shown in Figure 2.2 are the most common unit cells adopted in the cubic system.

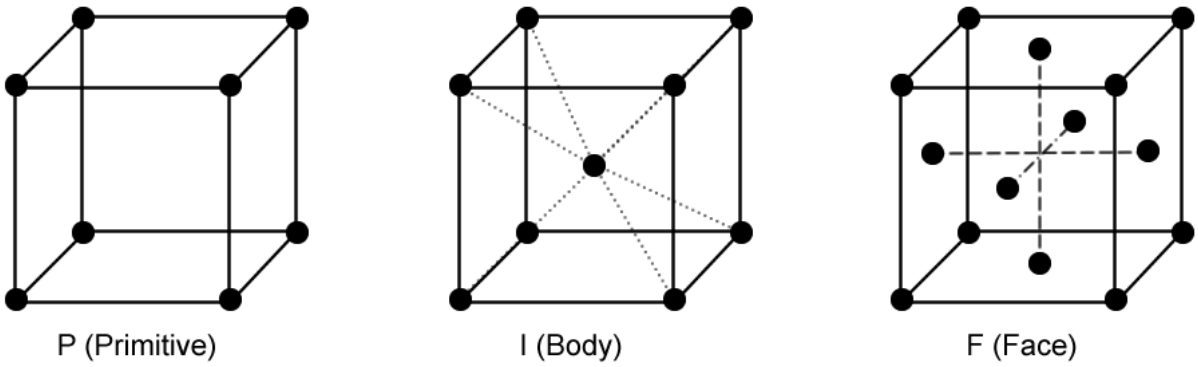


Figure 2.2 Cubic cell of primitive, body-centred and face-centred unit cell. Figure reproduced from ref.[5]

For a primitive cubic class, all integral values of the indices h, k and l are possible. Notably, the value 7 will be missing in the sequence, since there is no possible integral value that $h^2 + k^2 + l^2 = 7$ (same situation with value 15, 23 etc). However, the other two crystalline systems, body centred and face-centred, are different from the primitive. The differences arise because the centring leads to destructive interference for some reflections and the missing reflection is known as systematic absence. The Bragg's law only defines the diffraction condition for primitive unit cells, some of the diffraction predicted by the Bragg's law of the non-primitive structure may not occur due to the systematic absence.[6] The selection (or reflection) rules of some of the most common existing structures are summarized in Table 2.1.

Table 2.1 Selection (or reflection) rules of different bravais lattices and corresponding examples.

Bravais Lattice	Example Compounds/Structures	Allowed Reflections	Forbidden Reflections
Primitive (P) cubic	Simple Cubic	All h, k, l	None
Body-centred (I) cubic	Body-centred cubic metal	h+k+l = 2n (even)	h+k+l odd
Face-centred (F) Cubic	Face-centred cubic metal	h, k, l all odd or all even	h, k, l mixed odd or even
Face-centred (F) Cubic	Rock-salt (NaCl), Zincblende (ZnS)	h, k, l all odd or all even	h, k, l mixed odd or even
Face-centred (F) Cubic	C, Si, Ge – Diamond cubic	h, k, l all odd; h, k, l all even and h+k+l = 4n	h, k, l mixed odd or even; h, k, l all even and h+k+l ≠ 4n
Primitive (P)	Hexagonal closed packed metal	All other cases	l odd and h + 2k = 3n

The diffraction peaks may variant from the standard XRD PDF cards due to metal intercalation to expand the lattice causing diffraction peak shift, low crystallinity of the crystal leading to peak broadening, and dominant phase changes resulting in different peak intensity ratios. Particularly, the sharp and well-defined peaks are originated from diffraction on the well-aligned crystal planes with destructive interference at all incident angles. As particle size decreases, the influence of edges, surfaces and steps will increase, which leads to the non-aligned crystal planes and a wider distribution of adjacent interlayer spacing. As a result, diffraction occurs at a wider range of angles that causing peak broadening.[7] The Scherrer equation can be used to probe the estimated average particle size:

$$\tau = \frac{K\lambda}{\beta \cos\theta} \qquad (Equation\ 2.4)$$

where τ is the estimated particle size; K is a dimensionless shape factor (close to unity), which varies with the actual shape of the crystallite; λ is the wavelength of the incident photon; β is the peak width at full width half maximum (FWHM) (in radians) and θ is the diffraction angle. It is difficult to obtain a precise particle size from the Scherrer equation because the shape constant K varies with the actual shape of the crystallite (in the range 0.8 - 1.2) and the baseline of the diffraction peaks is hard to be determined accurately. Other circumstances such as crystal strain, instrument settings and dislocations would also aggravate the broadening effect.[8] As a result, TEM is introduced as a more accurate measurement of particle size.

2.3 Synchrotron XRD (SXRD)

On top of typical X-ray diffraction capability, synchrotron XRD offers light beams of high penetration and intensity that provide unparalleled resolution in the analysis of diffracted peaks. This can be used to identify chemical changes within a structure that are otherwise considered as negligible changes by low-resolution laboratory diffractometer. In combination with in-situ cell, samples can be tested under real working conditions at a range of temperatures and pressures. The short data collection time allows users to monitor structural changes that occur within short timescales.

Principally, synchrotron X-ray beams are generated by a specific type of particle accelerator known as synchrotrons, where fast electrons are accelerated to close to the speed of light.[9] The electrons are then injected into a storage ring in which they circulate and produce synchrotron radiation without gaining further energy.[10] The intense and tight collimation of the synchrotron beams result in small angular divergence of the beam and produce high angular resolution data. The high signal-to-noise ratio of the data allows the detection of minute features with high precision.[10]

In this thesis, in-situ synchrotron XRD is performed at Diamond Light Source, the third-generation synchrotron facility that produces brilliant X-ray beams from radiation sources conceived and optimized from the outset. The magnesium oxide material is positioned inside an electrochemical cell with potential difference applied in real-time which will be described in detail in chapter 3, section 3.2.3. Phase changes are identified through the analysis of diffracted peaks.

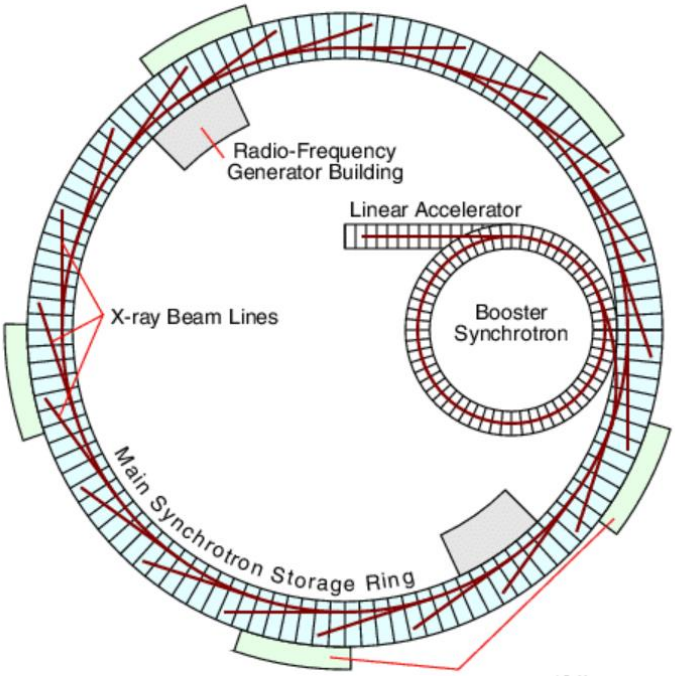


Figure 2.3 Schematic illustration of a synchrotron radiation facility.[11]

2.4 Transmission Electron Microscopy (TEM)

Transmission Electron Microscopy (TEM) is an accurate technique to analyse the morphology, size distribution and atom arrangements of nanoparticles via microscopic imaging. Great attention has been drawn by the researchers to correlate the outstanding catalytic activity with the unique morphology or size distribution of nanoparticles by using the electron microscope in conjunction with a series of characterization techniques.[12–15] Theoretically, TEM works like an optical microscope with the difference of using high energy electron beams instead of photon light sources and focusing the electron beam with electromagnetic lenses to replace the

optical lenses. In standard light microscopy, the wavelength of visible light (0.4-0.75 μm) leads to an Abbe resolution of around 1 μm, which limits the imaging to go down to the atomic level. However, de Broglie wavelength of electrons is significantly smaller than that of visible light, which leads to a much higher resolution even to the Angstrom scale.[16] The Abbe's Diffraction limit can be determined to be:[17]

$$\Delta x \cong \frac{\lambda}{2n \sin \alpha} \qquad (Equation\ 2.5)$$

where Δx is the distance of resolution; λ is the wavelength of the incident light; n is the refraction index of the medium; and α is the half-angle subtended by the objective lens.

Practically, the high energy electron beam is generated from an electron gun (usually composed of heated tungsten filament, LaB_6 cathode filament or a field emission filament) then accelerated by applied voltage (e.g., 200 kV) to a wavelength that smaller than interatomic spacing.[18] The TEM chamber is usually under high vacuum conditions in order to avoid collisions between electrons and gas molecules and ensure the electron beam is not stopped or diverted by other materials. The electron beam first passes through some electromagnetic condenser lenses for parallel ray generation, which is then aligned onto the surface of the sample. The TEM samples are required to be ultrathin and mounted onto holey carbon copper or gold grids. The electron beam can either be transmitted through the samples or diffracted by the samples then refocused and magnified via the objective lens, eventually imaged onto a fluorescent screen (Figure 2.3). Theoretically, as the electron beam bombards the sample, it will kick out an electron from the electron shell around the atomic nucleus, which leaves a highly unstable state. After that, an electron from a higher energy level will drop down to fill the space and release energy (in the form of X-rays) that depends on the energy difference between the two electron shells. At this time, an energy dispersive X-ray (EDX) detector can be deployed to detect the emission of X-rays and convert the individual X-rays pulses into

electrical voltages and denoising to counts. As each element has its specific wavelengths of the emission X-rays, EDX is considered to be a great technique in identifying the atomic compositions of the materials.[18,19]

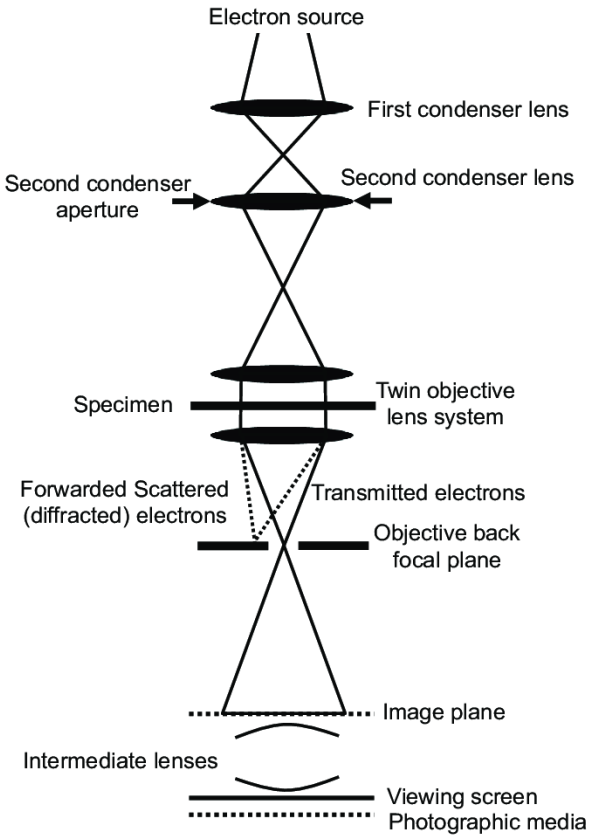


Figure 2.3 A schematic illustration of the transmission electron microscope. Figure reproduced from ref.[20]

Furthermore, there are two commonly used imaging modes of TEM, which are called bright field mode and dark field mode (Figure 2.4). As the objective apertures are installed in the back focal plane of the objective lens, the transmitted and diffracted electrons can be captured by the apertures to give imaging different modes. In the bright field mode, the transmitted electrons in the centre are captured, the heavier element with higher electron density appears darker when compared with the background in the image. Meanwhile, in the dark field mode, the diffracted electrons are captured by the apertures, the higher electron density element will be scattered to a higher extent and appear brighter.[21] The dark field mode is important to be a

supplemental technique in identifying the specific particle shapes, number of stacking layers and single metal dopants in the structure.[21–24]

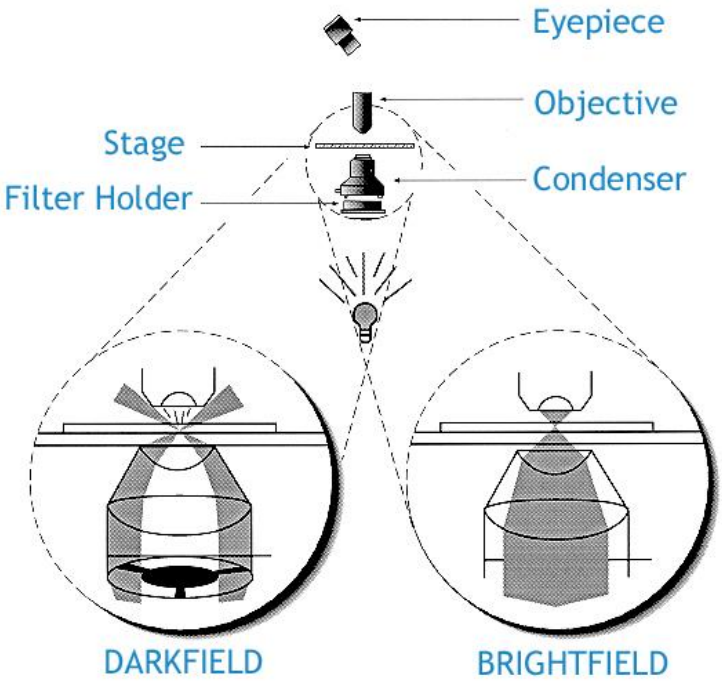


Figure 2.4 Comparison of the dark field and bright field modes in TEM imaging with an annular detector and bright field detector. Figure reproduced from ref.[25]

2.5 Scanning Transmission Electron Microscopy (STEM)

Scanning transmission electron microscopy (STEM) is a powerful microscopy technique with a beam of electron transmitting through an ultrathin sample (typically less than 50 nm thick) to generate microscopic images down to an atomic resolution.[26]

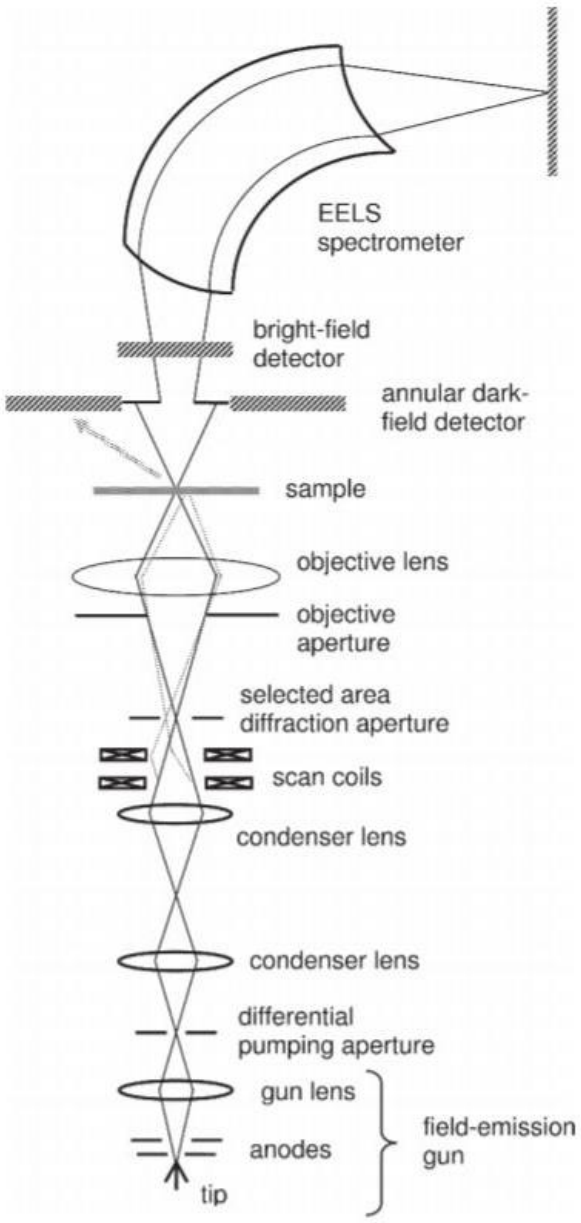


Figure 2.5 A schematic of the essential elements of a dedicated STEM instrument showing the most common detectors. Figure reproduced from ref.[27]

In STEM, an electron gun generates a beam of electrons that is converged by a series of condenser lenses to a very fine spot (around 0.05 -0.2 nm). Then the electron spot scans across the sample in a raster pattern by exciting scanning deflection coils. An annular dark-field detector is placed after the sample to detect the scattered electrons and exclude the unscattered electrons, then the scattered electron intensity is plotted as a function of probe position to form an image (Figure 2.5).[27] The HAADF-STEM imaging is an annular dark field image formed

by a very high angle (> 5°) and incoherently scattered electrons. When scattered electrons pass through the aperture, the dark field image will display electron dense regions as bright areas. The HAADF-STEM is highly sensitive to atomic number (Z) of the element that the ADF signal is proportional to the n^{th} power of the atomic number.[28] For a higher Z, more electrons will be scattered by the electron beams at high angles stemmed from stronger electrostatic interactions between the nucleus and the electron beam. As a result, the HAADF-STEM is a vital technique to differentiate the heavy atom on light support to show the loading nanoparticle dispersion and even the single atom dopant of the catalyst structure. Additionally, an EELS spectrometer can be placed after the detectors with a magnetic prism to analyse the energy loss of the inelastically scattered electrons.[29] Compared with EDX which is mainly used to identify the elemental components (particular the high Z elements) of the materials, EELS can learn much more in the depth of the material systems such as low Z elemental compositions (without disturbance of the Auger electrons or absorption of soft X-rays), bonding/valance states, free electron densities, band gap, surface properties, specimen thickness etc.

2.6 X-Ray Photoelectron Spectroscopy (XPS)

X-Ray Photoelectron Spectroscopy (XPS) is a surface sensitive analysis technique to provide useful information of chemical compositions, oxidation states and bonding environments of the target materials.[30] Unlink X-ray diffraction which uses the high photon energy Cu (8047.8 eV) as a source element, the XPS is commonly accommodated with an Al or Mg source which has significantly lower photon energy (Al Kα: hυ = 1486.6 eV, Mg Kα: hυ = 1253.6 eV) that generates soft X-ray beams.[31] In contrast to XRD, XPS is surface sensitive due to the strong inelastic scattering of the outward flux of low energy electrons. As a result, only electrons generated within a few nm of the surface can escape to the vacuum without losing energy, which leads to the high sensitivity for the material surface analysis (1-10 nm) of XPS.

In theory, the XPS is based on the photoelectric effect wherein the incident photons are absorbed by the core electrons in the atom of individual elements, leading to subsequent ejection of photoelectrons. The ejected photoelectrons are then collected by the electron detector for quantity counting and corresponding kinetic energy measuring. The relationship between the binding energy (B.E.) and the photoelectron kinetic energy is described as:

$$E_{binding} = h\upsilon - E_{kinetic} - \phi \qquad (Equation\ 2.6)$$

where $E_{binding}$ is the binding energy of the excited electron to the nucleus; h is the Planck constant ($h = 6.626\times10^{-34}$ J·Hz^{-1}); υ is the frequency of the incident X-ray; $E_{kinetic}$ is the kinetic energy of photoelectron; ϕ is the work function of the spectrometer, which is the amount of energy that required to get the photoelectrons from the solid material out into vacuum.

The emission of the photoelectron will lead to formation of an electron hole which is then relaxed by an electron from a higher energy orbital to drop down as shown in Figure 2.6. The excess energy can be released by the emission of X-ray radiation with a specific wavelength of element or be transferred to emit a secondary electron, which is called Auger electron. The Auger electrons can also be detected by the electron detector during XPS measurement that acts as another fingerprint to identify the elemental composition and oxidation state of the materials.

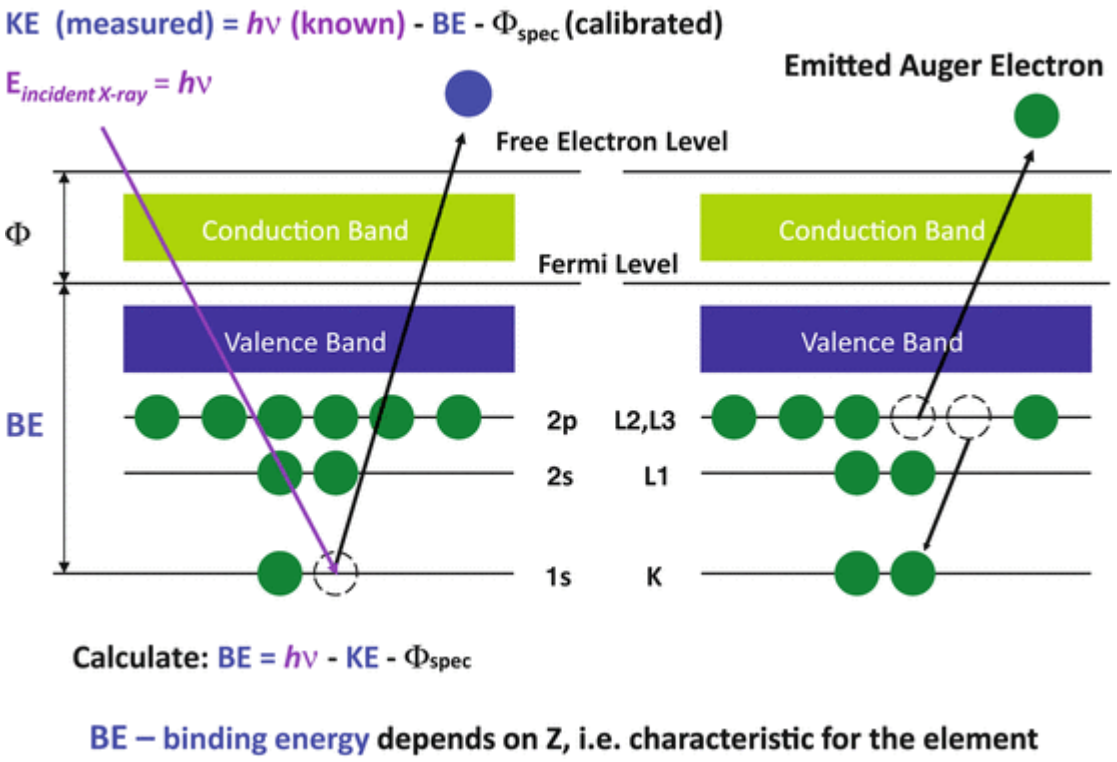


Figure 2.6 An illustration of the fundamental principle of X-ray photoelectron spectroscopy. Figure reproduced from ref.[30]

For XPS measurement, it requires ultra-high vacuum ($<10^{-8}$ torr) condition to avoid collisions between photoelectrons and gas molecules in the spectrometer and minimize surface contamination from residual gases.[31] A survey scan for elemental composition analysis can be acquired by scanning the binding energy from 0 eV to 1400 eV. The XPS spectra can be quantified in terms of peak intensities and peak positions. The peak intensities can measure the quantity of material at the surface while the peak positions can indicate the elemental and chemical compositions. Relative sensitivity factors (RSF) of photoelectric peaks are often taken into account to scale the measured intensities for the atomic concentration calculation.[32] In principle, the peak positions in terms of binding energy provide information about the chemical state of a material. By comparing the position of the binding energy of the sample with standard materials with known B.E. (e.g. metal chlorides, oxides etc), the oxidation state of the absorbing element can be estimated.[32] As for materials with multiple oxidation states, the resultant spectra might consist of different features (double humps, peak shoulder, etc) that

can be resolved into various Gaussian peaks (with a reasonable full width half maximum) to represent the species. Particularly, doublets with a fixed ratio of peak height can be identified as a result of spin-orbit coupling for p, d and f orbitals.

In this thesis, XPS is employed to monitor the phase change in MgO structure during the time-course of the hydrogen evolution reaction. Typically, O1s peaks can be resolved into 2 sub-peaks, namely [O^{2-}] component (lower B.E.) and [OH] component (higher B.E.). By keeping track of the ratio of these 2 peaks, the contribution of each phase (MgO/ $Mg(OH)_2$) can be calculated under dynamic situations.

2.7 UV-Visible Spectroscopy (UV-Vis)

UV-visible spectroscopy is an analytical technique to measure the amount of discrete wavelengths of UV or visible light that is absorbed by or transmitted through a sample in comparison to a reference.[33] The samples will absorb UV or visible light at specific wavelengths to excite the π-electrons or non-bonding electrons (n-electrons) to higher anti-bonding molecular orbitals.[34] The absorbance or transmittance is greatly correlated with the sample concentration and optical path length, which can be described by the Beer-Lambert law:

$$A = \varepsilon_\lambda \, l \, c = log_{10} \frac{I_0}{I} = log_{10} \frac{1}{T} \qquad (Equation\ 2.7)$$

where A is the absorbance; ε_λ is the molar extinction coefficient at specific wavelength λ, which is an intrinsic property of the species; l is the optical path length of light; c is the concentration of the species in the sample; I_0 is the detected light intensity of reference cell; I is the detected light intensity of sample cell; T is the transmittance.

For a lab-based UV-Visible spectrophotometer, a tungsten lamp is commonly used for the visible light source whereas the deuterium lamp is the common source of UV light (Figure 2.7). The instrument will switch the light source for a different range of wavelengths (typically

switch between 300 and 350nm) automatically according to the scan. In principle, the light source generates a variety of wavelengths of light, and the light passes the entrance slit of the monochromator then refracted by the prism into a rainbow of colours, which makes each wavelength of light is moving to a different place in space. In this case, only one wavelength of light can go through the exit slit of the monochromator striking the beam splitter and becoming two parallel beams of equal intensity. The two parallel beams then traverse the reference cell and sample cell respectively and reach the two photodetectors for data processing. By comparing the transmittance between the reference cell sand sample cell, the sample absorbance at different wavelengths can be derived and generate the UV-Visible spectra.

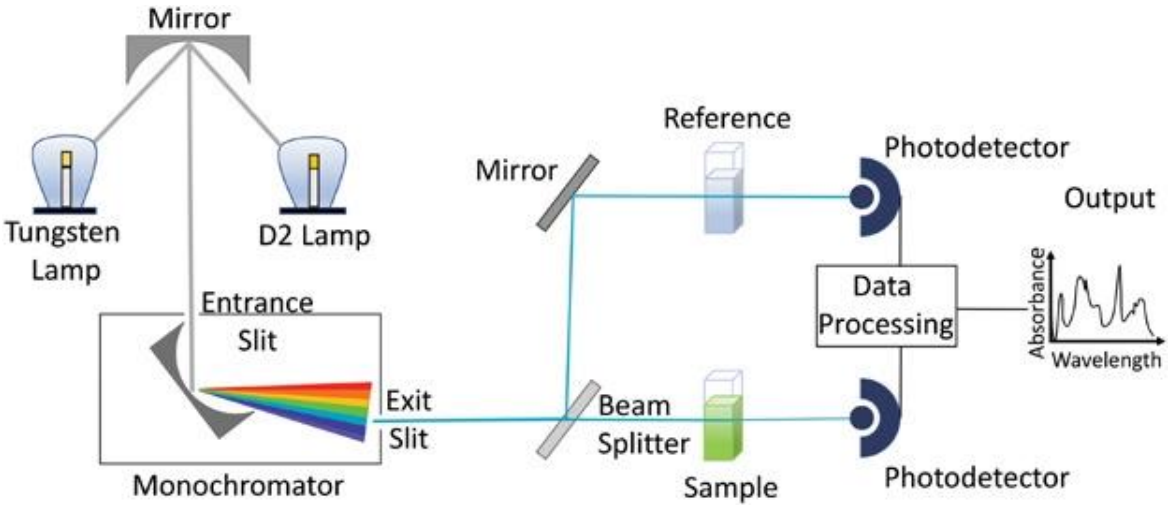


Figure 2.7 A schematic illustration of UV-Visible spectrometer instrument. Figure reproduced from ref.[35]

Additionally, some nanostructured materials (e.g., Au, Ag, Cu, doped semi-conductors, etc.) exhibit distinct optical features, known as localised surface plasmon resonance (LSPR), which is the collective oscillation of electrons in the conduction band of the materials in resonance with a specific wavelength of the incident light. LSPR effect of the plasmonic metals will then result in a strong absorbance band in UV/visible region and show a large absorption peak in the UV-Visible spectra. The LSPR spectrum measured by UV-Vis is greatly dependent on the shape, size, elemental composition, and dielectric environment of the nanoparticles.[36]

In this thesis, UV-Vis spectroscopy is employed to analyse the absorption peaks of Ag nanoparticles of different morphologies (cube, sphere, wire) and Au-Ag core-shell nanoparticles of different shell thicknesses to correlate the optical properties and catalytic performance of the materials.

2.8 Atom Probe Tomography (APT)

Atom probe tomography (APT) is a three-dimensional micro characterization technique that is used to visualize and quantify the microstructure of nanomaterials at atomic level (0.1-0.3 nm resolution in depth and 0.3-0.5 nm laterally).[37,38] This technique is complementary to other major microscopy techniques such as TEM/STEM and it can provide high spatial resolution for chemical analysis. APT allows the determination of elemental compositions and atomic arrangement at different positions within the material so as to enable the reconstruction of 3D images for the structure-activity correlation analysis. Particularly, for the core-shell materials, the core and shell boundary can be identified in detail and the concentrations of different compositions along the nanoparticle can be determined in APT analysis. In principle, the APT is a destructive technique to disassemble the sample atom by atom, where the atoms are then measured and identified, eventually the original sample is spatially reconstructed in a 3D model.[37]

In detail, the sample is prepared in the form of a needle-shaped specimen of 50-100 nm using focused ion beams (FIB) or electrochemical etching. During the APT measurement, the specimen is cooled to cryogenic temperature (typically 20 -100 k) to suppress diffusion of the surface atoms, and the chamber is performed under ultra-high vacuum conditions to suppress adsorption of residual gas molecules on the specimen.[37] Then a DC voltage (typically < 15 kV) is applied at the tip of the needle to induce a strong electrostatic field and superimpose voltage pulses to field evaporate the surface atoms as ions. The field evaporated ions are then projected on the detector that the projected positions and time of flight are recorded using a mass

spectrometer detector and position sensitive detector, which can simultaneously measure the original x, y, z position in the material and the identity of the atom. The path of the ions is determined by the position on the tip and the time of flight is determined by the mass of the ion. Particularly, the field evaporation is precisely controlled to remove only one atom at a time from the tip. Thus, the detector can analyse the data from each atom to provide the 3D position of it in the specimen and identify the elemental composition by the mass-to-charge ratio.[38]

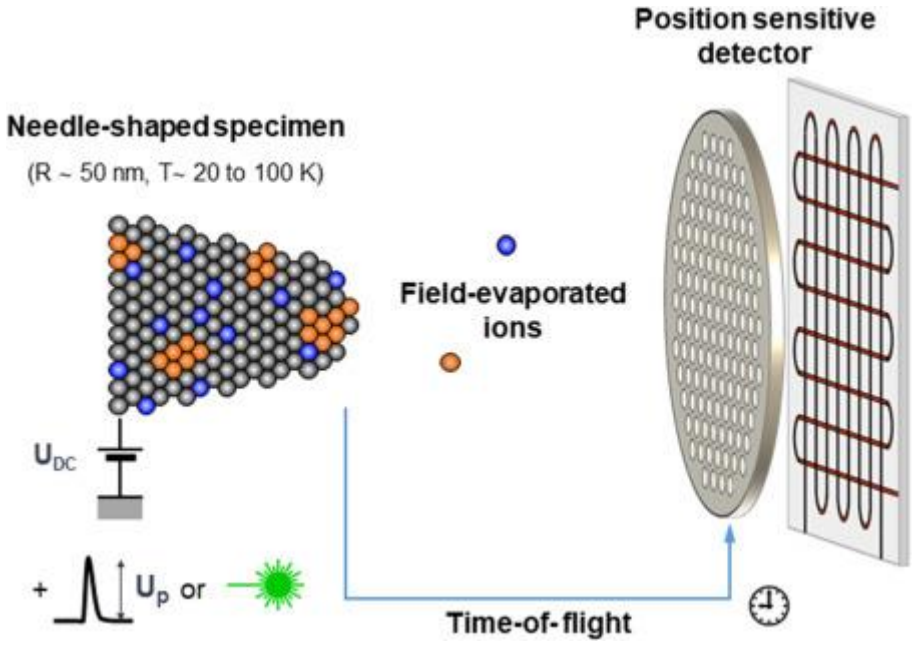


Figure 2.8 A schematic illustration of the APT working principle. The surface atom is field evaporated by the voltage or laser pulse as an ion and removed from the tip one at a time. The mass of the atom removed is measured by time-of-flight mass spectroscopy. Figure reproduced from ref.[37]

In this thesis, APT was employed to characterize the Au-Ag core-shell nanoparticles of different shell compositions and thicknesses. The elemental distributions of Ag and Au in the tailored shell are reconstructed in 3D models to show the difference in concentration of the Ag and Au as the shell thickness varied. The detailed atomic arrangement and shell homogeneity of a single nanoparticle is also studied, which can help to correlate the catalytic performance with the atomic arrangement of the catalyst materials.

2.9 X-Ray Absorption Spectroscopy (XAS)

X-ray absorption spectroscopy is a characterisation technique that can precisely measure the oxidation state, local coordination environment, disorderness in neighbouring atoms, and bonding geometry of individual elements of a compound.[39,40] XAS is mainly performed at synchrotron sources due to the strong intensity of the X-ray sources and tuneable energy range. Experimentally, a monochromatic X-ray is directed towards a sample to excite the electrons through 2 modes, namely transmission and fluorescence.[41] For the former, it is for the measurement of bulk materials to serve as standards for comparison (identify binding energy position of oxidised state and reduced state using metal oxide and respective metal foil); whereas the latter is used to measure dilutive samples (especially for cases of supported nanomaterials in this thesis). When the energy of the incident X-ray matches with that of the binding energy of a core-level electron, it will result in a strong absorption, which is known as the absorption edge in XAFS (X-ray Absorption Fine Structure) terms.[42] Since every atom has well-defined binding energies for each of the core electrons, the energies of the X-ray can be precisely tuned to excite targeted elements of desire. The energy of the edge is identified according to the electron's principal quantum number, namely n=1 for K-edge, n=2 for L-edge, and n=3 for M-edge.

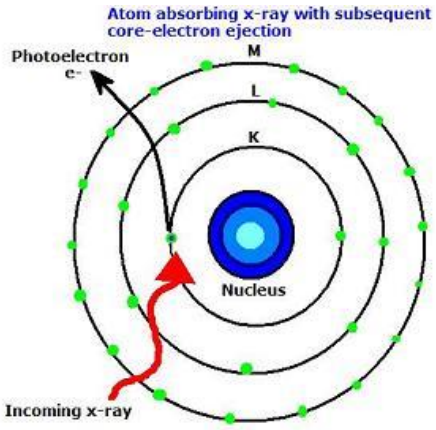


Figure 2.9 High energy synchrotron X-ray absorption for core electron transition. Figure reproduced from ref.[43]

There are 2 regions of interest for typical XAS spectra. The first one is XANES (X-ray Absorption Near Edge Spectroscopy) that includes the absorption edge as well as the area shortly before and after the edge. While the edge represents the excitation of the core electrons excited to the continuum, resulting in a strong characteristic absorption edge that can reflect information about the oxidation state of the absorbing element; the shoulder peaks in the pre-edge region represent bound state transition into higher energy orbitals that can be used to infer the spatial orientation and energy of the unoccupied orbitals, as well as neighbouring occupied ligand orbitals for some cases[41]. Thus, the bonding geometry and the coordination environment of the absorbing element can affect critically the shape and size of the peaks in the XANES region.

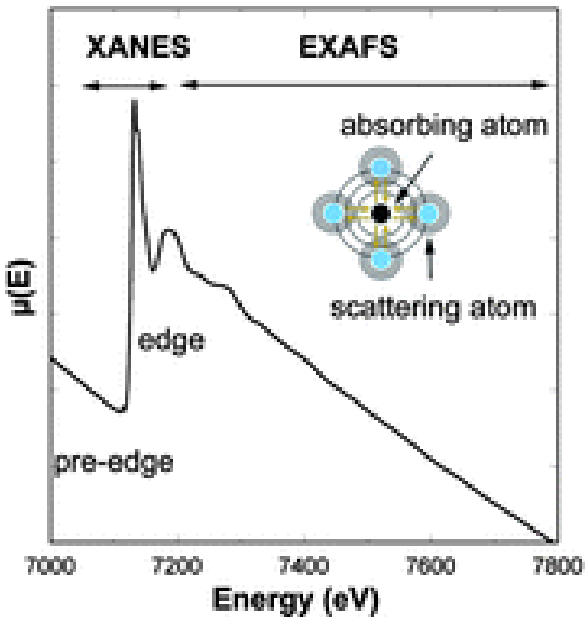


Figure 2.10 Typical XAS spectra depicting XANES (near-edge and edge) and EXAFS (post-edge oscillation) regions. Figure reproduced from ref.[44]

Another region of interest is EXAFS (Extended X-ray Absorption Fine Structure) that encompass the oscillation region after the absorption edge. The characteristic oscillation shape is originated from the interference between the emitted photoelectron and the backscattered electrons. The scattering process can be classified into 2 categories, namely single scattering

(1-D space-distance relationship) and multiple scattering (2-D polar coordinate system that includes more than 2 scattering atoms).[45] With the assist of Fourier Transform to decompartmentalize the signal, it is possible to infer the interatomic distance and the type/ number of ligands within the first coordination shell.

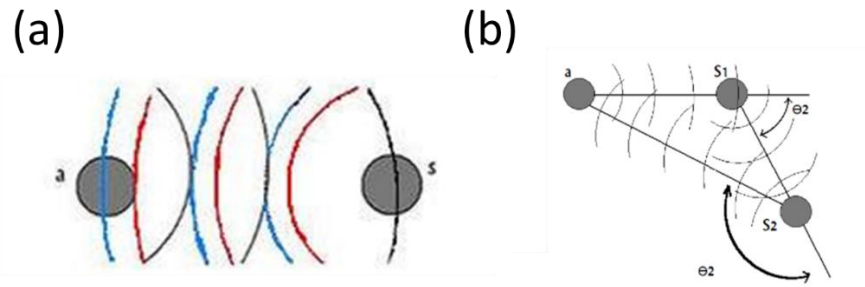


Figure 2.11 a) Single scattering; **b)** multiple scattering depiction in X-ray absorption spectroscopy. Figure reproduced from ref.[45]

In addition to typical EXAFS Fourier-transformed R-space spectra that provide information about the relationship between radial distance and peak intensity of the absorbing atom, Wavelet transform serves as a complementary tool that further resolves the energy space (k-space).[46,47] This is especially useful in distinguishing between close atomic distances within the same coordination shell.[48] By taking into account k-space contributions, it is possible to "separate" the elements in terms of atomic number (for example, distinguish between Zn-Zn and Zn-Al where Al is a lighter element).

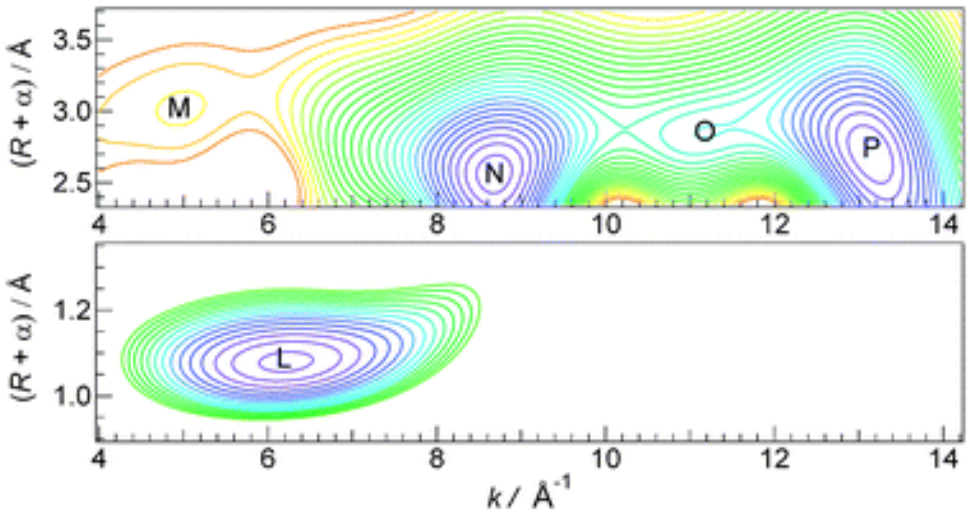


Figure 2.12 Typical Wavelet transform spectra that can be used to distinguish bonding interactions with close atomic distance. In this image, Mo-N (lighter element) is resolved at lower k energy maxima while Mo-P is at higher k energy maxima. Figure reproduced from ref.[49]

In this thesis, EXAFS is used to calculate the bond distances and coordination numbers around the first shell of the core-shell nanoparticles. By comparing between the Au-Ag coordination numbers, it can thus be inferred the thickness of the elemental layer (silver with immediate gold neighbours for atomic-shell sample versus silver staying in the vicinity of other silver neighbours for thicker-shells samples). Given the close atomic distance between Ag-Au (2.87 A) and Ag-Ag (2.88 A), wavelet transform is further employed to resolve the space-energy domain between Ag (lighter element with lower k maxima) and Au (heavier element with higher k maxima).

2.10 Brunauer–Emmett–Teller (BET) Theory

BET theory is a widely used technique in catalysis to measure the specific surface area of sample materials by means of physical adsorption. An inert probing gas, usually nitrogen, will be used as adsorbate onto the surface of the material. Due to the weak van der Waals' interaction between gas and solid, the BET measurement is usually carried out at the boiling temperature of nitrogen (77K).[50]

Theoretically speaking, BET theory is an extension of the Langmuir theory that depicts the surface coverage of the adsorbate as a function of the equilibrium pressure of the adsorbate at the temperature of adsorption. The resulting BET equation is described as follow:[51]

$$\frac{1}{v[\left(\frac{p_0}{p}\right)-1]} = \frac{c-1}{v_m\, c}\left(\frac{p}{p_0}\right) + \frac{1}{v_m\, c} \qquad (Equation\ 2.8)$$

where v is the adsorbed gas volume; v_m is the volume of a single monolayer of adsorbed gas; p_0 and p is the equilibrium and the saturation pressure of adsorbates at the temperature of adsorption respectively; and c is the BET constant, which is related to the adsorbent/adsorbate interactions, and it's normally between 100-200.

Therefore, by plotting the term $\frac{1}{v\left[\left(\frac{p_0}{p}\right)-1\right]}$ against $\left(\frac{p}{p_0}\right)$, a linear plot can be obtained and the monolayer adsorbate gas volume v_m can be calculated. The specific surface area (S_{BET}) can be further derived using:[51]

$$S_{BET} = \frac{S_{total}}{a} = \frac{(v_m\, N\, s)}{(a\, V)} \qquad (Equation\ 2.9)$$

where N is the Avogadro number; s is the surface area of a single gas molecule adsorbed on the solid; a is the mass of the sample; and V is the molar volume of the gas adsorbate.

In this thesis, the BET theory is used to measure the surface area of the MgO supports with different preferential exposed facets such as (111), (110) and (100), and the BET measurements are taken at the Surface Analysis Facility (SAF) at the Chemistry Research Laboratory at the University of Oxford.

2.11 Electrochemical Techniques

In this thesis, catalytic performance testings were carried out via a series of electrochemical methods within two different types of setups: PEM electrolyser with solid electrolyte and conventional three-electrode system with liquid electrolyte.

In PEM electrolyser, the two working electrodes (cathode for HER and anode for OER) are separated by a solid electrolyte membrane and connected to the potentiostat station. The major PEM cell components consist of membrane electrode assemblies (MEAs), current collectors and separator plates. As the heart of the electrolysis cell, MEA is formed by PEM membranes, ionomer solution, and electrocatalysts for both anode and cathode. The fabrication of MEA can be achieved by the catalyst-coated substrate (CCS) method, in which the homogenous electrocatalyst slurry is coated onto the gas diffusion layer (GDL), and is then combined with the PEM membrane using the hot-press process.[52] The addition of the ionomer solution is to promote the proton transport from the electrode layer to the membrane and the ionomer solution can act as a binder to stabilize the catalyst-electrode structure.[53] The current collector is used to allow the electrical current to flow between the electrodes, which is usually made of titanium meshes due to their good electrical conductivity, mechanical stability and corrosion resistance under acidic medium. At the same time, the separator plates are also made of titanium, which provides a conduction path for water input and produced gases output.[53] The catalytic performance of the electrocatalysts in the PEM water electrolyser can be accessed by the polarization curves. In this thesis, the polarization curve is obtained by a stepwise steady-state voltage sweep, which applies a series of consecutive ascending voltages between two specified voltages and the corresponding current density is recorded after stabilization. The detailed experimental method is described in chapter 3 (section 3.2.1).

The conventional three-electrode system usually consists of a working electrode (WE), a counter electrode (CE) and a reference electrode (RE) installed in the same container with a

liquid electrolyte. Glassy carbon electrodes (GCE), as well as carbon paper electrodes, are usually employed as the working electrodes due to their electrocatalytic inertness over a large potential window and good electrical conductivity, particularly the ease in handling of the carbon paper makes it flexible to be used in in-situ experiments.[54] On the other hand, fluorine-doped tin oxide (FTO) coated glass is widely used as the working electrode for photoelectrochemical reaction due to the transparency for light to pass through, good electrical conductivity and chemical stability.[55] The counter electrode is used to complete the circuit and allow charges to flow, which is usually made of inert materials such as Pt wire and graphite rod. The reference electrodes have stable and well-defined potentials that allow the potential applied to the electrochemical system controllable with respect to the reference potentials. Saturated calomel electrode (SCE), silver/silver chloride electrode (Ag/AgCl) and mercury/mercury oxide (Hg/HgO) are commonly used as reference electrodes. The reference electrode potentials can be calibrated to the reversible hydrogen electrode (RHE) potentials for comparison across different reference electrodes and pH. There are 2 common ways to experimentally convert the potential to the RHE scale, with the first being the potential difference measurement between the reference electrode of interest and a RHE; while the other being the zero-crossing potential measurement of a Pt wire in the hydrogen-saturated electrolyte.[54,56] Electrocatalyst ink is usually prepared by sonication of the catalyst and solvent mixture with the ionomer solution (such as Nafion), in which the link is subsequently cast on the working electrode for electrochemical testing.

The three electrodes (WE, CE and RE) are connected to the potentiostat that provides an applied potential between the working electrode and reference electrode. The performance of an electrocatalyst can be assessed by a series of electrochemical analysis methods such as linearly scanning voltammetry (LSV) and chronoamperometry (CR).

Voltammetry is one of the most widely used techniques to study the electrochemical properties of the electrocatalysts, which measures current (I) as a function of potential (V).[57] The potential is changed continuously between two specified values pre-set in the potentiostat. The voltammogram can be obtained by plotting the I-V curves, which provides electrochemical information such as overpotentials and performance evaluation of the electrocatalysts. Linear sweep voltammetry (LSV) is mainly used in this thesis, in which the applied potential is scanned across a potential range linearly with time. HER catalytic performance of different electrocatalysts is estimated by LSV in chapters 4 and 6, and the potential is scanned from a positive potential where no faradaic current flows to a fixed negative potential for proton reduction at a slow scan rate (<10 mV/s).

Another subclass electroanalytical technique used in the thesis is chronoamperometry (CR) that measures the current as a function of reaction time at a fixed potential.[57] The CR is used to analyse the long-term stability of the electrocatalysts and investigate the photocurrent response in the PEC analysis in this thesis. The detailed experimental method is described in chapter 3 (section 3.2.2).

2.12 References

1. Atkins, P., Overton, T., Rourke, J., Weller, M. & Fraser Armstrong. *Shriver & Atkins' Inorganic Chemistry*. (OUP oxford, 2009).
2. Pecharsky, V. & Zavalij, P. *Fundamentals of Powder Diffraction and Structural Characterization of Materials*. (Springer, 2008).
3. Miller, M. P. & Dawson, P. R. Understanding local deformation in metallic polycrystals using high energy X-rays and finite elements. *Curr. Opin. Solid State Mater. Sci.* **18**, 286–299 (2014).
4. Artioli, G. *Encyclopedia of Geoarchaeology*. *Springer* (Springer Netherlands, 2017). doi:10.1007/978-1-4020-4409-0.
5. Crystal Structure Studies. https://biochem.co/2008/08/crystal-structure-studies/ (2008).
6. Brown, J. G. Diffraction of X-Rays. in *X-Rays and Their Applications* 95–121 (Springer US, 1966). doi:10.1007/978-1-4899-5687-3_6.
7. Zachariah, A. K., Mishra, R. K., Thomas, S. & Thomas, R. *Microscopy Methods in*

Nanomaterials Characterization. (Elsevier science, 2017).

8. Clausing, R. E. *et al.* Surface Structure Determination By X-Ray Diffraction. *Surf. Sci. Rep.* **10**, 105–188 (1989).

9. Thompson, S. P. *et al.* Fast X-ray powder diffraction on I11 at Diamond. *J. Synchrotron Radiat.* **18**, 637–648 (2011).

10. Philip Willmott. *An Introduction to Synchrotron Radiation: Techniques and Applications*. (John Wiley & Sons, Ltd, 2011).

11. Barnes, P., Cockcroft, J. K., Jacques, S. & Vickers, M. How do Synchrotrons Work? http://pd.chem.ucl.ac.uk/pdnn/inst2/work.htm.

12. Mo, J. *et al.* Superior Performance of Ag over Pt for Hydrogen Evolution Reaction in Water Electrolysis under High Overpotentials. *ACS Appl. Energy Mater.* **2**, 1221–1228 (2019).

13. Zhang, Q., Li, W., Wen, L. P., Chen, J. & Xia, Y. Facile synthesis of Ag nanocubes of 30 to 70 nm in edge length with CF 3COOAg as a precursor. *Chem. - A Eur. J.* **16**, 10234–10239 (2010).

14. Wu, S. *et al.* Removal of Hydrogen Poisoning by Electrostatically Polar MgO Support for Low-Pressure NH 3 Synthesis at a High Rate over the Ru Catalyst. *ACS Catal.* **10**, 5614–5622 (2020).

15. Chen, J. Y., Jheng, S. Lou, Chan, C. Y. & Tuan, H. Y. Morphology controlled synthesis of Pd2Ge nanostructures and their shape-dependent catalytic properties for hydrogen evolution reaction. *Int. J. Hydrogen Energy* **44**, 12958–12970 (2019).

16. Michler, G. H. Electron Microscopy of Polymers. in *Electron Microscopy of Polymers* 15–51 (Springer Berlin Heidelberg, 2008).

17. Hell, S. W. & Robert N. Weinreb. *High Resolution Imaging in Microscopy and Ophthalmology*. (Springer, 2019).

18. Williams, D. B. & Carter, C. B. *Transmission Electron Microscopy*. (Springer US, 2009).

19. Abraham, J., Jose, B., Jose, A. & Thomas, S. Characterization of green nanoparticles from plants. in *Phytonanotechnology* 21–39 (Elsevier, 2020).

20. Das, P. Optical Properties of Low Dimensional Structures Using Cathodoluminescence in a High Resolution Scanning Electron Microscope. (University of Calcutta, 2014).

21. Wang, Z. L. Transmission Electron Microscopy of Shape-Controlled Nanocrystals and Their Assemblies. *J. Phys. Chem. B* **104**, 1153–1175 (2000).

22. Yin, J. S. & Wang, Z. L. Ordered self-assembling of tetrahedral oxide nanocrystals. *Phys. Rev. Lett.* **79**, 2570–2573 (1997).

23. Harfenist, S. A., Wang, Z. L., Whetten, R. L., Vezmar, I. & Alvarez, M. M. Three-dimensional hexagonal close-packed superlattice of passivated Ag nanocrystals. *Adv. Mater.* **9**, 817–822 (1997).

24. Bentzon, M. D. & Thölén, A. R. Phase contrast from a regular stacking of equally sized iron-oxide spheres. *Ultramicroscopy* **38**, 105–115 (1991).

25. MicroscopeWorld. Darkfield Microscopy. https://www.microscopeworld.com/t-darkfield_microscopy.aspx.

26. Reedijk, J. & Poeppelmeier, K. *Comprehensive Inorganic Chemistry II*. (Elsevier, 2013).

27. Nellist, P. D. Scanning Transmission Electron Microscopy. in *Science of Microscopy* 65–132 (Springer New York, 2007). doi:10.1007/978-0-387-49762-4_2.

28. Yamashita, S. *et al.* Atomic number dependence of Z contrast in scanning transmission electron microscopy. *Sci. Rep.* **8**, 12325 (2018).

29. Grogger, W., Hofer, F., Kothleitner, G. & Schaffer, B. An introduction to high-resolution EELS in transmission electron microscopy. *Top. Catal.* **50**, 200–207 (2008).

30. Haasch, R. T. X-Ray Photoelectron Spectroscopy (XPS) and Auger Electron Spectroscopy (AES). in *Practical Materials Characterization* 93–132 (Springer New York, 2014). doi:10.1007/978-1-4614-9281-8_3.

31. Mattox, D. M. Substrate ("Real") Surfaces and Surface Modification. in *Handbook of Physical Vapor Deposition (PVD) Processing* 25–72 (Elsevier, 2010). doi:10.1016/B978-0-8155-2037-5.00002-2.

32. *Casa XPS Manual*. *CasaXPS* (2013).

33. Thomas, M. J. K. & Ando, D. J. *Ultraviolet and Visible Spectroscopy*. (Wiley, 1996).

34. Wang, H. & Chu, P. K. Surface Characterization of Biomaterials. in *Characterization of Biomaterials* (eds. Bandyopadhyay, A. & Bose, S.) 105–174 (Elsevier, 2013). doi:10.1016/B978-0-12-415800-9.00004-8.

35. Rocha, F. S., Gomes, A. J., Lunardi, C. N., Kaliaguine, S. & Patience, G. S. Experimental methods in chemical engineering: Ultraviolet visible spectroscopy-UV-Vis. *Can. J. Chem. Eng.* **96**, 2512–2517 (2018).

36. Kale, M. J., Avanesian, T. & Christopher, P. Direct photocatalysis by plasmonic nanostructures. *ACS Catal.* **4**, 116–128 (2014).

37. Choi, P.-P., Im, H. J., Jung, C., Ryou, K. & Jeong, H. Atom Probe Tomography: Unveiling the Elemental Distribution in Nanostructured Materials With Near-Atomic Resolution. in *Encyclopedia of Materials: Metals and Alloys* 641–647 (Elsevier, 2022). doi:10.1016/B978-0-12-819726-4.00050-8.

38. Baer, D. R. & Thevuthasan, S. Characterization of Thin Films and Coatings. in *Handbook of Deposition Technologies for Films and Coatings* (ed. Martin, P. M.) 749–864 (Elsevier, 2010). doi:10.1016/B978-0-8155-2031-3.00016-8.

39. Rehr, J. J., Ankudinov, A. & Zabinsky, S. I. New developments in NEXAFS/EXAFS theory. *Catal. Today* **39**, 263–269 (1998).

40. Ravel, B. Quantitative EXAFS Analysis. in *X-Ray Absorption and X-Ray Emission Spectroscopy* vols 1–2 281–302 (John Wiley & Sons, Ltd, 2016).

41. Sakura Pascarelli. *X-RAY ABSORPTION SPECTROSCOPY: FUNDAMENTALS AND SIMPLE MODEL OF EXAFS Part I: Fundamentals of X-ray Absorption Fine Structure*. (2016).

42. Wang, M., Árnadóttir, L., Xu, Z. J. & Feng, Z. In Situ X-ray Absorption Spectroscopy Studies of Nanoscale Electrocatalysts. *Nano-Micro Lett.* **11**, 47 (2019).

43. XAS - Theory - Chemistry LibreTexts. https://chem.libretexts.org/Bookshelves/Physical_and_Theoretical_Chemistry_Textbook_Maps/Supplemental_Modules_(Physical_and_Theoretical_Chemistry)/Spectroscopy/X-ray_Spectroscopy/XAS_-_Theory.

44. Ortega, R., Carmona, A., Llorens, I. & Solari, P. L. X-ray absorption spectroscopy of biological samples. A tutorial. *J. Anal. At. Spectrom.* **27**, 2054 (2012).

45. EXAFS: Theory - Chemistry LibreTexts. https://chem.libretexts.org/Bookshelves/Physical_and_Theoretical_Chemistry_Textbook_Maps/Supplemental_Modules_(Physical_and_Theoretical_Chemistry)/Spectroscopy/X-ray_Spectroscopy/EXAFS%3A_Theory.

46. Harald Funke, M. C. *Wavelet analysis of EXAFS data - first studies*. (2002).

47. Funke, H., Chukalina, M. & Scheinost, A. C. A new FEFF-based wavelet for EXAFS data analysis. *J. Synchrotron Radiat.* **14**, 426–432 (2007).

48. Funke, H., Scheinost, A. C. & Chukalina, M. Wavelet analysis of extended x-ray absorption fine structure data. *Phys. Rev. B - Condens. Matter Mater. Phys.* **71**, 094110 (2005).

49. Savinelli, R. O. & Scott, S. L. Wavelet transform EXAFS analysis of mono- and dimolybdate model compounds and a Mo/HZSM-5 dehydroaromatization catalyst. *Phys. Chem. Chem. Phys.* **12**, 5660–5667 (2010).

50. Naderi, M. Surface Area. in *Progress in Filtration and Separation* 585–608 (Elsevier, 2015). doi:10.1016/B978-0-12-384746-1.00014-8.

51. Palchoudhury, S., Baalousha, M. & Lead, J. R. Methods for Measuring Concentration (Mass, Surface Area and Number) of Nanomaterials. in *Frontiers of Nanoscience* vol. 8 153–181 (Elsevier, 2015).

52. Lim, B. H. *et al.* Comparison of catalyst-coated membranes and catalyst-coated substrate for PEMFC membrane electrode assembly: A review. *Chinese J. Chem. Eng.* **33**, 1–16 (2021).

53. Shiva Kumar, S. & Himabindu, V. Hydrogen production by PEM water electrolysis – A review. *Mater. Sci. Energy Technol.* **2**, 442–454 (2019).

54. Brett, C. M. A. & Brett, A. M. O. *Electrochemistry: Principles, Methods, and Applications*. vol. 34 (Oxford University Press, 1994).

55. Korjenic, A., Raja, K. S. & Soc, J. E. Electrochemical Stability of Fluorine Doped Tin Oxide (FTO) Coating at Different pH Conditions. *J. Electrochem. Soc.* **166**, C169 (2019).

56. Compton, R. & Banks, C. *Understanding Voltammetry*. (Imperial College Press, 2010). doi:https://doi.org/10.1142/p726.

57. Scholz, F. *et al. Electroanalytical Methods Guide to Experiments and Applications*. (Springer Berlin Heidelberg, 2010). doi:10.1007/978-3-642-02915-8.

Chapter 3 Experimental Methods

Table of Contents

Chapter 3 Experimental Methods 90
3.1 Characterizations 91
3.1.1 XRD 91
3.1.2 Titan STEM and Super-X EDS 91
3.1.3 STEM-EELS 91
3.1.4 SEM 92
3.1.5 TGA 92
3.1.6 APT 92
3.1.7 XPS 93
3.2 HER Catalytic Testing 93
3.2.1 PEM Water Electrolyser 93
3.2.2 Three-electrode Aqueous Medium Systems 96
3.2.3 Operando Electrochemical SXRD 100
3.3 Computational Modelling and Calculations 102
3.3.1 DFT Calculations on Hydrogen Adsorption Energies 102
3.3.2 DDA Analysis of Au-Ag Core-shell Materials 102
3.3.3 DFT Modelling on MgO Supports 103
3.4 References 104

3.1 Characterizations

3.1.1 XRD

Powder X-ray diffraction patterns were performed using a Bruker D8 advance diffractometer with LynxEye detector and Cu K_α radiation ($\lambda = 1.5406$ Å) operating at 40 kV and 25 mA. XRD patterns were collected by scanning from 5° to 90° with a step size of 0.008° and a step time of 25.4 s.

3.1.2 Titan STEM and Super-X EDS

Atomic-resolution EDS mapping was performed with an aberration-corrected scanning transmission electron microscope (S/TEM, Thermo Fisher Titan Themis Z 300) operated at 300 kV with a convergence semi-angle of 23.6 mrad. The microscope was aligned before every experiment by using a gold standard sample ensuring 0.06 nm resolution under normal conditions. EDS analysis was carried out from its highly sensitive Super-X detector which contains a high-speed, high-throughput, quad-silicon drift detector optimized for rapid x-ray collection, and when combined with STEM enables EDS spectral mappings down to the atomic scale. The microscope was set to C2 aperture at 70 µm with beam current was set between 150~200 pA during the EDS data acquisition. The dwell time was set to 100 µs per pixel with a map size of 256 × 256 pixels; a complete process of EDS mapping took roughly 1 hour to reach an appropriately high signal-to-noise ratio.

3.1.3 STEM-EELS

High-resolution transmission electron microscopy was carried out on a JEOL JEM-2100F operated at 200 kV. The high-angle annular dark-field scanning transmission electron microscopy (HAADF-STEM) imaging was carried out using a cold FEG aberration-corrected JEOL ARM200F. The microscope was operated at 200 kV in HAADF-STEM mode with HAADF detector collection semi-angles from 73 to 271 mrad. Low-loss EELS were acquired by capturing many short acquisition spectra (< 10 ms each) and then summing the spectra for

a desired step size. This avoided saturation of the zero-loss peak, and minimized the zero-loss peak FWHM, while still giving satisfactory signal-to-noise. Rather than using Digital Micrograph's inbuilt live spectral averaging feature, which did not sufficiently account for energy drift, we 'over-sampled' many spectra along a line scan (e.g., using a step size of 0.01 nm to effectively acquire 50 spectra per 0.5 nm) and aligned and summed offline using Digital Micrograph. EELS were acquired with a 20 meV dispersion at 200 keV using a 2.5 mm entrance aperture.

3.1.4 SEM

The scanning electron microscopy (SEM) measurements were performed using a field emission scanning electron microscope (Tescan MAIA3) operated at 10 kV.

3.1.5 TGA

Thermal gravimetric analysis (TGA) was carried out using an SDT-TGA Q600 at a heating rate of 10 ^{o}C /min from 40 ^{o}C to 900 ^{o}C in air.

3.1.6 APT

The atom probe tomography (APT) experiments were conducted in a CAMECA LEAP 5000 XR instrument at a specimen temperature of 50 K, a detection rate of 0.5, a pulsing rate of 125 kHz, and a laser pulse energy of 30 pJ. To prepare the APT specimens, nanoparticles were first distributed on a Ni-coated Si flat wafer and subsequently embedded by a 150-nm thick protective Ni layer in Leica EM ACE600 high vacuum sputter coater.[1] The needle-shaped APT specimens were then prepared by a standard lift-out procedure using a focused ion beam/scanning electron microscope (FIB/SEM) in FEI G4 CX. Data reconstructions and analysis were performed using the commercial IVAS 3.8.2™ software.

3.1.7 XPS

X-ray photoelectron spectroscopy (XPS) measurements were conducted using a Thermo Fisher EscaLab 250Xi at 1° angle of emission using a monochromatic Al Kα source (E_{photon} = 1486.6 eV) with a 10-mA filament current and a 12 keV filament voltage source energy. All the samples were etched by Ar ions for 60 s to clean the surface before the experimental measurements. The Ar ion cleaning was conducted at an energy of 500 eV, 50 μA cm^{-2}. All the spectra are calibrated with respect to the Mg 2s peak of 88.1 eV since the standard carbon peaks overlap with Ru 3d peaks.[2]

3.2 HER Catalytic Testing

The hydrogen evolution reaction (HER) rates of different catalysts were tested either in a PEM water electrolyser or a conventional three-electrode aqueous medium cell for comparisons. In this section, the experimental details of the PEM water electrolyser and the conventional three-electrode cell would be discussed in detail.

3.2.1 PEM Water Electrolyser

3.2.1.1 Experimental Setup

In Figure 3.1, it shows an overview of the PEM water electrolyser. The flow of N_2 gas to the cell cathode side was adjusted by mass-flow controllers and control units (A1, Brooks instrument, Model 5878; A2 mass flow controller). A humidifier containing a small amount of deionised (DI) water (B) was connected to the N_2 flow to provide water vapour for efficient operation of the PEM membrane. Then the humidified N_2 flew into the PEM water electrolyser (C) at the cathode side and DI water was pumped into the anode side at the same time by the HPLC pump (D). The temperature of the electrolyser and DI water fed-in were controlled by the temperature controllers (E, Eurotherm), while the applied potentials were adjusted via a potentiostat/ galvanostatic (AUTOLAB PGSTAT320N) with a 20 A booster. All process

parameters (applied potential, gas-flows, cell temperature and cell currents) were controlled and monitored through dedicated software running on the host PC (F).



Figure 3.1 Picture of the complete laboratory bench setup.

The PEM water electrolyser consists of a membrane-electrode assembly (MEA) cell holder, gas feed system and heaters. In Figure 3.2, it shows the exploded view of the electrochemical cell. The reactor cell with dimensions of 25 mm x 25mm (15 mm x 15 mm of electrode active area) was used to accommodate the test catalysts. The cell was equipped with 4 cartridge heaters and a thermocouple, allowing for controlling of the operation temperatures.

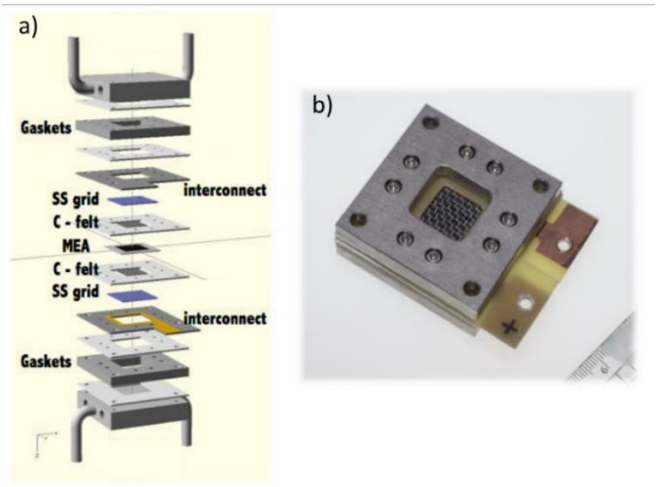


Figure 3.2 a) The construction of the electrochemical cell reactor; **b)** Image of MEA cell holder.

3.2.1.2 MEA Preparations

The membrane-electrode assemblies (MEA) were prepared by hot-pressing the Nafion membrane sandwiched in between the two electrodes, where the metal catalysts were loaded via spray-casting.

The Nafion 211 membranes purchased from FuelCellStore were cut into 2.5x 2.5 cm^2 pieces. These acidic membranes were pre-treated by soaking in 3% H_2O_2 at 80 ^oC for an hour to remove organic impurities, further soaking in 0.5 M H_2SO_4 at 80 ^oC for an hour to ion exchange the membrane completely and finally soaking in DI water at 80 ^oC for another hour. After that, the 20 wt% metal on vulcan carbon powder or the IrO_2 powdered catalyst (Aldrich) were mixed with Nafion ionomer solution (5 wt% solution, Aldrich) in a 3:1 weight ratio. The 20 wt% metal/C/ionomer or IrO_2 catalyst/ionomer mixtures were dispersed in the solution of isopropanol and DI water (3:1 volume ratio). The catalyst/ionomer mixture was then sonicated for 1 hour and deposited on the opposite sides of the Nafion membrane by spray casting via spray gun (Timbertech Airbrush). The 20 wt% metal/C was loaded onto the cathode at 0.4 ± 0.05 mg cm^{-2} of pure metal and IrO_2 catalysts was loaded on the anode side at 2.5 ± 0.2 mg cm^{-2} over a 1.5 x 1.5 cm^2 active area. The catalyst-loaded Nafion membrane was hot-pressed in between the carbon paper (Sigracet GDL 29BC) at the cathode side and Ti mesh (FuelCell Store) at the anode side at 135 ^oC for 3 min with 2.5 Mpa.

3.2.1.3 Reaction Conditions

The electrolyser performance was evaluated at 80 ^oC and under ambient pressure for all measurements. Deionized water was fed into the anode side at a flow rate of 4 mL/min. At each applied potential, the system was allowed to be stabilized for 30 minutes before recording the current densities. The polarization curves were recorded by the AUTOLAB programmable potentiostat (PGSTAT320N) with a 20 A booster.

The rate of hydrogen produced can be derived through the measurements of current densities. According to the current readings on the setup, hydrogen evolution rates from PEM water electrolyser can be calculated by:

Time (t, unit: s) × Current reading (I, unit: A) = Charge (Q, unit: C), which is

$$Q = I \times t \qquad \text{(Equation 3.1)}$$

From Faraday constant, 1 mol = 96485 C, also for per mol of H_2, 2 mol of electrons were required.

$$HER\ rate = \frac{Q}{Faraday\ constant \times 2} = \frac{I \times t}{Faraday\ constant \times 2}\ mol\ per\ time \qquad \text{(Equation 3.2)}$$

3.2.2 Three-electrode Aqueous Medium Systems

The electrochemical/photoelectrochemical testing were carried out in a conventional three-electrode configuration using either the AUTOLAB potentiostat (PGSTAT320N) or Vertex (Ivium Technologies) potentiostat. The electric current density (j, mA cm^{-2}) is used in this thesis to compare the catalytic performance among different electrocatalysts, which is obtained by dividing the current (I, mA) by the geometric area of the electrode (A, cm^2):

$$j = \frac{I}{A} \qquad (Equation\ 3.3)$$

The geometric area of the PEM water electrolyser electrode is 2.25 cm^2 (1.5×1.5 cm^2) and the glassy carbon electrode is 0.071 cm^2 ($\pi \cdot 0.15^2$ cm^2) in chapter 4, FTO glass working electrode is 1 cm^2 (1×1 cm^2) in chapter 5 and carbon paper electrode is 1 cm^2 (1×1 cm^2) in chapter 6.

Additionally, the potential measured against the Ag/AgCl (sat. KCl) reference electrode is converted to potential against RHE for more convenient comparison via the Nernst equation[3] in this thesis:

$$E_{RHE} = E_{Ag/AgCl} + \frac{2.303RT}{F} \cdot pH + E^0_{Ag/AgCl} \qquad (Equation\ 3.4)$$

$$= E_{Ag/AgCl} + 0.059 \cdot pH + E^0_{Ag/AgCl} \qquad (Equation\ 3.5)$$

where E_{RHE} is the potential measured against the reversible hydrogen electrode (RHE), $E_{Ag/AgCl}$ is the potential measured against the Ag/AgCl electrode, pH is the pH value of the electrolyte and $E^0_{Ag/AgCl}$ is the standard Ag/AgCl electrode potential ($E^0_{Ag/AgCl}$ = 0.198 vs NHE at T= 25 °C).

3.2.2.1 Standard Three-electrode System for HER on Ag NPs

In a standard three-electrode system, a platinum coil (CH instrument) was used as a counter electrode, an Ag/AgCl (Saturated KCl, CH instrument) electrode was used as the reference electrode and a glassy carbon rotating electrode (3 mm, Metrohm Ltd) was used as working electrode. To prepare the working electrode, 4 mg of the electrocatalyst and 80 µL of 5 wt% Nafion ionomer solution were dispersed in 1 mL of water/ethanol (4:1 v/v) mixture and then followed by 30 minutes sonication to create a homogeneous ink. 10 µL of the as-prepared ink was then drop-cast onto the surface of the glassy carbon electrode and dried in air for 30 minutes, yielding a catalyst loading of around 0.14 mg cm^{-2}. A series of different concentrations of H_2SO_4 solution (0.5, 1.0 1.5 and 2.0 M) were prepared as electrolyte and around 60 mL of the as-prepared electrolyte was filled into the electrochemical cell. Before testing, the electrolyte was purged with N_2 for at least 30 minutes to remove the dissolved dioxygen.

Before the catalysts were tested for their catalytic performance, they were cycled between -0.5 and 1.0 V vs RHE at 100 mV s^{-1} for at least 10 cycles. Linear sweep voltammetry was then carried out to evaluate the HER activities by scanning from 0.25 V to -2.5 V vs RHE at a scan rate of 5 mV s^{-1}.

3.2.2.2 Direct Plasmonic Chronoamperometry on Core-shell NPs

A standard three-electrode photoelectrochemical cell as shown in Figure 3.3 was used for the direct plasmonic chronoamperometry measurements. The catalysts spray-casting onto the FTO glass was used as the working electrode, Ag/AgCl (saturated KCl) as the reference electrode, and a Pt electrode as the counter electrode. A solution of 0.5 M Na_2SO_4 (pH 6.5) was used as electrolyte without addition of any sacrificial reagents, which was purged continuously in

flowing N_2 to remove dissolved dioxygen prior to the start of reaction. The temperature of the solution for reaction was controlled by a flow of circling water connected to thermal-control devices to keep a constant reaction temperature of 298K. All the experiments were carried out at room temperature and inside a dark room to exclude the influence of background light.

The working electrode were prepared as followed: First, fluorine-doped tin oxide (FTO) coated glass was washed sequentially with acetone, ethanol and DI water in an ultrasonic bath for 30 min. Next, 10 mg of photocatalysts and 80 uL of 5 wt% Nafion solution were added into 2 mL ethanol and sonicated for 30 min to obtain a catalyst ink. Then, the as-prepared catalyst ink was spray-cast directly onto the pre-cleaned FTO glass surface ($1cm^2$) and dried in air for 30 minutes yielding a catalyst loading of around 0.2 ± 0.08 mg·cm^{-2} metal. A UV-cut Tungsten light (Glamox Professional 2000, $\lambda > 420$ nm) with a power intensity of 110 mW cm^{-2} was used as a light source for the direct plasmonic electrochemical measurement and set up at a fixed distance of 5 cm from the catalyst-coated FTO working electrode. Additionally, an Oriel® solar simulator (1 sun, AM 1.5G, 100 mW cm^{-2}) was used to irradiate the working electrode at different wavelength ranges to further analyse the photocurrent/current density enhancement. The amounts of hydrogen evolved were measured by gas chromatography (GC) equipped with thermoconductivity detectors (TCD) with N_2 as carrier gas. The current densities with/without light illuminations on working electrode were recorded with chronoamperometry at a potential range of -0.3 V, -0.5 V, -0.8 V and -1.2 V versus Ag/AgCl respectively with a time interval of 200 s for stabilization.

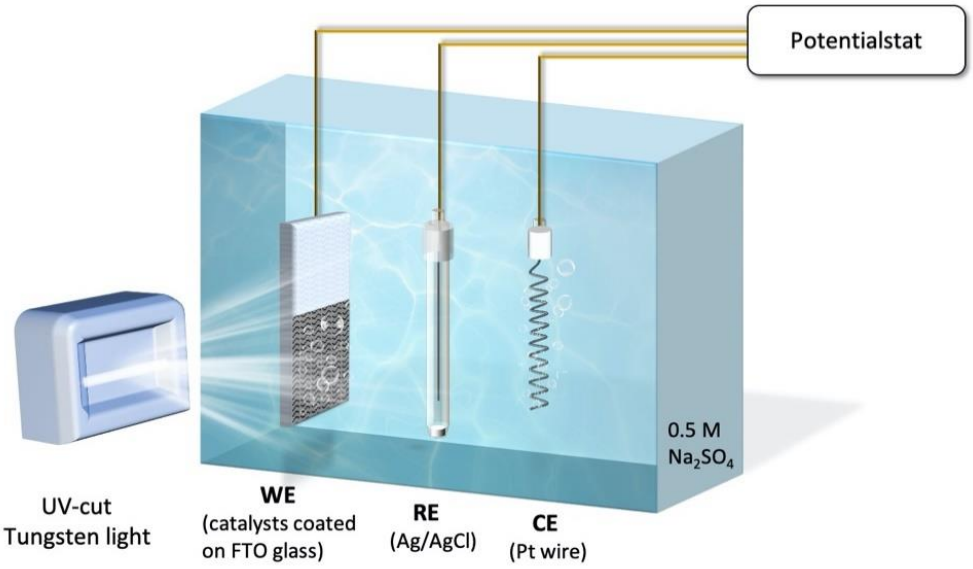


Figure 3.3 Schematic illustration of the three-electrode system with UV-cut Tungsten light as light source for the direct plasmonic chronoamperometry analysis.

3.2.2.3 Direct Plasmonic Linear Sweep Voltammetry on Core-shell NPs

For the direct plasmonic linear sweep voltammetry, the 0.5 M Na_2SO_4 (pH 6.5) was used as electrolyte without any addition of sacrificial reagents, which was purged continuously in flowing N_2 to remove O_2 prior to the start of reaction. In the three-electrode system, Ag/AgCl (Sat. KCl) was used as the reference electrode while the Pt electrode was used as the counter electrode. The AT-layer core-shell NPs was used as cathode catalyst on working electrode and the catalyst ink was prepared by the same method as mentioned in section 3.2.2.2. The as-prepared catalyst ink was then spray-casted on the pre-cleaned FTO glass until a metal loading of 1.2 mg/cm^2 was reached. A UV-cut Tungsten light ($\lambda > 420$ nm) was used as a light source in the experiment and set up at a fixed distance of 5 cm away from the working electrode. Before catalysts were tested for activity, it was cycled between -1.0 and 0.5 V vs Ag/AgCl at 100 mVs^{-1} for at least 10 cycles. Linear sweep voltammetry was carried out to determine the HER activity scanning from 0 V to -1.2 V vs Ag/AgCl at a scan rate of 1 mV s^{-1}.

3.2.3 Operando Electrochemical SXRD

In order to observe the phase changes during the electrochemical reactions, operando synchrotron XRD was employed for structural change analysis. In chapter 6, the operando synchrotron XRD was coupled with the electrochemical measurements to analyse the structural transformations of the polar MgO supports during the hydrogen evolution reactions.

3.2.3.1 Electrochemical Measurement

The electrochemical measurements were performed in a typical three-electrode system at room temperature with a programmable electrochemical workstation (AUTOLAB PGSTAT320N). The Ag/AgCl (saturated KCl) was used as a reference electrode while the graphite rod was acting as a counter electrode. The catalyst was prepared in a catalyst ink with a concentration of 5 mg/mL in ethanol. Briefly, 10 mg of the as-prepared catalyst and 100 uL of 5 wt% Nafion solution were added into 2 mL ethanol and sonicated for 30 minutes. Then, the as-prepared catalyst ink was spray-cast onto the carbon paper and dried in air for 30 minutes yielding a catalyst loading of around 0.5 ± 0.1 mg cm^{-2}. The catalyst-cast carbon paper was used as the working electrode. The electrolyte (0.5 M H_2SO_4) was purged with N_2 for 30 minutes to get rid of dissolved O_2 in the solution. Before catalysts were tested for their activity, they were cycled between 0.5 and -1.2 V vs RHE at 50 mV s^{-1} for at least 10 cycles to clean the surface impurities. Linear scan voltammetry was carried out to evaluate the HER activities by scanning from 0 V to -2.3 V vs RHE at a scan rate of 5 mV s^{-1}. The potential measured against Ag/AgCl (sat. KCl) reference electrode is converted to the potential versus RHE via Equation 3.5 using 0.5 M H_2SO_4 as electrolyte (pH≈0).

3.2.3.2 Operando Electrochemical SXRD Analysis

High-resolution synchrotron X-ray powder diffraction (SXRD) was performed at Beamline I11 in Diamond Light Source, UK. The energy of the incident X-ray flux was set at 25 keV. The tuned energy for each beamline emits the penetrating X-ray flux to achieve high contrast

(signal-to-noise ratio) and high angular resolution. The synchrotron data was collected by the pixel area detector in transmission geometry. The synchrotron X-ray wavelength was calibrated with the NIST SRMs 674b CeO_2 standard as λ = 0.49547(1) Å. The high resolution diffractograms were collected in the 2θ range of 0 to 41.54°. Each diffraction pattern was collected for 5 min. The electrochemical cell was placed in between the penetrated X-ray source and the detector as shown in Figure 3.4. The specially designed electrochemical cell was made of PTFE with sapphire windows in the middle to allow the X-ray beams going though and reaching the samples on the working electrode. After that, the synchrotron X-ray beams can scatter and diffract on the samples followed by data collection via the pixel area detector simultaneously during the electrochemical reaction process.

As shown in Figure 3.4, Ag/AgCl was used as a reference electrode (RE) and graphite rod was used as a counter electrode (CE), which were placed at the two sides of the sample cell. At the same time, the as-prepared Ru-MgO catalysts was spray-cast onto the carbon paper that acting as a working electrode (WE), and then it was placed at the centre of the sapphire window during the operando electrochemical measurements. The concentration of the electrolyte was diluted to 0.05 M in order to minimize the background originated from the solution scattering.

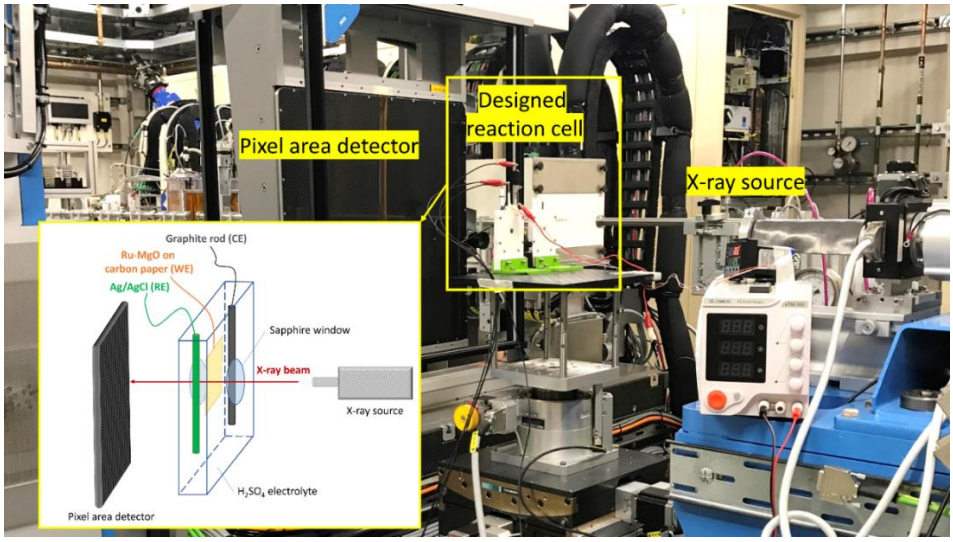


Figure 3.4 The operando electrochemical synchrotron XRD setup for the phase transformation analysis. The inset is the schematic illustration of the specially designed reaction cell used during the experiments.

3.3 Computational Modelling and Calculations

The computational modelling and calculations were employed in this thesis to support the experimental evidence. In this section, the calculation methods and details are outlined.

3.3.1 DFT Calculations on Hydrogen Adsorption Energies

DFT calculations were employed to analyse the hydrogen adsorption energies on different metal facets in order to gain further understandings of the hydrogen evolution reaction mechanisms in chapter 4.

All DFT calculations were performed using Vienna Ab-initio Simulation Package (VASP).[4] The exchange-correlation energy and potential were described by the generalized gradient approximation (GGA-PW91).[5,6] The kinetic energy cut-off for the wave function expanded in the plane-wave basis was set as 400 eV. To optimize the structures, the calculation was performed until the maximum force upon each relaxed atom was less than 0.05 eV/Å. The vacuum height was set as 15 Å to eliminate the interactions between neighbouring slabs.

The adsorption energy (E_{ads}) was calculated as follows:

$$E_{ads} = E_{total} - E_{substrate} - E_{gas-phase\ adsorbate} \qquad \text{(Equation 3.6)}$$

where E_{total} is the calculated total energy of the adsorption system; $E_{substrate}$ is the energy of the clean substrate; and $E_{gas\text{-}phase\ adsorbate}$ is the energy of the gas-phase molecule.

3.3.2 DDA Analysis of Au-Ag Core-shell Materials

Discrete dipole approximation (DDA) was employed to model the induced electric fields of different shell thicknesses of the Au-Ag core-shell materials at different wavelengths in chapter 5. The discrete dipole approximation (DDA) is an effective approach developed for calculating the far-field and near-field properties of metallic nanoparticles.

In this theoretical model, the nanostructure is described as a cubic array lattice of electric dipoles (N-point dipoles).[7-10] The E-field distributions for Au-Ag core-shell nanoparticles with a fixed diameter gold core of 26 nm were calculated using this approach in chapter 5. Based on the experimental evidence, the Ag thickness is defined as 1, 3 and 5 nm. In the case of 1 nm shell thickness, the E-fields for different Ag-Au compositions (increasing Ag content from 0-100%) were also calculated. In these calculations, a range of wavelengths from 450 to 550 nm were employed and the polarization directions for the spheres were along the y-axis. The medium refraction index was 1.0 (air) in all cases. The near-fields were described by a grid of 4.0×10^4 points on the yz plane, and the dielectric constants for Au, Ag, and Ag-Au NPs were obtained from the literature.[11,12]

3.3.3 DFT Modelling on MgO Supports

To understand how the polar MgO (111) surface can facilitate the structural transformation to hydroxide phases as well as the subsequent proton hopping mechanism on the surface, DFT modelling was carried out in chapter 6.

The spin-polarized DFT calculations were performed using the *Vienna ab initio Simulation Package* (*VASP*) software.[4,13,14] The generalized gradient approximation (GGA) based Perdew-Burke-Erzerhof (PBE) functional was used to describe the exchange and correlation effect of the valence electrons.[15] The kinetic energy cut-off of 450 eV was used for all the calculations. The project-augmented wave (PAW)[16,17] method was used to describe the core–valence electron interactions. Each atom was relaxed until the Hellman−Feynman force criterion were less than 0.01 eV/Å by using the conjugate gradient minimization algorithm. The bulk structure was optimized using a 10 × 10 × 10 Gamma centered grid of *k*-points mesh. The calculated lattice parameter of the bulk MgO is 4.249 Å, which is very close to the corresponding experimental value of 4.21 Å (calculated from XRD using Bragg's Law).

The pure MgO (111) surface was modeled using a twelve-layer slab repeated in a 5 × 5 surface unit cell; Symmetric slab model was considered for optimization by fixing the middle four layers to balance the dipole-moment. The *k*-point mesh was sampled using a 1 × 1 × 1 Gamma centered grid. To avoid interactions between slabs, all slabs were separated by a vacuum gap greater than 15 Å. After complete convergence testing studies, the geometric and electronic structures of the slabs were analyzed. The charge transfer was investigated by Bader charge analysis. A Gaussian smearing with σ = 0.01 eV was used for density of state analysis.

The H adsorption energy (E_{ads}) on the clean substrate was calculated by:

$$E_{ads} = E(_{H/sub}) - E(_{sub}) - ½E(_{H2}) \quad \text{(Equation 3.7)}$$

where $E(_{H/sub})$, $E(_{sub})$, and $E(_{H2})$ are the DFT energies of the adsorption complex, clean substrate, and gas-phase H_2 molecule, respectively.

The H adsorption energy on Ru/MgO was calculated by:

$$E_{ads} = \{E_{(nHRu/MgO)} - E_{(Ru/MgO)} - n/2E_{(H2\ )}\}/n \quad \text{(Equation 3.8)}$$

where $E_{(nHRu/MgO)}$, $E_{(Ru/MgO)}$, and $E(_{H2})$ are the DFT energies of the adsorption complex, main catalyst, and gas-phase H_2 molecule, respectively while n is number of H atoms.

The binding energy of Ru atom on MgO surfaces was calculated by:

$$E_b = E_{(Ru/MgO)} - E_{(Ru)} - E_{(MgO)} \text{ (w.r.t. Ru atom)} \quad \text{(Equation 3.9)}$$

where $E_{(Ru/MgO)}$, $E_{(MgO)}$, and $E_{(Ru)}$ are the DFT energies of the adsorption complex, clean substrate, and Ru atom in gas-phase, respectively.

3.4 References

1. Felfer, P. *et al.* New approaches to nanoparticle sample fabrication for atom probe tomography. *Ultramicroscopy* **159**, 413–419 (2015).

2. Larichev, Y. V, Moroz, B. L., Prosvirin, I. P., Likholobov, V. A. & Bukhtiyarov, V. I. XPS Study of Metal-Support Interaction in Ru / MgO Catalyst for Low-Temperature Ammonia Synthesis. *Chem. Sustain. Dev.* **11**, 155–160 (2003).

3. Niu, S., Li, S., Du, Y., Han, X. & Xu, P. How to Reliably Report the Overpotential of an Electrocatalyst. *ACS Energy Lett.* **5**, 1083–1087 (2020).

4. Kresse, G. & Furthmüller, J. Efficient iterative schemes for *ab initio* total-energy calculations using a plane-wave basis set. *Phys. Rev. B* **54**, 11169–11186 (1996).

5. Perdew, J. P. *et al.* Atoms, molecules, solids, and surfaces: Applications of the generalized gradient approximation for exchange and correlation. *Phys. Rev. B* **46**, 6671–6687 (1992).

6. White, J. A. & Bird, D. M. Implementation of Gradient-corrected Exchange-correlation Potentials in Car-Parrinello Total-energy Calculations. *Phys. Rev. B* **50**, 4954–4957 (1994).

7. Collinge, M. J. & Draine, B. T. Discrete-dipole approximation with polarizabilities that account for both finite wavelength and target geometry. *J. Opt. Soc. Am. A* **21**, 2023–2028 (2004).

8. Draine, B. T. & Goodman, J. Beyond Clausius-Mossotti - Wave propagation on a polarizable point lattice and the discrete dipole approximation. *Astrophys. Journal, Part 1 (ISSN 0004-637X)* **405**, 685–697 (1993).

9. Goodman, J. J., Draine, B. T. & Flatau, P. J. Application of fast-Fourier-transform techniques to the discrete-dipole approximation. *Opt. Lett.* **16**, 1198–1200 (1991).

10. Draine, B. T. & Flatau, P. J. Discrete-Dipole Approximation For Scattering Calculations. *J. Opt. Soc. Am. A* **11**, 1491–1499 (1994).

11. P. B. Johnson and R. W. Christy. Optical Constant of the Nobel Metals. *Phys. L Re View B* **6**, 4370–4379 (1972).

12. Rioux, D. *et al.* An analytic model for the dielectric function of Au, Ag, and their Alloys. *Adv. Opt. Mater.* **2**, 176–182 (2014).

13. Kresse, G. & Furthmüller, J. Efficiency of ab-initio total energy calculations for metals and semiconductors using a plane-wave basis set. *Comput. Mater. Sci.* **6**, 15–50 (1996).

14. Kresse, G. & Hafner, J. *Ab initio* molecular dynamics for liquid metals. *Phys. Rev. B* **47**, 558–561 (1993).

15. Perdew, J. P., Burke, K. & Ernzerhof, M. Generalized gradient approximation made simple. *Phys. Rev. Lett.* **77**, 3865–3868 (1996).

16. Blöchl, P. E. Projector augmented-wave method. *Phys. Rev. B* **50**, 17953–17979 (1994).

17. Kresse, G. & Joubert, D. From ultrasoft pseudopotentials to the projector augmented-wave method. *Phys. Rev. B - Condens. Matter Mater. Phys.* **59**, 1758–1775 (1999).

Chapter 4 Hydrogen Evolution in PEM Water Electrolyser

"Superior Performance of Ag Over Pt for Hydrogen Evolution Reaction in Water Electrolysis under more Negative Potentials"[1]

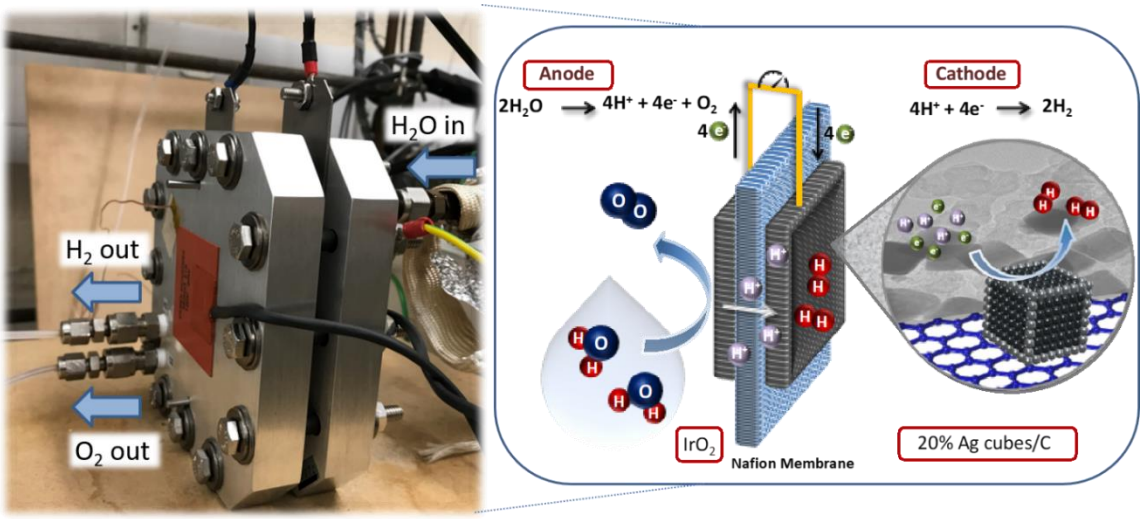


Table of Contents

Chapter 4 Hydrogen Evolution in PEM Water Electrolyser 106
4.1 Background 108
4.2 Materials 109
4.3 Synthesis 110
4.3.1 Synthesis of Silver Cubes 110
4.3.2 Synthesis of Silver Spheres 111
4.3.3 Synthesis of Silver Wires 111
4.3.4 Synthesis of Metal Supported on Vulcan Carbon 112
4.4 Characterizations 113
4.4.1 X-Ray Diffractions (XRD) 113
4.4.2 Thermogravimetric Analysis (TGA) 115
4.4.3 Transmission Electron Microscopy (TEM) 116
4.4.4 Energy-dispersive X-Ray Spectroscopy (EDX) 119
4.4.5 UV-Visible Spectroscopy (UV-Vis) 120
4.5 Hydrogen Evolution Reactions in Water Electrolysis 122
4.5.1 Experimental Methods 122
4.5.2 Catalytic Performance 123
4.5.3 Structure-Activity Correlations in PEM Electrolyser 125
4.5.4 The Surface Electrochemistry of Morphology-controlled Ag NPs 131
4.5.5 Post-reaction Analysis and Stability 136
4.6 Conclusions 139
4.7 References 139

4.1 Background

The advent of renewable energies such as wind power and photovoltaic means has drastically reduced the barrier for cost-effective production of green hydrogen from water electrolysis.[2,3] The ultra-purity of hydrogen means that the fuel-vector can be fed into the highly sensitive proton exchange membrane fuel cell without the installation of cumbersome purification set-ups.[4,5] Mechanistically speaking, water-splitting occurs at the anode where a H_2O molecule is oxidized to give protons that subsequently migrate through the proton exchange membrane (PEM) to recombine as hydrogen at the cathode (hydrogen evolution reaction). Wherein effective electrochemical catalysts are prerequisites that enable labile chemical conversion, platinum-based catalysts are always regarded as the industrial benchmark having excellent performance over its counterparts.

Nonetheless, despite the high efficiency of Pt-based catalysts for HER, it is not without its shortcomings. Firstly, the high cost of the noble metal has occupied a significant portion of capital expenditure of the PEM electrolyser; secondly, limited extraction of platinum mineral (when compared to non-noble alternatives) poses demographic constraints in wide deployment of electrolyser; last but not least, platinum on carbon catalysts are prone to aggregation and degradation under prolonged usage.[6] As a result, cheaper alternatives with no extraction limitation might offer a new avenue in the promotion of such technology. On the other hand, morphology-controlled silver-based nanoparticles have been widely applied in heterogenous catalysis due to their tuneable surface active sites at various exposed metal facets.[7,8] Thus, it is possible to replace platinum with non-noble metal variants as long as the surface sites can be precisely tuned.

Meanwhile, another challenge faced by industrial electrolysers is unavoidably the high operation cost of such unit. The use of high applied potential might potentially be a remedy that could give a higher hydrogen production with lower energy losses due to non-faradic

processes.[9,10] This is complimented by the low internal resistance that results in a high faradic efficiency of nearly 100%. Above all, it is recently demonstrated that a high current density of 3-6 A cm^{-2} can be maintained for over 1000 hours in the long-term durability test of a reactor cell.[11,12]

In this chapter, we are going to employ a series of silver nanoparticles with different morphologies, namely cubes, wires, and spheres, in an attempt to replace platinum for electrocatalytic HER in a PEM electrolyser under a range of applied potential. Particularly, we investigate the application of such catalysts at the cathode at different current densities from 0 to 3.5 A cm^{-2} over negative applied potentials and critically compare them with the benchmark platinum-based catalysts.

4.2 Materials

Reagents used in the material synthesis and the catalyst testing in this chapter were triruthenium dodecacarbonyl ($Ru_3(CO)_{12}$, ≥ 99%, Sigma Aldrich), gold(III) chloride trihydrate (≥99.9%, Sigma Aldrich), palladium(III) nitrate (solution 12%-16%, Alfa Aesar), vulcan carbon (XC72R, Cabot), sodium borohydride (≥99%, Fluka), 20% iridium on carbon (FuelCell Store), ethylene glycol (EG, anhydrous, ≥ 99.8%, Sigma Aldrich), polyvinylpyrrolidone (PVP, average Mw~55,000,Sigma Aldrich), sodium hydrosulfide hydrate (NaSH, Sigma Aldrich), silver trifluoroacetate (CF_3COOAg, ≥99.99%, Sigma Aldrich), glycerol(≥99.5%, Sigma Aldrich), silver nitrate ($AgNO_3$, ≥99.9999%, Sigma Aldrich), tetraethylammonium chloride (≥98%, Sigma Aldrich), platinum on graphitized carbon (20wt.% loading, Sigma Aldrich), 2-propanol (≥99.5%, Sigma Aldrich), tetrahydrofuran (THF, ≥99.9%, Sigma Aldrich) hydrochloric acid S.G.1.18 (~37%, Fisher Chemical), Nafion perfluorinated resin solution (5wt.% in mixture of lower aliphatic alcohols and water, Sigma Aldrich), Nafion N-211 membrane (25.4 um thick, FuelCell Store), Sigracet gas diffusion layer (type GDL 29BC, SGL Group).

4.3 Synthesis

At the outset of this study, six candidates (Ru, Pd, Ir, Au, Ag and Pt) were chosen as the cathode catalyst for HER catalytic activity comparison. The synthesis involved the preparation of 20 wt% Ru/C, Pd/C, Au/C and 20 wt% morphology-controlled silver nanoparticles (cubes, spheres and wires)/C. The 20 wt% Ru/C, Pd/C, Au/C were synthesized via wet impregnation followed by calcination reduction. The 20 wt% of morphology-controlled silver nanoparticles were synthesized via the polyol process, followed by wet impregnation. The commercially available 20 wt% Pt/C and Ir/C were supplied from the FuelCell Store.

4.3.1 Synthesis of Silver Cubes

The Ag cubes were synthesized with the polyol process following the methods of Xia et al.[13,14]

5 mL ethylene glycol (EG) was added into a 25 mL round bottom flask and heated under magnetic stirring at 150 ℃. After its temperature reached 150 ℃, 0.06 mL NaSH (3 mM in EG) was quickly injected into the heated solution. Two minutes later, 0.5 mL HCl solution (3 mM in EG) was injected into the reaction solution, followed by the addition of 1.25 mL poly(vinylpyrrolidone) (PVP, average Mw~55,000, Sigma Aldrich; 20 mg/mL in EG). 0.4 mL CF_3COOAg (282 mM in EG) was then added into the resulting mixture after another two minutes. During the whole process, the reaction temperature was kept at 150 ℃ and the flask was capped with a glass stopper except when adding the reagents. After 40 minutes, the reaction solution was quenched by placing the flask in an ice-water bath. The silver cubes were collected by centrifugation at 3000 rpm for 20 min with acetone to remove the unreacted precursors and EG followed by washing with deionized (DI) water four times to remove excess PVP. The as-prepared silver cubes samples were preserved in DI water.

4.3.2 Synthesis of Silver Spheres

The silver spheres synthesis procedure was similar to that of the silver cubes mentioned in section 4.3.1 above. However, the capping agents (NaSH and HCl solutions) were not required in synthesis of silver nanospheres.[13,14]

5 mL EG was added into a 25 mL round bottom flask and heated under magnetic stirring at 150 ℃. 1.25 mL poly(vinylpyrrolidone) (20 mg/mL in EG) was then injected into the reaction solution. After two minutes, 0.4 mL CF_3COOAg (282 mM in EG) was added into the resulting mixture. During the whole process, the reaction temperature was kept at 150 ℃. After 40 minutes, the reaction solution was quenched by placing the flask in an ice-water bath. The silver spheres were collected by centrifugation at 3000 rpm for 20 min with acetone to remove the unreacted precursors and EG followed by washing with deionized (DI) water four times to remove excess PVP. The as-prepared silver spheres samples were preserved in DI water.

4.3.3 Synthesis of Silver Wires

100 mL glycerol (≥99.5%, Sigma Aldrich) was added into a 250 mL round bottom flask and heated under magnetic stirring in an oil bath pre-set to 150 ℃. 1.7g PVP and 25 mg tetraethylammonium chloride (TEAC) were added into the reaction solution. After all the PVP and TEAC were dissolved in the reaction solution, 0.578 g $AgNO_3$ was added into the solution and the reaction temperature was maintained at 150 ℃. After 40 minutes, the reaction solution was quenched by placing the flask in an ice-water bath. The resulting solution was added to DI water and acetone mixture (1:4) to remove the unreacted precursors and then collected by centrifugation (3000 rpm, 20 min). After that, the solution was washed with DI water to remove excess PVP. Finally, silver wires samples were preserved in DI water.[15]

4.3.4 Synthesis of Metal Supported on Vulcan Carbon

4.3.4.1 20 wt% Ru/C

26.35 mg Triruthenium dodecacarbonyl ($Ru_3(CO)_{12}$) was dispersed in tetrahydrofuran (THF) for 2 hours under sonication. The mixture was then transferred to 50 mg Vulcan Carbon (XC-72R) and allowed to sonicate at ambient temperature for 2 hours followed by rotary evaporation to remove the solvent. The obtained powder was dried in a 95 ^oC oven for 12 hours under vacuum. After that the powder was transferred to a temperature-programmed furnace and heated to 300 ^oC for 3 hours under Ar to remove the CO ligand from the Ru precursor.

4.3.4.2 20 wt% Au/C

Citrate stabilized Au NPs were synthesized by the Turkevich method.[16,17] 25 mg sodium citrate was added to 100 mL deionized water where the mixture was immersed in oil bath at a temperature of 100 °C. Once the solution starts to boil, 2 mL of Gold(III) chloride trihydrate (25 mM in DI water) was added to the reaction mixture and kept at 100 °C. The solution was boiled for 15 min and then cooled to room temperature. 200 mL of the as-prepared Au NPs solution (~0.1g/L) was transferred to 100 mg vulcan carbon under magnetic stirring for wet impregnation for 4 h followed by drying at 80^oC overnight.

4.3.4.3 20 wt% Pd/C

42.2 mg Palladium(II) acetate ($Pd(OAc)_2$) and 100 mg vulcan carbon were ground for 30 minutes by a mortar and pestle to form a homogeneous solid. After that the resultant powder was transferred to a temperature-programmed furnace and heated to 250^oC for 2 hours under Ar then cooled to room temperature.

4.3.4.4 20 wt% Morphology-controlled Ag NPs/C

19.2 mL of the morphology-controlled Ag NPs solution (~0.52g/L) was transferred to 50 mg Vulcan carbon with 5 mL of 2-propanol in a 100 mL round bottom flask. The resultant mixture

was then sonicated at ambient temperature for 1 hour followed by magnetic stirring at 70^{o}C overnight to get rid of the solvent.

4.4 Characterizations

The structure of 20 wt% metal supported on vulcan carbon catalysts were confirmed by XRD whereas the metal loadings were analysed by TGA in this section. TEM, EDX, SEM and UV-visible measurements were carried out to confirm the morphology and particle distribution of the three as-prepared silver NPs.

4.4.1 X-Ray Diffractions (XRD)

X-ray diffraction patterns of 20 wt% Au/C, Ru/C, Ir/C, Pd/C, Pt/C and Ag/C were obtained and displayed in Figure 4.1 and Figure 4.2. The XRD patterns in Figure 4.1 confirm the identity of the metal species loaded on the vulcan carbon with reference to the ICDD® database. The broad reflection peak observed in all samples at around 26.5^{o} can be identified as the (002) plane of graphite support. As Au, Ag, Pd, Pt and Ir are all adapting a face-centred cubic (FCC) structure with similar lattice constants (4.078, 4.085, 3.891, 3.924 and 3.839 Å), their (111), (200) and (220) peaks occur at similar positions according to the Bragg's Law and d-spacing equation (chapter 2, section 2.2). By contrast, Ru is adapting a hexagonal close packed structure with lattice constant of 2.706 Å, 2.706 Å and 4.282 Å diffracting (100), (002), (101), (102) and (110) peaks using the d-spacing equation for hexagonal structure in equation 2.3.

The peak broadening of the Ru/C, Ir/C, Pd/C and Pt/C samples in Figure 4.1 are caused by the small particle sizes of the metal NPs. When the crystallite size is decreased, the interlayer spacing distribution is widened due to increased influence of edges and surfaces, resulting in a wide range of Bragg's diffraction angle that causes peak broadening.

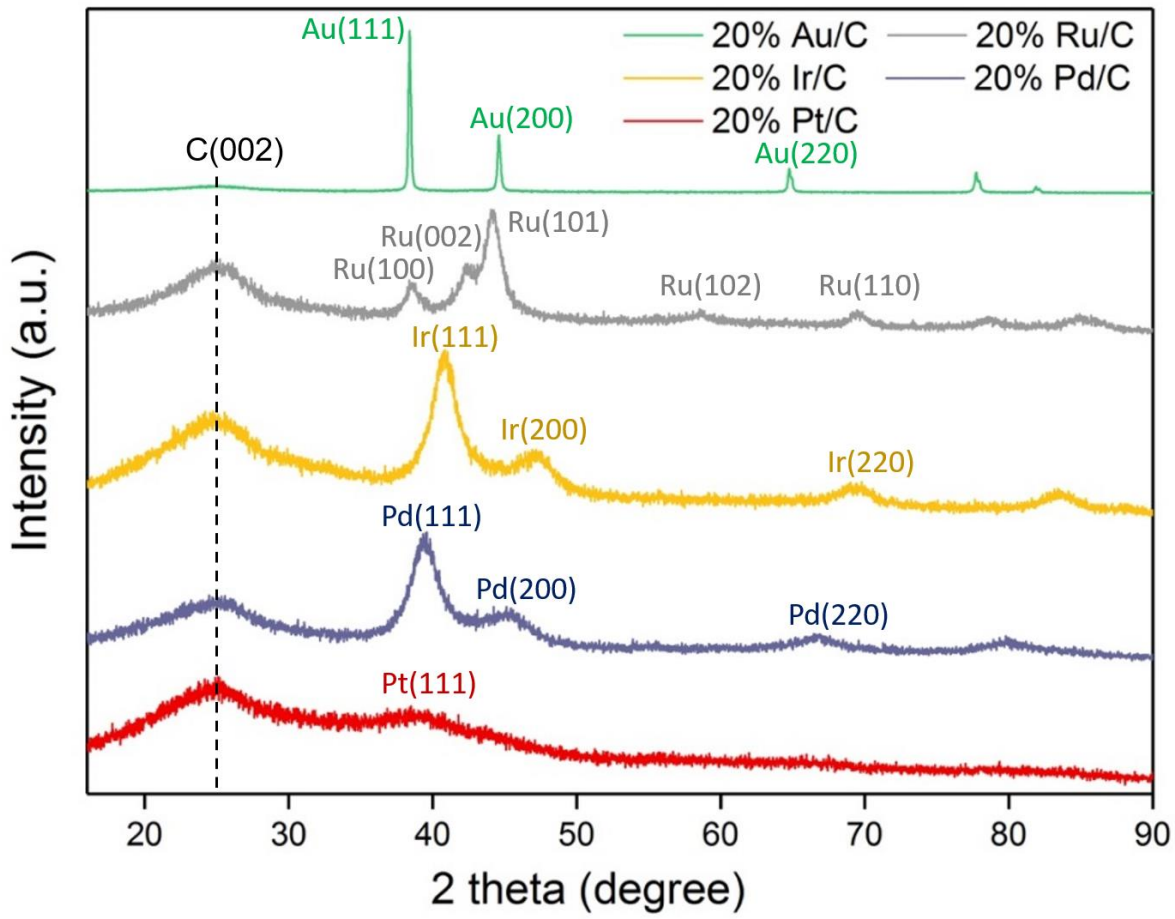


Figure 4.1 XRD profile of nanoparticle samples of 20 wt% Au/C, Ru/C, Ir/C, Pd/C and Pt/C. The intensity of 20 wt% Ru/C, Ir/C, Pd/C and Pt/C is multiplied by a factor of 10 for easy comparison.

In Figure 4.2, it shows the three morphology-controlled Ag NPs (wires, spheres and cubes) diffractograms. Analysis of Ag nanoparticles on flat substrate confirms the as-prepared Ag spheres, wires and cubes, are highly crystalline silver. As it can be observed in the diffractograms of Ag cubes, a significant change in the relative intensity of (111) and (200) peaks corresponds to a change in morphology. The intense (200) peak (higher ratio of (200) peak to (111) peak) indicates the Ag cubes are abundant in {100} facets, and thus their {100} planes tend to be preferentially oriented parallel to the surface of the flat supporting substrate.[14,18]

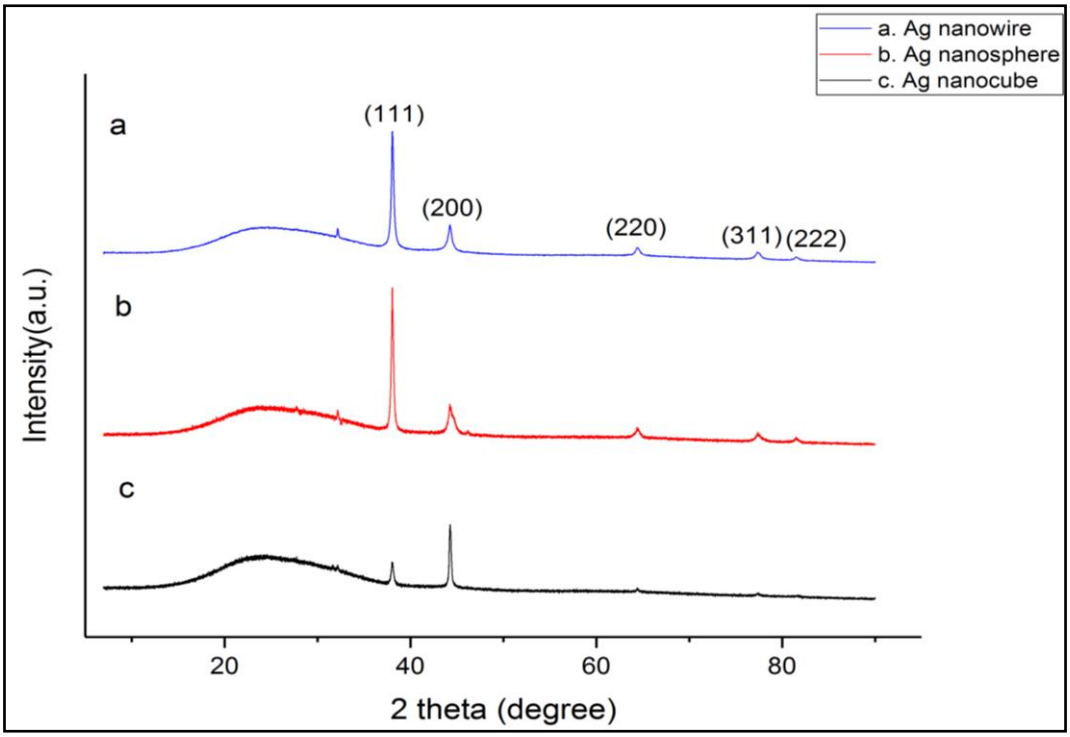


Figure 4.2 XRD profiles of the as-prepared Ag wires, spheres and cubes.

4.4.2 Thermogravimetric Analysis (TGA)

Thermal Gravimetric Analysis (TGA) was used in this chapter to estimate the metal loading of the samples supported on vulcan carbon through the controlled combustion of carbonaceous support. The samples were heated in air at a rate of 10 ^{o}C/min from 40 ^{o}C to 900 ^{o}C. The metal loading information obtained by TGA is summarized in the Table 4.1 below.

Table 4.1 Metal loading (Pt, Ru, Pd, Ir, Au and Ag) percentage of the metal supported on Vulcan carbon samples obtained from TGA estimation.

Sample	Pt/C	Ru/C	Pd/C	Ir/C	Au/C	Ag cubes/C	Ag wire/C	Ag spheres/C
Metal wt%	20.4	22.5	20.4	22.4	19.0	20.1	20.1	22.2

From the TGA estimations, it shows that the metal loading of each sample is approximately 20 wt% (±2%). The error is derived from the standard deviations across 3 batch of samples.

4.4.3 Transmission Electron Microscopy (TEM)

Transmission electron microscopy (TEM) was performed to investigate the morphology of the Ag nanoparticle catalysts. Figure 4.3 to Figure 4.5 show the TEM micrographs, corresponding schematic illustrations and size distributions of the as-prepared Ag cubes, spheres and wires.

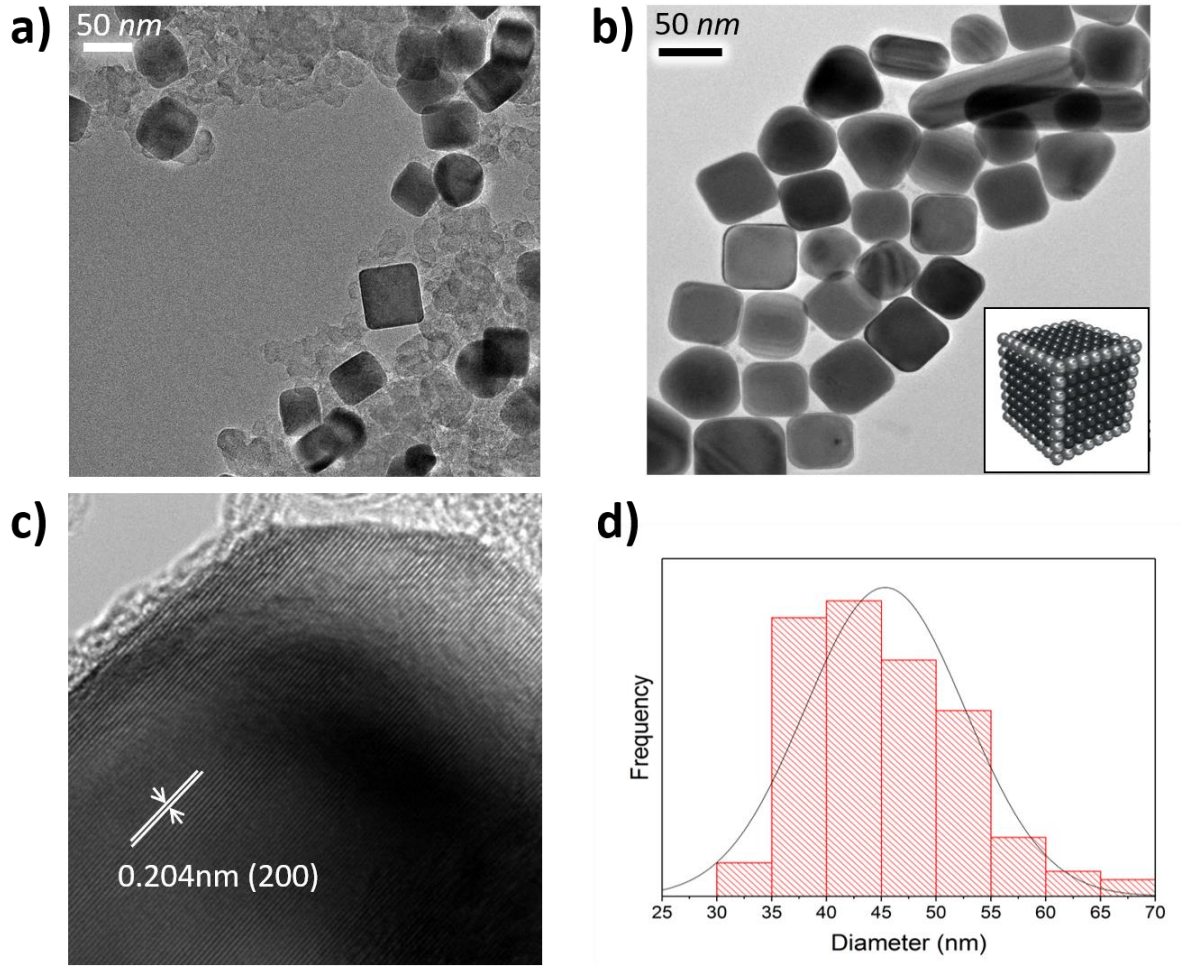


Figure 4.3 a) TEM image of 20 wt% Ag cubes supported on vulcan carbon; **b)** TEM image of Ag cubes with schematic illustrations inserted. In the insert, light grey: {111} facets, black: {100} facets; **c)** corresponding HRTEM image of b) showing the single crystal Ag cubes indexing a lattice spacing of 0.204 nm; **d)** TEM corresponding size distribution of the Ag cubes.

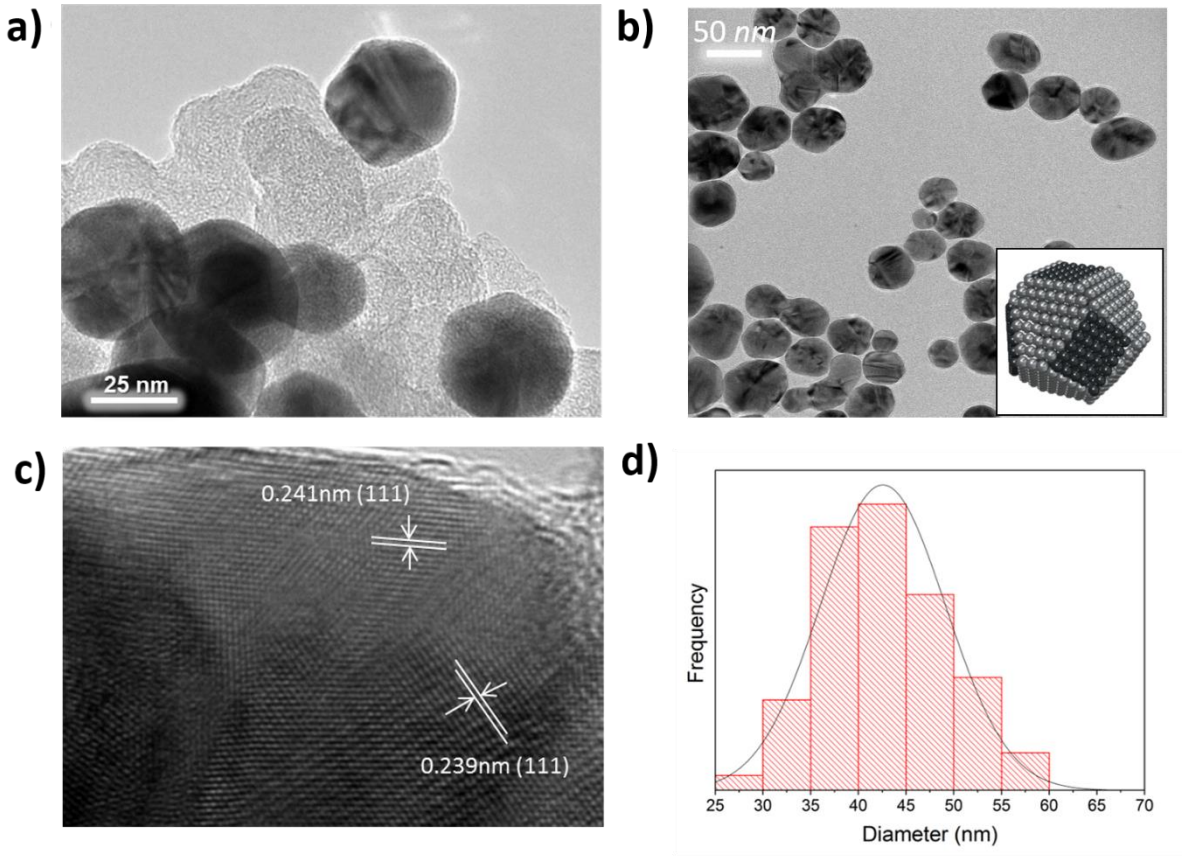


Figure 4.4 a) TEM image of 20 wt% Ag spheres supported on vulcan carbon; **b)** TEM image of Ag spheres with schematic illustrations inserted. In the insert, light grey: {111} facets, black: {100}facets; **c)** corresponding HRTEM image of a) on polycrystalline Ag spheres; **d)** TEM corresponding size distribution of the Ag spheres.

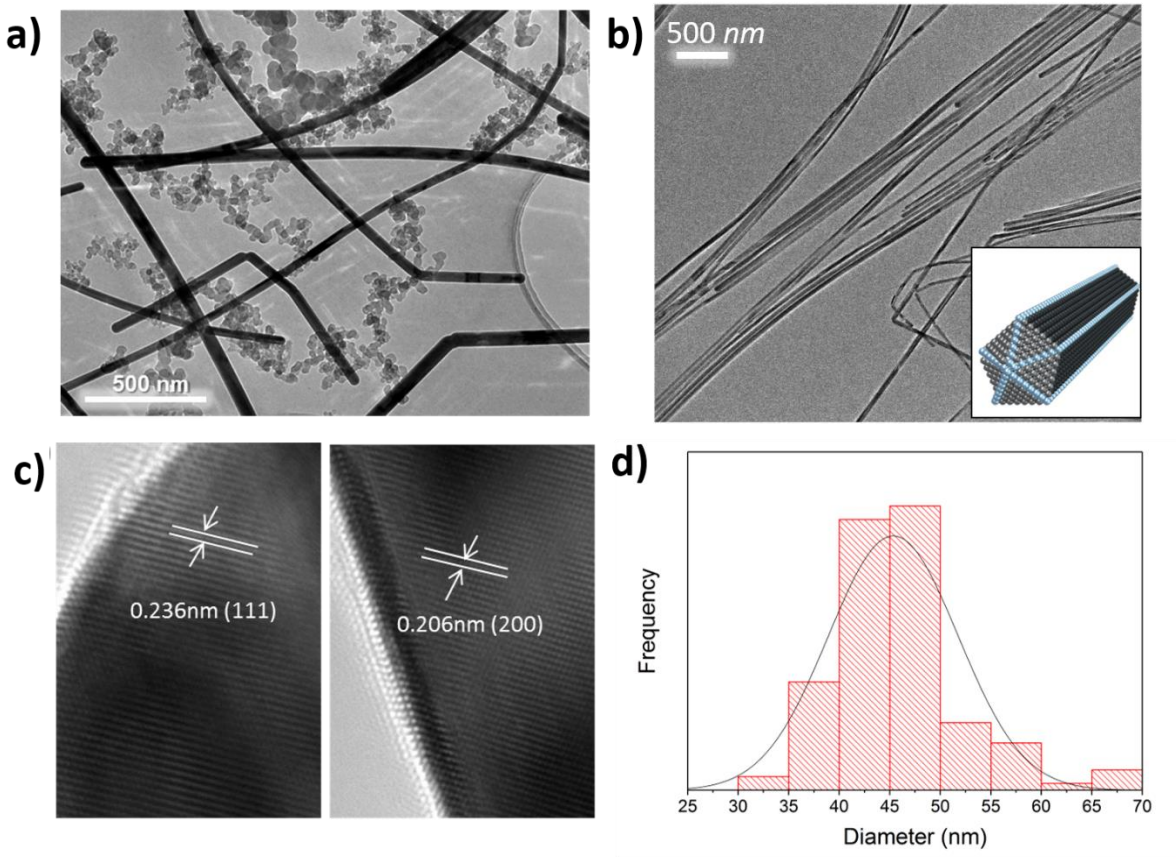


Figure 4.5 a) TEM image of 20 wt% Ag wires supported on vulcan carbon; **b)** TEM image of Ag wires with schematic illustrations inserted. In the insert, light grey: {111} facets, black: {100} facets, blue: {111} twin planes; **c)** corresponding HRTEM image of a) on bicyrstalline Ag nanowires, which is taken from different edges, showing the single crystallinity of each side; **d)** TEM corresponding size distribution of the Ag wires.

As suggested by the size distribution histograms in Figure 4.3, 4.4 and 4.5, the average edge length of the Ag cubes is shown to be 45 ± 3 nm whereas the average diameter of the Ag wires is 45 ± 2 nm. As for the polycrystalline Ag spheres, the average size is 43 ± 2 nm.

In Figure 4.3, the corresponding high-resolution (HR) TEM image (Figure 4.3b) of Ag cube micrograph (Figure 4.3a) shows the d-spacing value is 2.0 Å on Ag cubes, which can be assigned to the d-spacing of {200} facets for the face-centred-cubic (FCC) Ag.[19] The <200> axes indicates that the Ag cubes' surfaces are bounded by {100} facets.[18] In contrast, the

conventional polycrystalline Ag spheres are terminated with higher index planes and more thermodynamically favourable Ag {111} facets (Figure 4.4 c).[19]

As the schematic illustration shown above, the Ag cubes are dominated by the {100} facets and Ag wires with both {100} and {111} facets and the Ag nanospheres is majority terminated with the high index facets. Particularly for Ag wires, they are composed of five single-crystalline domains separated by {111} twin planes and each nanowire has five equivalent flat side surfaces, giving a pentagonal cross section. To shed light on the formation of Ag wires, it has been proposed that they grew from decahedral seed at the early stage of the reaction.[20] The actual morphology of the seed is obtained by elongating the classic decahedron in the <110> directions and replacing the edges at the twin boundaries with re-entrant surfaces composed of {111} facets, which is similar in shape to a Mark's decahedron. This modification lowers the energy of the decahedron and produces {100} planes on its sides.[20] The Ag wires are then formed with {100} side facets and {111} facets end. With the morphology-controlled Ag NPs, it allows us to study the HER on different exposed Ag surfaces.

4.4.4 Energy-dispersive X-Ray Spectroscopy (EDX)

Energy-dispersive X-ray spectroscopy (EDX) analysis was performed to investigate the distributions of the Ag NPs on the vulcan carbon support. In Figure 4.6, it indicates the morphological Ag NPs, namely spheres, cubes and wires, are loaded onto the carbon support homogeneously.

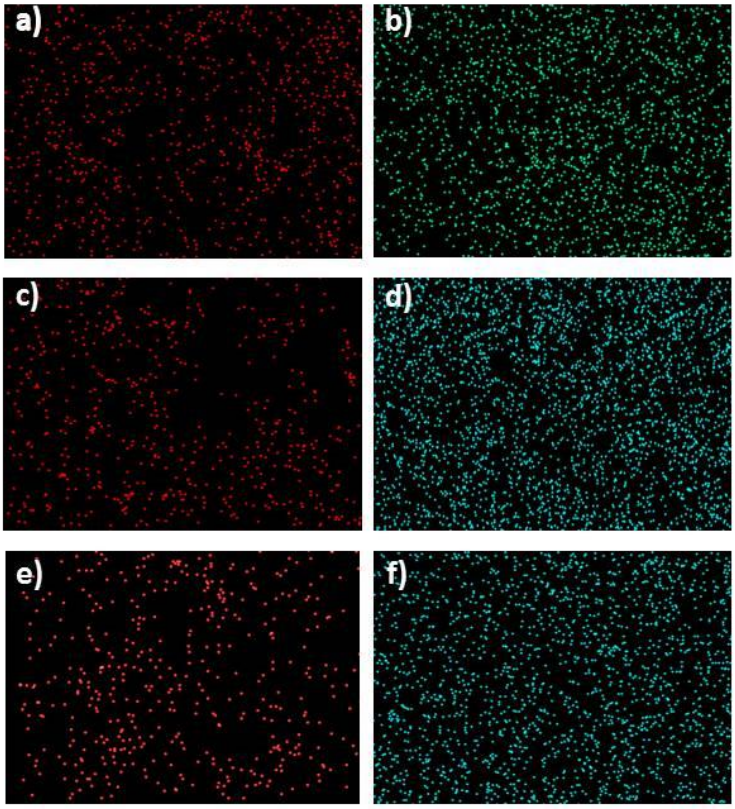


Figure 4.6 EDX of **a)** and **b)** 20 wt% Ag cubes on carbon; **c)** and **d)** 20 wt% Ag wires on carbon; **e)** and **f)** 20 wt% Ag spheres on carbon. Red spots: Ag, Green spots: Carbon.

4.4.5 UV-Visible Spectroscopy (UV-Vis)

Figure 4.7 shows the respective UV-visible absorption spectra of Ag cubes, Ag spheres, and Ag wires when suspended in DI water. For each of the morphologies, the main peak can be ascribed to the surface plasmon resonance (SPR) caused by the conduction electrons. As the electromagnetic wave reaches the nanoparticle, a dipole is formed where conduction electrons are migrated towards one side of the particle sphere and leave behind a positively charged region on the other end of the particle. A dipole in the opposite direction will then be induced following the change of sign in the electric field as a result of the Coulombic attraction force. Hence, the conduction electrons are driven to oscillate at the same frequency as the incoming light, giving rise to a strong dipole resonance.[21]

In Figure 4.7 a and b, it can be observed that the peak for Ag cubes (~430 nm) is red shifted when compared to sphere (~410 nm) even though Ag cubes have similar size as Ag spheres. This difference can be attributed to the greater degree of charge separation presence in particles with sharp corners.[22,23] The large charge separation reduces the Coulombic restoring force such that the time needed for each oscillation increases and the frequency lowers (versus a spherical particle).[21] Apart from the red-shifted resonance, a number of additional peaks (~350 nm and ~390 nm) can be observed in the spectra for Ag cubes. It can be attributed to the decreased symmetry of the cubic structure, where the number of peaks observed correlates to the number of ways in which the electron density can be polarized.[21,24] Furthermore, as shown in Figure 4.7 c, the sample exhibits two SPR peaks (~380 nm and ~350 nm) in which both of them are considered as the optical signatures of relatively long silver nanowires.[25]

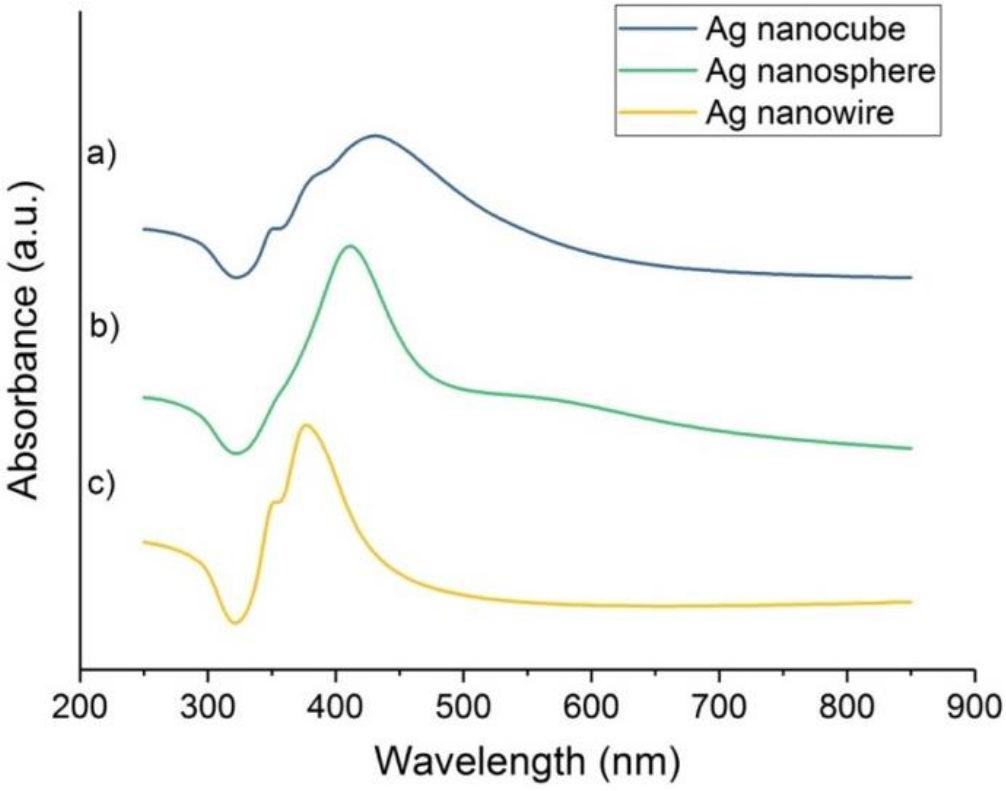


Figure 4.7 UV-Visible absorption spectra of a) Ag cubes; b) Ag spheres and ;c) Ag wires.

4.5 Hydrogen Evolution Reactions in Water Electrolysis

4.5.1 Experimental Methods

For details on the experimental methods, see chapter 3 section 3.2.1.

In summary, a PEM water electrolyser and a standard three-electrode cell were used to carry out the catalytic performance in this chapter. In the PEM electrolyser, the six different 20 wt% metals (Ru, Pd, Ir, Au, Ag and Pt) loaded onto the carbon each were used as the cathode catalyst while IrO_2 was used as the anode catalyst for all the measurements. The 20 wt% metal/C was loaded on the cathode side at 0.4 ± 0.05 mg cm^{-2} of the pure metal and IrO_2 catalysts was loaded on the anode side at 2.5 ± 0.2 mg cm^{-2} over a 1.5 x 1.5 cm^2 active area. The membrane-electrode assemblies (MEA) were then placed in the PEM electrolyser for testing. The electrolyser performance was evaluated at 80 ^oC and under ambient pressure for all measurements. The current density is obtained from dividing the current by the geometric area of electrode (2.25 cm^2) in the electrolyser as described in Equation 3.3. Deionized water was fed into the anode side at a flow rate of 4 mL/min. At each applied potential, the system was allowed to be stabilized for 30 min before recording the current density. Testing of 20 wt% metal/C from separate batches of electrodes were repeated at least three times and showed similar results with error bars presented in the figures.

In the three-electrode system, different concentrations of H_2SO_4 solutions were used as the electrolyte. Before testing, the electrolyte was sparged with N_2 for at least 30 min to remove dissolved oxygen. The working electrode was prepared by drop-casting the homogenous ink of the catalyst of interest onto the glassy carbon rotating electrode, yielding a catalyst loading of around 0.14 mg cm^{-2}. Before catalysts were tested for their activity, they were cycled between -0.5 and 1.0 V vs RHE at 100 mVs^{-1} for at least 10 cycles. Linear scan voltammetry was carried out to determine the HER activity scanning from 0.25 V to -2.5 V vs RHE at a scan rate of 5 mV s^{-1}. The current density is obtained from dividing the current by the geometric

area of the glassy carbon electrode (0.071 cm^2). The potential measured against Ag/AgCl (sat. KCl) reference electrode is converted to the potential versus RHE via Nernst equation (Equation 3.5) using 0.5 M H_2SO_4 as electrolyte ($pH \approx 0$).

4.5.2 Catalytic Performance

The electrochemical HER performance of 20 wt% metal/C acting as cathode catalysts in water electrolysis was first explored with the PEM electrolyser. In Figure 4.8, it shows the HER polarization curves of the six different metals (Ag, Pt, Au, Pd, Ir and Ru) at a range of applied potentials (-1.0 V to -2.5 V). The rate of hydrogen produced can be derived through the measurement of current density as described in chapter 3, section 3.2.1.3.

As observed in Figure 4.8, at more positive applied potentials (-1.0 ~ -2.0 V), the current density of 20 wt% Pt/C, the commercial catalyst for PEM water electrolysis, is indeed the benchmark and larger than all other metal catalysts including the Ag NPs. Surprisingly, when more negative potential (-2.5 V) is applied, the current density of the Ag catalyst increases dramatically to around 3.5 A cm^{-2}, giving the highest H_2 productivity. Particularly, the HER performance of Ag nanoparticles is 20% higher than that of the commercial 20 wt% Pt/C reference at -2.5 V.

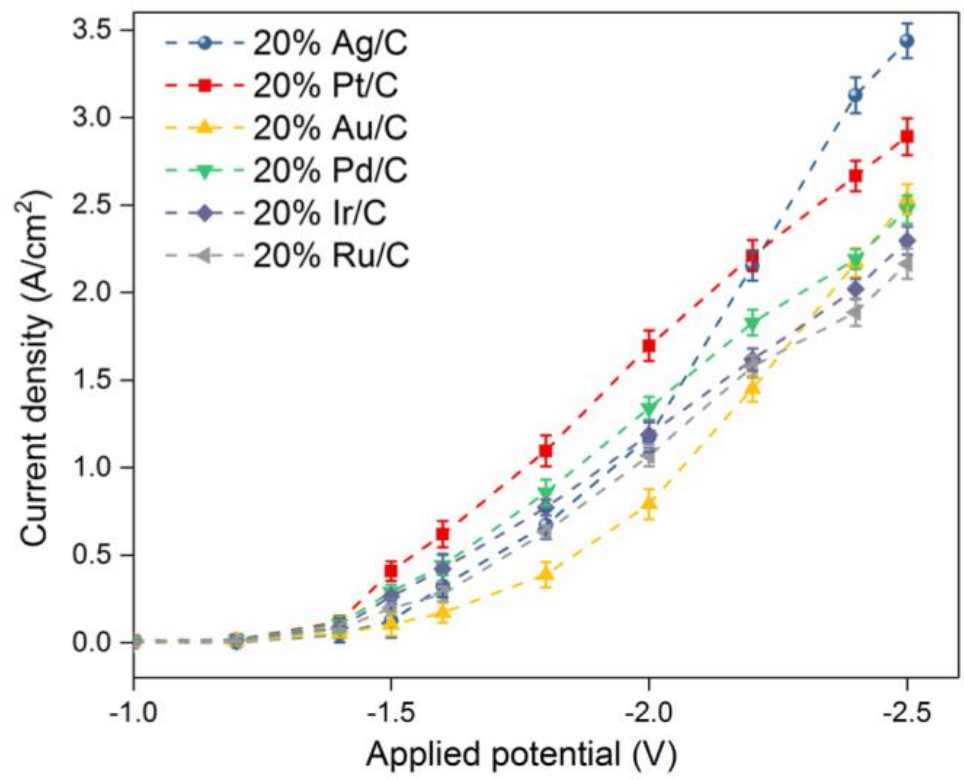


Figure 4.8 Current-Voltage polarization curves of electrolyser with different catalysts at T= 80 ^{o}C under PEM conditions. Error bars represent the error in using separate electrodes.

In order to probe the rationale behind the tremendous improvement in HER activity, silver nanoparticles with different surface properties were synthesised and tested. The three as-prepared morphology-controlled silver nanoparticles were used as cathode catalysts for HER under the same conditions in PEM electrolyser. Among the three silver NPs, the 20 wt% Ag cubes/C and Ag wires/C give better catalytic performance on HER than that of the commercial 20 wt% Pt/C at the applied potential of -2.5 V. However, at more positive applied potentials (-2.0 V), the order is reversed and resulting in the current density trend of Pt > Ag cube >Ag wire > Ag sphere (Figure 4.9).

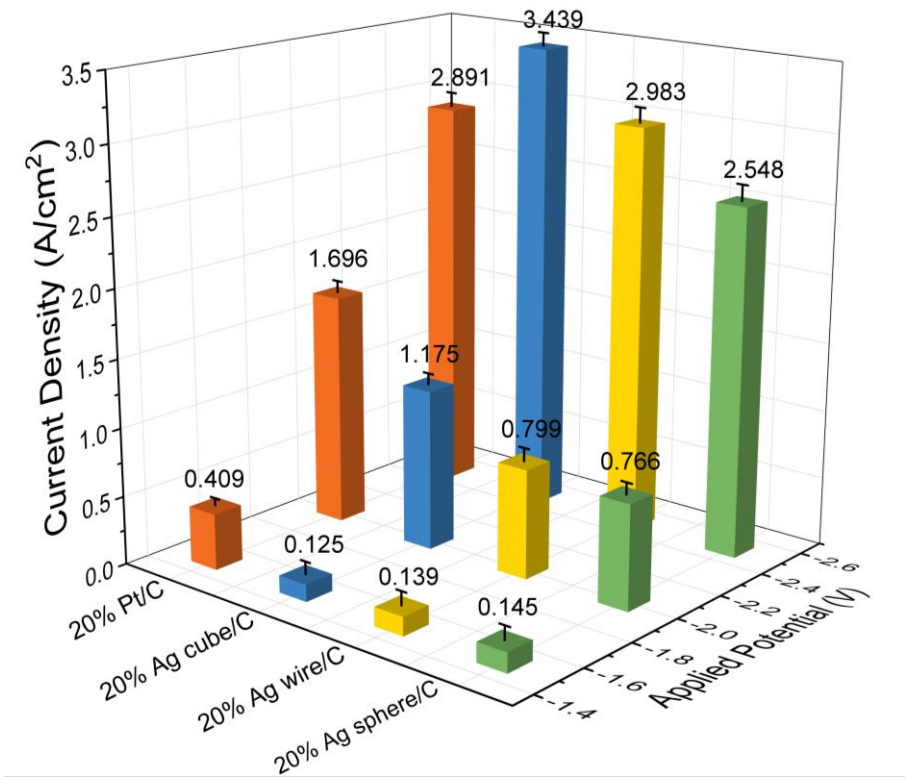


Figure 4.9 Comparison of three morphology-controlled Ag catalysts with commercial Pt/C catalyst under PEM conditions. 20% Pt/C (orange line), 20% Ag cubes/C (blue line), 20% Ag wires/C (yellow line) and 20% Ag spheres/C (green line) are cathode catalysts. Error bars represent the error in using separate electrodes.

4.5.3 Structure-Activity Correlations in PEM Electrolyser

In order to rationalize the electrochemical HER performances of morphology-controlled Ag catalysts when compared to commercial Pt/C, the fundamental steps for dihydrogen formation from proton reduction should be considered.

As mentioned in section 1.2.2 of chapter 1, a typical HER reaction under acidic medium comprises two possible elementary reaction routes, namely Volmer-Heyrovsky and Volmer-Tafel (Figure 1.6). If the rate determining step (RDS) involves M-H bond formation, it is referred to as ‘Volmer’ limiting reaction. On the other hand, if the RDS involves M-H bond breaking on metal surface to form surface dihydrogen, it is described as ‘Tafel’ limiting (Figure 4.10a). Tafel slope can be employed as a good indicator for the rate determining step, which

hinges on the binding energy between the metal catalyst surface and hydrogen atoms with a typical 'volcano' response.[26,27] Pt is generally believed to give optimal M-H bond strength in the volcano in overpotentials with constant acidity and coverage hence giving the highest rate in a catalytic cycle. In fact, in the literature, various Tafel slopes dependent on reaction conditions have been reported. The 20 wt% Pt/C catalyst exhibits a Tafel slope of 30 mV/dec in 0.5 M H_2SO_4 in CV/LSV at lower overpotential range, 120 mV/dec under PEM conditions with a wider overpotential range and 125 mV/dec in 0.5 M NaOH solution.[28,29] Detailed microkinetic analysis shows that the electrocatalytic activity is strongly dependent on electrolyte pH and applied potentials and hence affected by surface species coverage.[29]

Obviously, at more positive applied potentials (-1.0V ~ -2.0V) under PEM conditions, protons (H^+) travelling through the PEM membrane are of limited availability and hence lower the external current density, rendering the Volmer reaction (M-H bond formation) rate limiting (Figure 4.10b). However, at more negative applied potential (-2.5 V) in local polarized acidic environment in PEM electrolysers, the metal catalyst surface is readily covered with adsorbed hydrogen at a significant quantity, which eventually leads to a change of the rate determining step to M-H bond breaking Tafel step (Figure 4.10c).

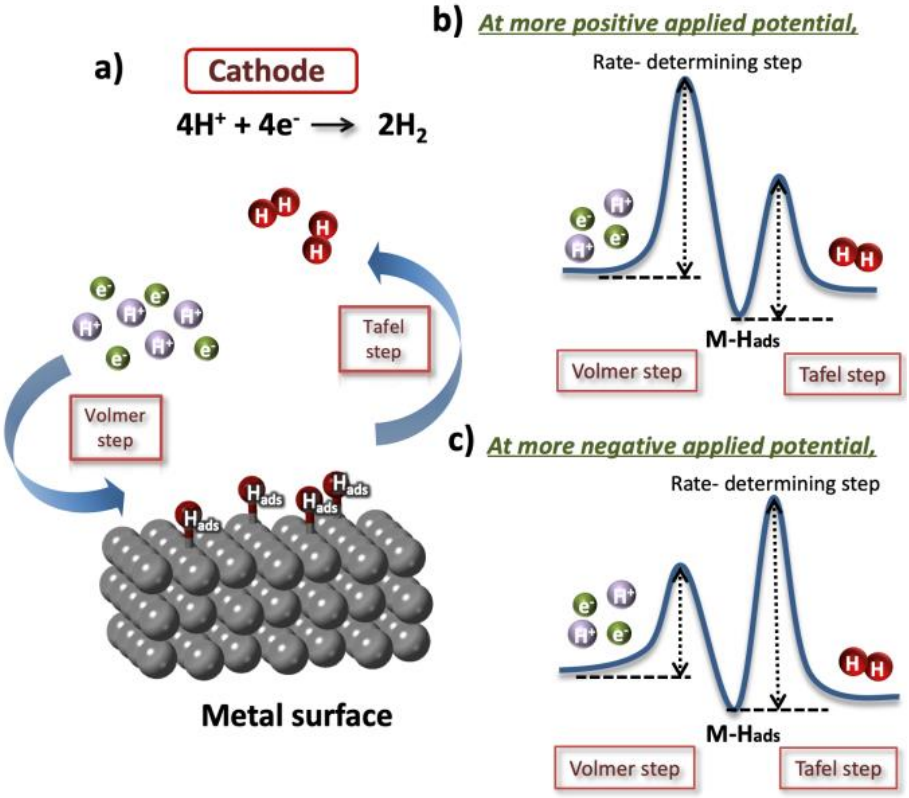


Figure 4.10 a) A schematic overview of hydrogen evolution reaction pathway at the cathode side; **b)** Higher Volmer barrier as the rate determing step at more positive applied potential; **c)** Higher Tafel barrier as the rate-determing step at more negative applied potential for HER on cathodic catalyst under acidic conditions.

To gain further understanding on the reaction mechanism, the adsorptions of hydrogen at platinum and silver surfaces were studied by Density Functional Theory (DFT) calculations. As we mentioned in chapter 3, section 3.3.1, the adsorption energy (E_{ads}) was calculated as follows:

$$E_{ads} = E_{total} - E_{substrate} - E_{gas-phase\ adsorbate} \qquad \text{(Equation 4.1)}$$

where E_{total} is the calculated total energy of the adsorption system; $E_{substrate}$ is the energy of the clean substrate; and $E_{gas\text{-}phase\ adsorbate}$ is the energy of the gas-phase molecule.

Different adsorption sites of H at Pt (100), Pt (111), Ag (100) and Ag (111) were taken into account and presented as shown in Figure 4.11. The adsorption energy values were calculated and summarized in Table 4.2.

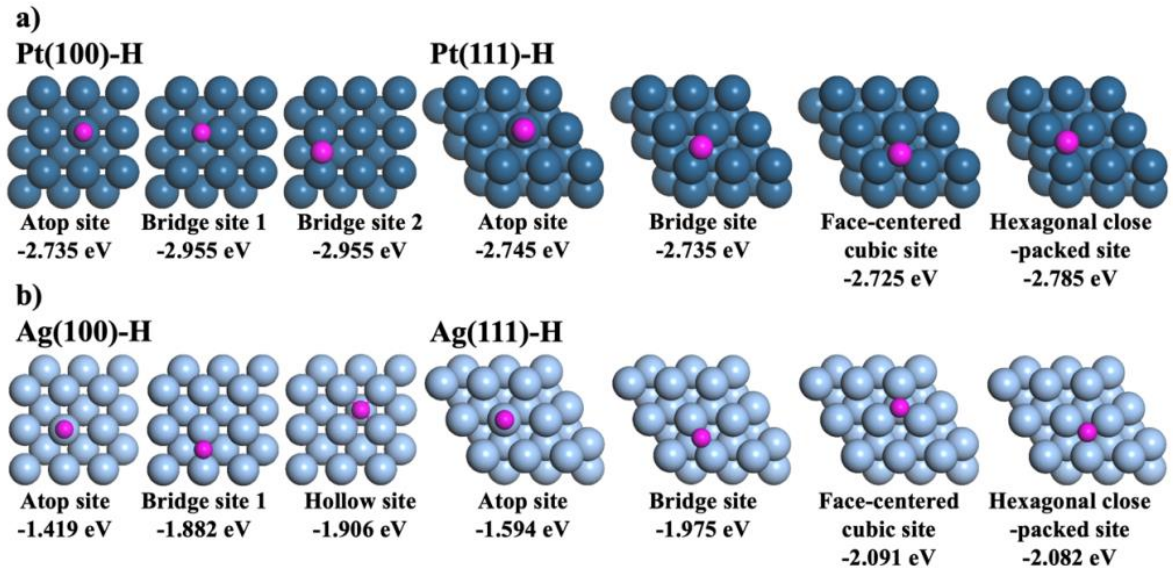


Figure 4.11 Different adsorption modes of H on the **a)** Pt (100), Pt (111) and **b)** Ag (100), Ag (111) surfaces and the corresponding calculated adsorption energies (E_{ads}, in eV). Dark green sphere: Pt, light blue sphere: Ag, and pink sphere: H.

Table 4.2 Calculated H adsorption energies at different sites of Pt (100), Pt (111), Ag (100) and Ag (111).*

	$\mathbf{E_{ads1}}$/eV	$\mathbf{E_{ads2}}$/eV	$\mathbf{E_{ads3}}$/eV	$\mathbf{E_{ads4}}$/eV
Pt (100)	-2.735	-2.955	-2.955	/
Pt (111)	-2.745	-2.735	-2.725	-2.785
Ag (100)	-1.419	-1.882	-1.906	/
Ag (111)	-1.594	-1.975	-2.091	-2.082

*For (100) facets, ads1 is atop site, ads2 is bridge site and ads3 is hollow site for Ag and bridge site for Pt; while for (111) facets, ads1 is atop site, ads2 is bridge site, ads3 is face-centered cubic site and ads 4 is hexagonal close-packed site.

According to Figure 4.11 and Table 4.2, the H adsorption energy of Pt is more negative than that of Ag (100) and (111) facets at the corresponding sites, which means the H is adsorbed more strongly on Pt metal surface compared with Ag surface. At more positive applied potentials, the proton flux through the membrane is of limited availability, and thus results in a low coverage of H atoms at Pt metal surface. The RDS of the HER reaction in this case is Volmer step such that the strongest Pt-H bond results in the highest HER catalytic activity.[28,29]

It is also well-known that the hydrogen adsorption energy depends on the facet of the active metal.[30] As shown in XRD (Figure 4.2) and TEM (Figure 4.3-3.5) analysis, the Ag cubes are mainly covered with (100) facets while short Ag wires are covered with (100) facet at the sides and (111) facet at the ends. The majority of polycrystalline Ag spheres is terminated with thermodynamically stable (111) facets as shown in Figure 4.4. In Figure 4.11b, the adsorption energy indicates that the H is adsorbed more strongly on close-packed Ag (111) when compared to the loose-packed Ag (100) in the same absorption sites. Notably, at more positive applied potentials (-1.5V), the rate determining step is the adsorption of proton onto the metal catalyst surface (Volmer step), suggesting that Ag spheres (with dominant (111) facet exposed) would give the highest hydrogen evolution rate among the Ag samples due to strong M-H bonds. Thus, the adsorption strength order agrees with the catalytic activity trends of Pt > Ag spheres > Ag wires > Ag cubes at -1.5 V (see Figure 4.9).

However, at more negative applied potential (-2.5 V) in PEM conditions, the RDS pathway is associated with the H recombination from M-H bond in Tafel step, the weaker M-H bond of Ag (100) cubes this time allows surface migration and facilitates H_2 formation. As a result, the trend in activity as Ag spheres < Pt ~ Ag wires < Ag cubes is established at an applied potential of -2.5 V (Figure 4.9). The order of the three morphology-controlled Ag NPs is totally reverse of that at more positive potentials, as shown from our experiments.

In order to get a general picture of the structure-activity correlations, the theoretical H adsorption energies of the other four metals (Au, Pd, Ir, Ru) used in the experiments (Figure 4.8) were calculated. However, metal dispersion and stability under potentials might possibly be dominating factors as well. According to the DFT calculations shown in Figure 4.12, we have obtained a trend of M-H bond strengths as Ag < Au < Pt < Pd ~ Ir < Ru (111), which is similar to that proposed by Ferrin et al.[30] By comparing with the catalytic performance in Figure 4.8, it is shown that the activity ranks as Ag > Pt > Au > Pd > Ir > Ru at a more negative potential of -2.5 V. In this case, the above trend is inversely proportional to the calculated M-H bond strength, suggesting the rate limiting step is the M-H breaking process where weaker M-H gives higher activity. Thus, it implies that intensive proton coverage on the metal surface could result in the Tafel step being rate limiting, that is, the weaker M-H bonds, the higher the activity.

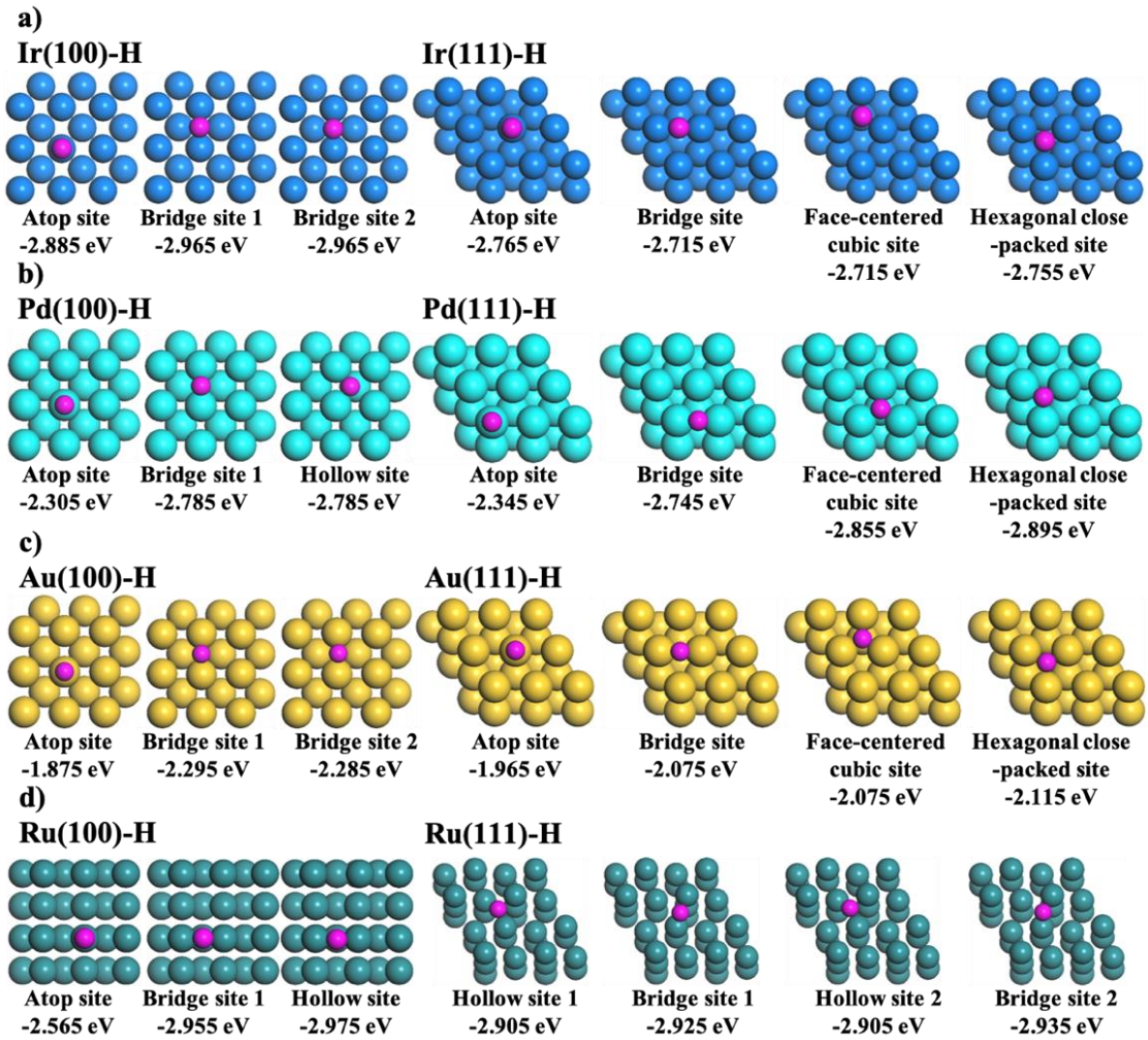


Figure 4.12 Different adsorption modes of H on the **a)** Ir (100), Ir (111); **b)** Pd (100), Pd (111); **c)** Au (100), Au (111) and **d)** Ru (100), Ru (111) surfaces and the corresponding calculated adsorption energies (E_{ads}, in eV). Blue sphere: Ir, light green sphere: Pd, yellow sphere: Au, dark green sphere: Ru and pink sphere: H.

4.5.4 The Surface Electrochemistry of Morphology-controlled Ag NPs

To get insight into the surface electrochemical redox process, linear sweep voltammetry (LSV) was measured with a three-electrode system for the HER polarization curves. The potential was raised from 0.25 V to -2.5 V/ RHE in N_2-purged 0.5 M H_2SO_4 as described in section 4.5.1 to monitor the activity of the three morphology-controlled Ag NPs and the commercial Pt/C catalysts.

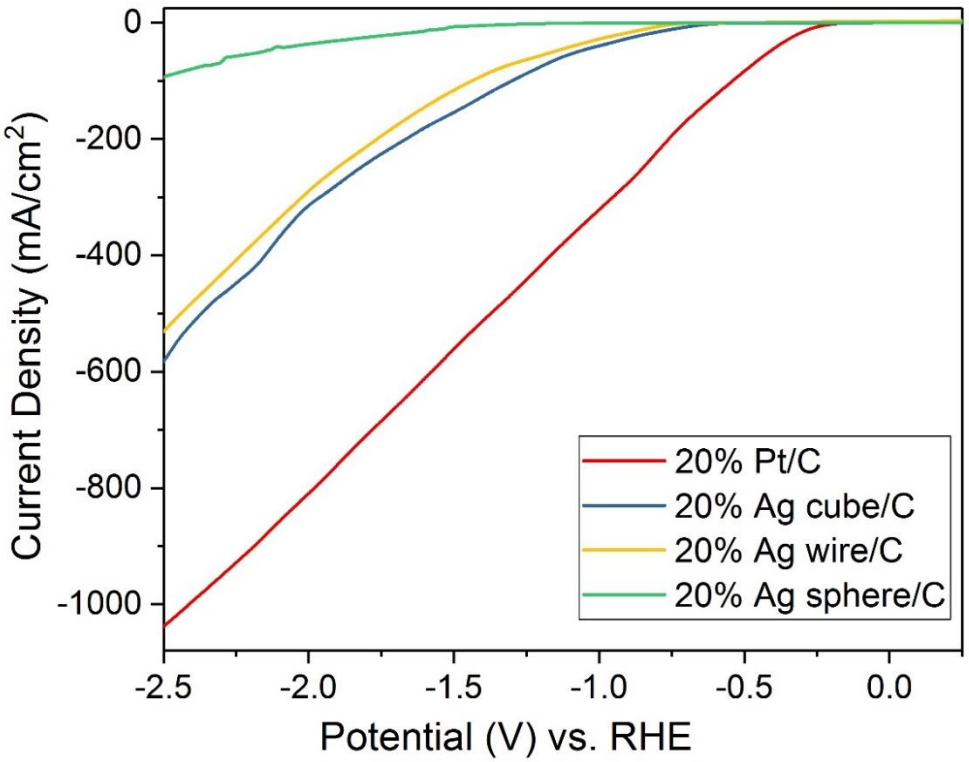


Figure 4.13 LSV of the 20 wt% Ag cubes/C, wires/C, spheres/C and 20 wt% Pt/C reference in N_2-purged 0.5 M H_2SO_4 solution. The LSV was measured from 0.25 V to -2.5 V at a scan rate of 5 mV s^{-1} with a glassy carbon rotating electrode at a rotation rate of 2000 rpm.

As seen from Figure 4.13, the onset potential for proton reduction observed for commercially available 20 wt% Pt/C is much more positive than that of the silver catalysts, which sheds light on the higher HER activity. At more positive potentials (> -1.5 V), higher rates of hydrogen evolution (in the form of current densities) are observed over the Pt/C than the three as-prepared Ag catalysts under low acidity condition (0.5 M H_2SO_4). At more negative potentials, the same trend is seen as well. This is somewhat contradictory to the activity rank measured at more negative potential using the PEM electrolyser as mentioned. The discrepancy can be ascribed to poor proton availability for the catalyst in 0.5 M H_2SO_4 versus the case of the fully acidified Nafion membrane (~0.1 S cm^{-1}) that possesses an unparalleled proton diffusion rate.[31] Therefore a more acidic electrolyte was used to mimic the PEM cathodic conditions in Figure 4.14 below.

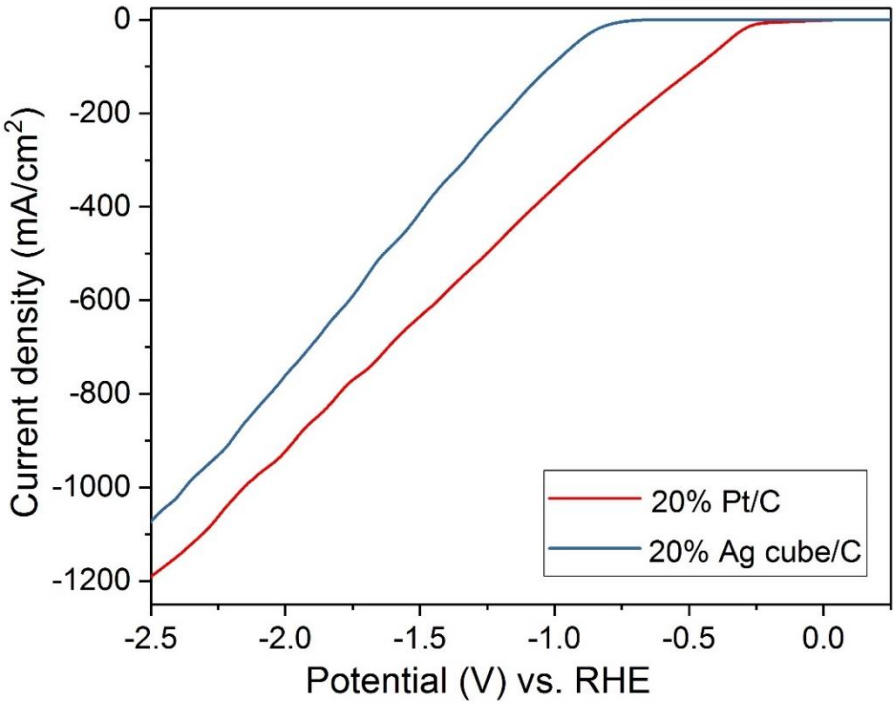


Figure 4.14 LSV of 20 wt% Ag cubes/C and 20 wt% Pt/C reference in N_2-purged 2.0 M H_2SO_4 solution. The LSV are measured from 0.25 V to -2.5 V at a scan rate of 5 mV s^{-1} with a glassy carbon rotating electrode at a rotation rate of 2000 rpm.

In order to mimic the PEM cathodic conditions, the electrolyte (H_2SO_4) acidity in the three-electrode system is increased from 0.5 M to 2.0 M, while holding the rest of the experimental conditions identical as the experiment in Figure 4.13. In Figure 4.14, it is interesting to find that the current densities between 20 wt% Ag cubes/C and 20 wt% Pt/C reference are becoming comparable at -2.5 V under 2.0 M H_2SO_4 when comparing with Figure 4.13. It can be attributed to higher proton availability for HER under 2.0 M H_2SO_4 on the morphology-controlled Ag catalysts. At more negative applied voltage (-2.5 V) with higher surface coverage of H, the weaker Ag-H surface bond becomes more favourable for H recombination to sustain higher HER activity (Tafel limiting step). As a result, an increase in proton flux can be achieved by increasing the electrolyte acidity in the three-electrode system, leading to an increase in the current density at a more negative applied potential.

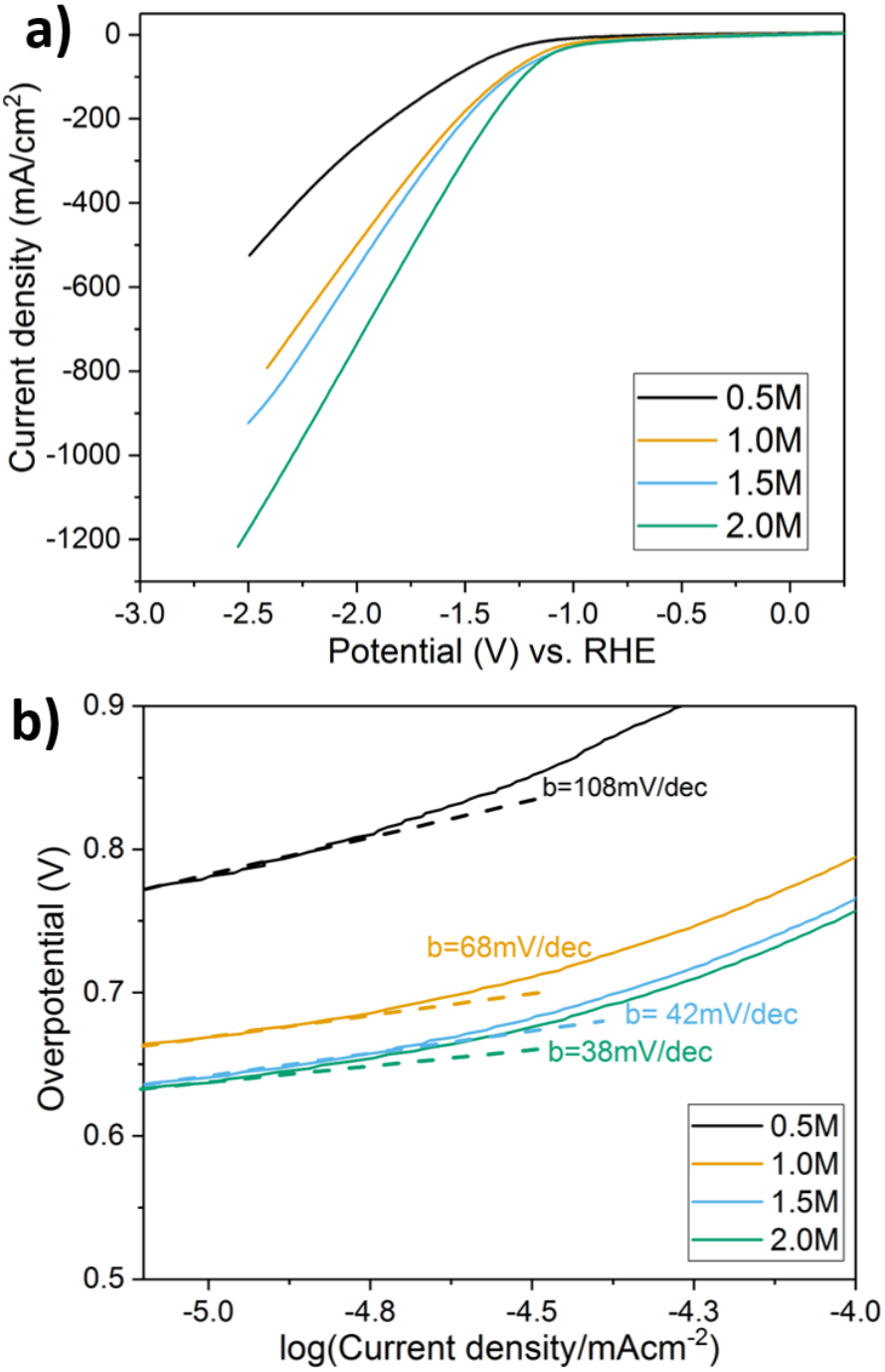


Figure 4.15 a) LSV of 20 wt% Ag cubes/C in N_2-purged 0.5 M H_2SO_4, 1.0 M H_2SO_4, 1.5 M H_2SO_4, 2.0 M H_2SO_4 solution; **b)** Corresponding Tafel plots recorded on glassy carbon electrodes with 20 wt% Ag cubes/C catalysts in N_2-purged 0.5 M H_2SO_4, 1.0 M H_2SO_4, 1.5 M H_2SO_4, 2.0 M H_2SO_4 solution. All the LSV are measured from 0.25 V to -2.5 V at a scan rate of 50 mV s^{-1} with a glassy carbon rotating electrode at a rotation rate of 2000 rpm.

To further study the correlation between proton availability and HER activity on the Ag catalysts, a series of different electrolyte concentrations (0.5 M, 1.0 M, 1.5 M and 2.0 M) was

used in the three-electrode systems. It can be observed in Figure 4.15a that the HER activity increases significantly as the electrolyte acidity increases, especially under 2.0 M H_2SO_4 condition. It illustrates that the higher proton availability in the system will greatly enhance the surface coverage of H on Ag catalyst, thus rendering H recombination more favourable on the metal surface and give higher HER rates.

Tafel analysis is also carried out to determine the Tafel slopes of the 20 wt% Ag cubes/C under different acidities of the electrolyte (Figure 4.15b). It is interesting to reveal that the Tafel slopes are becoming less steep as the electrolyte acidity increases. Under 0.5 M H_2SO_4, a Tafel slope of 108 mV/dec is obtained, suggesting the initial proton adsorption (the Volmer step) is the rate limiting step. However, under 2.0 M H_2SO_4, a slope of 38 mV/dec can be deduced indicating the RDS is a H recombination step (Tafel or Heyrovsky step) as previously mentioned in chapter 1 section 1.2.2. These observations agree with the analysis from Conway et.al. that the lower surface coverage of H at lower overpotential gives Volmer limited process whereas the higher H coverage at higher overpotential is changed to Tafel limited process.[32] Therefore, this result once again confirms that the proton availability and surface coverage must be one of the crucial factors for HER for morphology-controlled catalysts. In other words, the onset potential of the same cathode catalyst will be more positive with increasing electrolyte acidity.

Meanwhile for LSV, the reverse trend in current density: 20 wt% Ag cubes/C > 20 wt% Pt/C at higher overpotential may also be obtained if more acidic electrolytes with greater proton availability is applied. As a result, this polarization (negative potentials) study clearly illustrates the same trend of reversed activity when more negative potential is used and eliminates any potential artefacts introduced in anode and PEM components.

4.5.5 Post-reaction Analysis and Stability

After water electrolysis testing in the electrolyser, the three as-prepared 20 wt% silver NPs/C were collected and characterized by SEM and TEM to check the post-reaction morphology after high workload conditions.

As seen from Figure 4.16, the post-mortem catalysts were collected by scrapping the catalyst powder from the carbon paper that were then dispersed in isopropanol for TEM. The population of particles is low due to the great dilution by carbon particles from the carbon paper. Meanwhile, the TEM images of the as-prepared catalysts before reaction (Figure 4.3-4.5) show comparable sizes and morphologies to that of the post-reaction TEM analysis (Figure 4.16), suggesting a minimal amount of changes during the reaction.

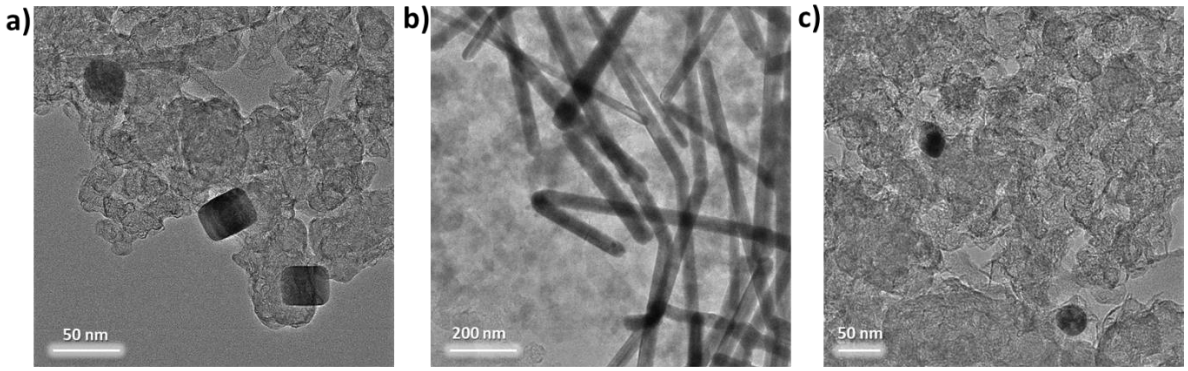


Figure 4.16 TEM of post reaction **a)** 20 wt% Ag cubes (45 ± 3nm) on carbon; **b)** 20 wt% Ag wires (45± 2 nm) on carbon and **c)** 20 wt% Ag spheres (43 ± 2 nm) on carbon.

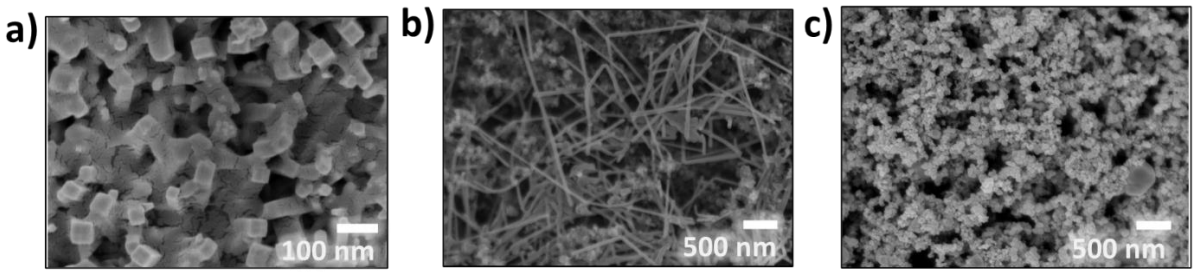


Figure 4.17 SEM images of the post-reaction **a)** 20 wt% Ag cubes/C; **b)** 20 wt% Ag wires/C and **c)** 20 wt% Ag spheres/C on carbon paper after HER testing at an applied potential of -2.5 V.

In Figure 4.17, post-mortem samples for SEM imaging were collected by removing the carbon paper from MEA after HER catalytic testing at an applied potential of -2.5 V. It also confirms that the nanoparticle shape and average particle size remained unchanged which agrees with the TEM analysis. The SEM images at wider views clearly showed consistent size and morphology of these Ag NPs despite the exposure to large negative potential for the HER reaction in PEM electrolyser.

The stability of the 20 wt% Ag cube/C as a cathode catalyst in a PEM electrolyser was also carried out in this chapter. The stability test is performed at 80 ^{o}C under ambient pressure at an applied potential of -2.5 V for 500 min.

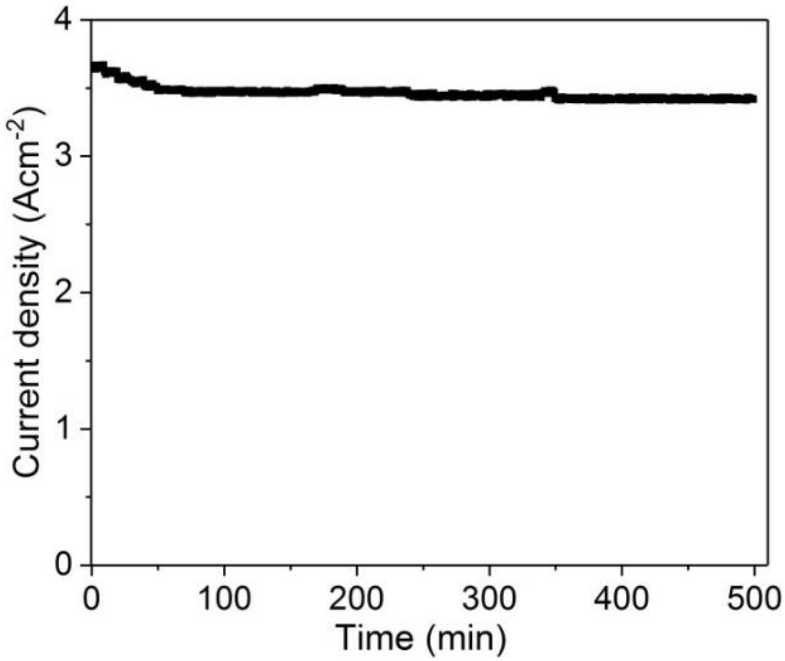


Figure 4.18 The stability test of 20 wt% Ag cube/C as cathode catalyst in PEM electrolyser under an applied potential of -2.5 V at 80 ^{o}C.

In Figure 4.18, it is interesting to reveal that the current density is stable at around 3.5 A cm^{-2} for a continuous 500 min, showing almost no deactivation in the PEM electrolyser water electrolysis. The results clearly demonstrate the economical Ag catalysts can be a potential replacement for the 'Holy-grail' Pt catalyst in PEM electrolyser under high workload

conditions with sustainable activity. Nevertheless, a longer stability test should be carried out for further investigation.

As mentioned in chapter 1, normalizing the total electrode activity by the mass of the precious metal is an essential performance parameter for catalytic activity comparison. As shown in Table 4.3, as both the Pt and Ag cube are both 20 wt%, the current density per mg of catalysts shows the same trend of 20 wt% Ag cube/C > 20 wt% Pt/C. Regarding the manufacture of the cathode catalyst, there is a significant advantage in using a metal of lower cost: Ag is £16.6 per oz versus Pt is £700.9 per oz. As a result, although the current density of Ag-catalyst is only higher than Pt by 16%, the cost of the former is only 2.4% of that of the latter.

Table 4.3 Comparison of catalytic activity in current density per mg of cathode catalyst used.

Sample name	Metal price (£ per oz)	Current density at 2.5 V (A cm^{-2})	Mole of metal per cm^2 of active area	Current density per mg of cathode catalyst (A cm^{-2} mg^{-1})
20 wt% Ag cube/C	16.6	3.44	3.71×10^{-6}	8.60
20 wt% Pt/C	700.9	2.89	2.05×10^{-6}	7.23

To summarise, Ag nanoparticles could be a practical replacement of the Pt catalyst for water electrolysis hydrogen evolution reaction when higher potential is used, particularly from the economical and catalytic performance perspective.

4.6 Conclusions

This chapter focuses on exploring the potential candidates to replace the commercially available and expensive 20 wt% Pt/C catalysts for HER in the PEM electrolyser. Activity measurements towards the hydrogen evolution reactions of the as-prepared 20 wt% metal/C materials are carried out in which Ag cubes are found to outperform the Pt catalysts at more negative applied potentials.

Furthermore, it has been demonstrated in this chapter that the subtle change from low to high H_2 production rate of the morphology-controlled Ag/C, particularly the Ag cubes, can be triggered by a change of rate determining step from Volmer limiting to Tafel limiting. The higher HER activities of the Ag cube catalysts can thus be attributed to the weaker Ag-H bond strengths (compared with that of the Pt-H bond) in the PEM electrolyser when practically more negative potential (-2.5 V) is used.

It is believed that this study could rectify the misconception that Pt is always at the 'optimal volcano' position among all mono-metals in HER, which has led to an inaccurate description of the surface electrocatalysis under real PEM conditions at high workload. This work may provide new insights into designing economical and highly efficient catalysts that can potentially replace the expensive noble metal counterparts in a working electrolyser.

4.7 References

1. Mo, J. *et al.* Superior Performance of Ag over Pt for Hydrogen Evolution Reaction in Water Electrolysis under High Overpotentials. *ACS Appl. Energy Mater.* **2**, 1221–1228 (2019).
2. Dincer, I. & Zamfirescu, C. *Sustainable Hydrogen Production*. *Sustainable Hydrogen Production* vol. 305 (Elsevier, 2016).
3. Dincer, I. Green methods for hydrogen production. *Int. J. Hydrogen Energy* **37**, 1954–1971 (2012).
4. Davis, S. J. *et al.* Net-zero emissions energy systems. *Science (80-.).* **360**, 9793 (2018).
5. Rau, G. H., Willauer, H. D. & Ren, Z. J. The global potential for converting renewable

electricity to negative-CO2-emissions hydrogen. *Nat. Clim. Chang.* **8**, 621–625 (2018).

6. Yu, X. & Ye, S. Recent advances in activity and durability enhancement of Pt/C catalytic cathode in PEMFC. Part II: Degradation mechanism and durability enhancement of carbon supported platinum catalyst. *J. Power Sources* **172**, 145–154 (2007).

7. Wen, C., Yin, A. & Dai, W. L. Recent advances in silver-based heterogeneous catalysts for green chemistry processes. *Appl. Catal. B Environ.* **160**–**161**, 730–741 (2014).

8. Tang, Q. *et al.* Flexible and macroporous network-structured catalysts composed of conducting polymers and Pt/Ag with high electrocatalytic activity for methanol oxidation. *J. Mater. Chem.* **21**, 13354–13364 (2011).

9. Ayers, K. E. *et al.* Research Advances towards Low Cost, High Efficiency PEM Electrolysis. *ECS Trans.* **33**, 3–15 (2010).

10. Carmo, M., Fritz, D. L., Mergel, J. & Stolten, D. A comprehensive review on PEM water electrolysis. *Int. J. Hydrogen Energy* **38**, 4901–4934 (2013).

11. Suermann, M., Schmidt, T. J. & Buchi, F. N. Investigation of Mass Transport Losses in Polymer Electrolyte Electrolysis Cells. *ECS Trans.* **69**, 1141–1148 (2015).

12. Lewinski, K. A., van der Vliet, D. & Luopa, S. M. NSTF Advances for PEM Electrolysis - the Effect of Alloying on Activity of NSTF Electrolyzer Catalysts and Performance of NSTF Based PEM Electrolyzers. *ECS Trans.* **69**, 893–917 (2015).

13. Zeng, J. *et al.* Controlling the shapes of silver nanocrystals with different capping agents. *J. Am. Chem. Soc.* **132**, 8552–8553 (2010).

14. Sang, H. I., Yun, T. L., Wiley, B. & Xia, Y. Large-scale synthesis of silver nanocubes: The role of HCl in promoting cube perfection and monodispersity. *Angew. Chemie - Int. Ed.* **44**, 2154–2157 (2005).

15. Sun, Y., Mayers, B., Herricks, T. & Xia, Y. Polyol synthesis of uniform silver nanowires: A plausible growth mechanism and the supporting evidence. *Nano Lett.* **3**, 955–960 (2003).

16. Turkevich, J., Stevenson, P. C. & Hillier, J. A study of the nucleation and growth processes in the synthesis of colloidal gold. *Discuss. Faraday Soc.* **11**, 55–75 (1951).

17. Samal, A. K. *et al.* Size tunable Au@Ag core-shell nanoparticles: Synthesis and surface-enhanced raman scattering properties. *Langmuir* **29**, 15076–15082 (2013).

18. Sun, Y. G. & Xia, Y. N. D. A.-D. 13. Shape-controlled synthesis of gold and silver nanoparticles. *Science (80-.).* **298**, 2176–2179 (2002).

19. Zeng, J. *et al.* Controlling the shapes of silver nanocrystals with different capping agents. *J. Am. Chem. Soc.* **132**, 8552–8553 (2010).

20. Wiley, B. *et al.* Shape-controlled synthesis of silver and gold nanostructures. *MRS Bull.* **30**, 356–361 (2005).

21. Cobley, C. M., Skrabalak, S. E., Campbell, D. J. & Xia, Y. Shape-controlled synthesis of silver nanoparticles for plasmonic and sensing applications. *Plasmonics* **4**, 171–179 (2009).

22. Xia, Y., Xiong, Y., Lim, B. & Skrabalak, S. E. Shape-Controlled Synthesis of Metal Nanocrystals : Simple Chemistry Meets Complex Physics ? *Angew. Chemie - Int. Ed.* **48**, 60–103 (2009).

23. Haes, A. J., Haynes, C. L., Mcfarland, A. D. & Schatz, G. C. Plasmonic Materials for Surface-Enhanced Sensing and Spectroscopy. *Mater. Res. Bull.* **30**, 368–375 (2005).

24. Fuchs, R. Theory of the optical properties of ionic crystal cubes. *Phys. Rev. B* **11**, 1732–1740 (1975).

25. Sun, Y., Yin, Y., Mayers, B. T., Herricks, T. & Xia, Y. Uniform silver nanowires synthesis by reducing AgNO3 with ethylene glycol in the presence of seeds and poly(vinyl pyrrolidone). *Chem. Mater.* **14**, 4736–4745 (2002).

26. Skúlason, E. & Tripkovic, V. Modeling the electrochemical hydrogen oxidation and evolution reactions on the basis of density functional theory calculations. *J. Phys. Chem. C* **114**, 18182–18197 (2010).

27. Nørskov, J. K., Bligaard, T., Rossmeisl, J. & Christensen, C. H. Towards the computational design of solid catalysts. *Nat. Chem.* **1**, 37–46 (2009).

28. Durst, J., Simon, C., Hasche, F. & Gasteiger, H. A. Hydrogen Oxidation and Evolution Reaction Kinetics on Carbon Supported Pt, Ir, Rh, and Pd Electrocatalysts in Acidic Media. *J. Electrochem. Soc.* **162**, F190–F203 (2014).

29. Shinagawa, T., Garcia-Esparza, A. T. & Takanabe, K. Insight on Tafel slopes from a microkinetic analysis of aqueous electrocatalysis for energy conversion. *Sci. Rep.* **5**, 1–21 (2015).

30. Ferrin, P., Kandoi, S., Nilekar, A. U. & Mavrikakis, M. Hydrogen adsorption, absorption and diffusion on and in transition metal surfaces: A DFT study. *Surf. Sci.* **606**, 679–689 (2012).

31. Liu, L., Chen, W. & Li, Y. An overview of the proton conductivity of nafion membranes through a statistical analysis. *J. Memb. Sci.* **504**, 1–9 (2016).

32. Conway, B. E. & Tilak, B. V. Interfacial processes involving electrocatalytic evolution and oxidation of H2 , and the role of chemisorbed H. *Electrochim. Acta* **47**, 3571–3594 (2002).

Chapter 5 Hydrogen Evolution in Direct Electrochemical-Plasmonic water electrolysis

"Atomic-Precision Tailoring of Au-Ag Core-shell Composite Nanoparticles for Direct Electrochemical-Plasmonic Hydrogen Evolution in Water Splitting"[1]

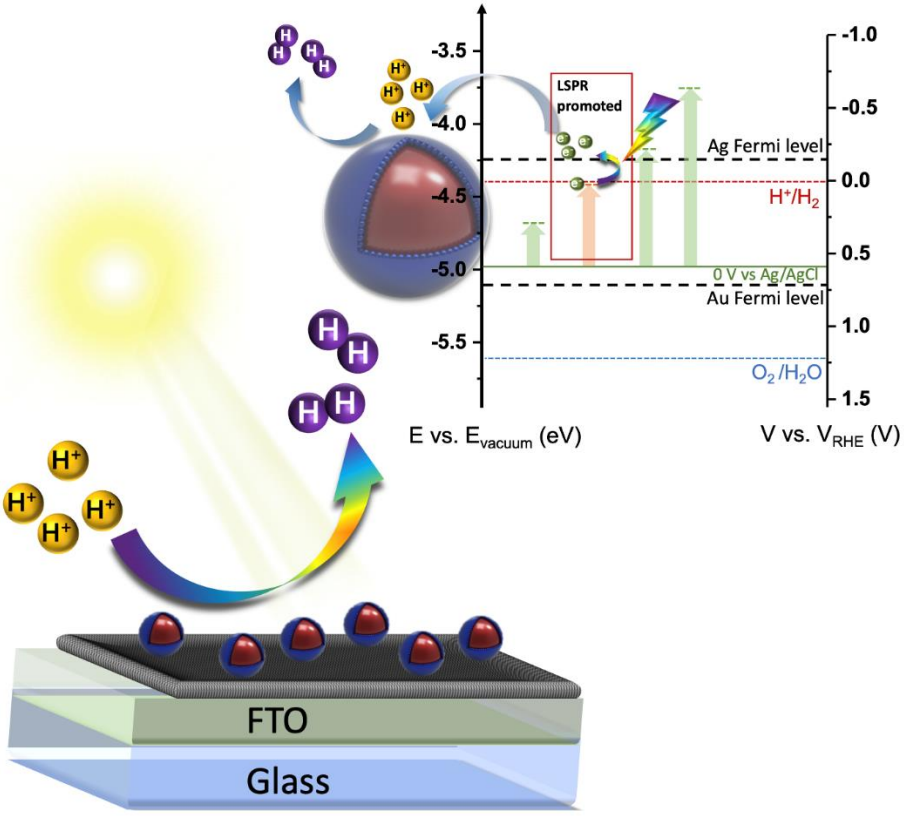


Table of Contents

Chapter 5 Hydrogen Evolution in Direct Electrochemical-Plasmonic water electrolysis 142
5.1 Background 144
5.2 Materials 145
5.3 Synthesis 145
5.3.1 Synthesis of Au Nanoparticles 146
5.3.2 Synthesis of Ag Nanoparticles 146
5.3.3 Synthesis of Au-Ag core-shell NPs 147
5.4 Characterizations 148
5.4.1 Transmission Electron Microscopy (TEM) 148
5.4.2 Energy Dispersive X-Ray Spectroscopy (EDX) 151
5.4.3 Atom Probe Tomography (APT) 154
5.4.4 UV-Visible Spectroscopy (UV-Vis) 159
5.4.5 X-Ray Absorption Spectroscopy (XAS) 160
5.5 Surface Plasmon Analysis 167
5.6 Direct Electrochemical-Localized Surface Plasmon Resonance (EC-LSPR) 173
5.6.1 Experimental Methods 173
5.6.2 Direct Plasmonic Chronoamperometry 176
5.6.3 Stability Test and Control Experiments 186
5.6.4 Plasmonic Chronoamperometry with Solar Simulator 189
5.6.5 Linear Sweep Voltammetry (LSV) Analysis 191
5.7 Discrete Dipole Approximation (DDA) 193
5.8 Conclusions 195
5.9 References 196

5.1 Background

To potentially reduce power consumption by electrochemical means as mentioned in chapter 4, one of the solutions is to effectively utilise additional energy, preferably from renewable sources, to power the system. Photo-energy from sunlight appears to be a promising choice due to its ease in extraction. Bandgap materials are often employed to capture sunlight and applied in photocatalysis and electrochemical photolysis due to their ability to harness a reasonable range of solar spectrum. Notwithstanding the low cost and wide abundance of bandgap materials, the inevitable high impedance across the bandgap and the low concentration of intrinsic charge carriers have significantly limited their energy conversion causing a low solar-to-hydrogen (STH) efficiency.[2–4] In contrast, the use of metal nanoparticles (NPs) with a sea of mobile conductive electrons will not lead to significant impedance as that of semiconductors. In particular, the plasmonic metals, such as gold and silver, give outstanding conductivity and promote electron transition to excited states via localized surface plasmon resonance (LSPR) in the visible and/or near infrared ranges.

Meanwhile, to exploit plasmonic metal nanoparticles' role as light absorbers and electron mediators, it is recently reported that these NPs can be used to assist semiconductors in photocatalysis by lowering the electron-hole recombination rates.[5–8] The nature of the bandgap materials (semiconductors) renders them to act as electron acceptors for hydrogen production with the LSPR-excited hot electrons being injected to the conduction band. However, the inevitable high impedance across the band gap and low concentration of mobile electrons in semiconductors have concomitantly limited their electronic conductivity. Therefore, the main objective of this chapter is to evaluate alternative options, i.e., visible light capture by EC-LSPR, in promoting hydrogen production in the absence of bandgap materials.

In this chapter, silver-gold core-shell materials are employed owing to their bifunctional capabilities of light capture and electron transfer. Specifically, plasmonic absorption occurs on

gold to capture major solar radiations whereas higher energy excited states are provided by silver to allow efficient LSPR-promoted hot electron transfer for proton reduction. Gold nanoparticles are structured as the core whereas a layer with tuneable mixed shell composition (Ag/Au) and thickness is fabricated by gradual reduction process. Ag-Au core-shell materials with 3 different thicknesses have been synthesised, in which they are christened as atomic (AT)-layer, intermediate (IN)-layer and thick (TH)-layer. It was experimentally found that the atomic layer core-shell nanoparticle can deliver a high hydrogen production rate with an order of magnitude higher than that of most semiconductor catalysts under similar reaction conditions.[9–15] The underlying mechanism is further revealed by EDX, APT, and DDA calculations where a maximum optical absorption is found to be obtained from the significant amplification of the plasmonic electric field in the near-shell region.

5.2 Materials

The reagents used are as follows: trisodium citrate dehydrate (≥ 99%, Sigma-Aldrich), gold(III) chloride trihydrate (≥ 99.99%, Sigma-Aldrich), potassium hydroxide pellets (reagent grade, Fisher scientific), L-ascorbic acid (≥ 99%, Sigma-Aldrich), silver nitrate (≥ 99.9999%, Sigma-Aldrich), ethylene glycol (anhydrous, ≥ 99.8%, Sigma-Aldrich), polyvinylpyrrolidone (PVP, average Mw~55,000, Sigma-Aldrich), silver trifluoroacetate (≥99.99%, Sigma Aldrich), sodium sulphate (≥ 99%, Sigma-Aldrich), Vulcan carbon (Vulcan XC 72R, FuelCellStore), platinum on graphitized carbon (20 wt.% loading, Sigma Aldrich), 2-Propanol (≥ 99.5%, Sigma Aldrich), Nafion perfluorinated resin solution (5wt.% in mixture of lower aliphatic alcohols and water, Sigma Aldrich), ethanol (≥ 99.8%, Sigma Aldrich), Nitrogen gas (99.99%, BOC).

5.3 Synthesis

In this chapter, pure Au, pure Ag and three different shell thickness Au-Ag core-shell NPs were chosen as the working electrode catalysts for direct electrochemical-plasmonic water electrolysis. The three Au-Ag core-shell type NPs with a tuneable mixed-shell composition and

shell thickness were christened as atomic (AT)-layer, intermediate (IN)-layer, and thick (TH)-layer. The synthesis involved the preparation of pure Au, pure Ag and the three different shell thickness Au-Ag core-shell NPs. The 20 wt% metal on carbon catalyst were prepared by wet impregnating the as-prepared metal NPs onto the Vulcan carbon.

5.3.1 Synthesis of Au Nanoparticles

Citrate stabilized Au NPs were synthesized by the Turkevich method.[16,17] 5 mL sodium citrate (5 mg/mL) was added into 95 mL deionized water in a round bottom flask. The flask was then placed in an oil bath at a temperature of 100 °C. Once the solution started to boil, 2 mL of $HAuCl_4 \cdot 3H_2O$ (25 mM) Au precursor was added into the reaction mixture and the temperature was kept at 100 °C. The solution mixture was boiled for 8 min and then cooled to room temperature. The as-prepared Au NP samples were stored in the fridge (1-4 ^oC) before use.

5.3.2 Synthesis of Ag Nanoparticles

The Ag NPs were synthesized with the polyol process following the methods of Xia et. al.,[18] which is similar to the synthesis method described in chapter 4, section 4.3.1 but with a different reaction time. In detail, ethylene glycol (EG, 5 mL) was added into a 25 mL round bottom flask and heated under magnetic stirring in an oil bath pre-set to 150 °C. Poly(vinylpyrrolidone) (PVP, 1.25 mL, 20 mg/mL in EG) was injected into the reaction solution after 150 °C was reached. After 2 minutes, CF_3COOAg (0.4 mL, 282 mM in EG) was added into the reaction solution. Another 2 minutes later, the reaction solution was quenched by placing the flask in an ice-water bath. The sample was collected by centrifugation followed by washing with acetone once, and with DI water four times.

5.3.3 Synthesis of Au-Ag core-shell NPs

The synthesis of Au-Ag core-shell NPs is based on the gradual reduction of Ag^+ ion on the as-prepared citrate-stabilized Au NPs through adding the $AgNO_3$ (Ag precursor) stepwise as shown in Figure 5.1, accompanying an obvious colour change from wine red to orange.

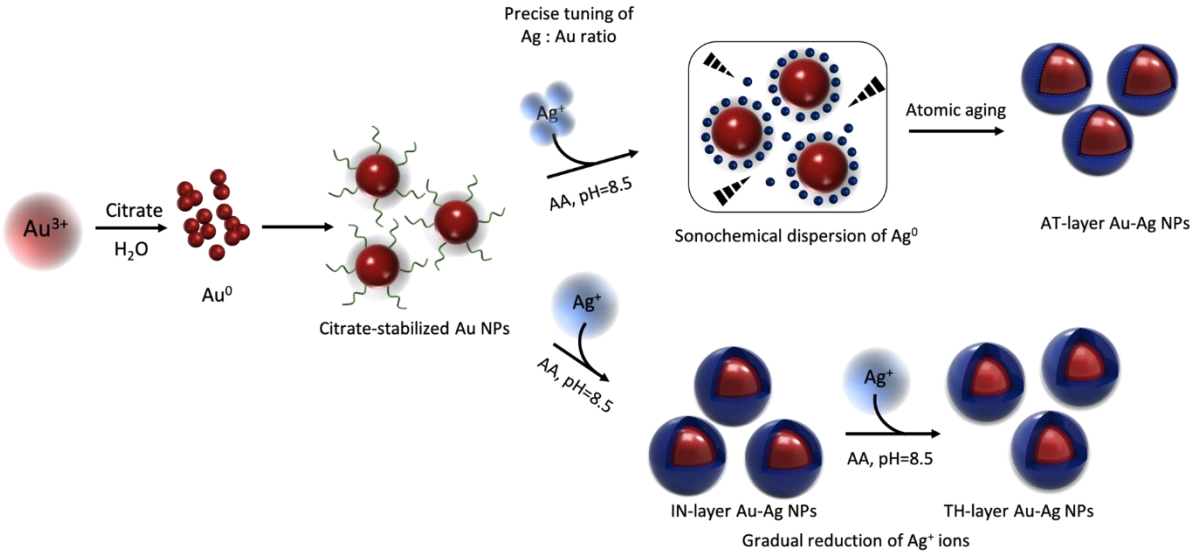


Figure 5.1 Schematic illustration of sonochemical dispersion and gradual reduction process used to synthesize the Au-Ag core-shell nanoparticles.

For the Atomic (AT)-layer of the Au-Ag core-shell NPs, 10 mL of the as-prepared Au NPs was added into a round bottom flask which was then placed in a sonication bath under ambient conditions. Typically, 150 µL of potassium hydroxide (0.1 M) and 120 µL of ascorbic acid (0.1 M) were added into the flask followed by sonication (120 s). 30 µL of silver nitrate (0.01 M) was then added into the reaction mixture and sonicated for another 120 s to obtain a well sonochemical dispersion of Ag. This is to ensure the reduction of Ag^+ onto the Au cores while inhibiting the formation of free Ag nuclei. After that the reaction mixture was stirred constantly for 30 min at room temperature. The as-prepared AT-layer samples were stored in the fridge (1-4 ^oC) before use.

The intermediate (IN)-layer and the thick (TH)-layer were synthesized via the gradual reduction cycles of Ag^{+} ion on the Au core NPs. For the first cycle, 150 µL of potassium hydroxide (0.1 M), 120 µL of ascorbic acid (0.1 M) and 30 µL of silver nitrate (0.1 M) were added into 10 mL of the as-prepared Au NPs at room temperature respectively, and then the reaction mixture was stirred constantly for 30 min to obtain IN-layer Au-Ag core-shell sample. Repeat the reduction cycles for three times with reaction time of 30 min for each cycle, the TH-layer Au-Ag core-shell sample can be obtained. The as-prepared IN-layer and TH-layer samples were stored in the fridge (1- 4 ^{o}C) before use.

The sample prepared above were supported on the Vulcan carbon via wet impregnation method as 20 wt% Au/C, 20 wt% Ag/C, 20 wt% AT-layer/C, 20 wt% IN-layer/C, 20 wt% TH-layer/C for electrochemical reactions.

5.4 Characterizations

The particle size and distribution of the pure Au, pure Ag and Au-Ag core-shell NPs were confirmed by TEM measurement. EDX, APT and EXAFS analysis were employed in this chapter to characterize the core-shell structures of the as-prepared samples. Also, UV-Visible spectroscopy was carried out to investigate the plasmonic absorption properties of the samples.

5.4.1 Transmission Electron Microscopy (TEM)

Transmission electron microscopy (TEM) was performed to investigate the particle size and distribution of the pure Au, pure Ag and the three Au-Ag core-shell NPs with different shell thickness. The TEM micrographs and the corresponding size distribution histograms of the as-prepared samples are shown in Figure 5.2 – Figure 5.6 below.

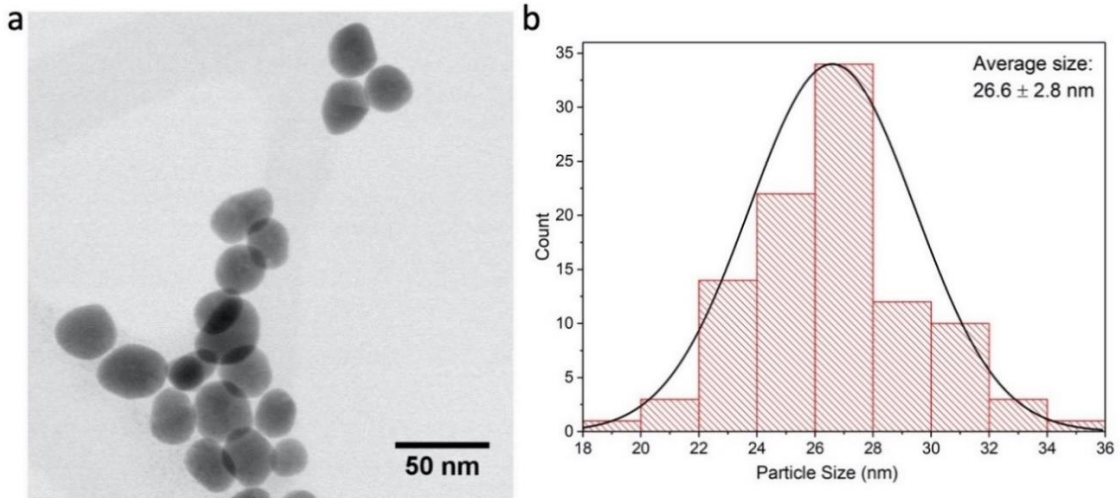


Figure 5.2 a) TEM image of pure Au NPs and **b)** corresponding histogram of size distribution.

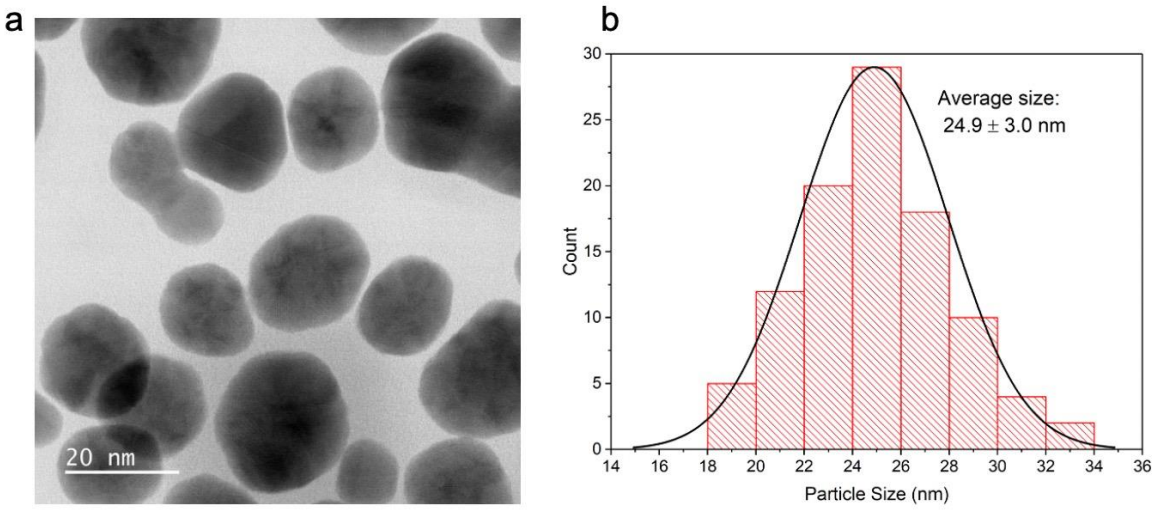


Figure 5.3 a) TEM image of pure Ag NPs and **b)** corresponding histogram of size distribution.

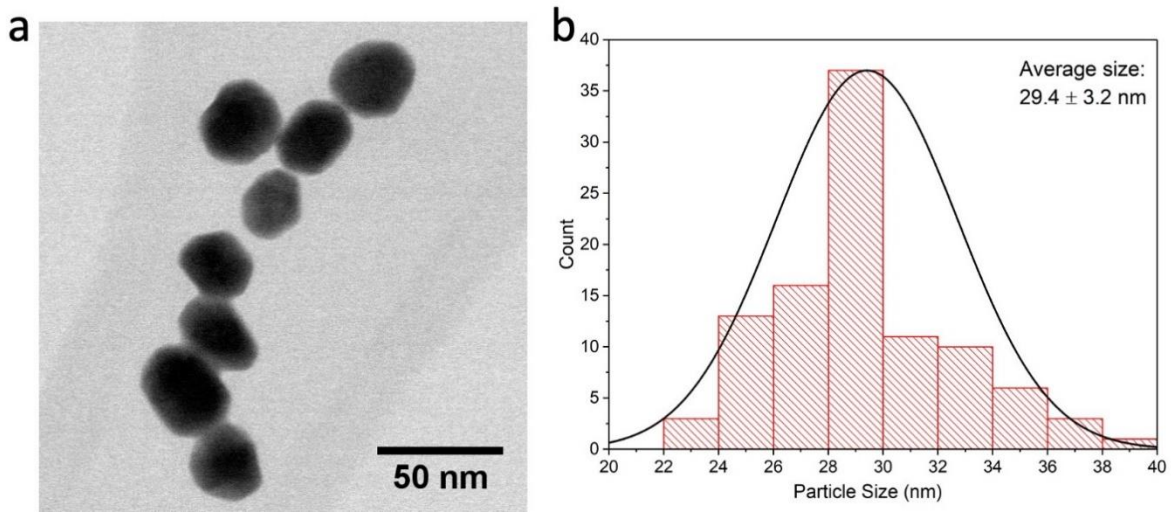


Figure 5.4 a) TEM image of AT-layer Au-Ag core-shell NPs and **b)** corresponding histogram of size distribution with a mean Ag shell thickness of 1.4 nm.

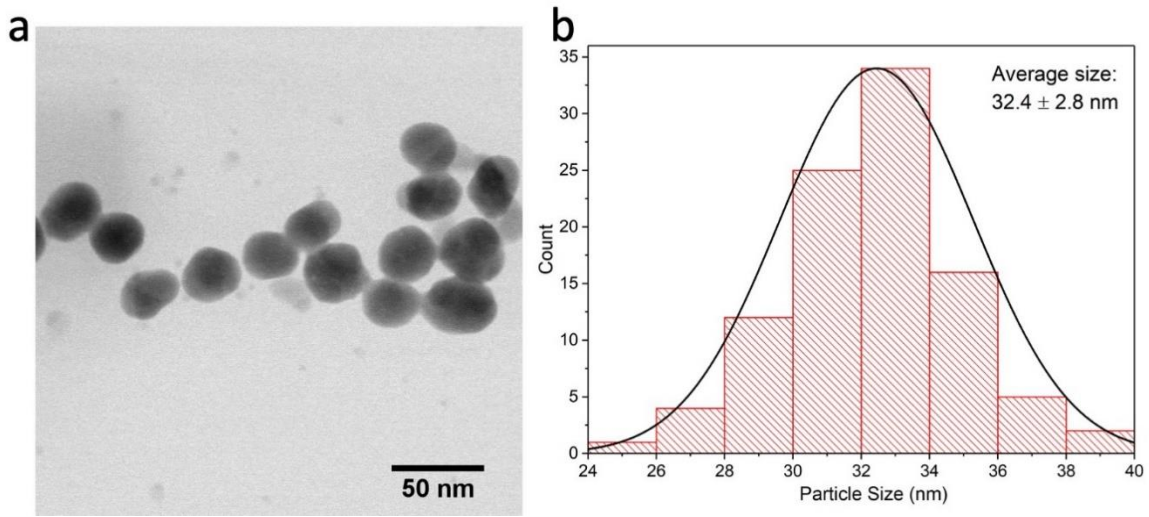


Figure 5.5 a) TEM image of IN-layer Au-Ag core-shell NPs and **b)** corresponding histogram of size distribution with a mean Ag shell thickness of 2.9 nm.

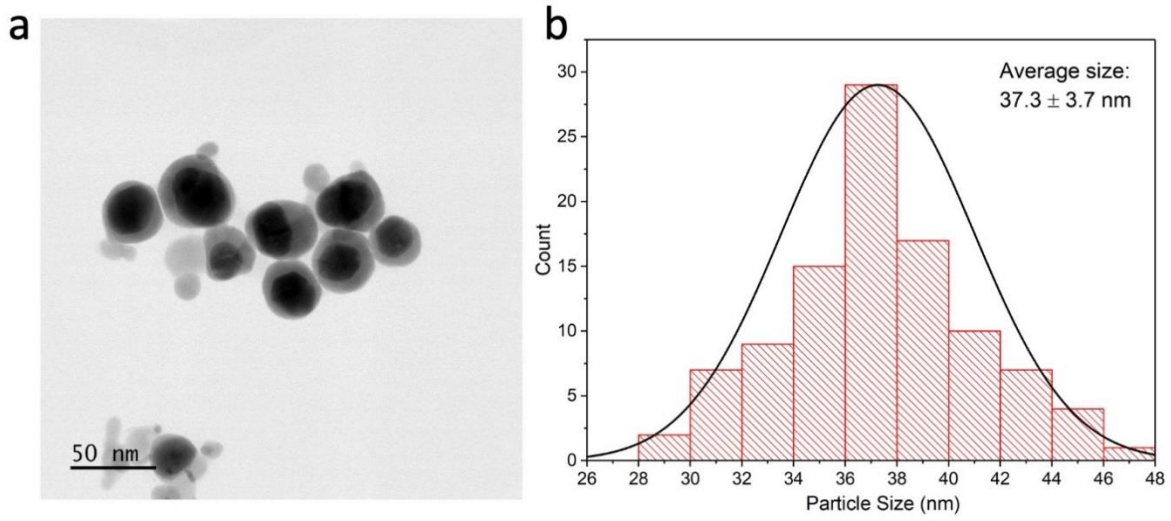


Figure 5.6 a) TEM image of TH-layer Au-Ag core-shell NPs and **b)** corresponding histogram of size distribution with a mean Ag shell thickness of 5.4 nm.

As seen from the Figure 5.2 - Figure 5.6, the pure Au, pure Ag and core-shell NPs are evenly distributed with spherical morphology, and their corresponding size distribution histograms are obtained by counting 100 nanoparticles of each sample. The mean diameters of pure Au and pure Ag are 26.6 nm and 24.9 nm respectively as suggested by the size distribution histogram. As for the AT-layer and IN-layer NPs, it shows average diameters of 29.4 nm and 32.4 nm respectively with the mean Ag shell thickness of 1.4 nm and 2.9 nm. Both pure Ag and pure Au NPs were rarely found in the AT-layer and IN-layer samples, which were carefully examined by TEM, suggesting the highly selective growth of Ag on the Au cores. In Figure 5.6, it gives the mean diameter of 37.3 nm for the TH-layer NPs with a mean Ag shell thickness of 5.4 nm. It should be noted that the nonuniform coatings, as well as nucleation of Ag NPs in TH-layer samples may be caused by high $AgNO_3$ concentration in the reduction step.[17]

5.4.2 Energy Dispersive X-Ray Spectroscopy (EDX)

As the plasmonic resonance is critically dependent on chemical composition and interfacial structure of the NPs, it is essential to investigate the detailed interfacial nanoscale structure and composition of the core-shell NPs. However, it is very challenging to characterize NP materials'

interface in the composite Au-Ag core-shell even by the help of high-resolution TEM imaging. As a result, high resolution super-EDX was particularly employed to obtain elemental mapping of the core-shell structures.

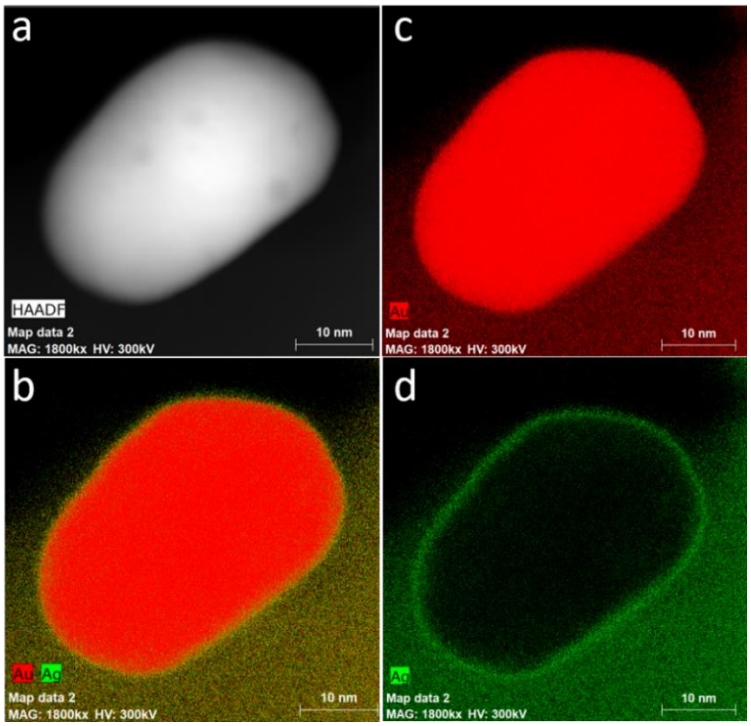


Figure 5.7 a) HAADF-STEM images and **b)-d)** the corresponding super-EDX spectrum for individual AT-layer Au-Ag core-shell NP showing the elemental mapping of the core and shell. Au (red), Ag (green).

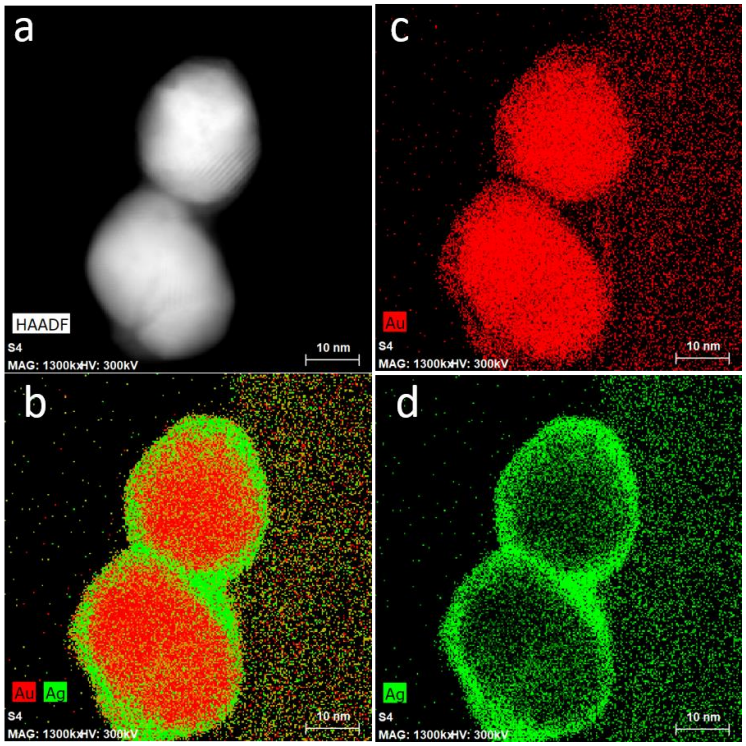


Figure 5.8 a) HAADF-STEM images and **b)-d)** the corresponding super-EDX spectrum for IN-layer Au-Ag core-shell NPs showing the elemental mapping of the core and shell. Au (red), Ag (green).

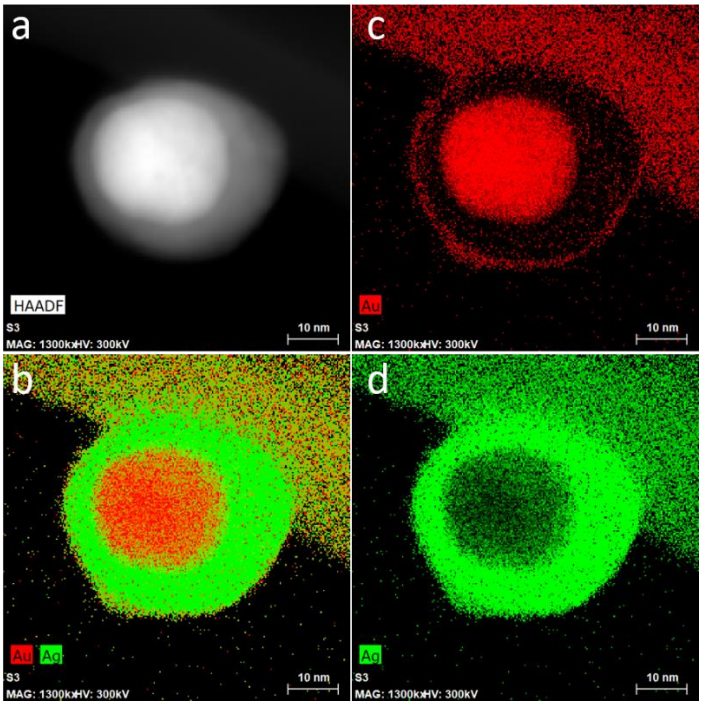


Figure 5.9 a) HAADF-STEM images and **b)-d)** the corresponding super-EDX spectrum for individual TH-layer Au-Ag core-shell NP showing the elemental mapping of the core and shell. Au (red), Ag (green).

The distribution of the two elements (Au and Ag) was studied in detail by means of STEM-EDX spectroscopy of individual nanoparticles. As shown in Figure 5.7- Figure 5.9, the elemental maps of the individual representative nanoparticle reveal a defined core-shell nanostructure of the Au core (red) and complete Ag shell (green) for all the three as-prepared core-shell samples. In Figure 5.7 and Figure 5.8, both AT-layer and IN-layer show uniform Ag layer shell on the Au core, giving a mean shell thickness of 1.2 nm and 3.2 nm, which is similar to that obtained by the TEM size distribution analysis. As for the TH-layer samples, the Ag shell (mean thickness of 5.9 nm) shown in Figure 5.9 is relatively less uniform when compared with the other two core-shell samples, which might be caused by high/excess $AgNO_3$ concentration in the reduction step as mentioned in the TEM section. The super-EDX analysis clearly indicated an integrated shell with mixed chemical composition of both Ag and Au, especially at the interface of core and shell in the structure.

5.4.3 Atom Probe Tomography (APT)

The two-dimensionally projected Ag and Au signals of the core-shell nanoparticle obtained by EDX analysis make it difficult to differentiate their precise locations. However, atom probe tomography (APT) can provide uniquely powerful atomic-scale mapping of nanoparticles in three-dimensions. Thus, APT was employed to analyse the elemental concentration in the shell and the core.

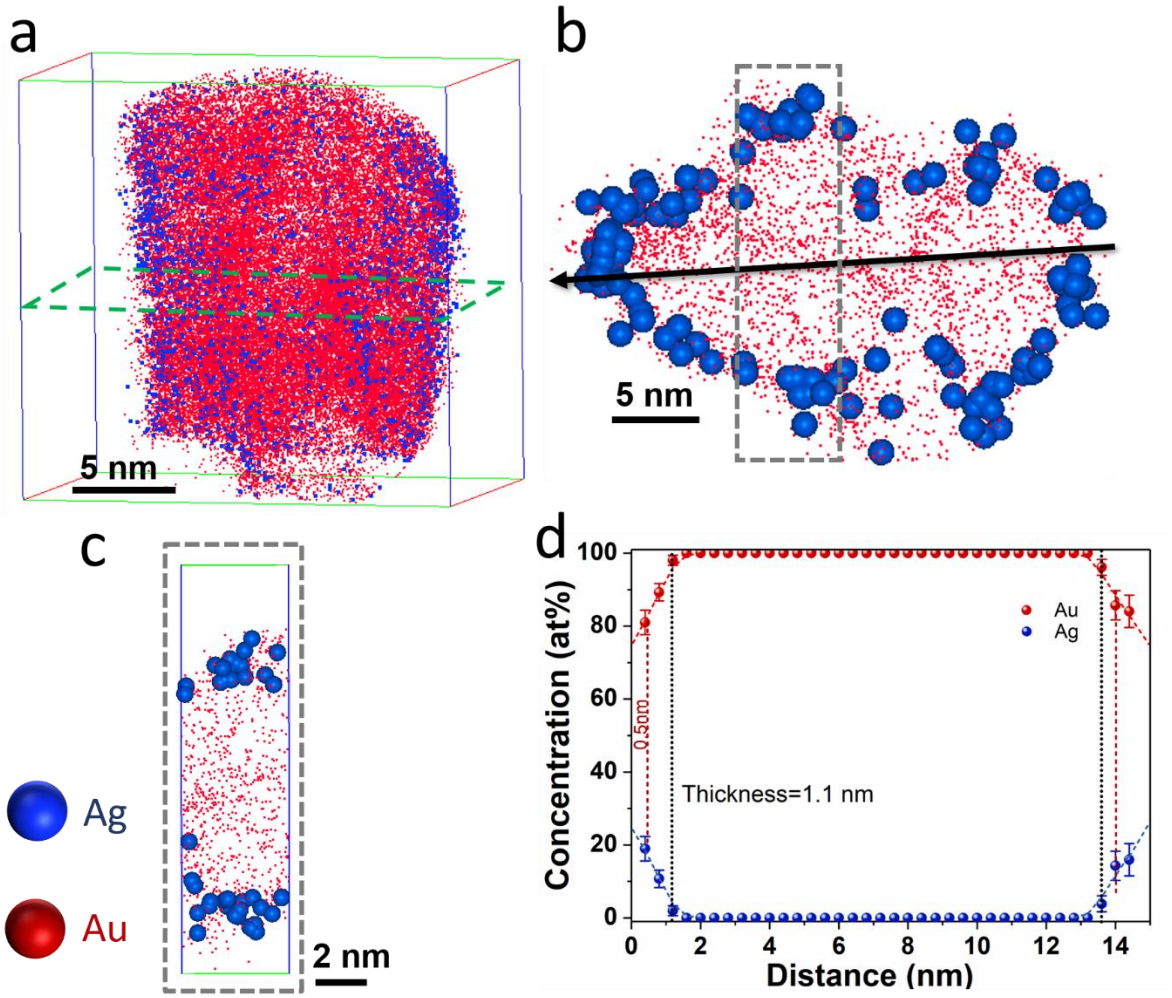


Figure 5.10 a) 3D APT reconstruction of AT-layer Au-Ag NP; **b)** Cross-sectional atom map as indicated by the green dotted box in the 3D APT reconstruction diagram (a); **c)** Highlighted area as indicated in (b) (grey dotted box); **d)** 1D concentration profile of Ag and Au across the line from shell to core based on the arrow in the cross-sectional atom maps in (b). Au (red), Ag (blue).

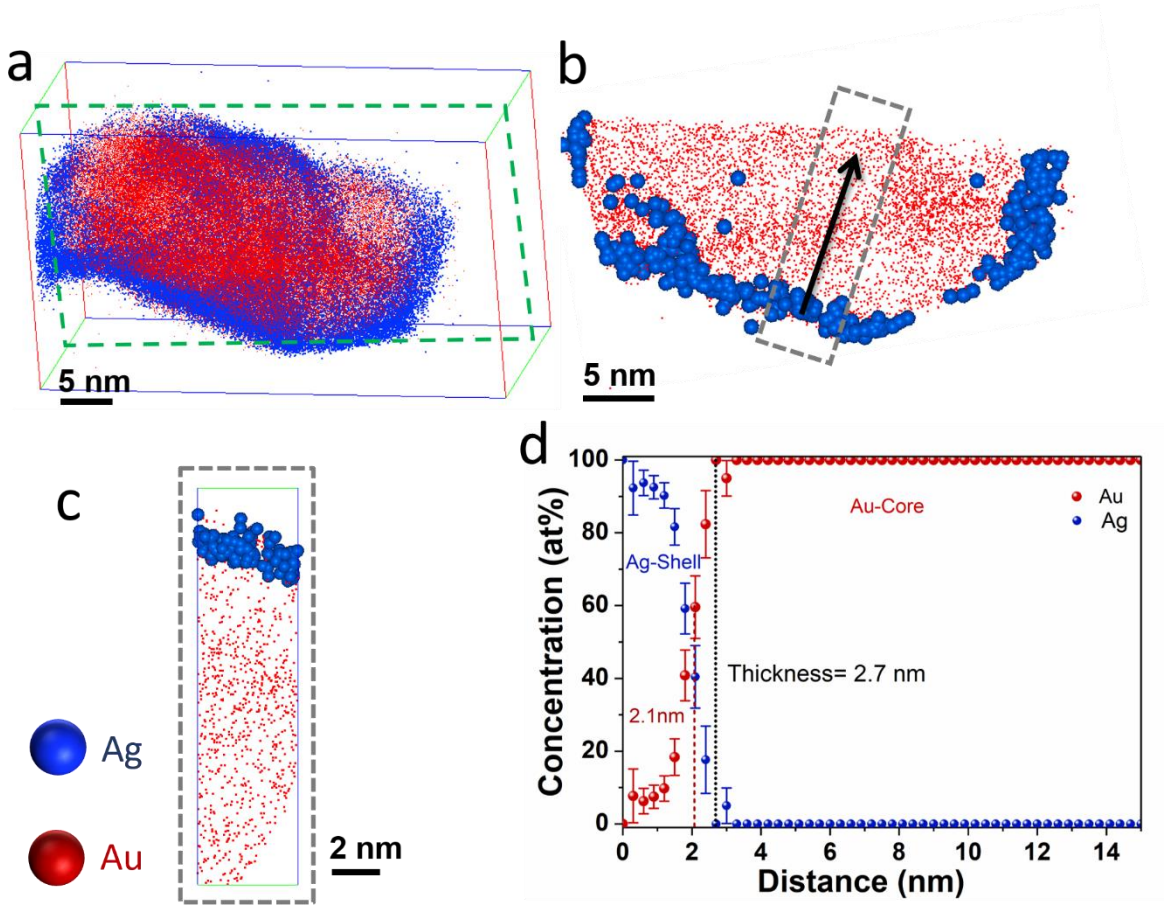


Figure 5.11 a) 3D APT reconstruction of IN-layer Au-Ag NP; **b)** Cross-sectional atom map as indicated by the green dotted box in the 3D APT reconstruction diagram (a); **c)** Highlighted area as indicated in (b) (grey dotted box); **d)** 1D concentration profile of Ag and Au across the line from shell to core based on the arrow in the cross-sectional atom maps in (b). Au (red), Ag (blue).

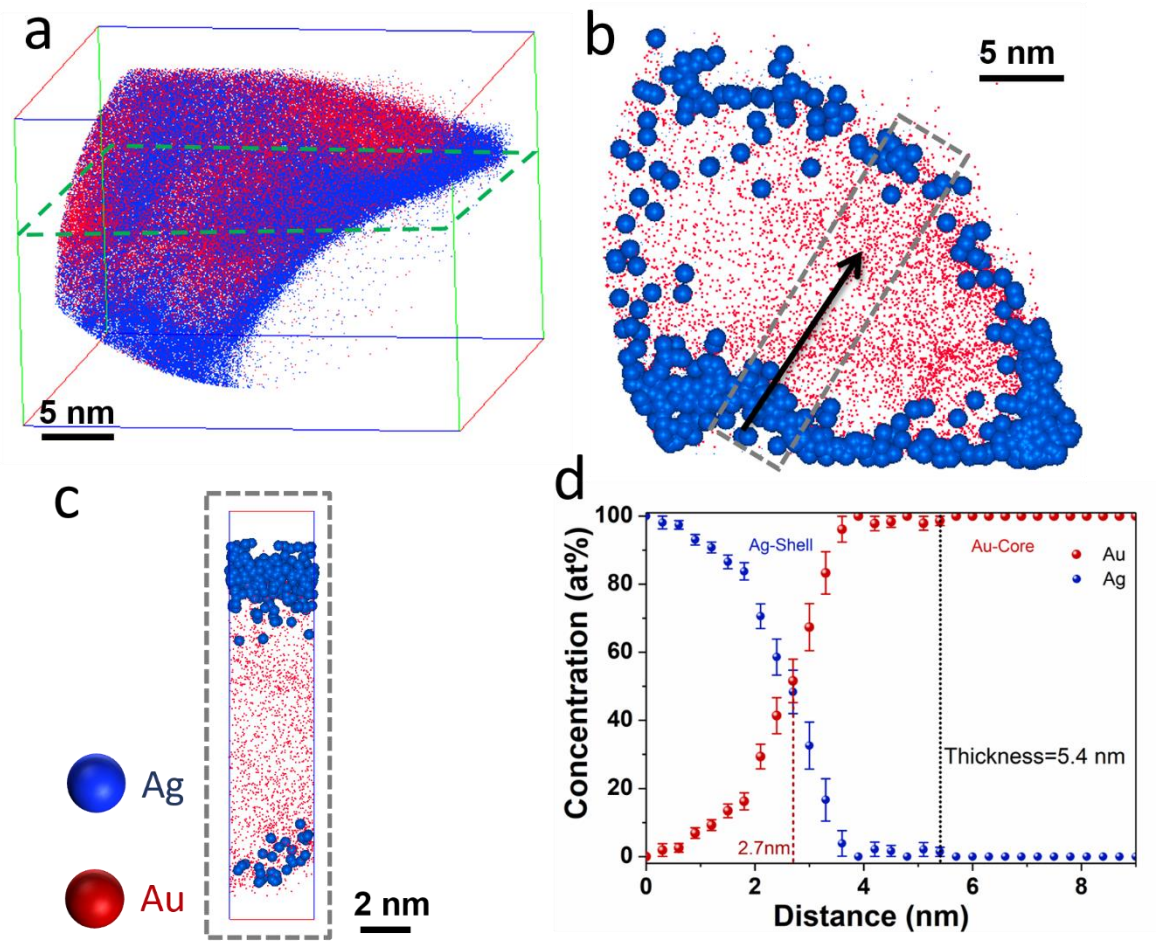


Figure 5.12 a) 3D APT reconstruction of TH-layer Au-Ag NP; **b)** Cross-sectional atom map as indicated by the green dotted box in the 3D APT reconstruction diagram (a); **c)** Highlighted area as indicated in (b) (grey dotted box); **d)** 1D concentration profile of Ag and Au across the line from shell to core based on the arrow in the cross-sectional atom maps in (b). Au (red), Ag (blue).

In Figure 5.10-5.12, it shows the atom probe tomography (APT) atomic-scale mapping of the three different Ag shell thickness NPs in three-dimensions. Slices shown in Figure 5.10b, Figure 5.11b and Figure 5.12b were taken from the 3D APT reconstructions (Figure 5.10a, Figure 5.11a and Figure 5.12a) respectively through each particle for atomic depth profiling. As shown in Figure 5.10d, Figure 5.11d and Figure 5.12d, the average shell thickness of AT-layer, IN-layer and TH-layer were determined to be 1.1 nm, 2.7 nm and 5.4 nm respectively, which is consistent with the TEM size distribution histogram and EDX analysis with an error of ± 0.5 nm. The mean interfacial regions in the shells of AT-layer, IN-layer and TH-layer of

Au-Ag core-shell NPs were analysed by the 1D concentration profile and determined to be 0.5 nm, 2.1 nm and 2.7 nm, respectively. APT reveals their concentration profiles at the interface regions of the core-shell heterostructures varying from almost pure Ag (except the AT-layer) at outermost layer to pure Au core in Figure 5.11d and Figure 5.12d. For the AT-layer case, although the shell thickness is similar to atomic thickness, there is no pure Ag atomic shell but rather a mixture of Ag and Au atoms on Au core. The average compositions of the interfaces in AT-layer, IN-layer and TH-layer Au-Ag core-shell are determined to be "*20% Ag and 80% Au*", "*40% Ag and 60% Au*" and *50% Ag and 50% Au*", respectively.

As a result, there is no clear ordered segregation of Ag atoms in any local region but both Au and Ag atoms clearly have diffused across the material boundaries to give the atomically disordered interfaces, reinforcing their excellent mutual atomic miscibility. This leads to a gradual mixing of Au and Ag atoms at the interfacial regions as also evidenced by both super-EDX and APT analyses. The resultant compositions are also in good agreement with the synthesis ratio when the self-nucleation and trace size variation are taken into account.

5.4.4 UV-Visible Spectroscopy (UV-Vis)

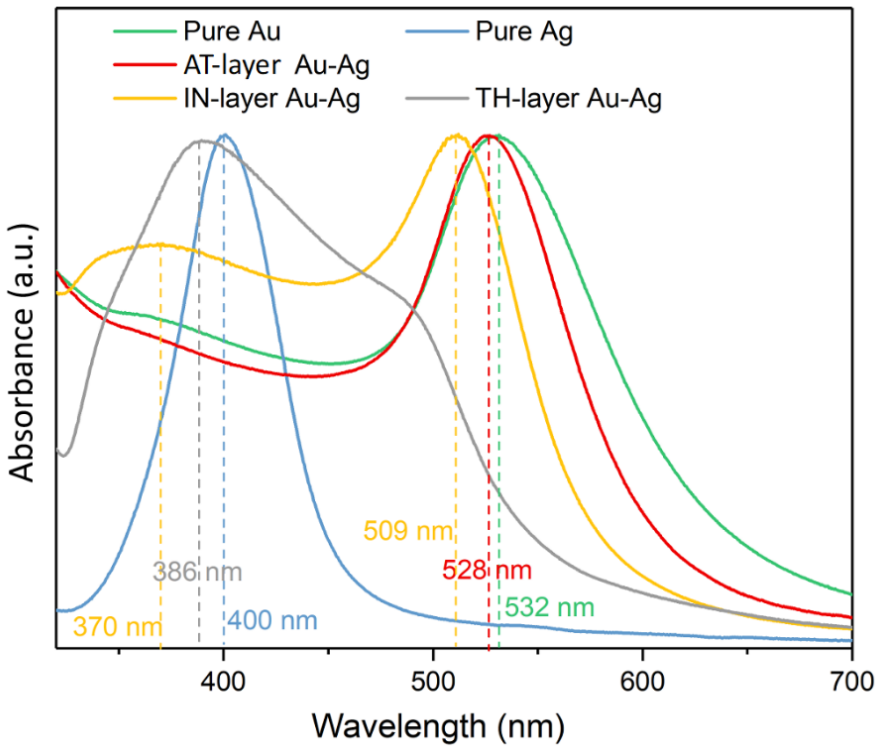


Figure 5.13 The normalized UV-Vis absorption spectra of pure Au, pure Ag and different Ag shell thickness of the Au-Ag core-shell NPs.

In Figure 5.13, it shows the normalized UV-Vis absorption spectra of pure Au, pure Ag and different Ag shell thickness of the Au-Ag core-shell NPs. The as-prepared pure Au and pure Ag NPs exhibit strong plasmonic absorption peaks in the visible light regime and are well separated at the peak maxima of 532 nm and 400 nm respectively. As a result, it follows logically that the optical properties of the core-shell Au-Ag NPs lie between the two plasmon resonance frequencies of pure Ag and Au. From Figure 5.13, it can be observed that the peak position of the UV-Vis spectrum of the AT-layer NP is similar to that of Au core with a clear blue shift to 528 nm. Thus, the position of the LPSR absorption peak can even be sensitized by the single atomic alloy layer (20% Ag and 80% Au) on Au core as shown by the super-EDX and APT. When the shell thickness increases to 2.7 nm (IN-layer), the plasmon resonance is blue-shifted further to 509 nm with a new extinction peak appearing at 370 nm. The latter can clearly be attributed to the outermost primarily Ag shell with a similar absorption to that of the pure Ag but the alloy

interfacial regions (40% Ag and 60% Au) on Au core shown by 509 nm peak can also exert their effect on the absorption. When the shell thickness reaches 5.4 nm (TH-layer), Ag outer shell absorption becomes dominant with the major absorption peak shifted to 386 nm but the strongly shifted Au absorption peak (~500 nm) can only be visible as a small shoulder. Within experimental errors and materials variations, as a general observation, the plasmon resonance of the Au core nanosphere thus appears to be strongly masked or attenuated by that of the shell, and the Ag/Au alloyed shell resonances dominate.

5.4.5 X-Ray Absorption Spectroscopy (XAS)

Obviously, the shell composition may also be altered with the shell thickness as evidenced by the APT measurements (section 5.4.3). As a result, X-ray absorption fine structure (EXAFS) of both Ag K-edge and Au L_3-edge have also been used to analyse the composition of Ag and Au by probing the coordination environment of the two metals.

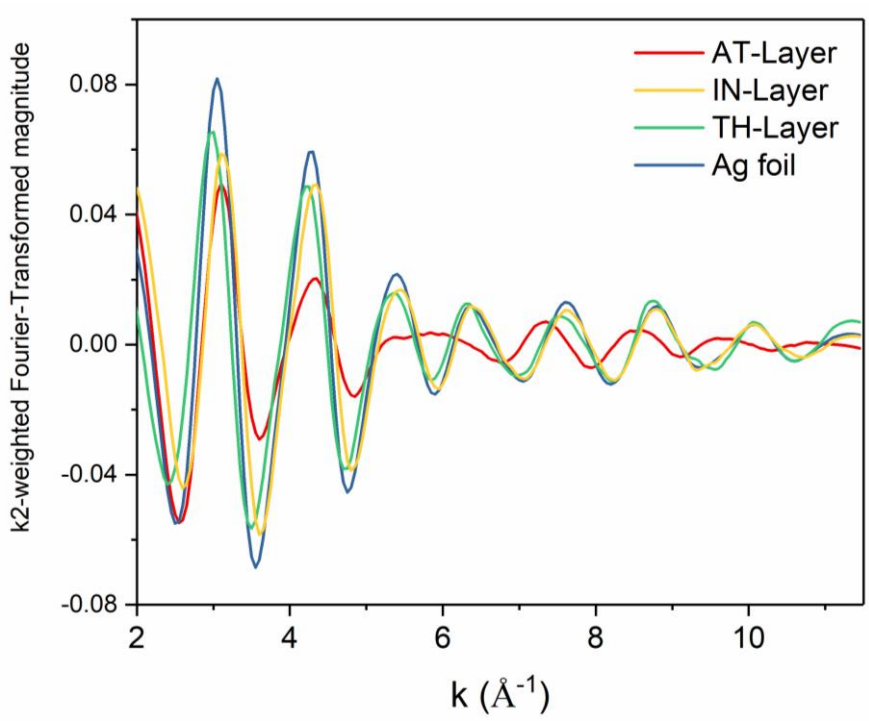


Figure 5.14 Fourier-Transformed (FT) k-space spectra (k-2 weighted) of the as-prepared core-shell NPs (AT-layer, IN-layer, TH-layer, and the reference Ag foil).

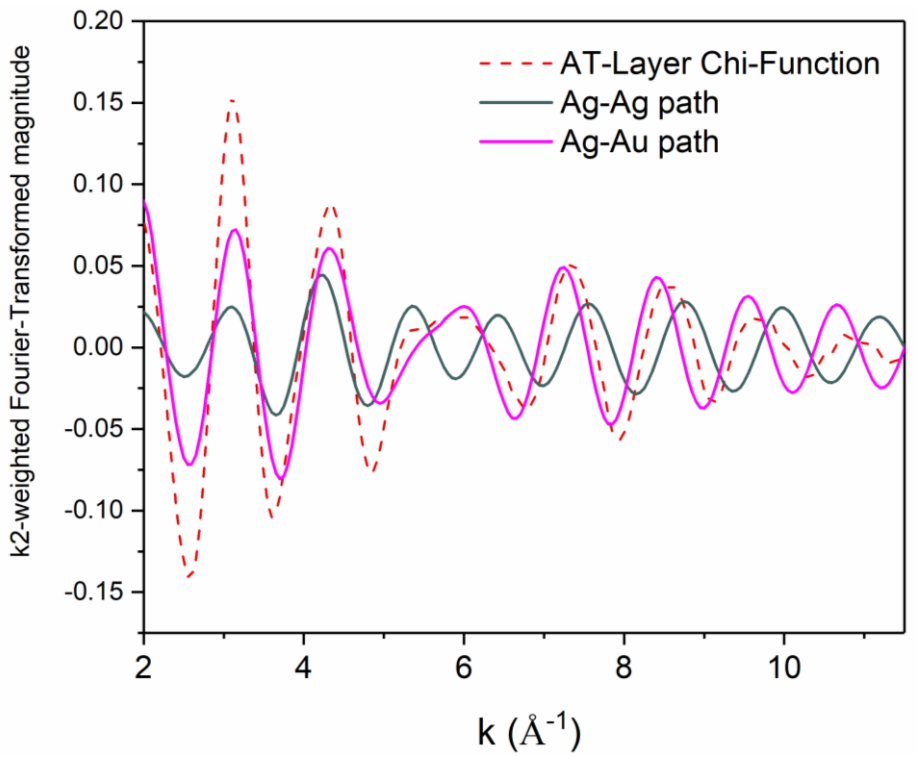


Figure 5.15 FT k-space compositional spectra (k-2 weighted) of AT-layer with fitted Ag-Ag and Ag-Au scattering path contribution.

Fourier transformed chi functions of Ag K-edge are first used to disseminate the difference between the atomic layer and the other shell-thickness core-shell NPs. As displayed in Figure 5.14, the chi functions of IN-Layer and TH-layer resemble that of the Ag foil while that of AT-layer shows a stark contrast in peak shapes and peak positions especially at the higher k values (> 6Å^{-1}). It is indicating that the Au core is strongly masked by the Ag shell in IN-layer and TH-layer with more characteristic property of the Ag shell. Fitting with Ag-Ag and Ag-Au scattering paths suggest some heavier elements, in this case Au, are coordinating to Ag in the shell, which supports our argument in atomic probe tomography of an apparent Ag:Au interface (Figure 5.15).

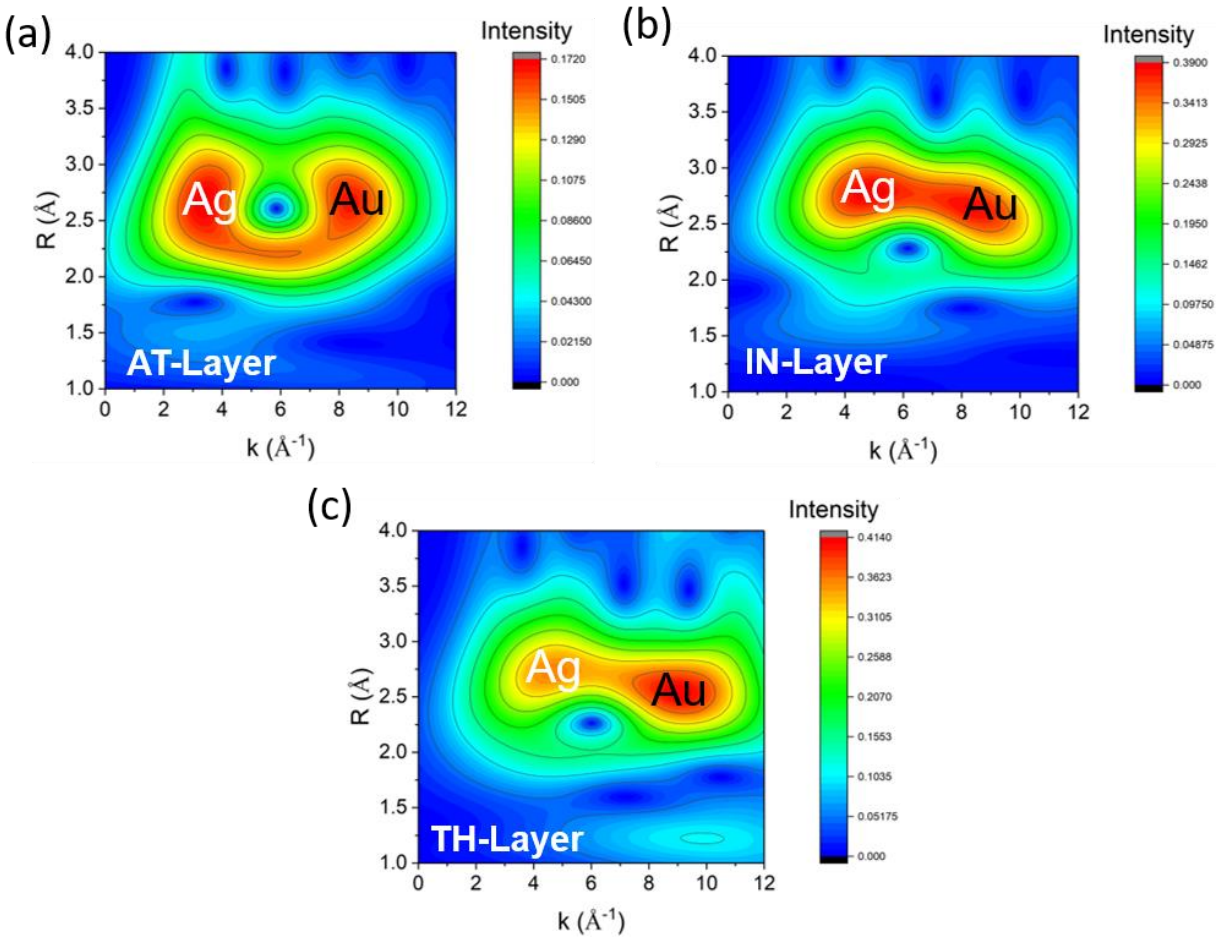


Figure 5.16 Wavelet restoration for **a)** AT-layer, **b)** IN-layer, and **c)** TH-layer Au-Ag core-shell NPs respectively. Parameters used: R-range: 1-4, Morlet function, Kappa Morlet: 8, Sigma Morlet: 1.

Meanwhile, wavelet restorations have been implemented in order to spatially resolve the close bond distance between Au-Ag (~2.88 Å) and Ag-Ag (~2.89 Å). As observed in Figure 5.16, the wavelet is clearly resolved into 2 different energy maxima at low k (~ 3.5 Å^{-1}, assign to lighter element Ag) and high k (~ 8.2 Å^{-1}, assign to heavier element Au) at approximately 2.5 Å (2.9 Å after phase transfer). As Figure 5.16b and Figure 5.16c suggests, the lower energy maxima (Ag) in the wavelet of IN-layer and TH-layer are heavily biased towards the higher energy maxima, which suggests the substantial interaction between Ag and Au atoms. On the other hand, the wavelet for AT-layer (Figure 5.16a) is clearly resolved in two peaks which stems from the distinct interaction of Ag-Au and Ag-Ag at the interface.

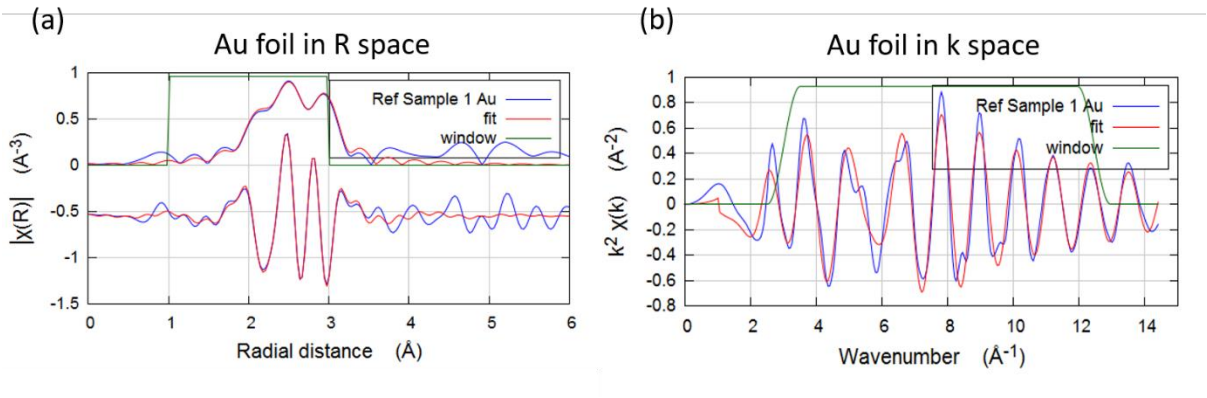


Figure 5.17 Least square fitting for the k3-weighted EXAFS spectra for **a)** R-space, **b)** k-space for the Au foil (Au L_3 edge). Amplitude reduction factor is derived from this spectrum which is used as a fixed parameter for subsequent fittings for the core-shell samples. Both R-space and k-space fitting profiles are provided.

Table 5.1 Parameters obtained from least-square fitting of the Au foil. Parameters used: k-range: 3-12.5, R-range: 1-3, R-factor: 0.4%.

Scattering Path	Bond length [Å]	Coordination number	Debye-Waller factor
Au-Au	2.86 (1)	12	0.008 (1)

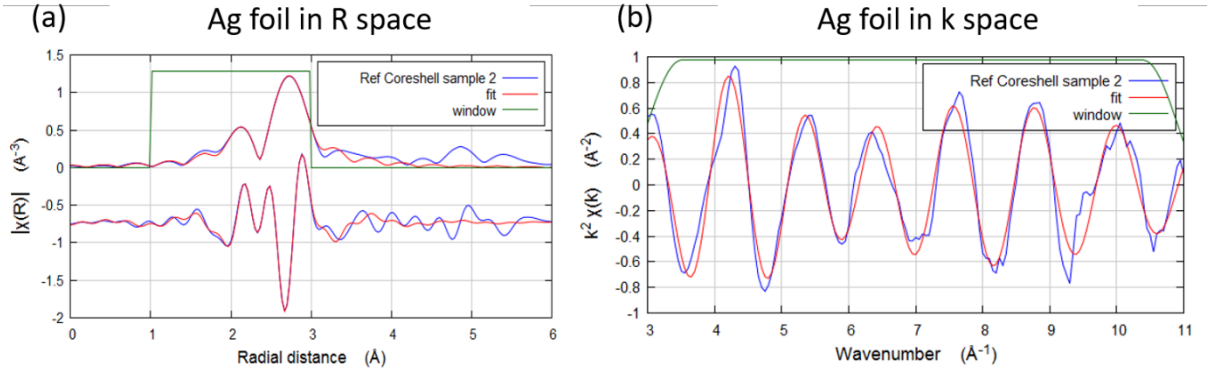


Figure 5.18 Least square fitting for the k3-weighted EXAFS spectra for **a)** R-space, **b)** k-space for the Ag foil (Ag K edge). Amplitude reduction factor is derived from this spectrum which is used as a fixed parameter for subsequent fittings for the core-shell samples. Both R-space and k-space fitting profiles are provided.

Table 5.2 Parameters obtained from least-square fitting of the Ag foil. Parameters used: k-range: 3-10.9, R-range: 1-3, R-factor: 0.5%.

Scattering Path	Bond length [Å]	Coordination number	Debye-Waller factor
Ag-Ag	2.89 (1)	12	0.010 (1)

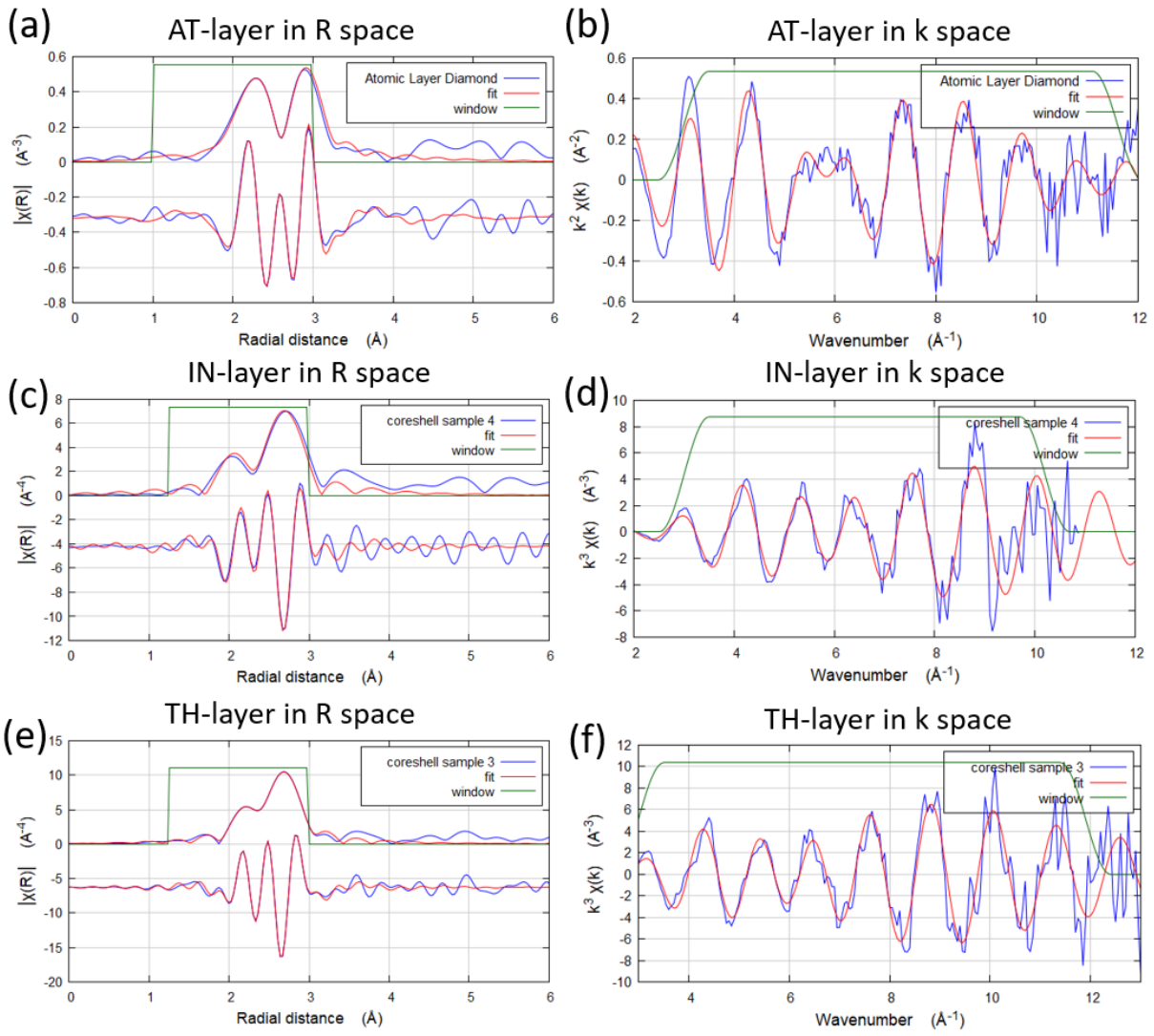


Figure 5.19 a)-b) Least square fitting for the k3-weighted EXAFS spectra (Ag K edge) for (a) R-space, (b) k-space for the AT-layer Au-Ag core-shell NPs, k-range: 3-11.6; R-range: 1-3; R-factor: 1.4%; **c)-d)** Least square fitting for the k3-weighted EXAFS spectra (Ag K edge) for (c) R-space, (d) k-space for the IN-layer Au-Ag core-shell NPs, k-range: 3-9.8; R-range: 1.25-3; R-factor: 0.9%; **e)-f)** Least square fitting for the k3-weighted EXAFS spectra (Ag K edge) for (e) R-space, (f) k-space for the TH-layer Au-Ag core-shell NPs, k-range: 3-11.9; R-range: 1.25-3; R-factor: 0.5%.

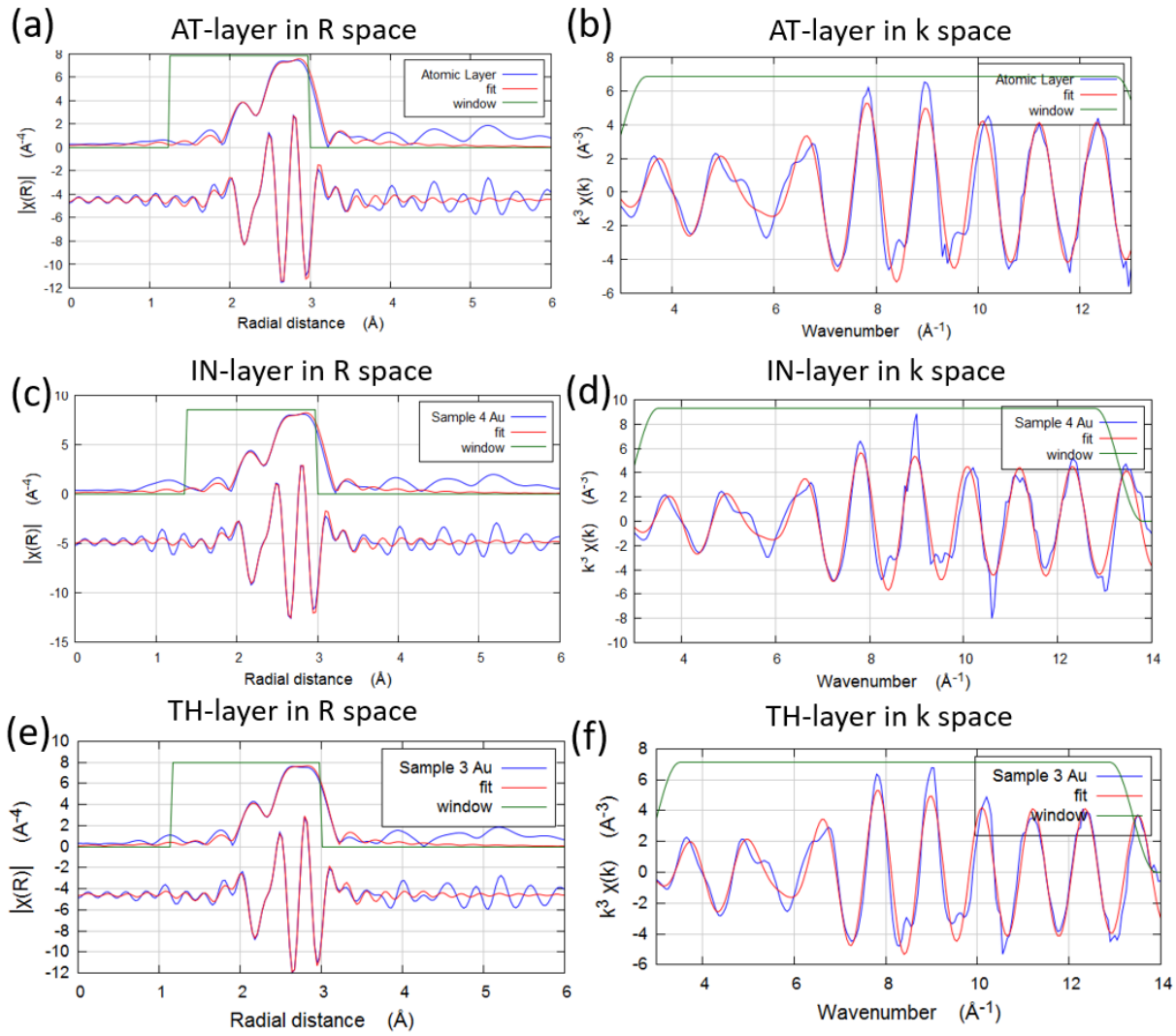


Figure 5.20 a)-b) Least square fitting for the k3-weighted EXAFS spectra (Au L_3 edge) for (a) R-space, (b) k-space for the AT-layer Au-Ag core-shell NPs, k-range: 3-13.2; R-range: 1.25-3; R-factor: 0.6%; **c)-d)** Least square fitting for the k3-weighted EXAFS spectra (Au L_3 edge) for (c) R-space, (d) k-space for the IN-layer Au-Ag core-shell NPs, k-range: 3-13.3; R-range: 1.35-3; R-factor: 0.5%; **e)-f)** Least square fitting for the k3-weighted EXAFS spectra (Au L_3 edge) for (e) R-space, (f) k-space for the TH-layer Au-Ag core-shell NPs, k-range: 3-13.4; R-range: 1.15-3; R-factor: 0.5%.

Table 5.3 Least square fitting of the Ag K edge EXAFS spectra for the core-shell NPs.

Ag K edge	Scattering Path	Bond length [Å]	Coordination number (CN)	Debye-Waller factor
AT-layer	Ag-Ag	2.88 (2)	2.1 (3)	0.005
	Ag-Au	2.89 (2)	5.7 (4)	0.005
IN-layer	Ag-Ag	2.86 (1)	11.1 (5)	0.010
	Ag-Au	2.89 (3)	1.8 (7)	0.010
TH-layer	Ag-Ag	2.87 (1)	11.4 (4)	0.009
	Ag-Au	2.90 (3)	1.1 (4)	0.003

Table 5.4 Least square fitting of the Au L_3 edge EXAFS spectra for the core-shell NPs.

Au L_3 edge	Scattering Path	Bond length [Å]	Coordination number (CN)	Debye-Waller factor
AT-layer	Au-Au	2.87 (1)	10.0 (4)	0.008
	Au-Ag	2.92 (1)	1.2 (5)	0.014
IN-layer	Au-Au	2.87 (1)	10.6 (4)	0.008
	Au-Ag	2.89 (4)	0.9 (4)	0.011
TH-layer	Au-Au	2.86 (1)	10.7 (7)	0.008
	Au-Ag	2.87 (1)	0.5 (6)	0.009

Least square fitting, with amplitude reduction factor obtained from Au (Figure 5.17 and Table 5.1) and Ag (Figure 5.18 and Table 5.2), further reveals the major contribution of the signal for the IN-layer and TH-layer sample comes from the Ag-Ag scattering path (CN~11 with Ag-Au of 1CN), which is in stark contrast to the AT-layer sample that has only 2-coordination of Ag-

Ag but ~6-coordination of Ag-Au in the NP (Figure 5.19 and Table 5.3). Given the similar size of the gold core and hence a similar surface area of Ag-Au interface, the results imply that some of the silver-gold interaction must originate from the shell of mixed atoms. This is in good agreement with the APT results that show a significant composition of mixed Ag-Au atoms in the AT-layer sample. Regarding the Au L_3 edge absorption (Figure 5.20 and Table 5.4), it also shows a descending order of Au-Ag coordination as the shell thickness increases. It is worthwhile to note the Au-Ag interaction in the AT-layer is comparatively smaller than that of the Ag K-edge since the majority of the signal is dominated by the gold core in this analysis.

5.5 Surface Plasmon Analysis

It is reported that the electromagnetic confinement enhancement in LSPR is particularly strong at the surface/edge of the composite nanoparticle[19–21], which is usually termed as "hot spots", where photocatalysis would be promoted effectively. It is expected that hot spots will generate the localized energetic electrons (hot electrons) efficiently and thus higher rates of direct plasmonic photocatalysis.[5,22,23] Scanning transmission electron microscope-electron energy loss spectroscopy (STEM-EELS) appears to be a sophisticated technique to characterise the LSPR-induced surface plasmons (hot electrons) in sub-angstrom spatial resolution given its capability to excite the full set of LSPR modes.[24,25] In order to visualize the electromagnetic eigenmodes of the surface plasmons in the core-shell NPs directly, low-loss EELS (below 50 eV) with a probe-corrected TEM at 200 keV was employed in this chapter.[24,25]

The line-scan EELS combined with HAADF-STEM imaging (high angle annular dark field scanning transmission electron microscope) can greatly reveal the spatial variations to sub-nanometre spatial accuracy of the LSPR-induced electromagnetic field, which was caused by the different chemical composition of the composite core-shell NPs. In this chapter, the HAADF-STEM images were taken across an individual NP of the five as-prepared samples

and the corresponding EELS spectra were collected across 10 different positions on the NP. The starting position begins at the peripheral space of the NP, moving on to the edge of the shell and across to the gold core, and finally back to the shell at the opposite end and eventually back to the periphery. On another note, following each acquisition recorded, it was ensured that no visible beam damage or carbon contamination were observed in the HAADF image.

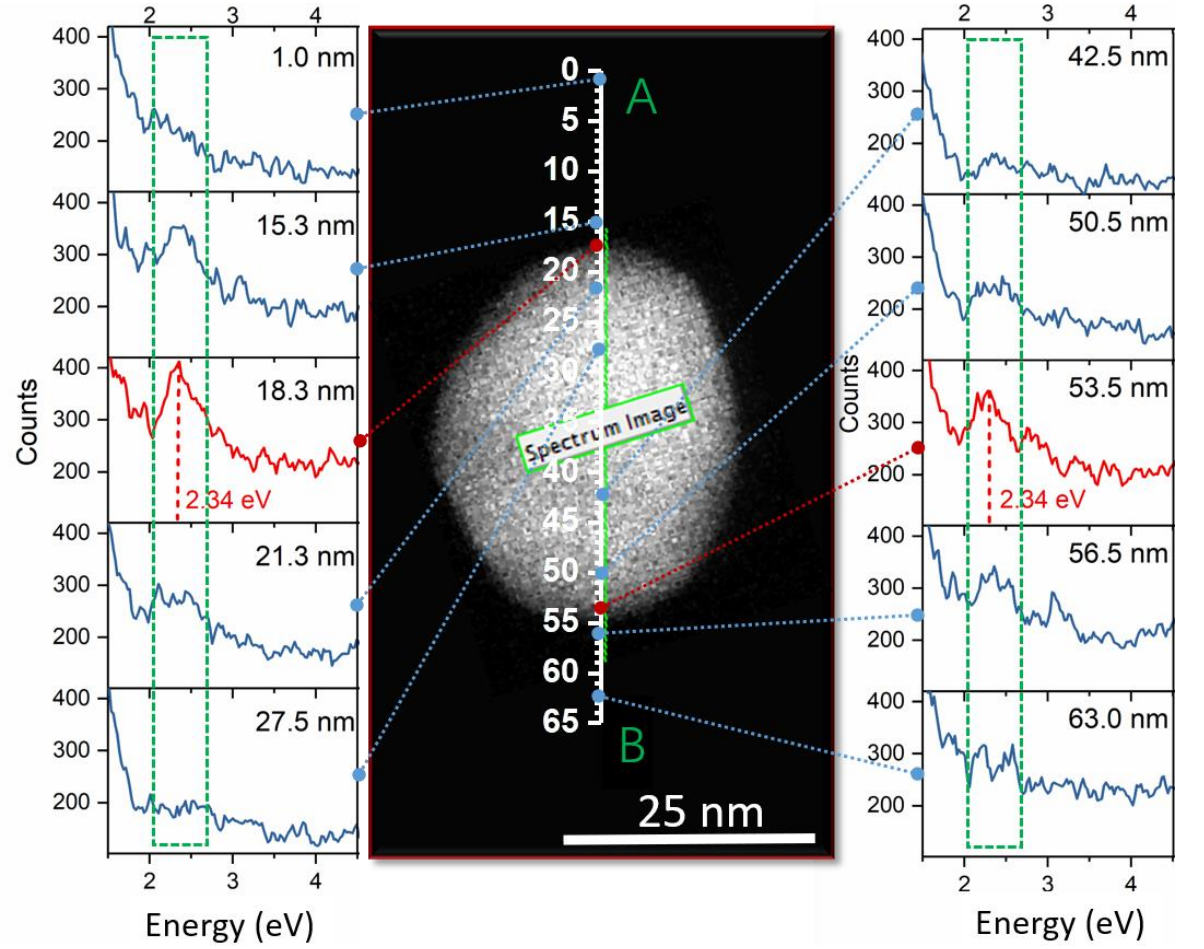


Figure 5.21 A series of 10 successive low-loss STEM–EEL spectra acquired of a single AT-layer Au-Ag core-shell NP in the spectrum-image mode, along an axis (A to B) of the nanosphere as illustrated in the inset. The position of the main resonance detected along the line scan are marked by dotted lines.

In Figure 5.21, it shows a series of 10 successive low-loss STEM-EELS spectra of an as-prepared AT-layer Au-Ag core-shell NP. Pronounced changes were observed along the carefully pre-calibrated electron beam probe positions. As the beam position approaches the AT-layer NP, the normalized intensity of the plasmonic EELS peak starts to grow gradually in the vicinity of the shell then reaches the maxima once it is positioned at the edge of the core-

shell NP, depicting the radiative field strength from the particle surface. Within the tolerances of zero-loss peak (ZLP) broad tails, uneven thickness of shell and low carbon contamination from the microscopic chamber, the maximum intensity plasmonic EELS peak is positioned at 2.34 eV, which is corresponding to the major absorption peak in its UV-Vis spectrum at 530 nm as shown in Figure 5.13 (based on the Planck-Einstein equation[26]). In fact, a double hump pattern is observed that is attributed to the variation of peak intensity as it moves across the particle (diminishes at the core but increases again giving a plasmon energy at 2.34 eV at the opposite edge of the particle). This agrees with the fact that a plasmon manifests itself as a collective dynamic oscillation of charges accumulated mainly at the surfaces.[27]

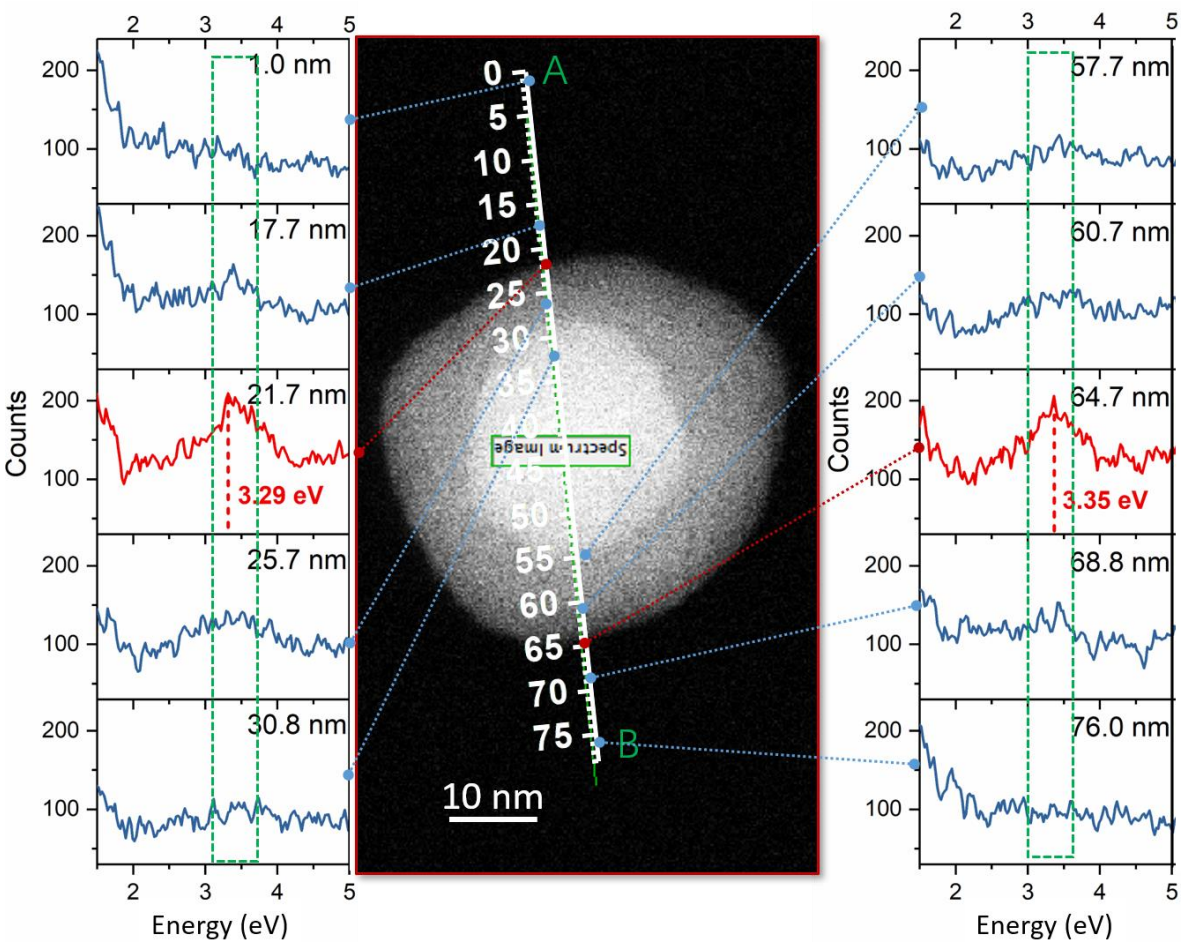


Figure 5.22 A series of 10 successive low-loss STEM–EEL spectra acquired of a single TH-layer Au-Ag core-shell NP in the spectrum-image mode, along an axis (A to B) of the nanosphere as illustrated in the inset. The position of the main resonance detected along the line scan are marked by dotted lines.

In Figure 5.22, an individual TH-layer core-shell NP was also analysed by the line-scan EELS for comparison. For the TH-layer core-shell NP, the maximum plasmon energy peak positions at 3.29 eV at the edge of the Ag shell and then greatly diminishes at the Au core and grows again to a maximum at 3.35 eV at the opposite side of the Ag shell edge. The plasmon energy peak positions are similar to the major absorption peaks of the TH-layer NP in UV-Visible spectra (~386 nm) in Figure 5.13. The discrepancy of the plasmon energy peak positions (3.29 eV and 3.35 eV) may be caused by the uneven shell thickness and different chemical compositions of the Ag/Au integrated shell at different locations of the shell.

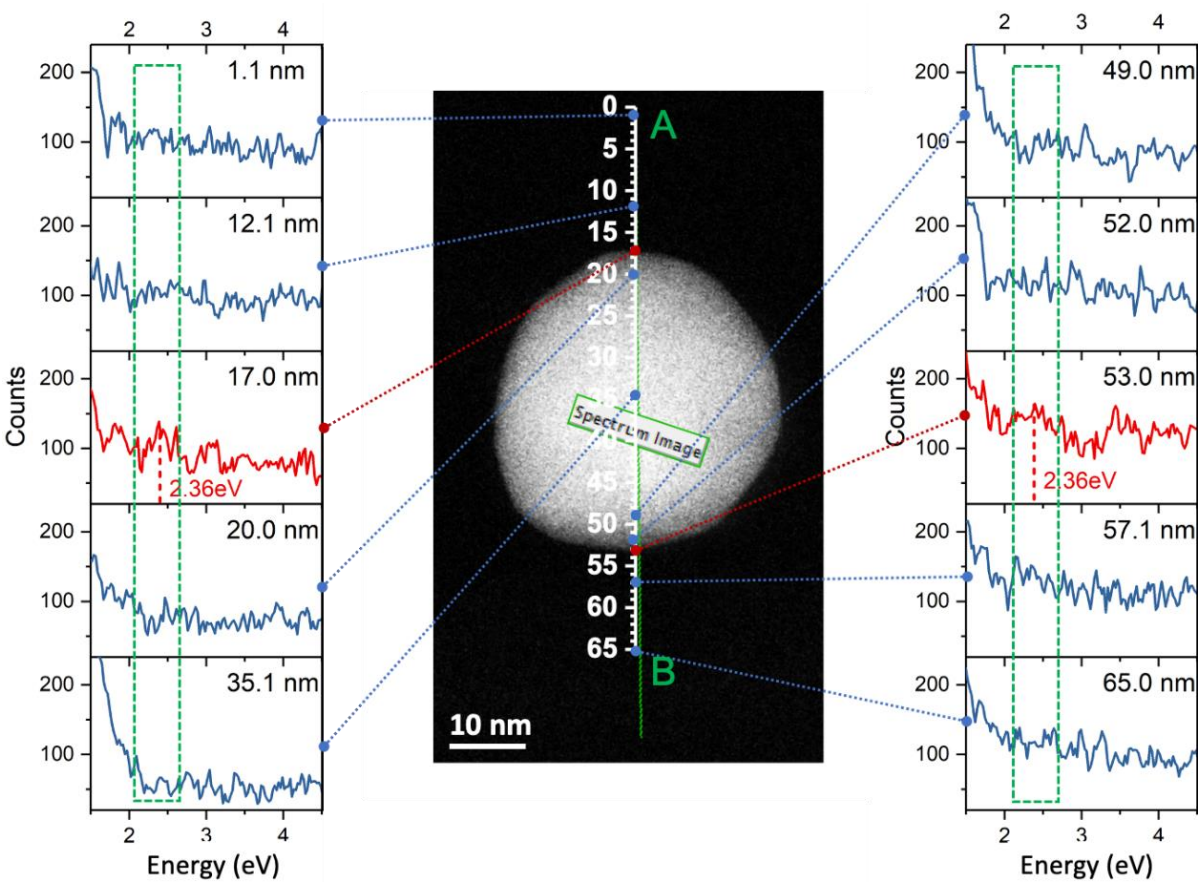


Figure 5.23 A series of 10 successive low-loss STEM–EEL spectra acquired of a single pure Au NP in the spectrum-image mode, along an axis (A to B) of the nanosphere as illustrated in the inset. The position of the main resonance detected along the line scan are marked by dotted lines.

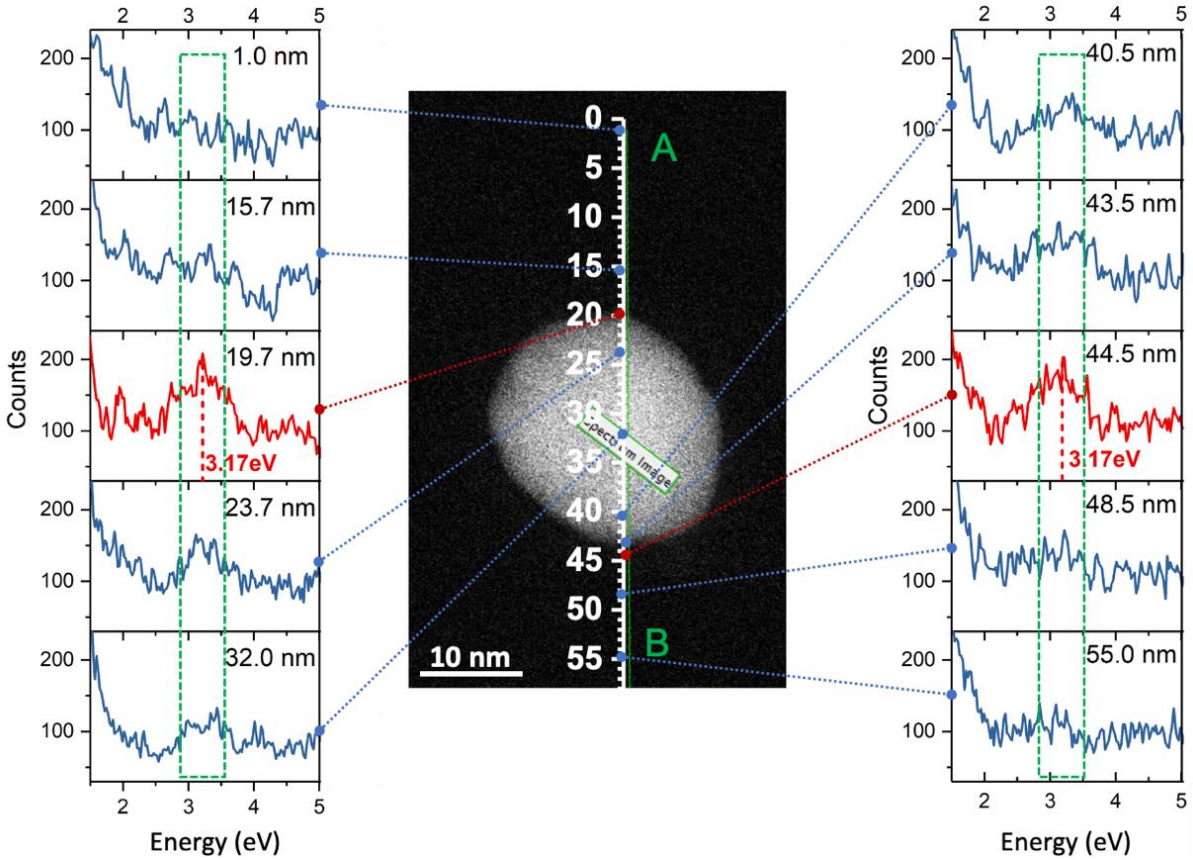


Figure 5.24 A series of 10 successive low-loss STEM–EEL spectra acquired of a single pure Ag NP in the spectrum-image mode, along an axis (A to B) of the nanosphere as illustrated in the inset. The position of the main resonance detected along the line scan are marked by dotted lines.

As shown in Figure 5.23 and Figure 5.24, the STEM-EELS was employed to analyse the plasmon energy of a single pure Au and pure Ag NP respectively. The plasmon energy peaks reach maximum intensity when the beam position is at the edge of the pure Ag and pure Au NP and then reduce at the middle of the nanosphere NP. The plasmon energy peaks are determined to be at 2.36 eV for pure Au and 3.17 eV for pure Ag.

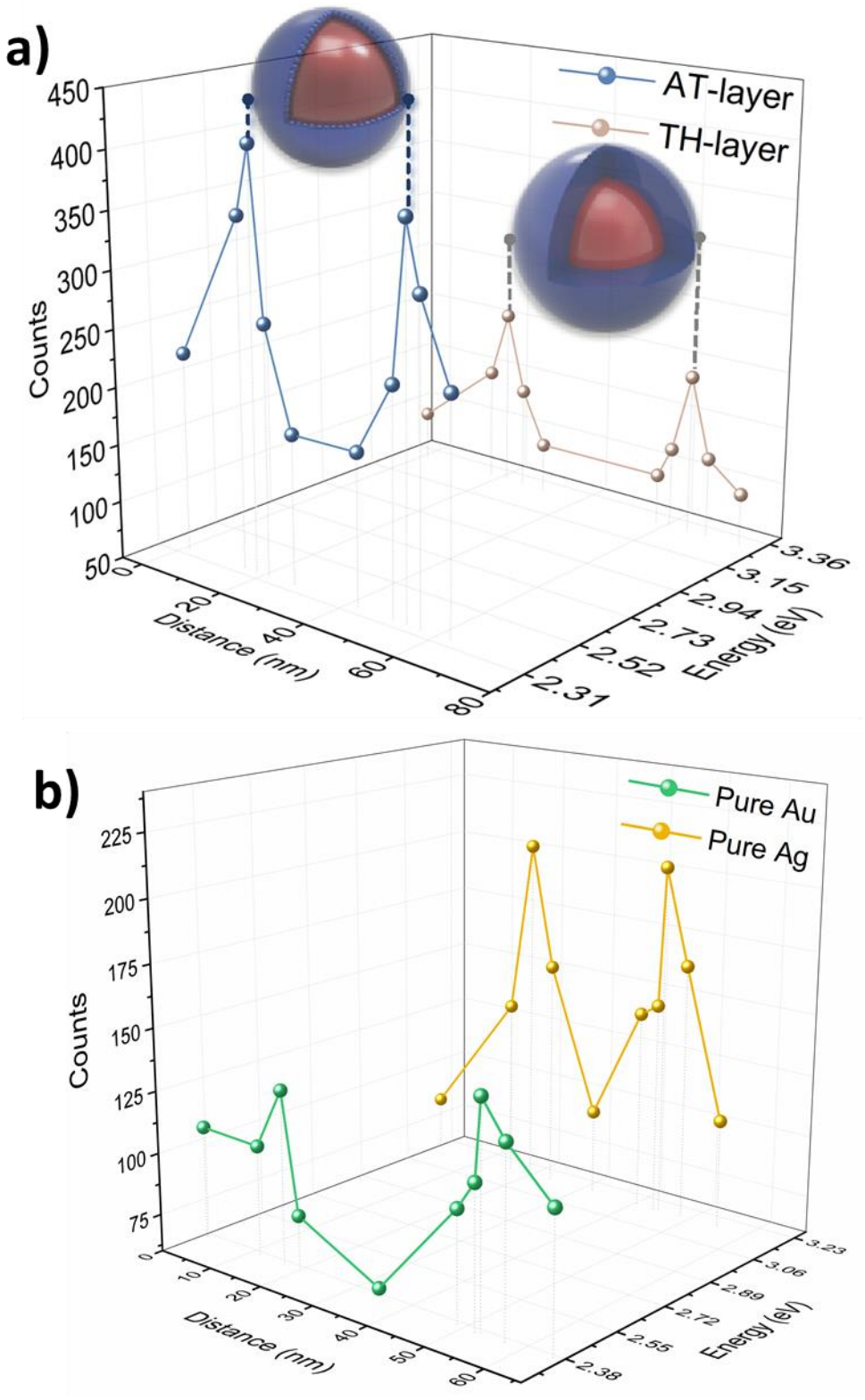


Figure 5.25 a) Comparison of the plasmonic energy intensity between AT-layer and TH-layer core-shell NPs as a function of the electron probe position (intensity map) at 2.34 eV and 3.29 eV, respectively; **b)** Comparison of the plasmonic energy intensity between pure Au and pure Ag NPs as a function of the electron probe position (intensity map) at 2.36 eV and 3.17 eV, respectively.

According to Figure 5.25 a and b, all the four samples show double hump patterns with maximum plasmon energy peaks appearing at the edge of the NPs. It is worthwhile to mention that the normalized maximum energy peak intensities at the edge of these samples are greatly different. In fact, the plasmon energy intensity is significantly higher for the AT-layer NP (arbitrary unit of 410) when compared with the TH-layer NP with an intensity of 206 arbitrary unit as shown in Figure 5.25a. At the same time, the pure Ag shows an intensity of 203 arbitrary unit at 3.17 eV while the intensity of pure Au is determined to be 130 at 2.36 eV at the edge of the nanosphere, which are both greatly lower than that of the AT-layer sample. It again confirms that the electromagnetic enhancement is particularly strong at the surface of the plasmonic nanoparticles, and "hot spots" are formed for non-thermal hot electron (HE) generations. And the significant difference of plasmon energy intensities of these samples at the "hot spots" clearly indicates that electromagnetic enhancement depends critically on the chemical compositions of the sole or composite nanoparticles. The tailored Ag and Au integrated shell in AT-layer core-shell NP that gives the highest plasmon energy peak intensity is presumably generating the most non-thermal HEs.

5.6 Direct Electrochemical-Localized Surface Plasmon Resonance (EC-LSPR)

5.6.1 Experimental Methods

5.6.1.1 Three-electrode Systems

For details on the experimental methods, see chapter 3, section 3.2.2.2.

In summary, a three-electrode system was used to evaluate the electrocatalytic HER activities of the Au-Ag core-shell NPs in 0.5 M Na_2SO_4 electrolyte (pH 6.5) without any addition of sacrificial reagents under visible light illuminations (Figure 3.3). The current density is obtained from dividing the current by the geometric area of the FTO glass electrode (1 cm^2). All the catalyst ink were sprayed casted on the precleaned fluorine-doped tin oxide (FTO) glass and evaluated at a bias potential of -0.3 V, -0.5 V, -0.8 V and -1.2 V versus Ag/AgCl (sat. KCl)

reference electrode with a time interval of 200 s for stabilization. The Pt wire is working as a counter electrode in the system. A UV-cut Tungsten light ($\lambda > 420$ nm) and an Oriel® solar simulator (1 sun, AM 1.5G, 100 mW cm^{-2}) were used as light sources to irradiate the catalyst-coated FTO working electrode for direct plasmonic electrochemical analysis. The amount of hydrogen evolved was measured by gas chromatography (GC) equipped with thermoconductivity detectors (TCD) with N_2 as carrier gas.

5.6.1.2 Linear Sweep Voltammetry (LSV)

For details on the experimental methods, see chapter 3, section 3.2.2.3.

A solution of 0.5 M Na_2SO_4 (pH 6.5) was used as electrolyte without any addition of sacrificial reagents, which was purged continuously in flowing N_2 to remove O_2 prior to the start of reaction. The AT-layer core-shell NPs were used as the cathode catalysts (working electrode) with a metal loading of 1.2 mg/cm^2. The scan rate was 1mV/s. A UV-cut Tungsten light ($\lambda >$ 420 nm) was used as the light source and set up at a fixed distance of 5 cm from the working electrode.

5.6.1.3 Apparent Quantum Efficiency (AQE)

In chapter 5, the apparent quantum efficiency (AQE) was measured in the same conditions as those of a typical EC-LSPR measurement mentioned above, where a solar simulator (1 sun, AM 1.5G, 100 mW cm^{-2}) was used to irradiate the working electrode at three different wavelength ranges of 400-500 nm, 500-600 nm and 600-700 nm. The numbers of photons were calculated from the irradiation powers in each wavelength region measured by a light metre at the corresponding wavelengths. The AQE can be calculated by the following equation 5.1:

$$AQE(\%) = \frac{Number\ of\ evolved\ hydrogen\ molecules\ \times 2}{Number\ of\ incident\ photons} \times 100\% \quad (Equation\ 5.1)$$

A typical calculation of AQE is shown below at a wavelength range of 500-600 nm as an example:

Under an applied potential of -0.5V vs Ag/AgCl, the AT-layer catalyst gives photocurrent in which the amount of hydrogen generated is 0.36 μmol/h, (equivalent to 2.168×10^{17} hydrogen molecules per hour).

For every 1 hour of reaction,

the energy of light irradiation: $W=P \times t$

Within the wavelength range of 500-600 nm, the light irradiation power is measured to be

$P = 1.1$ mW

Therefore the energy $W = 0.00110 \times 3600 = 3.96$ J, which contains the photon (550 nm) number of 1.096×10^{19}.

AQE (%) = $(2 \times 2.168 \times 10^{17})/(1.096 \times 10^{19}) = 4.0\%$

5.6.2 Direct Plasmonic Chronoamperometry

In order to evaluate the efficiencies of the direct electrochemical LSPR, chronoamperometry was employed on the five as-prepared samples at different applied potentials (-0.3 V, -0.5 V, -0.8 V and -1.2 V versus Ag/AgCl) under illuminations of UV-cut Tungsten light to mimic the solar spectrum.[27,28]

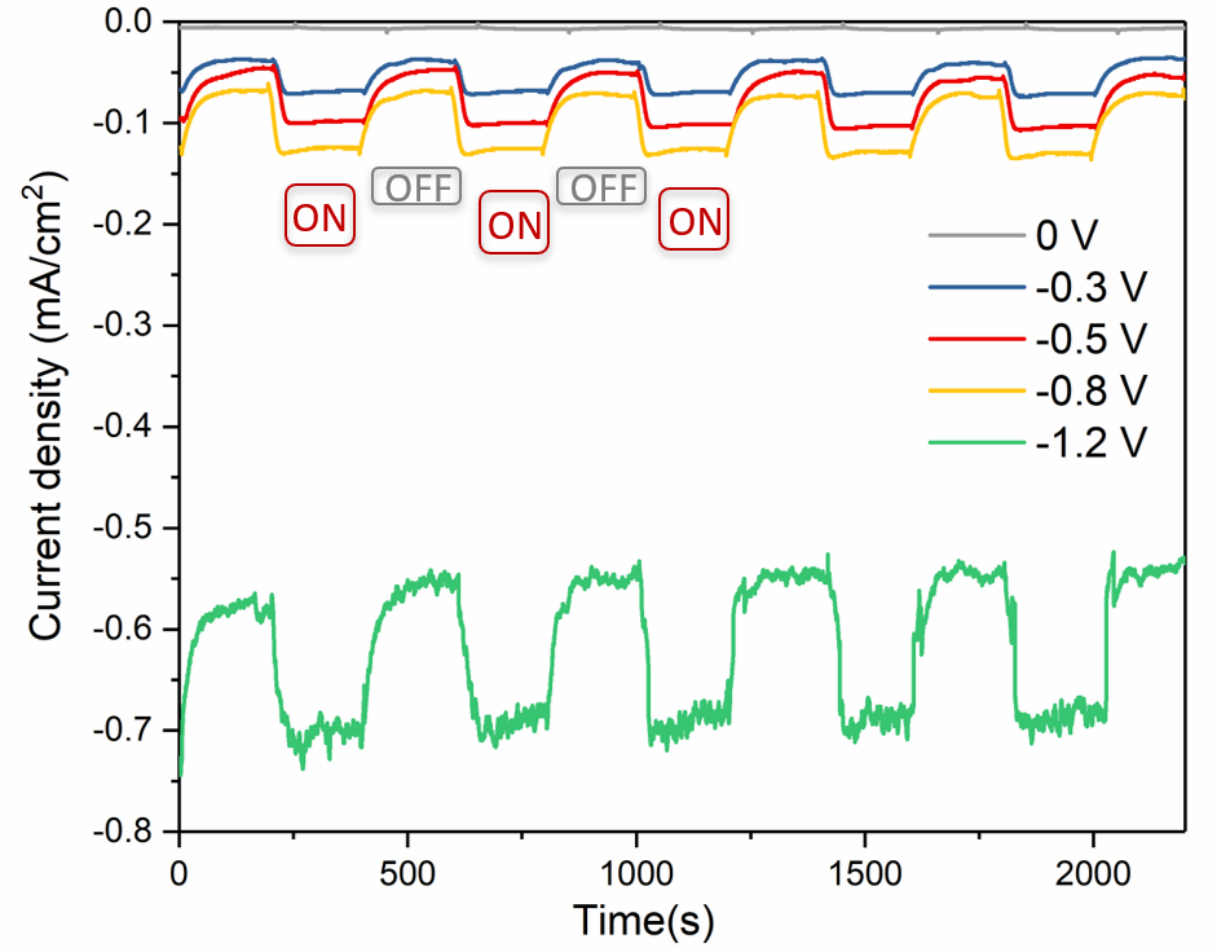


Figure 5.26 Current density as a function of reaction time of the 20 wt% AT-layer Au-Ag/C at 0 V, -0.3 V, -0.5 V, -0.8 V and -1.2 V versus Ag/AgCl (sat. KCl) under UV-cut ($\lambda > 420$ nm) tungsten light in 0.5 M Na_2SO_4. The Pt wire is used as the counter electrode; and the working electrode is obtained by spray-casting the electrocatalysts onto the FTO glass.

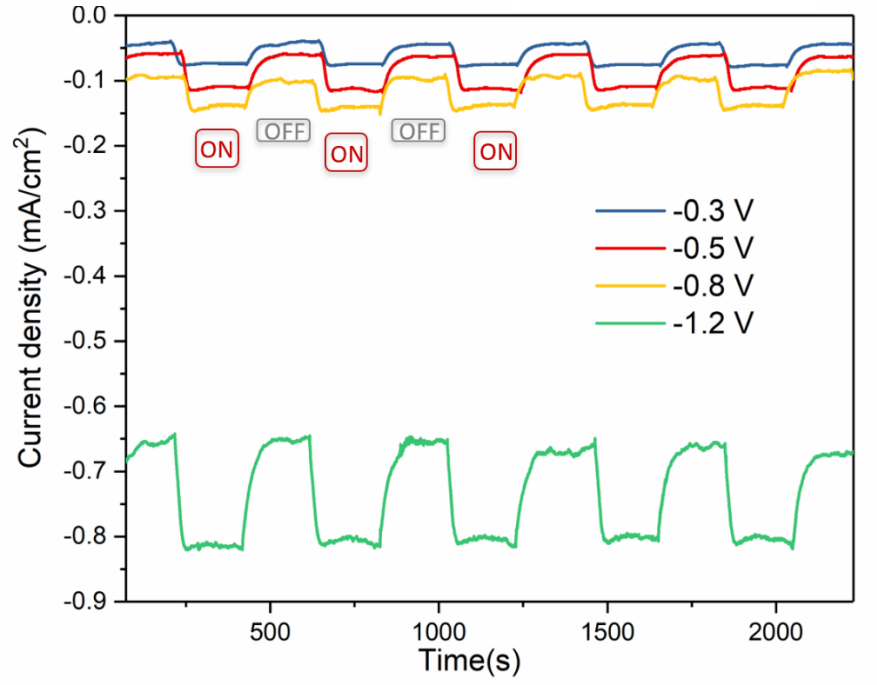


Figure 5.27 Current density as a function of reaction time of the 20 wt% IN-layer Au-Ag/C at -0.3 V, -0.5 V, -0.8 V and -1.2 V versus Ag/AgCl (sat. KCl) under UV-cut (λ > 420 nm) tungsten light in 0.5 M Na_2SO_4. The Pt wire is used as the counter electrode; and the working electrode is obtained by spray-casting the electrocatalysts onto the FTO glass.

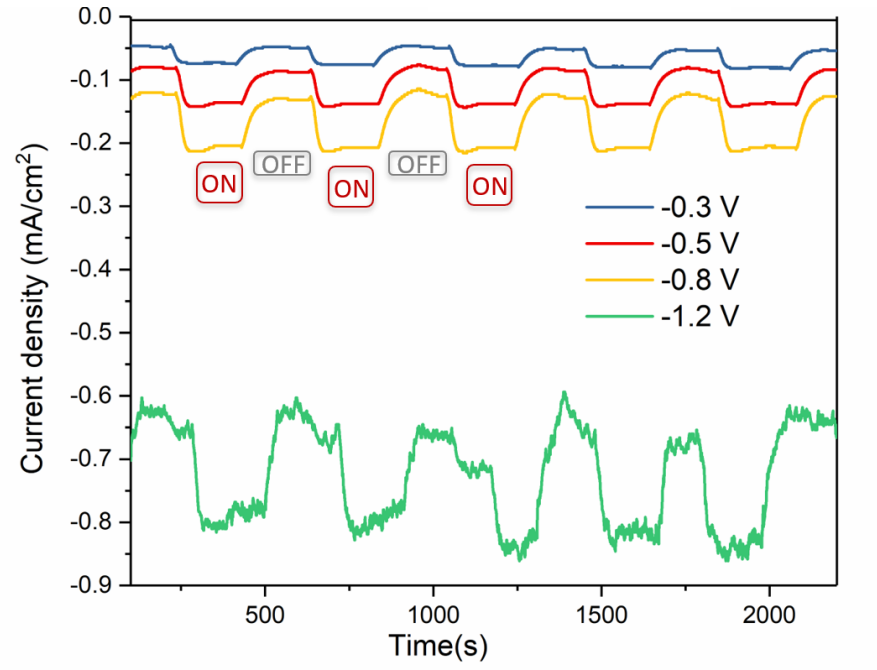


Figure 5.28 Current density as a function of reaction time of the 20 wt% TH-layer Au-Ag/C at -0.3 V, -0.5 V, -0.8 V and -1.2 V versus Ag/AgCl (sat. KCl) under UV-cut (λ > 420 nm) tungsten light in 0.5 M Na_2SO_4. The Pt wire is used as the counter electrode; and the working electrode is obtained by spray-casting the electrocatalysts onto the FTO glass.

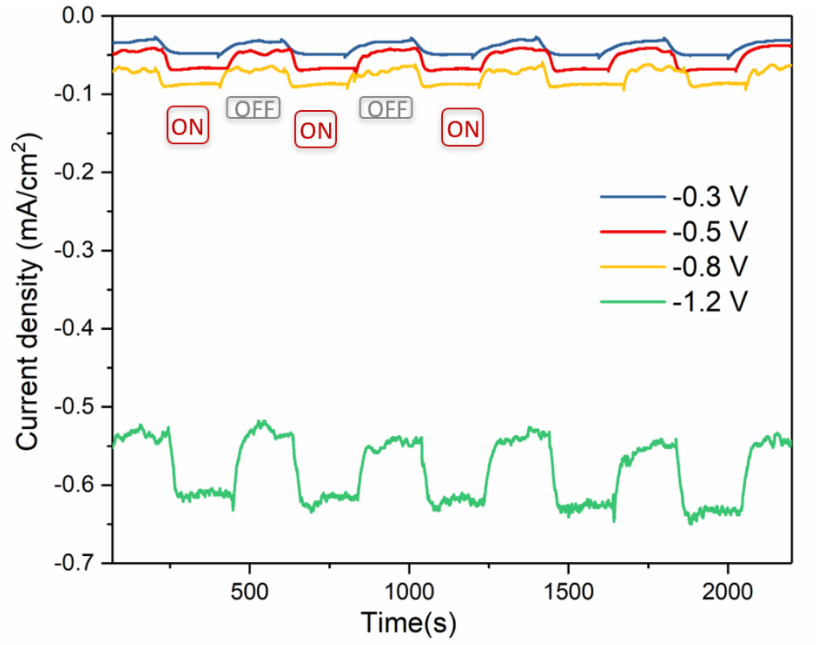


Figure 5.29 Current density as a function of reaction time of the 20 wt% Au/C at -0.3 V, -0.5 V, -0.8 V and -1.2 V versus Ag/AgCl (sat. KCl) under UV-cut ($\lambda > 420$ nm) tungsten light in 0.5 M Na_2SO_4. The Pt wire is used as the counter electrode; and the working electrode is obtained by spray-casting the electrocatalysts onto the FTO glass.

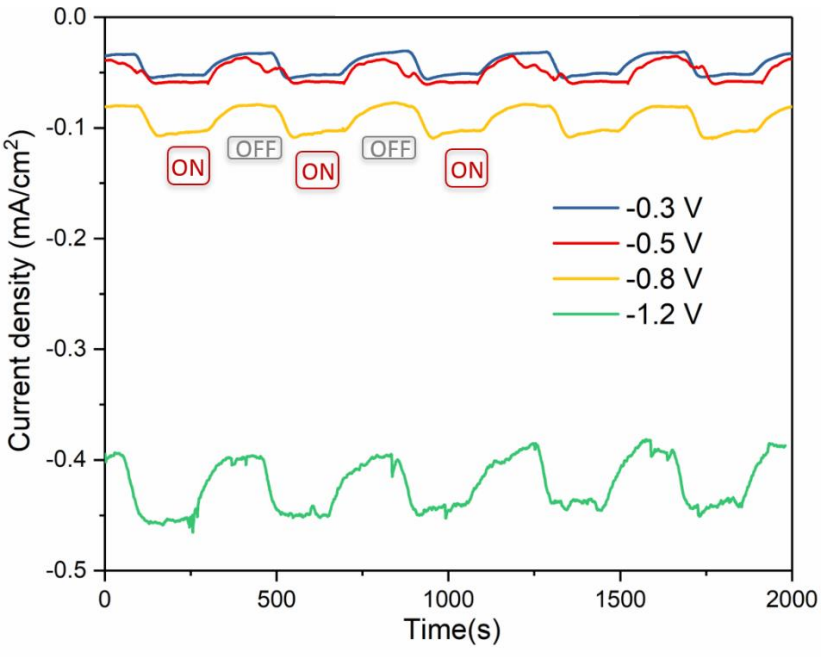


Figure 5.30 Current density as a function of reaction time of the 20 wt% Ag/C at -0.3 V, -0.5 V, -0.8 V and -1.2 V versus Ag/AgCl (sat. KCl) under UV-cut ($\lambda > 420$ nm) tungsten light in 0.5 M Na_2SO_4. The Pt wire is used as the counter electrode; and the working electrode is obtained by spray-casting the electrocatalysts onto the FTO glass.

In Figure 5.26 - 5.30, it shows the variations in hydrogen production rate in the form of current density of the AT-layer, IN-layer, TH-layer, pure Au and pure Ag samples at different applied potentials under visible light illumination ($\lambda > 420$nm) with 200-second on/off repeating cycles. Notably, there is a significant enhancement in cathodic current density under visible light illumination on the catalyst surface at all applied potentials of the samples when compared with the light off conditions. This enhancement in cathodic photocurrent is caused by LSPR generated hot-electrons that have been transferred to the electron acceptors (H^+) in the system under visible light illuminations.[29]

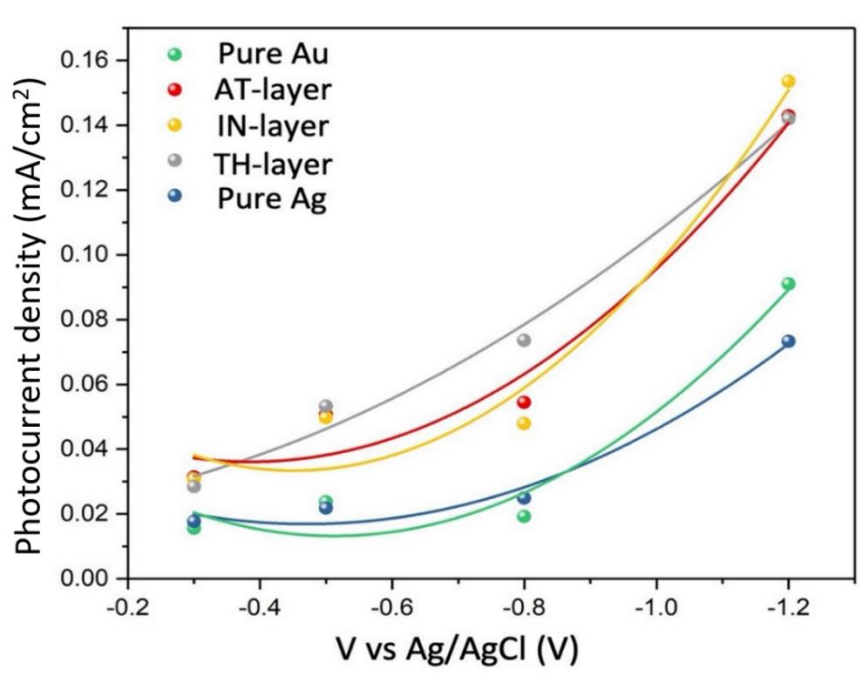


Figure 5.31 Photocurrent densities (current densities at light on minus current densities at light off) as a function of applied negative bias potentials of 20 wt% Au/C, 20 wt% Ag/C, 20 wt% AT-layer Au-Ag/C, 20 wt% IN-layer Au-Ag/C and 20 wt% TH-layer Au-Ag/C at -0.3 V, -0.5 V, -0.8 V and -1.2 V versus Ag/AgCl respectively under UV-cut ($\lambda > 420$ nm) Tungsten light illuminations in 0.5M Na_2SO_4.

According to the current density analysis of all the five samples in Figure 5.31, a larger photocurrent is obtained when a higher degree of polarization is applied at more negative bias potentials under visible light illuminations. It implies that the LSPR generated HEs for proton reduction can be proportionally promoted in negative bias potential, suggesting this charge

separation process is fundamentally favoured. Recently, researchers have put tremendous efforts in the generation of plasmoelectric potential by plasmonic absorption to offer thermodynamic driving force in order to alter the chemical potential of metallic particle.[30] The phenomenon described above looks like the reverse effect—the use of electric potential to increase plasmonic absorption of the metallic particle.

Notably, the mixed Ag/Au atoms in core-shell samples outperform their pure Au and Ag NPs counterparts as the LSPR generated HEs depend on the sample chemical compositions as suggested in section 5.5 above. However, TH-layer shows higher current values than expected that might stem from additional pure Ag NPs as a result of excessive addition of Ag precursors during the synthesis of the core-shell particles (refer to Figure 5.6). Thus, the light excitation is enhanced following the increase in the total number of NPs.

Under light illumination, a gradual increase in photocurrent density can be observed for the core-shell and pure Ag and Au NPs in contrast to the sharp rise as shown in semiconductors. It can be ascribed to the Gouy-Chapman double charged layer around the catalyst surface in aqueous solution as illustrated in Figure 5.32. Particularly, the Gouy-Chapman model can be used to account for a higher concentration of the counter-ions near the catalyst surface compared with the bulk solution. By assuming that the ions are point charges (as such finite ion size is ignored),[31] the electric potential decreases exponentially as the distance from the surface increases, agreeing well with the diffuse model of the electrical double layer.[32,33]

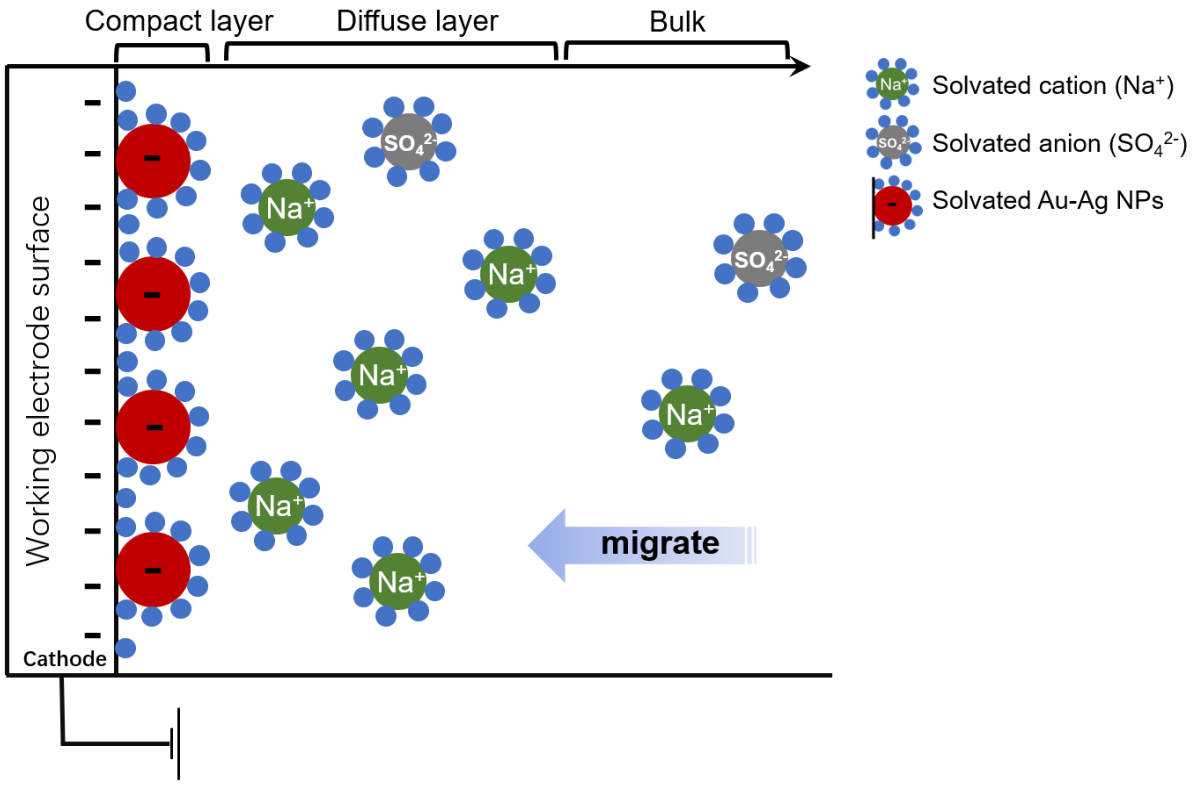


Figure 5.32 Schematic representations of electric double layer structures according to the Gouy–Chapman electrical double layer model.

Based on the electrical double layer model, the working electrode (cathode) in the system is negatively charged implying that the catalysts spray-casted onto the working electrode surface are also negatively charged. The concentration of solvated cation (Na^+) decreases exponentially as the distance increases from the cathode surface.

As visible light illuminates on the catalyst surface of the working electrode, the equilibrium between the metal surface charge and the concentration of the solvated cation around the catalyst surface in diffuse layer is disrupted, which stems from the rapid promotion of photocatalytic hydrogen evolution reaction driven by the LSPR-generated HEs. Hence, a buffer period is required for cations in the outer layer to diffuse through and migrate towards the working electrode surface until a new equilibrium is reached. Therefore, the time-delay in attaining the equilibrium results in a gradual increase in the photocurrent as observed.

In order to analyse the photocurrent directly, the current density enhancement of pure Au, pure Ag, AT-layer, IN-layer and TH-layer Au-Ag core-shell NPs at different applied potentials under light on/ff cycles are summarized in Table 5.5 for further comparison.

Table 5.5 The EC-LSPR current density enhancement of pure Au, pure Ag, AT-layer Au-Ag, IN-layer Au-Ag and TH-layer Au-Ag supported on Vulcan carbon (/C) at applied potentials of -0.3 V, -0.5 V, -0.8 V and -1.2 V, respectively under visible light illuminations ($\lambda > 420$ nm) compared with dark conditions.

Applied potentials	Au/C	AT-layer Au-Ag/C	IN-layer Au-Ag/C	TH-layer Au-Ag/C	Ag/C
-0.3 V	50.8%	82.1%	70.4%	59.8%	53.4%
-0.5 V	54.7%	112.5%	79.3%	62.7%	57.5%
-0.8 V	28.3%	76.8%	54.3%	53.2%	31.3%
-1.2 V	17.0%	26.1%	23.5%	21.3%	19.2%

It is worthwhile to mention that the AT-layer Ag-Au NPs show the highest current density enhancement across the whole applied potential range from -0.3 V to -1.2 V as shown in Table 5.5. The AT-layer core-shell NP gives an impressive hydrogen production rate of 1870 μmol $g^{-1}h^{-1}$ at -0.5 V under visible light illumination, which matches well with the surface plasmon analysis (section 5.5) that the AT-layer shows highest plasmon energy intensity. This can be explained by the superior Ag-Au atomic surface that gives the most LSPR-generated HEs for photocatalytic hydrogen evolution reaction. Simultaneously, the other four samples follow the trend of the plasmon energy intensity in surface plasmon analysis that the intensity increases with HEs generation under visible light illumination, giving a corresponding current density enhancement trend of AT-layer > TH-layer > pure Ag > pure Au.

A volcano relationship of the current density enhancement can be observed of the four samples with a maximum enhancement peak at -0.5 V. Compared to dark conditions, the current density enhancement is attributed to the LSPR-generated HEs under visible light illumination increases to the maximum at -0.5 V and then decreases on both sides of this negative bias potential. This volcano relationship can be observed for all the four samples as shown in Table 5.5, which can be explained briefly by the light energy capture variations of different applied potentials as illustrated in energy diagram Figure 5.33.

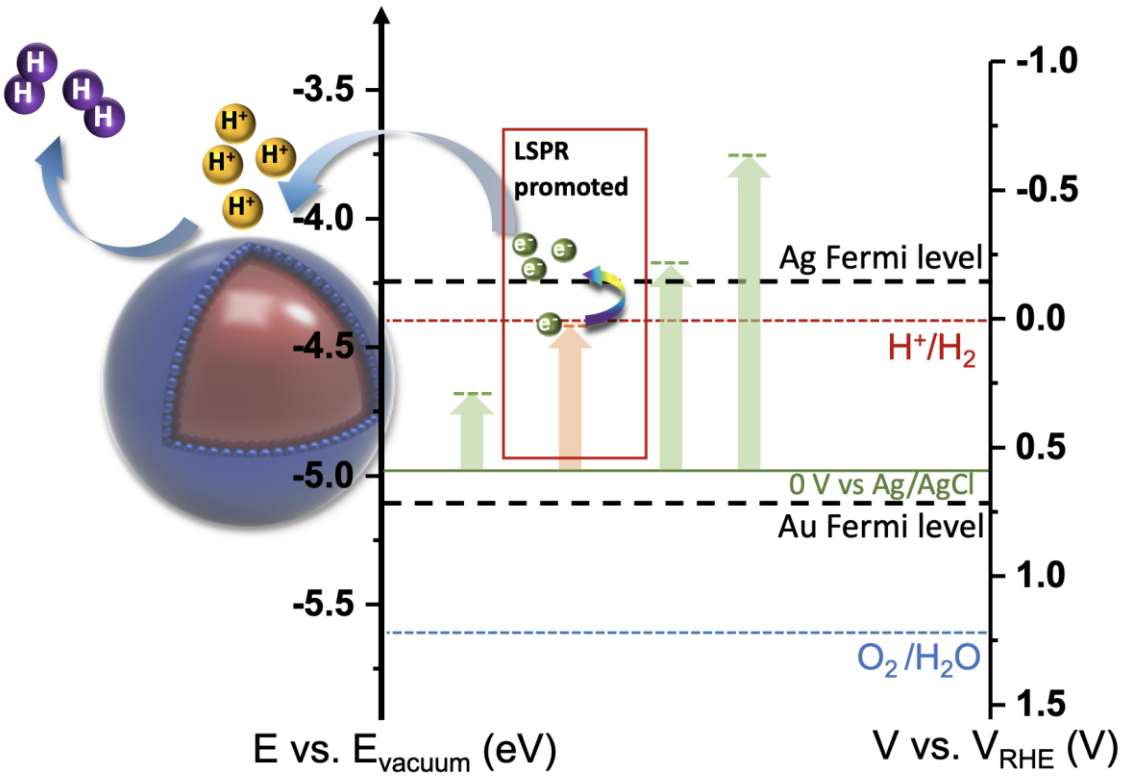


Figure 5.33 Schematic illustration of energy diagram and hot electrons transfer mechanism using LSPR excitation on AT-layer Au-Ag core-shell NPs, green bars from left to right represent: -0.3 V, -0.8 V and -1.2 V versus Ag/AgCl while the red bar is -0.5 V versus Ag/AgCl.

Taking AT-layer core-shell NPs as an example, in Figure 5.33, it showcases the envisaged energy diagram of overall water splitting process referencing to standard reduction potential of proton to hydrogen and fermi level of Ag and Au, which are the major chemical composition of the as-prepared samples. Holmberg et. al. have examined the equilibrium Fermi level of

bimetallic model system composed of mixed Au-Ag NPs in different surface coverage of metals, it shows a Fermi level of -5.11 eV for pure Au NP and -4.25 eV for pure Ag NP versus vacuum level in the model.[34] Noting that the exact Fermi level of core-shell NPs in our case are not yet known, the pure Au and pure Ag values are only arbitrarily expressed. The Fermi levels in electron volts (eV) of Ag and Au can be converted into electrochemical energy potentials in volts (V) with reference to the reversible hydrogen electrode (RHE), which can be calculated as 0 V versus RHE (equivalent to -4.44 eV versus vacuum level.[35–37])

As illustrated in Figure 5.33, it shows sufficient energy for hydrogen evolution reaction to take place thermodynamically at the bias potentials of -0.8 V and -1.2 V without light irradiation, at which the energy levels are above the energy threshold of the proton reduction process in water electrolysis. However, in the case of -0.3 V and -0.5 V, the electrical energy itself cannot provide enough driving force for HER to happen. Under visible light illumination, the electrons are effectively promoted by LSPR that can greatly raise the energy to a higher level that overcome the energy barrier for proton reduction on top of the applied electrical energy. According to the energy diagram, the volcano relationships as mentioned can be attributed to the observation that the light energy capture contributes to a lower extent to the proton reduction current either at too low negative bias potential (insufficient promotion energy) or at too high over-potential that starts electrolysis.

From energy perspective, the optimum practice of this integrated process depends on cost and energy sources for efficient light capture. As a result, the LSPR of Au enables effective light energy capture at 530 nm where the oscillated electrons in the present of Ag and Au mixed atoms on the AT-layer core-shell surface can be promoted to HEs for proton reduction. The presence of the surface Ag atoms in Au atom matrix on NP surface greatly facilitates the energy transfer for electron excitation which is consistent with the fact that the higher energy (more positive) and greater mobility of electrons are associated with Ag (Au gives higher ionization

energy with higher effective nuclear charge than Ag because of lanthanide contraction and relativistic effect of 6 s electrons).

The tailored AT-layer core-shell NPs of 20% Ag-80% Au offer an impressive 112.5 % current enhancement in the presence of visible light during electrolysis, giving a hydrogen production rate of 1870 μmol $g^{-1}h^{-1}$ at room temperature, which is 62.5% higher than the commercially used Pt catalyst at -0.5V.

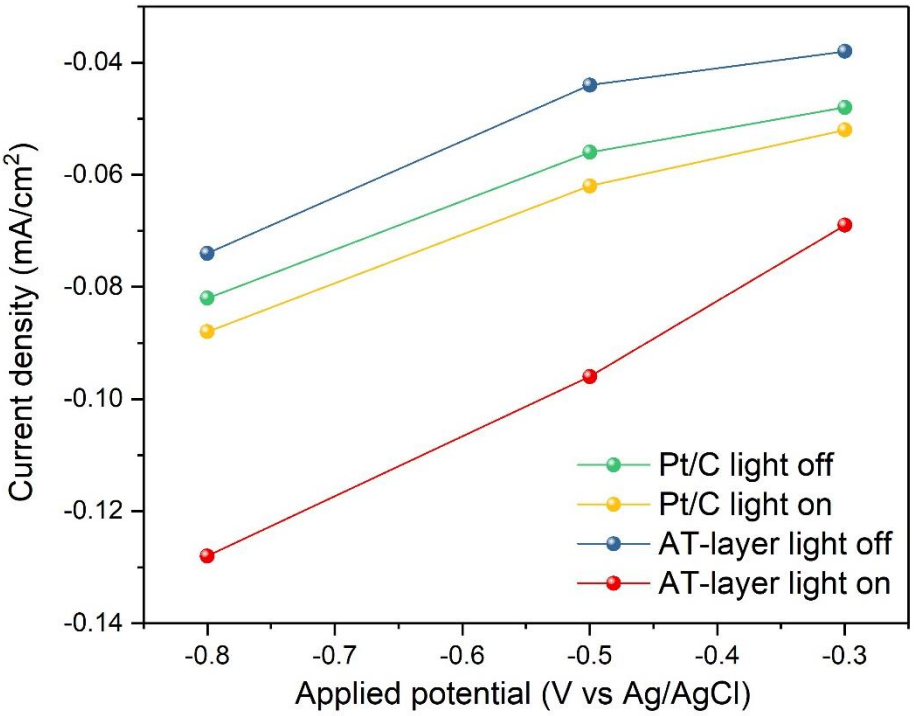


Figure 5.34 The effect of visible light illumination (λ > 420 nm) on the current densities of the commercial 20 wt% Pt/C and 20 wt% AT-layer Au-Ag/C at various potentials (-0.3 V, -0.5 V and -0.8 V versus Ag/AgCl) in 0.5 M Na_2SO_4. The Pt wire is used as the counter electrode; and the working electrode is obtained by spray-casting the electrocatalysts onto the FTO glass.

In Figure 5.34, it shows the current density of AT-layer core-shell NPs with/without light irradiation and compares the current density of the AT-layer NPs with the benchmark Pt catalyst for HER. As the plasmonic absorption of Pt is beyond the visible light region,[38] the HER activity promoted by the visible light illuminations is very limited for Pt catalysts as shown in Figure 5.34. It can be observed that the current density of AT-layer NPs was lower

than that of the Pt catalyst under dark conditions whereas the current density was greatly enhanced and significantly higher than that of the Pt catalyst under light irradiation at potential range of -0.3 to -0.8 V. It implies that the light energy can greatly enhance the HER activity and reduce the electrical energy input to develop an efficient and energy-saving system.

5.6.3 Stability Test and Control Experiments

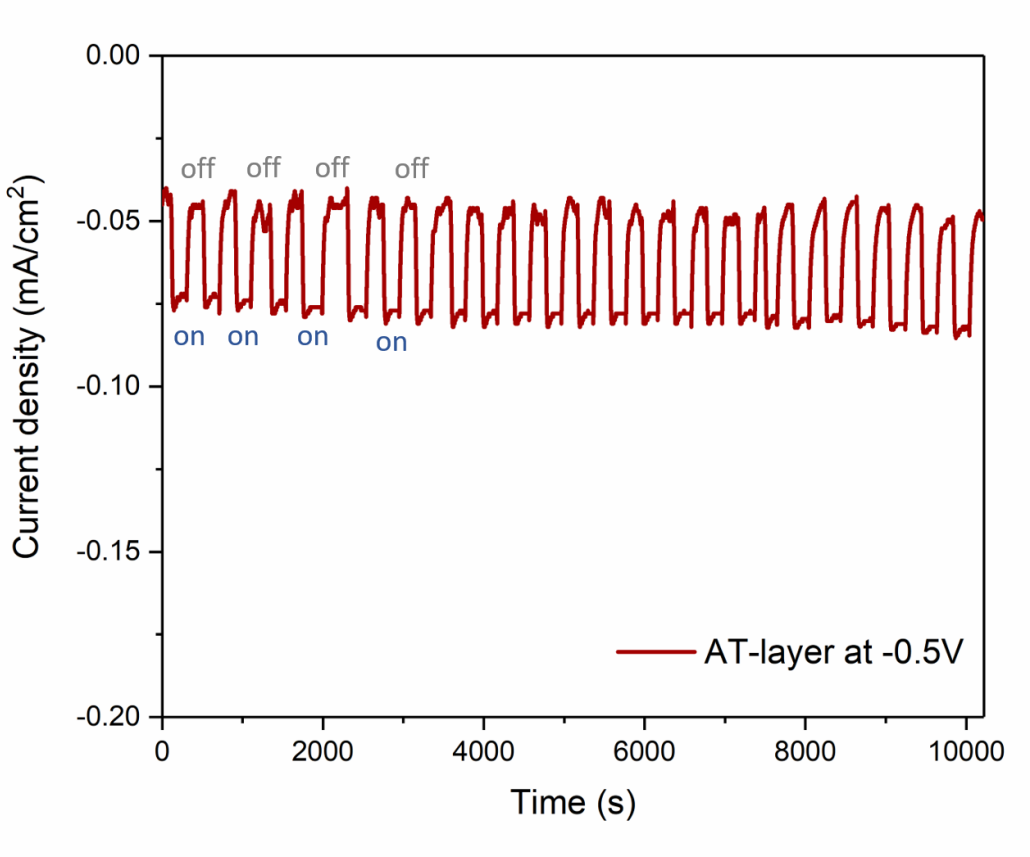


Figure 5.35. The cycling stability test of 20 wt% AT-layer Au-Ag/C at -0.5 V versus Ag/AgCl under visible light (λ > 420 nm) illuminations with around 200-second on-off cycles in 0.5 M Na_2SO_4. The Pt wire is used as the counter electrode; and the working electrode is obtained by spray-casting the electrocatalysts onto the FTO glass.

A separate experiment was performed on the AT-layer core-shell NPs in order to evaluate the cycling stability of the core-shell materials. The stability test was carried out under the same conditions as described in section 3.2.2.2 at an applied potential of -0.5 V vs Ag/AgCl for 10000 s with interval of 200-second on-off cycles under UV-cut Tungsten light (λ >420 nm).

In Figure 5.35, it shows a stable and reproducible current density enhancement during the light on/off repeating cycles under visible light illuminations with negligible fluctuations.

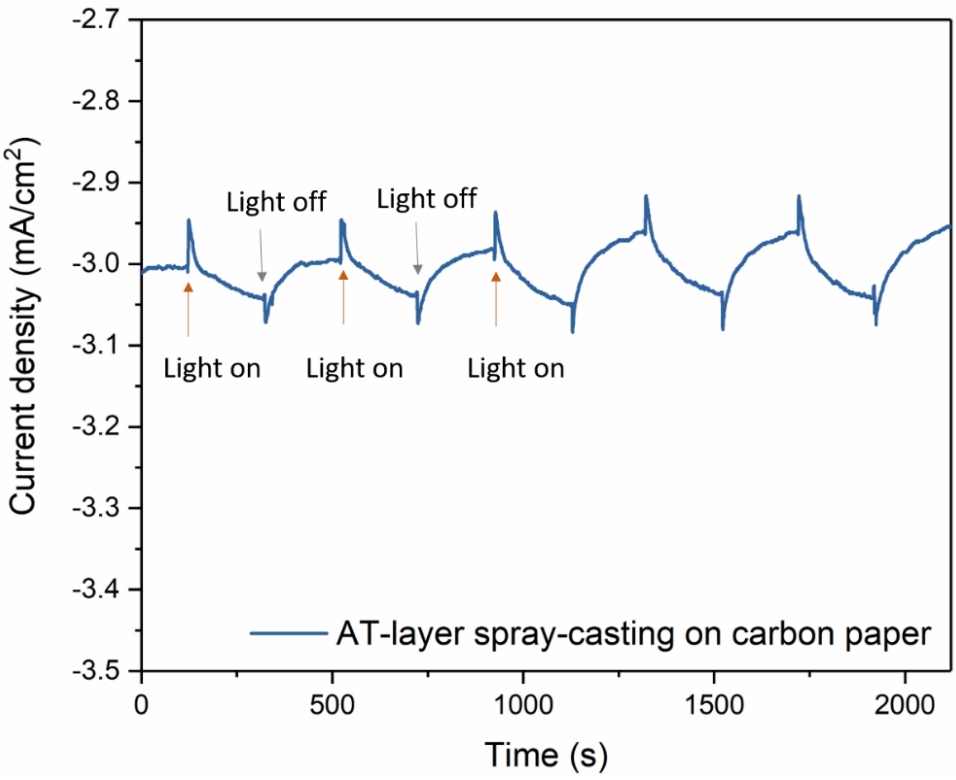


Figure 5.36 Current density of the 20wt% AT-layer Au-Ag/C at -0.3 V versus Ag/AgCl under visible light ($\lambda > 420$ nm) illuminations with around 200-second on-off cycles in 0.5 M Na_2SO_4. The Pt wire is used as the counter electrode; and the working electrode is obtained by spray-casting the electrocatalysts onto the carbon paper (instead of FTO glass).

In order to preclude the possible role of FTO glass as semiconductors for photocatalysis in the system, a control experiment was performed by replacing the FTO glass with carbon paper (Sigracet 39BC) as the working electrode to repeat the plasmonic chronoamperometry on AT-layer core-shell NPs at -0.3 V. According to Figure 5.36, similar phenomenon in current density enhancement under visible light illuminations is shown when using carbon paper as the support for working electrode. It clearly indicates that the FTO glass plays little role in the system for photo-electrochemical proton reduction, which shows similar performance as the carbon paper in this case. Notice that the extent of current density increase using carbon paper as the support is different from the FTO glass, which can be ascribed to the significant difference in

conductivity between the two supporting materials. Therefore, the more conductive carbon paper results in a less extent of polarisation that leads to a smaller percentage change in current density enhancement when compared with the FTO glass.

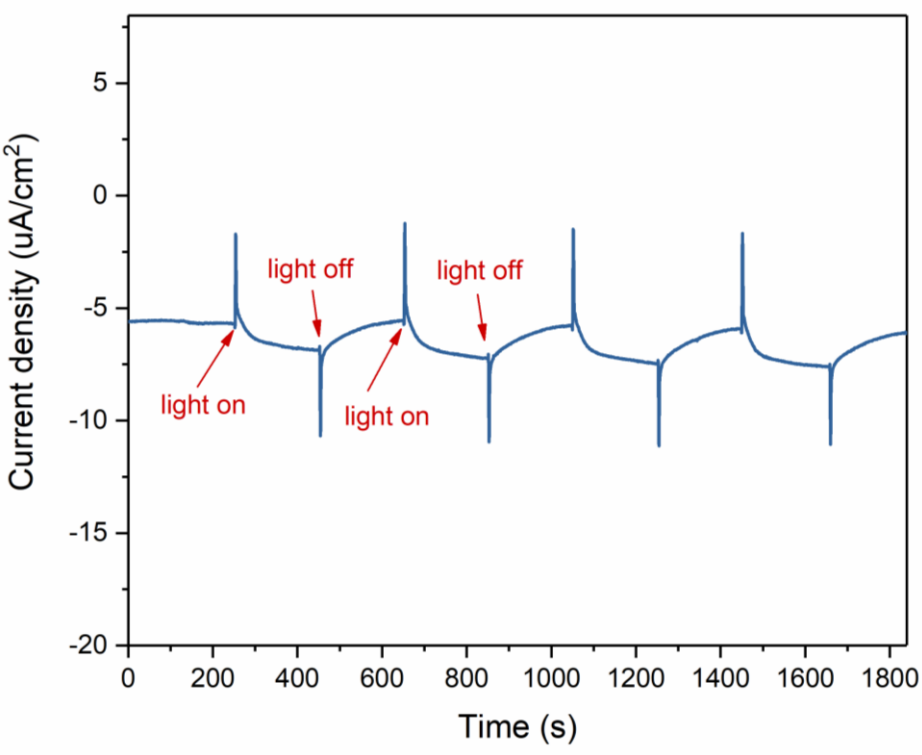


Figure 5.37 Current density of the 20wt% AT-layer Au-Ag/C at 0 V versus Ag/AgCl under visible light (λ > 420 nm) illuminations in 0.5 M Na_2SO_4. The Pt wire is used as the counter electrode; and the working electrode is obtained by spray-casting the electrocatalysts onto the FTO glass.

As the Au/Ag NPs can convert the absorbed light into heat via a series of non-radiative process, which may result in additional thermal induced current in the system.[39–42] As a result, a separate direct plasmonic chronoamperometry experiment was applied on the AT-layer core-shell NPs at 0 V under on/off visible light illumination cycles to evaluate the maximum temperature effect, if there is any in the system. According to the GC-TCD analysis, no H_2 was detected at 0 V bias potential either with or without illuminations. In Figure 5.37, it shows a current density enhancement of 1.68 μA/cm^2 at 0 V under visible light illuminations, which is the thermal induced current that can be ascribed to the temperature rise caused by nonradiative thermal energy transfer of Ag/Au NPs.[42] The thermal induced current density enhancement of 1.68

$\mu A/cm^2$ under light illumination is negligible when compared with the photocurrent density measured at the other four applied potentials in Figure 5.27. It can confirm that the photocurrent generated under visible light illumination mainly stems from the promotion of electrons induced by LSPR for proton reductions.

5.6.4 Plasmonic Chronoamperometry with Solar Simulator

A solar simulator (AM 1.5G, 100 mW cm^{-2}) equipped with an ultraviolet filter was employed in the experiments to evaluate the EC-LSPR current density enhancement at different wavelength ranges. In detail, the experiments were carried out at -0.5 V bias potentials on AT-layer core-shell samples at similar power density in the wavelength ranges of 400-500 nm, 500-600 nm and 600-700 nm set by the solar simulator.

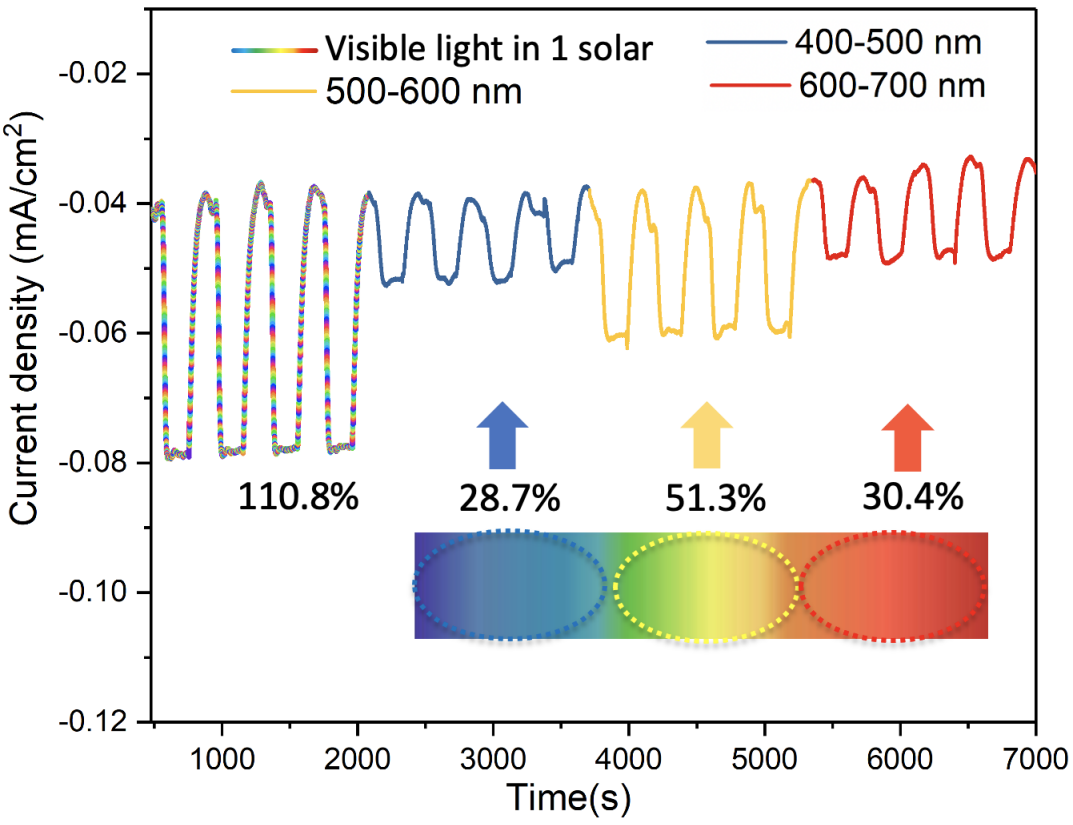


Figure 5.38 Current density as a function of reaction time of the 20 wt% AT-layer Au-Ag/C at -0.5 V versus Ag/AgCl under selected ranges of wavelengths (400-500 nm, 500-600 nm and 600-700 nm) of a solar simulator in 0.5 M Na_2SO_4. The Pt wire is used as the counter electrode; and the working electrode is obtained by spray-casting the electrocatalysts onto the FTO glass.

According to Figure 5.38, the result indicates that the overall current density enhancement of AT-layer core-shell NPs at -0.5 V under solar simulator illumination (110.8%) is similar to that under Tungsten light (112.5%). Particularly, the major current enhancement (51.3%) locates in the wavelength range of 500-600 nm region, which is in good agreement with the UV-Vis spectra (Figure 5.13) that the major plasmonic absorption peak of AT-layer NPs lies in 500-600 nm with a maximum peak at 528 nm.

With the help of the wavelength analysis in Figure 5.38, the corresponding apparent quantum efficiencies (AQE) at different wavelength is calculated via Equation 5.1 then summarized in Table 5.6.

Table 5.6 The corresponding apparent quantum efficiencies (AQE) at different wavelength ranges under the same conditions at an applied potential of -0.5 V vs Ag/AgCl of the AT-layer catalyst.

Wavelength/ nm	400-500	500-600	600-700
AQE	2.5%	4.0%	0.9%

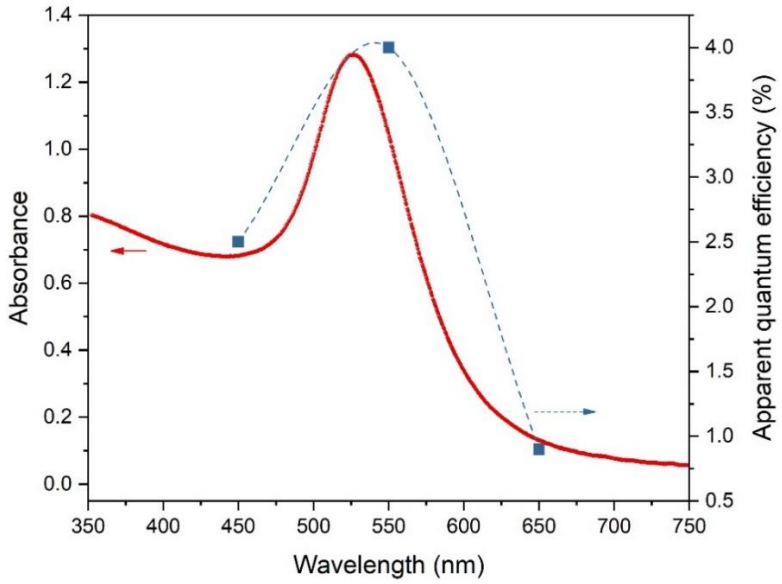


Figure 5.39 Apparent quantum efficiency (AQE) action spectrum of the 20wt% AT-layer Au-Ag/C electrodes and the corresponding absorption spectra of the AT-layer Au-Ag core-shell nanoparticles.

In Table 5.6, the AQE of AT-layer NPs at 400-500 nm, 500-600 nm and 600-700 nm wavelength ranges are calculated to be 2.5%, 4.0% and 0.9% respectively. When comparing the AQE and UV-visible spectrum of AT -layer NPs as shown in Figure 5.39, it is clearly demonstrated that the trend of the spectra profile (in terms of AQE) matches well with the absorption spectra of AT-layer NPs in general. It is evidenced that the photocurrent generated in the reaction is resulted from photocatalysis and thus, the enhancement in the photocatalytic hydrogen evolution rate can be attributed to the plasmon resonance of the Au-Ag core-shell NPs.

5.6.5 Linear Sweep Voltammetry (LSV) Analysis

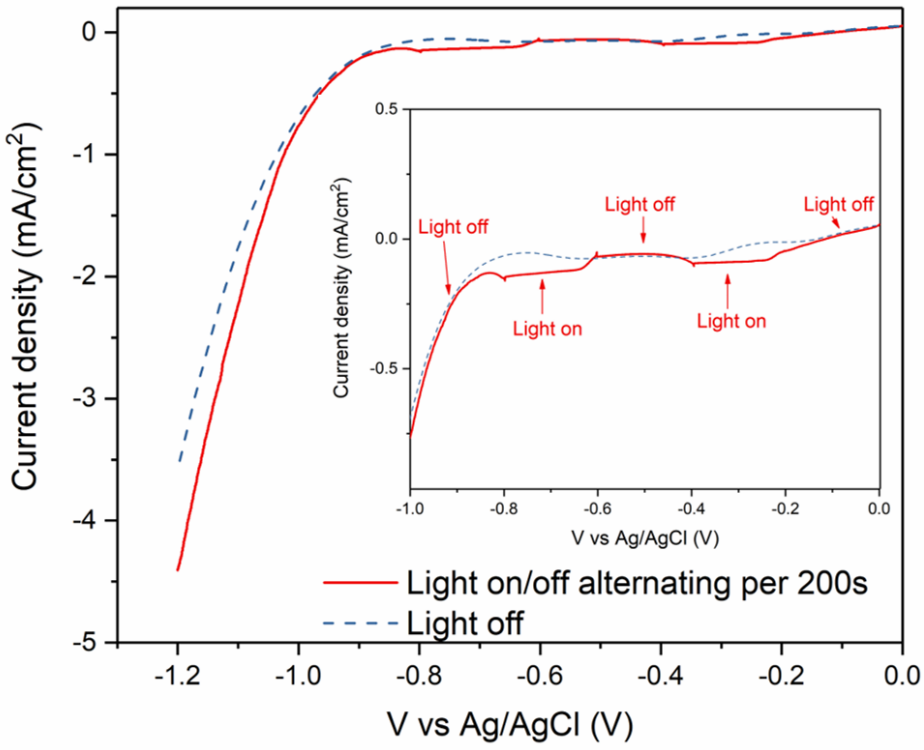


Figure 5.40 Linear sweep voltammetry (LSV) curves and photocurrent densities of the 20 wt% AT-layer Au-Ag/C in 0.5 M Na_2SO_4 electrolyte under visible light illumination ($\lambda > 420$ nm) with 200-second light-on/off cycles. The scan rate is 1mV/s. The Pt wire is used as the counter electrode; the Ag/AgCl (sat. KCl) is used as reference electrode; and the working electrode is obtained by spray-casting the electrocatalysts onto the FTO glass. The insert image is the enlarge LSV curve in the range of 0 V-1.0 V versus Ag/AgCl.

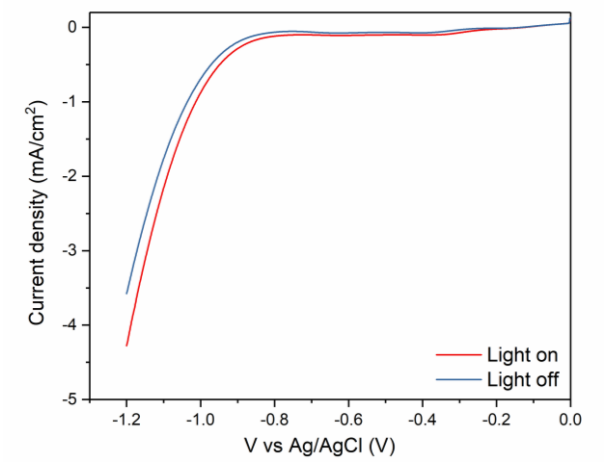


Figure 5.41 Linear sweep voltammetry (LSV) curves of the 20 wt% AT-layer Au-Ag/C in 0.5 M Na_2SO_4 electrolyte with/without visible light illuminated ($\lambda > 420$ nm) on the working electrode. The scan rate is 1mV/s. The Pt wire is used as the counter electrode; the Ag/AgCl (sat. KCl) is used as reference electrode; and the working electrode is obtained by spray-casting the electrocatalysts onto the FTO glass.

Moreover, the photocurrent response of the AT-layer core-shell sample was analysed by the continuously linear sweep voltammetry (LSV) under on/off visible light illumination. In Figure 5.40, it shows the LSV analysis of the AT-layer core-shell NPs with 200-second light on/off cycles at a potential range of 0 V-1.2 V (vs Ag/AgCl). An obvious cathodic current enhancement is observed when the sample is under visible light illumination compared with the dark condition that the current exhibits no changes, which clearly indicates that HEs induced by LSPR effect of the core-shell NPs can greatly promote the hydrogen evolution reaction.

In Figure 5.41, the current density under visible light illumination is generally more negative than the light-off condition at the whole potential range (0 V-1.2 V vs Ag/AgCl). With help of the visible light, the energy barrier for proton reduction on the AT-layer core-shell NPs is overcome, which gives a more positive onset potential compared with the dark conditions. In other words, with the aid of LSPR generated HEs under light illuminations, less electrical energy is required to promote the HER, showing the effective conversion of the light energy to hydrogen.

5.7 Discrete Dipole Approximation (DDA)

As evidenced by the results in section 5.4 to 5.6, EC-LSPR can be significantly affected by shell composition and thickness during visible light capture at negative bias potential for HER.[43] As a result, discrete dipole approximation (DDA) was employed to model the induced electric fields of different shell thicknesses at different wavelengths.

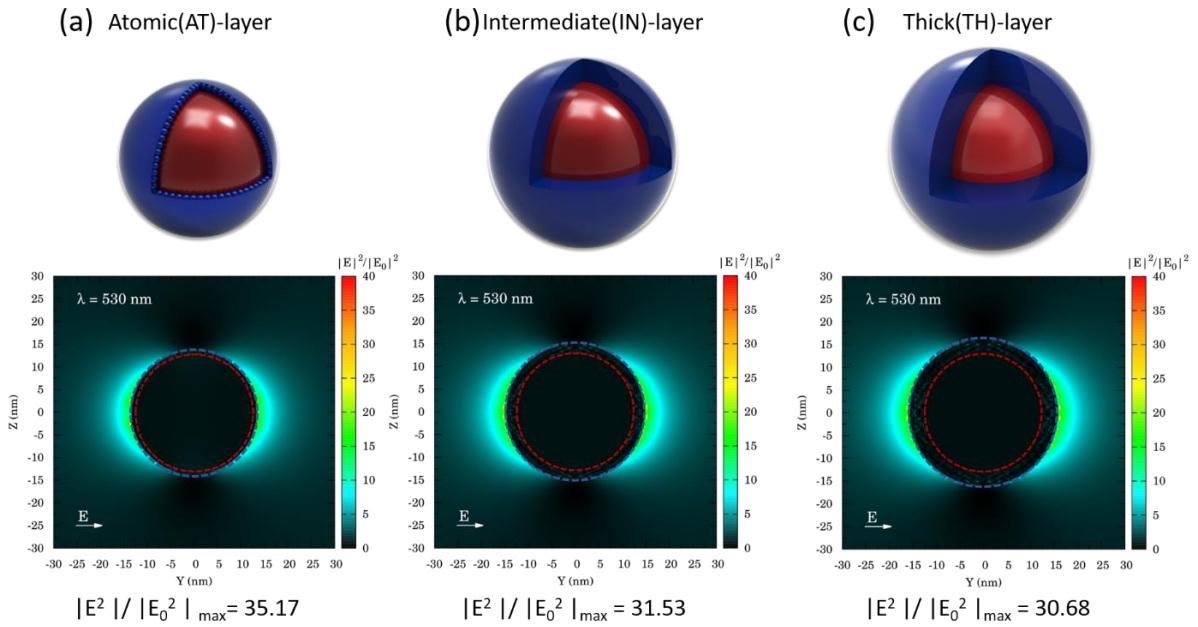


Figure 5.42 Induced electric field $|E^2|/|E_0^2|$ simulated by discrete dipole approximation (DDA) for Au-Ag core-shell NPs with overall 26.6 nm diameter of Au core and **a)** 1 nm Ag-shell (AT-layer), **b)** 3 nm Ag shell (IN-layer) and **c)** 5 nm Ag shell (TH-layer) at a wavelength of 530 nm.

In Figure 5.42, the simulated models are based on Au-Ag core-shell NPs with the same Au core size (26.6 nm) but different Ag shell thickness (1 nm, 3 nm and 5 nm) at 530nm. Obviously, the maximum electric field strength (E^2) induced by LSPR occurs at the top atomic surface of the Au-Ag core-shell NP. Amongst the three DDA simulations, the thinner shell shows a higher induced electric field $|E^2|/|E_0^2|$ at a wavelength of 530 nm. This well corresponds to the observation that the AT-layer has the highest induced electric field which gives the strongest plasmonic energy at the particle surface that generates most non-thermal HEs for proton reductions, and thus gives the highest current density enhancement under visible light illuminations.[44]

Table 5.7 Optimized structures of Au-Ag core-shell nanoparticles with fixed diameter gold core of 26 nm and fixed shell thickness with 1 nm composed of different Ag-Au (increasing Ag content from 0-100%). The response of induced electric field $|E^2|/|E_0^2|$ of the nanoparticles with different shell compositions as a function of wavelength can be seen.

λ/nm	**100 Au**	**30/70 Ag/Au**	**40/60 Ag/Au**	**70/30 Ag/Au**	**80/20 Ag/Au**	**100 Ag**
450	13.35	14.95	15.78	18.29	19.21	19.41
460	13.41	15.62	16.50	18.79	19.35	25.23
470	13.55	16.46	17.33	20.10	22.00	29.35
480	14.01	17.74	18.90	23.85	26.64	33.11
490	15.83	21.41	23.55	30.49	33.77	39.69
500	19.88	28.48	31.20	38.88	41.84	46.66
510	25.22	36.50	38.97	45.03	47.04	**49.99**
520	29.94	42.21	43.78	47.44	**48.51**	49.49
530	32.81	44.61	**45.41**	**47.51**	48.07	48.40
540	**33.73**	**44.80**	45.29	46.87	47.36	48.19
550	33.31	44.12	44.57	46.20	46.84	48.15

In order to figure out the correlation between the induced electric field and shell composition, DDA simulation was employed to model the E-field at the same Au core diameter and shell thickness. In Table 5.7, it shows the variations of induced electric field at different incident radiation wavelengths on fixed size Au-Ag core-shell NPs with a 26 nm Au core and 0.8 nm

shell of different Au/Ag compositions. As the Ag concentrations in the thin atomic shell increases, the electric field strength progressively resonates at lower wavelength, which is in good agreement with the blue-shifted observed in the UV-Vis spectrum in Figure 5.13 that more Ag component in the shell, more blue-shifted of the major absorption peak. As describe in surface plasmon analysis and the current density enhancement in Table 5.5, electric field strength dramatically enhances when Ag is present in the shell, depicting the fact that Ag plays an important role for the provision of higher energy (more positive) excited states as an avenue to allow LSPR-promoted hot electrons to carry out proton reduction at mixed Ag-Au surfaces. Hence, this result opens up a potential way to fine-tune the light absorption in EC-LSPR process by varying the shell compositions.

5.8 Conclusions

In conclusion, this chapter has provided a detailed study in the use of a tailor-made core-shell material in electrochemical hydrogen evolution reaction (HER) with solar energy as an additional input. A fine-tuned Au/Ag layer with precise control in metal ratio was fabricated onto an Au core, forming a unique atomic layer core-shell nanoparticle. An in-depth surface plasmon study on the core-shell materials was carried out via STEM-EELS whereas the 3D structure of the particle was reconstructed by APT. It was experimentally shown that AT-layer core-shell NPs serves as an excellent cathode catalyst for the HER, which displayed an increase of 112.5% when compared to light-off conditions, outperforming the commercial Pt catalyst. It was proposed that hot electrons excited by LSPR play an important role in proton reduction, in which the extent is affected by the shell's chemical compositions as evidenced by DDA simulation and X-ray absorption spectroscopy. Looking forward, solar energy can be exploited as effective means to reduce the electrochemical input of typical HER catalytic systems when plasmonic metal nanoparticles are employed, taking advantage of their higher electron density, energy confinement and conductivity with no impedance.

5.9 References

1. Mo, J. *et al.* Atomic-Precision Tailoring of Au–Ag Core–Shell Composite Nanoparticles for Direct Electrochemical-Plasmonic Hydrogen Evolution in Water Splitting. *Adv. Funct. Mater.* **31**, 1–11 (2021).
2. Shaner, M. R., Atwater, H. A., Lewis, N. S. & McFarland, E. W. A comparative technoeconomic analysis of renewable hydrogen production using solar energy. *Energy Environ. Sci.* **9**, 2354–2371 (2016).
3. Wang, Q. *et al.* Scalable water splitting on particulate photocatalyst sheets with a solar-to-hydrogen energy conversion efficiency exceeding 1%. *Nat. Mater.* **15**, 611–615 (2016).
4. Qiu, Y. *et al.* Efficient solar-driven water splitting by nanocone BiVO4-perovskite tandem cells. *Sci. Adv.* **2**, e1501764 (2016).
5. Kale, M. J., Avanesian, T. & Christopher, P. Direct photocatalysis by plasmonic nanostructures. *ACS Catal.* **4**, 116–128 (2014).
6. Liu, G. *et al.* Controllable Ag Migration To Form One-Dimensional Ag/Ag2S@ZnS for Bifunctional Catalysis. *ACS Appl. Energy Mater.* **3**, 6146–6154 (2020).
7. Li, X. *et al.* Au Multimer@MoS2 hybrid structures for efficient photocatalytical hydrogen production via strongly plasmonic coupling effect. *Nano Energy* **30**, 549–558 (2016).
8. Mukherjee, S. *et al.* Hot Electrons Do the Impossible: Plasmon-Induced Dissociation of H2 on Au. *Nano Lett.* **13**, 240–247 (2013).
9. Zheng, D., Cao, X. & Wang, X. Precise Formationofa HollowCarbon Nitride Structure with aJanus Surface To Promote Water Splitting by PhotoredoxCatalysis. **55**, 11512–11516 (2016).
10. Che, W. *et al.* Fast Photoelectron Transfer in (Cring)−C3N4 Plane Heterostructural Nanosheets for Overall Water Splitting. *J. Am. Chem. Soc.* **139**, 3021–3026 (2017).
11. Fang, W. *et al.* Effect of Surface Self-Heterojunction Existed in BixY1−xVO4 on Photocatalytic Overall Water Splitting. *ACS Sustain. Chem. Eng.* **5**, 6578–6584 (2017).
12. He, H. *et al.* Distinctive ternary CdS/Ni2P/g-C3N4 composite for overall water splitting: Ni2P accelerating separation of photocarriers. *Appl. Catal. B Environ.* **249**, 246–256 (2019).
13. Zhong, Y. *et al.* A CoP/CdS/WS2 p-n-n tandem heterostructure: A novel photocatalyst for hydrogen evolution without using sacrificial agents. *J. Mater. Chem. A* **7**, 14638–14645 (2019).
14. Liu, W. *et al.* Single-Site Active Cobalt-Based Photocatalyst with a Long Carrier Lifetime for Spontaneous Overall Water Splitting Angewandte. *angew* **129**, 9440–9445 (2017).
15. Article, E. *et al.* Overall water splitting by Pt/g-C3N4 photocatalysts without using sacrificial agents. *Chem. Sci.* **7**, 3062–3066 (2016).
16. Turkevich, J., Stevenson, P. C. & Hillier, J. A study of the nucleation and growth

processes in the synthesis of colloidal gold. *Discuss. Faraday Soc.* **11**, 55–75 (1951).

17. Samal, A. K. *et al.* Size tunable Au@Ag core-shell nanoparticles: Synthesis and surface-enhanced raman scattering properties. *Langmuir* **29**, 15076–15082 (2013).

18. Zeng, J. *et al.* Controlling the shapes of silver nanocrystals with different capping agents. *J. Am. Chem. Soc.* **132**, 8552–8553 (2010).

19. Koh, A. L. *et al.* Electron energy-loss spectroscopy (EELS) of surface plasmons in single silver nanoparticles and dimers: Influence of beam damage and mapping of dark modes. *ACS Nano* **3**, 3015–3022 (2009).

20. Arenal, R. *et al.* Local plasmonic studies on individual core-shell gold-silver and pure gold nano-bipyramids. *J. Phys. Chem. C* **118**, 25643–25650 (2014).

21. Schaffer, B., Hohenester, U., Trügler, A. & Hofer, F. High-resolution surface plasmon imaging of gold nanoparticles by energy-filtered transmission electron microscopy. *Phys. Rev. B - Condens. Matter Mater. Phys.* **79**, 1–4 (2009).

22. Sykes, M. E. *et al.* Enhanced generation and anisotropic Coulomb scattering of hot electrons in an ultra-broadband plasmonic nanopatch metasurface. *Nat. Commun.* **8**, 986 (2017).

23. Kong, X. T., Wang, Z. & Govorov, A. O. Plasmonic Nanostars with Hot Spots for Efficient Generation of Hot Electrons under Solar Illumination. *Adv. Opt. Mater.* **5**, 1–10 (2017).

24. Wu, Y., Li, G. & Camden, J. P. Probing Nanoparticle Plasmons with Electron Energy Loss Spectroscopy. *Chem. Rev.* **118**, 2994–3031 (2018).

25. Mirsaleh-kohan, N. *et al.* Single-Molecule Surface-Enhanced Raman Scattering : Can STEM /EELS Image Electromagnetic Hot Spots? *J. Phys. Chem. C* **3**, 2303–2309 (2012).

26. Pais, A. Einstein and the quantum theory. *Rev. Mod. Phys.* **51**, 863–914 (1979).

27. Cortie, M. B. & McDonagh, A. M. Synthesis and optical properties of hybrid and alloy plasmonic nanoparticles. *Chem. Rev.* **111**, 3713–3735 (2011).

28. Marzo, A. *et al.* Standard or local solar spectrum? Implications for solar technologies studies in the Atacama desert. *Renew. Energy* **127**, 871–882 (2018).

29. Ryzhkov, N. V., Yurova, V. Y., Ulasevich, S. A. & Skorb, E. V. Photoelectrochemical photocurrent switching effect on a pristine anodized Ti/TiO2 system as a platform for chemical logic devices. *RSC Adv.* **10**, 12355–12359 (2020).

30. Sheldon, M. T., De Groep, J. Van, Brown, A. M., Polman, A. & Atwater, H. A. Plasmoelectric potentials in metal nanostructures. *Science (80-.).* **346**, 828–831 (2014).

31. Greathouse, J. A., Feller, S. E. & McQuarrie, D. A. The Modified Gouy–Chapman Theory: Comparisons between Electrical Double Layer Models of Clay Swelling. *Langmuir* **10**, 2125–2130 (1994).

32. Nootchanat, S. *et al.* Investigation of localized surface plasmon/grating-coupled surface plasmon enhanced photocurrent in TiO2 thin films. *Phys. Chem. Chem. Phys.* **16**, 24484–24492 (2014).

33. Compton, R. G. & Banks, C. E. *Understanding voltammetry, 2nd edition*. *Understanding Voltammetry, 2nd Edition* (Imperial College Press, 2010). doi:10.1142/P726.

34. Holmberg, N., Laasonen, K. & Peljo, P. Charge distribution and Fermi level in bimetallic nanoparticles. *Phys. Chem. Chem. Phys.* **18**, 2924–2931 (2016).

35. Liu, J. *et al.* Metal-free efficient photocatalyst for stable visible water splitting via a two-electron pathway. *Science (80-.).* **347**, 970–974 (2015).

36. Wu, Q. *et al.* A metal-free photocatalyst for highly efficient hydrogen peroxide photoproduction in real seawater. *Nat. Commun.* **12**, 483 (2021).

37. Li, C., Wang, T., Luo, Z., Liu, S. & Gong, J. Enhanced Charge Separation through ALD-Modified Fe2O3/Fe2TiO5 Nanorod Heterojunction for Photoelectrochemical Water Oxidation. *Small* **12**, 3415–3422 (2016).

38. Gharibshahi, E., Saion, E., Ashraf, A. & Gharibshahi, L. Size-Controlled and Optical Properties of Platinum Nanoparticles by Gamma Radiolytic Synthesis. *Appl. Radiat. Isot.* **130**, 211–217 (2017).

39. Link, S., Burda, C., Mohamed, M., Nikoobakht, B. & El-Sayed, M. Femtosecond transient-absorption dynamics of colloidal gold nanorods: Shape independence of the electron-phonon relaxation time. *Phys. Rev. B - Condens. Matter Mater. Phys.* **61**, 6086–6090 (2000).

40. Link, S. & El-Sayed, M. A. Spectral Properties and Relaxation Dynamics of Surface Plasmon Electronic Oscillations in Gold and Silver Nanodots and Nanorods. *J. Phys. Chem. B* **103**, 8410–8426 (1999).

41. Link, S., Burda, C., Wang, Z. L. & El-Sayed, M. A. Electron dynamics in gold and gold-silver alloy nanoparticles: The influence of a nonequilibrium electron distribution and the size dependence of the electron-phonon relaxation. *J. Chem. Phys.* **111**, 1255–1264 (1999).

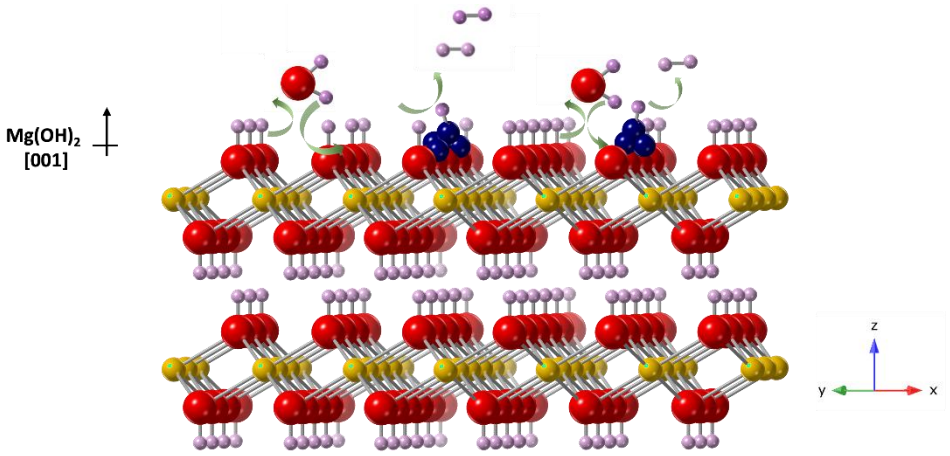
42. Huang, X. & El-sayed, M. A. Gold nanoparticles : Optical properties and implementations in cancer diagnosis and photothermal therapy. *J. Adv. Res.* **1**, 13–28 (2010).

43. Holmberg, N., Laasonen, K. & Peljo, P. Charge distribution and Fermi level in bimetallic nanoparticles. *Phys. Chem. Chem. Phys.* **18**, 2924–2931 (2016).

44. Clavero, C. Plasmon-induced hot-electron generation at nanoparticle/metal-oxide interfaces for photovoltaic and photocatalytic devices. *Nat. Photonics* **8**, 95–103 (2014).

Chapter 6 Enhanced Hydrogen Evolution Reactions on Polar MgO Supports

"In-situ Phase Transformations on Polar MgO Supported Ru-based Catalysts for Enhanced Hydrogen Evolution Reactions"



Enhanced proton conductivity by structural transformation to $Mg(OH)_2$ (001).

Table of Contents

Chapter 6 Enhanced Hydrogen Evolution Reactions on Polar MgO Supports 199
6.1 Background 201
6.2 Materials 204
6.3 Synthesis 204
6.3.1 MgO Support Preparations 205
6.3.2 Ru-loading MgO Catalysts 206
6.4 Characterizations 206
6.4.1 X-Ray Diffraction (XRD) 206
6.4.2 Transmission Electron Microscopy (TEM) 208
6.4.3 Brunauer–Emmett–Teller (BET) Analysis 210
6.4.4 ICP-MS Analysis 210
6.5 Catalytic Performance in HER 211
6.5.1 Experimental Methods 211
6.5.2 Results and Discussions 212
6.6 Structure-Activity Correlations on MgO Supports 216
6.6.1 XPS Analysis 216
6.6.2 Operando SXRD Measurements 219
6.6.3 Electron Microscopy (EM) Analysis 226
6.6.4 DFT Modelling and Calculations 230
6.7 Conclusions 236
6.8 References 237

6.1 Background

The strategies in tuning the electronic structures and catalytic properties of the metal catalysts can be classified in 3 main categories, namely morphology engineering of metals for different exposed facets, multi-metal assemblies to make use of metal components with distinctive electronic properties, and metal-support interactions to construct active catalytic pathways for reactions.[1–5] In chapter 4 and chapter 5, we have used the morphology-controlled Ag NPs and bifunctional Au-Ag core-shell NPs to enhance the catalytic activities of the hydrogen evolution reactions, and outperformed the benchmark 20 wt% Pt/C catalysts in different electrochemical systems. In this chapter, the metal-support interactions will be studied to investigate the support effects in the catalytic systems and further enhance the HER activities.

In industrial metal based heterogeneous catalysis, finely divided metal nanoparticles are commonly loaded on high surface area, but inexpensive solid metal oxide supports in order to reduce the use of expensive metal for high catalytic activity per metal site. It is later becoming clear that the structural and electronic properties of catalysts can also be modified through the strong metal–support interactions (SMSI) to influence catalytic activities.[4,6] Among various metal oxide supports, non-redox magnesium oxide (MgO) shows superior properties as supports due to its versatile tuneability in surface properties and chemical stability. For example, the significant morphology effect of MgO in heterogeneous catalysis has drawn attention in different areas of catalysis.[7–9] Particularly, for an energetic MgO (111) polar facet, the atoms are arranged in a layered structure which consists of pure O^{2-} layers and pure Mg^{2+} layers leading to both O-terminated and Mg-terminated surfaces. Meanwhile for MgO (110) and MgO (100) facets, it is arranged in intermixed of more stable O^{2-} and Mg^{2+} species on both the top surface and the bulk[10]

The underlying principle for the formation of such high energy polar facet can be attributed to the interaction between the filled O^{2-} 2p and unoccupied Mg^{2+} orbitals attenuated by the

Madelung potential. When polarization occurs as a result of preferential exposure of the MgO {111} facet, the orbital energy for the vacant Mg^{2+} will be lowered while that of O^{2-} will be raised, causing a significant reduction in binding energies of the electrons in the occupied energy states, and hence subsequent formation of new energy bands from the overlapping of ions electrostatic field.[11] Meanwhile, the high energy polar facets also require different forms of relaxation to lower the surface energy, and it is usually circumvented by defect formation, surface reconstruction or adsorption of charge-balancing molecules. In the case of non-redox polar MgO (111) facet, counterions adsorption is adopted for the surface relaxation due to the rigid Madelung potential and difficulty to form defects.[11,12]

Wu *et al.*[13] have recently reported a high loading of single-atom Ru^{2+} species dispersed on MgO (111) polar surface, which catalysed the reversible conversion of H_2 from Ru^{2+} ($Ru^{2+} + H_2 \rightarrow Ru^0 + 2H^+$) to H^+ on MgO (111) by the Ru^{2+}-O^{2-} Frustrated Lewis pair at the interface in gas phase. Therefore, it is of interest to study different facets of MgO as a host for metal NPs in electrochemical hydrogen evolution reaction (HER) in aqueous medium.

So far, commercially available catalysts for HER are Pt-based materials (mainly 20% Pt/C) due to their superior intrinsic activity.[14,15] Li *et al.*[16] also confirmed that the HER exchange currents and the metal-hydrogen bond strengths of the catalysts presented in a volcano relationship, in which the platinum-group metals (such as Pt, Ru and Ir) were at the apex of the plot and displayed excellent HER activities. Unfortunately, the scarcity and high cost of Pt have inevitably inhibited its commercial applications in large scales for HER. However, compared with the commonly used Pt-based catalysts, ruthenium (Ru) is expected to be a good alternative because of its similar bonding energy for hydrogen (65 kcal mol^{-1}), lower water decomposition barrier, and considerably lower price (only 4% cost of Pt).[17,18]

In order to develop more cost-effective alternatives, significant effort has been exerted in attempt to minimize the usage of noble metals in electrocatalysts and utilize the SMSI to enhance the HER activity. To increase metal dispersion and provide a platform for metal-support interactions, metal oxides have been widely used as catalyst supports in electrode applications, due to their particular chemical and electrochemical stability against corrosion.[19–21] However, the main drawback of the metal oxide supports in the context of electrode materials is their insulating or semiconductor behaviour and hence subsequently limiting electronic conductivity. This can be generally circumvented by formation of composites, mixed with carbon materials, or modification of the supports' preferentially-exposed facets to enhance conductivity.[22–26]

It is envisaged that the high proton affinity of MgO (111) facet as demonstrated by Wu *et al.*[13] may also contribute to trap the surface hydrogen atoms from the noble metal in aqueous medium and the close interatomic distance between the surface oxygen sites may allow protons to hop across through an extensive hydrogen-bond network via a Grotthuss mechanism.[7]

In this chapter, Ru is immobilized on MgO supports with different preferential exposed facets, namely Ru-MgO (111), Ru-MgO (110) and Ru-MgO (100), which are acting as the cathode catalysts for HER in acidic medium for the first time. The Ru loaded on polar MgO (111) delivers an exceptional hydrogen production rate, which outperforms the benchmark Pt/C for 10 % at -2.3 V after a structural activation process. Using a combination of in-situ synchrotron XRD technique and ex-situ TEM, SAED and XPS analysis to study the activation process, it is discovered that the Ru-MgO (111) interface is electrochemically hydrolysed to Ru-$Mg(OH)_2$ (001) in the acidic medium, which creates efficient hopping channels for protons to travel across the support for reduction.

6.2 Materials

The chemicals, reagents, and gases used are as followed: Triruthenium dodecacarbonyl (≥ 99%, Sigma-Aldrich); Magnesium chloride (anhydrous, ≥ 98% Sigma-Aldrich); Magnesium nitrate hexahydrate (ACS reagent, 99%, Sigma-Aldrich); Vulcan carbon (Vulcan XC 72R, FuelCellStore); Benzoic acid (ACS reagent, ≥ 99.5%, Sigma-Aldrich); Sodium hydroxide (ACS reagent, ≥ 97%, Sigma-Aldrich); Tetrahydrofuran (anhydrous, ≥ 99.9%, inhibitor-free, Sigma-Aldrich); Magnesium oxide (ACS reagent, 97%, Sigma-Aldrich); Ethanol (absolute ≥ 99.8% (GC), Sigma-Aldrich); Acetone (99.9%, Sigma-Aldrich); platinum on graphitized carbon (20wt.% loading, Sigma Aldrich), 2-Propanol (≥ 99.5%, Sigma Aldrich); nafion perfluorinated resin solution (5wt.% in mixture of lower aliphatic alcohols and water, Sigma Aldrich); Sigracet carbon paper (29BC, FuelCellStore); Sulfuric acid (ACS reagent, 95.0-98.0%, Sigma-Aldrich). H_2 (99.99%, BOC); Argon (99.99%, BOC); 5% H_2 in Ar (5% H_2, 95% Ar, BOC).

6.3 Synthesis

At the outset of this chapter, MgO with different preferential exposed facets, such as (111), (110) and (100), were synthesized as electrode catalyst supports for HER. The synthesis involved the preparation of the MgO (111), MgO (110), MgO (100) supports, and the corresponding Ru loaded catalysts: 20 wt% Ru-MgO (111) and 20 wt% Ru-MgO (110). The 20 wt% Ru-MgO (100) was excluded in this study because the MgO (100) samples have significantly smaller surface area compared with the MgO (111) and MgO (110) supports (of which will be discussed further in section 6.4.3). And the commercially available 20 wt% Pt/C was supplied from Sigma Aldrich. The 20 wt% Ru/C was synthesized with the same method as mentioned in chapter 4, section 4.3.4.1.

6.3.1 MgO Support Preparations

6.3.1.1 Polar MgO (111) Supports

The MgO (111) supports were synthesized via the hydrothermal process, which was optimised from the synthesis methods of Wu *et al.*[7] $MgCl_2$ (0.94 g) was dissolved in DI water (30 mL) at room temperature. Benzoic acid (0.12 g) which acting as a surfactant was dissolved in another 30 mL of DI water. The above two solutions were then mixed and stirred for 10 min. NaOH (2 M, 20 mL) was added into the mixture drop by drop and formed white slurry. After aging for 1 hour at room temperature, the white slurry was transferred into a 100 mL autoclave. The autoclave was then put into the pre-heated oven at 180 ^oC. After 24 hours, the oven was switched off then cooled down to room temperature. The $Mg(OH)_2$ precursors can be collected by centrifuging the slurry from the hydrothermal process and then washed with DI water for 3 times. The $Mg(OH)_2$ precursor powder was obtained after drying the slurry at 80 ^oC in a vacuum oven overnight. Finally, the MgO (111) nanosheets were obtained after calcination of the $Mg(OH)_2$ precursor powder at 500 ^oC under air for 6 hours.

6.3.1.2 Non-Polar MgO (110) Supports

The MgO (110) supports were synthesized via the vacuum calcinations.[27] Commercial MgO (500 mg) was boiled in DI water at 110 ^oC for 5 hours with stirring. The powder was then collected via centrifuge followed by drying in the vacuum oven at 120 ^oC for 12 hours. After drying, the powder was then calcined under vacuum at 500 ^oC for 6 hours.

6.3.1.2 Non-Polar MgO (100) Supports

The MgO (100) supports were synthesized via the traditional thermal decomposition method.[27] The MgO (100) powder was obtained by calcining the $Mg(NO_3)_2$ (500 mg) under compress air at 500 ^oC for 5 hours.

6.3.2 Ru-loading MgO Catalysts

In typical synthesis of the 20 wt% Ru-MgO catalysts, triruthenium dodecacarbonyl (46.8 mg) was dispersed in 30 mL of tetrahydrofuran (THF) under sonication for 10 minutes at room temperature. The above mixture was then transferred to the as-prepared MgO supports (200 mg) and allowed to sonicate at ambient temperature for 4 hours, followed by rotary evaporation to remove the solvent. The obtained powder was then heated at 95 ^{o}C in a vacuum oven overnight. After that, the powder was transferred to a temperature-programmed furnace and heated at 300 ^{o}C for 4 hours under Ar gas to remove the CO ligands from the Ru precursors.

6.4 Characterizations

The MgO supports with preferential exposed (111), (110) and (100) facets were namely as MgO (111), MgO (110) and MgO (100), which were characterized by XRD and TEM in this section. The surface area of the MgO supports was measured by the Brunauer–Emmett–Teller (BET) analysis and the metal loading concentrations on the supports were measured by the inductively coupled plasma mass spectrometry (ICP-MS).

6.4.1 X-Ray Diffraction (XRD)

The X-ray diffraction patterns of the three MgO powders were obtained and shown in Figure 6.1, which confirmed the rock-salt periclase nature of MgO.[28] As the MgO has a face-centred cubic (FCC) structure, which allows the reflections of (h, k, l) all odd or all even in the selection rules while (h, k, l) with mixed odd or mixed even reflections are forbidden in the XRD diffractograms of the MgO samples.

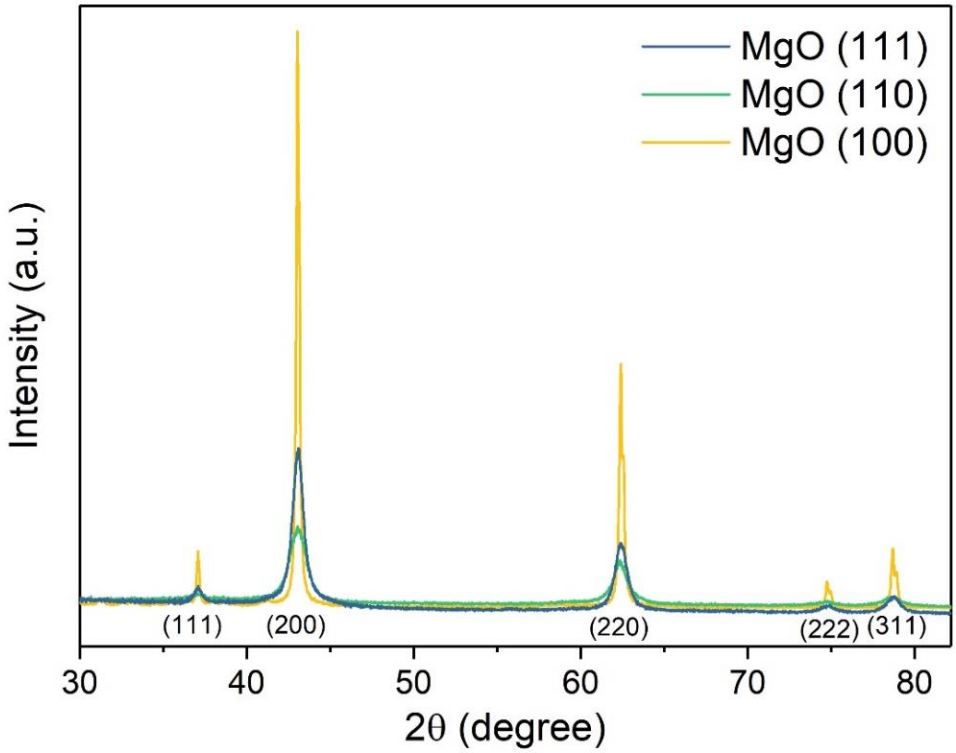


Figure 6.1 XRD profiles of the MgO (111), MgO (110) and MgO (100) supports.

In Figure 6.1, all the three samples show the highest XRD peak intensities at (200) peak but not the preferentially exposed facets. This can be attributed to the nanosized nature of the samples in which the orientations are scattered in random directions on the XRD slides with the most thermodynamically stable (200) facets being diffracted. Since XRD reflects the bulk properties rather than the surface features, (200) peak is thus the dominant diffracted peak. Additionally, the peak widths follow the trend of MgO (100) < MgO (111) < MgO (110), which implies a descending order of crystallite sizes of MgO (100) > MgO (111) > MgO (110) according to the Scherrer equation as mentioned in chapter 2, section 2.2.

6.4.2 Transmission Electron Microscopy (TEM)

In contrast, TEM can be used to investigate the morphologies and lattice spacings of the MgO nanostructures to determine the dominated exposed facets of the three samples. As shown in Figure 6.2a and d, the polar MgO (111) samples show hexagonal nanosheet structures with a corresponding lattice spacing of 0.243 ± 0.010 nm, which is in good agreement with the literatures.[27,29] In Figure 6.2b and e, the non-polar MgO (110) supports exhibit stacked leaf-shape nanostructures with the lattice fringes of 0.148 ± 0.008 nm which is corresponding to the (220) exposed facets.[27,30] As for the MgO (100) shown in Figure 6.2c, the (100) facet is the most thermodynamically stable exposed facet in the MgO samples with amorphous structures, which gives a lattice spacing of 0.213 ± 0.010 nm as analysed in the HRTEM (Figure 6.2f).[7]

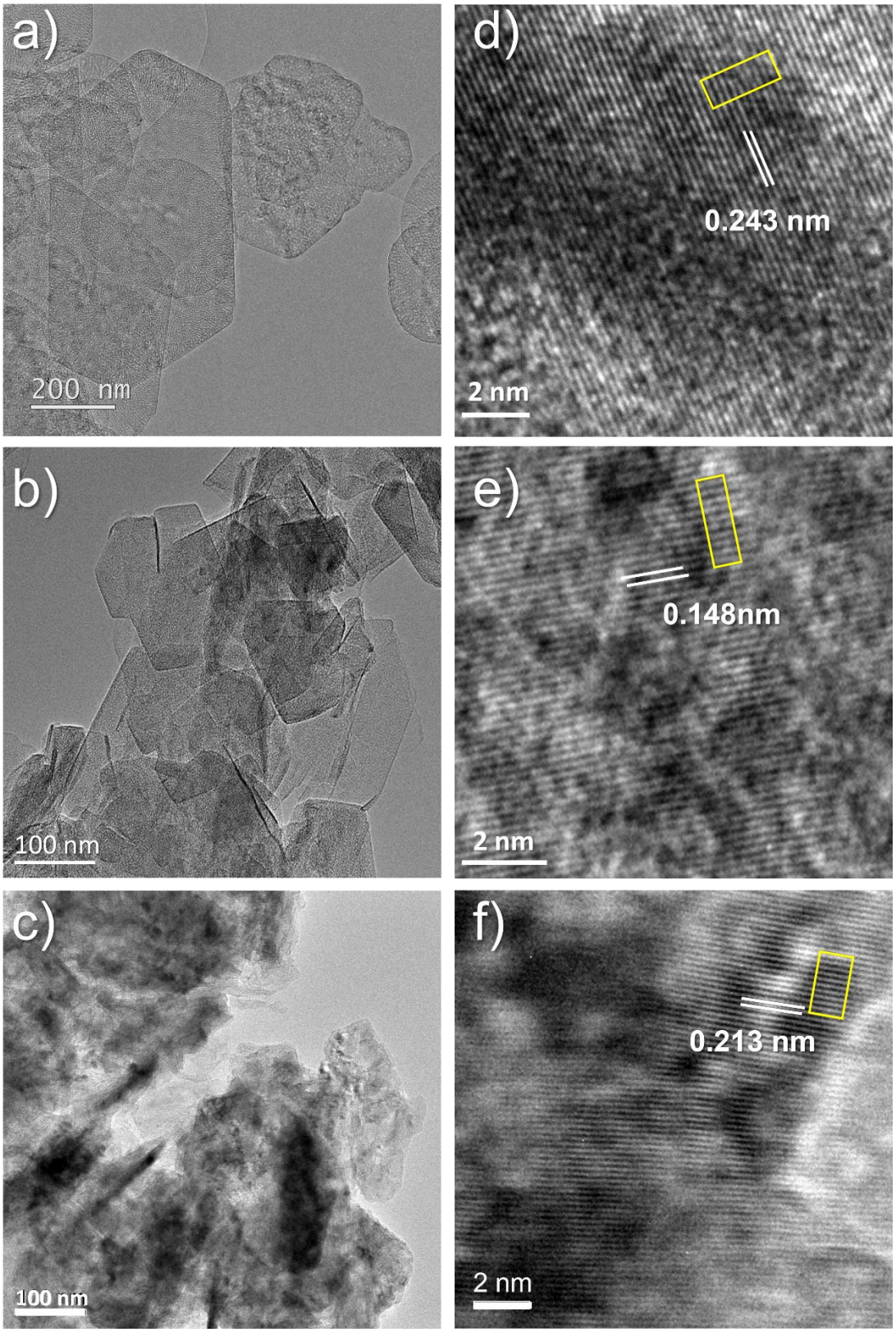


Figure 6.2 The TEM images of **a)** MgO (111), **b)** MgO (110) and **c)** MgO (100) supports with their corresponding HRTEM **d), e)** and **f)**, which showing the lattice spacings of (111), (220) and (200) facets. The lattice spacings are calculated from the average of 10 spacings where a perpendicular line is drawn across 11 lattice fringes as shown in the yellow squares.

6.4.3 Brunauer–Emmett–Teller (BET) Analysis

Table 6.1 BET analysis of the three as-prepared MgO supports and commercial activated carbon.

MgO supports	MgO (111)	MgO (110)	MgO (100)	Activated carbon[31]
BET surface area (m^2 g_{cat}^{-1})	170.9	214.1	13.4	1734

The surface area is also a critical factor for the supports in catalysis. Brunauer–Emmett–Teller (BET) analysis was employed on the three MgO supports for surface area measurements. As shown in Table 6.1, the MgO (110) samples give the largest surface area (214.1 m^2 g_{cat}^{-1}), which is around 16 times higher than that of the MgO (100) supports (13.4 m^2 g_{cat}^{-1}). The MgO (111) polar supports give a medium value of 170.9 m^2 g_{cat}^{-1}. The BET surface area trend of MgO (100) < MgO (111) < MgO (110) is in a good agreement with the crystallite sizes as interpreted by the XRD analysis. It is evidenced from XRD and BET analysis that the surface area of MgO (100) is significantly smaller than that of the MgO (111) and MgO (110) supports, which is regarded as unsuitable for fair comparisons on the electrochemical properties between the supports. Therefore, Ru NPs were only loaded onto the MgO (111) and MgO (110) supports for further investigations.

6.4.4 ICP-MS Analysis

Table 6.2 ICP-MS analysis of metals concentrations loaded on different supports.

Samples	Ru-MgO (110)	Ru-MgO (111)	Commercial Pt/C	Ru/C
Metal concentrations (wt%)	15.7	14.2	20.2	21.4

The accurate concentrations of Ru NPs loaded on different MgO supports were analysed by the ICP-MS. In Table 6.2, it can be observed that the Ru concentrations are 15.7 wt% and 14.2 wt% on the MgO (110) and MgO (111) supports respectively, which are comparable with the theoretical values (20 wt%) obtaining by the stoichiometry calculations. The as-prepared Ru/C catalysts give a metal loading of 21.4 wt% while the commercial Pt/C catalysts used for comparisons in this chapter have a Pt concentration of 20.2 wt% as analysed in ICP-MS techniques.

6.5 Catalytic Performance in HER

6.5.1 Experimental Methods

For details on experimental methods, see chapter 3 section 3.2.3.

Briefly, the as-prepared catalyst ink of 20 wt% Pt/C, 20 wt% Ru/C, 20 wt% Ru-MgO (111) and 20 wt% Ru-MgO (110) were spray-cast on the carbon paper respectively until obtaining the catalyst loadings of 0.5 ± 0.1 mg cm^{-2}. All electrochemical measurements were performed at room temperature using a standard three-electrode system on the electrochemical workstation (AUTOLAB PGSTAT320N) with the graphite rods as counter electrodes and catalyst-cast carbon paper as working electrodes. Ag/AgCl (saturated KCl) was used as reference electrode in 0.5 M H_2SO_4 electrolyte. The electrolyte was purged with N_2 gas for 30 minutes to get rid of dissolved O_2 in the solution. Before catalysts were tested for their activities, they were cycled between 0.5 V and -1.2 V vs RHE at 50 mVs^{-1} for at least 10 cycles. Linear scan voltammetry was carried out to evaluate the HER activities by scanning from 0 V to -2.3 V vs RHE at a scan rate of 5 mV s^{-1}. The current density is obtained from dividing the current by the geometric area of the carbon paper electrode (1 cm^2). The potential measured against Ag/AgCl (sat. KCl) reference electrode is converted to the potential versus RHE via Nernst equation (Equation 3.5) using 0.5 M H_2SO_4 as electrolyte ($pH \approx 0$).

The operando electrochemical synchrotron XRD measurements was carried out via a specially designed Teflon cell with sapphire windows that allowed the synchrotron X-ray beam going through. The catalyst-cast working electrode was placed at the centre of the window, and the graphite rod counter electrode and Ag/AgCl reference electrode were placed on the sides. The electrolyte concentration was diluted to 0.05 M to minimize the problems associated with the high background generated from the solution scattering.

6.5.2 Results and Discussions

The electrochemical HER performance of the 20 wt% Ru on MgO supports, 20 wt% Ru/C and commercial 20 wt% Pt/C catalysts, encoded respectively as Ru-MgO (111), Ru-MgO (110), Ru/C and Pt/C, were explored with linear sweep voltammetry (LSV) in a conventional three-electrode system.

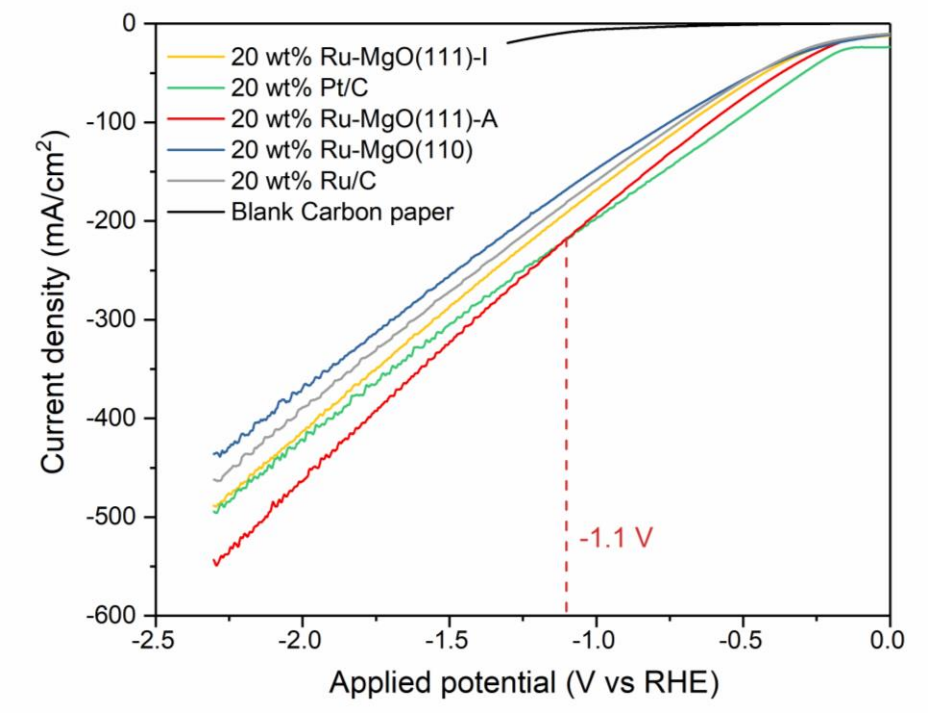


Figure 6.3 LSV polarization curves of the as-prepared Ru-MgO (111), Pt/C, Ru/C, Ru-MgO (110) and blank carbon paper in 0.5 M H_2SO_4. I (initial) and A (after) are corresponding to the Ru-MgO (111) catalysts before and after 100 scans respectively. The scan rate is 5 mV/s.

In Figure 6.3, it shows the LSV polarization curves of the four electrocatalysts and blank carbon paper at a range of applied potentials from 0 V to -2.3 V vs RHE in 0.5 M H_2SO_4 electrolyte. The LSV polarization curves were obtained at a scan rate of 5 mV s^{-1} after the initial cyclic voltammetry (CV) scans for 10 cycles at a scan rate of 50 mV s^{-1}. The Ru-MgO (111)-I and Ru-MgO (111)-A are the LSV polarization curves before and after 100 scans at a scan rate of 5 mV s^{-1} at the potential range between 0 and -2.3 V vs RHE. As observed in Figure 6.3, the blank carbon paper shows negligible activity while the commercial Pt/C gives the highest value in current density compared with the other three catalysts at 0 to -1.1 V region. Surprisingly, after 100 scans of activations, the Ru-MgO (111)-A shows an outstanding catalytic performance that outperforms the commercial Pt/C catalysts from -1.1 V onwards. And it is found that the Ru-MgO (111)-A gives a higher current density of 10 % than that of the benchmark Pt/C at -2.3 V (548 mA cm^{-2} versus 495 mA cm^{-2}), even though the latter has a higher support surface area and higher noble metal loadings as shown in Table 6.1 and 6.2.

At the same time, Ru/C and Ru-MgO (110) were also analysed by LSV for comparison. The Ru-MgO (110) shows more positive current densities followed by Ru/C and Ru-MgO (111) at the whole applied potential range. To further investigate the catalytic activity difference based on cycling numbers of the support, 100 scans of LSV were carried out on Ru-MgO (110) as shown in Figure 6.4.

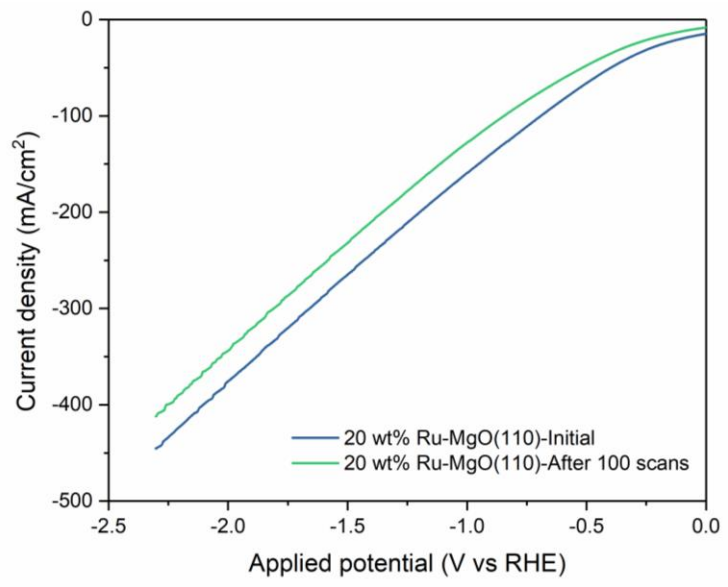


Figure 6.4 LSV polarization curves before and after 100 scans on the Ru-MgO (110) in 0.5M H_2SO_4. The scan rate is 5 mV/s.

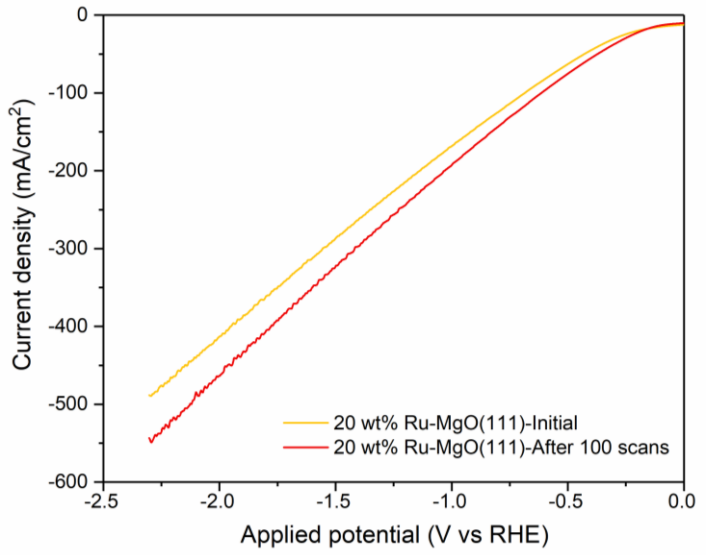


Figure 6.5 LSV polarization curves before and after 100 scans on Ru-MgO (111) in 0.5M H_2SO_4. The scan rate is 5 mV/s.

In Figure 6.4 and 6.5, the LSVs were conducted between 0 V and -2.3 V vs RHE at a scan rate of 5 mV/s in 0.5 M H_2SO_4. Ru-MgO (110) show decreased activities with increasing cycling numbers, which is in contrast to the Ru-MgO (111) (Figure 6.5). This phenomenon is also verified by the chronoamperometry measurements as shown in Figure 6.6 that the current

densities of Ru-MgO (110) decrease gradually as the electrochemical reaction progresses due to the degradation of catalytic activities.

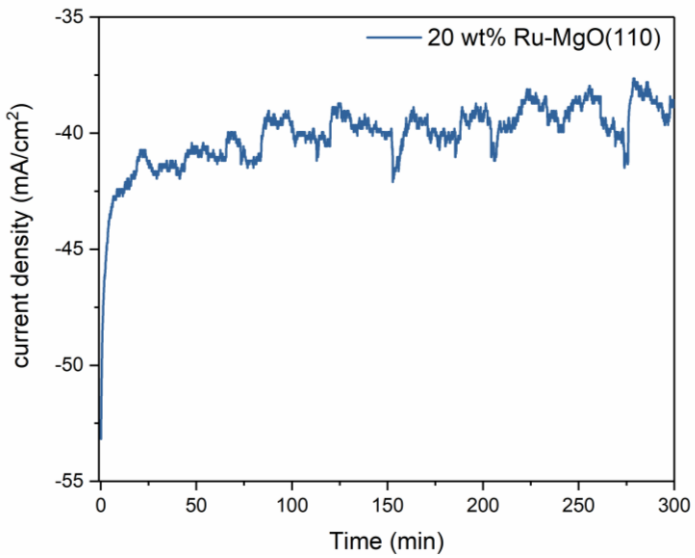


Figure 6.6 Chronoamperometric curve of the Ru-MgO (110) at -1.8 V versus RHE for 300 min in 0.05 M H_2SO_4 electrolyte.

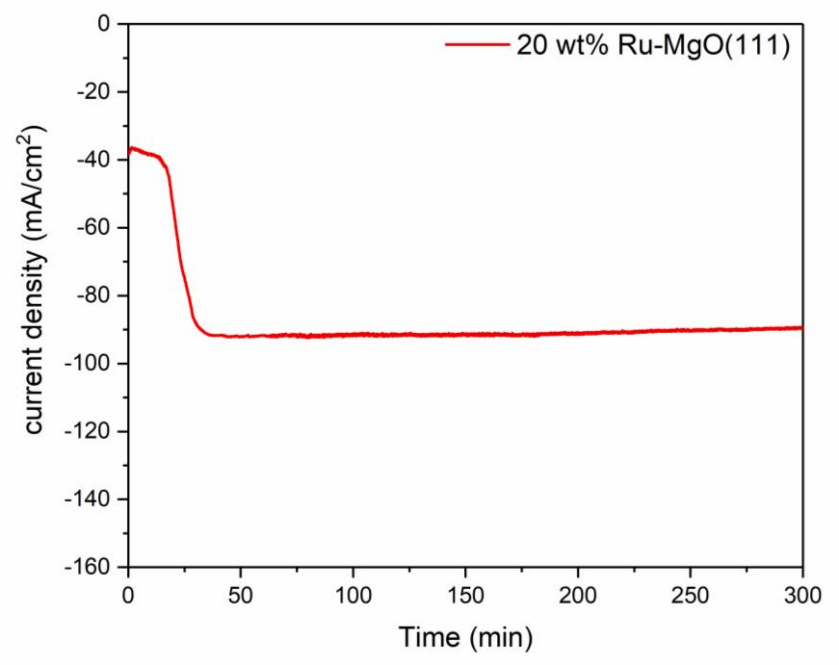


Figure 6.7 Chronoamperometric curve of the Ru-MgO (111) at -1.8 V versus RHE for 300 min in 0.05 M H_2SO_4 electrolyte.

In contrast to the Ru-MgO (110), the current densities of Ru-MgO (111) are found to gradually increase from -36.8 to -91.8 mA cm^{-2} in the first 35 minutes, resulting in an enhancement of 149.5% as shown in Figure 6.7. It is therefore indicated that the Ru-MgO (111) is transforming to an active phase that displays outstanding HER activity, and the activity is subsequently stabilized without obvious degradations. As a result, both the LSV measurements and chronoamperometric analysis imply a probable electrochemical activation process of the Ru-MgO (111) catalyst during HER, which is then explored by the operando SXRD characterizations.

6.6 Structure-Activity Correlations on MgO Supports

In this section, a series of techniques were employed to investigate the underlying activation process of the Ru-MgO (111) under acidic conditions, which includes the operando synchrotron XRD and ex-situ TEM, SAED and XPS analysis.

6.6.1 XPS Analysis

To further investigate the changes in surface structure of the Ru-MgO (111) sample during HER, XPS characterization was employed. All the samples were etched by Ar ions for 60 s to clean the surface before the experimental measurements. All the spectra are calibrated with respect to the Mg 2s peak of 88.1 eV since the standard carbon peaks overlap with Ru 3d peaks.[32] As shown in Figure 6.8, the O1s XPS spectra can be resolved into [OH] (higher binding energy at 531-532.5 eV) and [O^{2-}] (lower binding energy at 529-530 eV) components (Table 6.3).[32] It can be observed that a considerable percentage of [OH] (~33%) presents at the beginning of the reaction (0 min). This may be due to the extensive proton stabilization effect on the oxygen-terminated surfaces of the highly energetic polar facets during the synthesis. Interestingly, as seen from the Figure 6.8, when the electrochemical reduction time proceeds, the [OH] component increases gradually while the [O^{2-}] decreases proportionally. After around 3 hours of reaction, the protons are extensively covered on the MgO surface while the [OH]

portion almost doubles when compared with the starting point (from 33.3% to 65.1%). On the other hand, a control experiment in the absence of applied potential was carried out for comparison and no enhancement in [OH] was recorded from the sample. Such unusual high [OH] content may suggest that the OH is formed by electrochemical H^+ hydrolysis to MgO (111) beyond the top surface layer.

Table 6.3 Resolved components area ratio of OH and O^{2-} in XPS analysis.

	OH (BE eV)	**Intensity**	**Ratio (%)**	**O^{2-} (BE eV)**	**Intensity**	**Ratio (%)**
0 min	532.5	27198	33.3	530.7	54598	66.7
10 min	532.4	23984	37.1	530.7	40602	62.9
50min	532.1	34548	44.7	530.2	42691	55.3
100 min	532.1	46291	52.9	530.1	41184	47.1
200 min	532	55831	65.1	530	29911	34.9

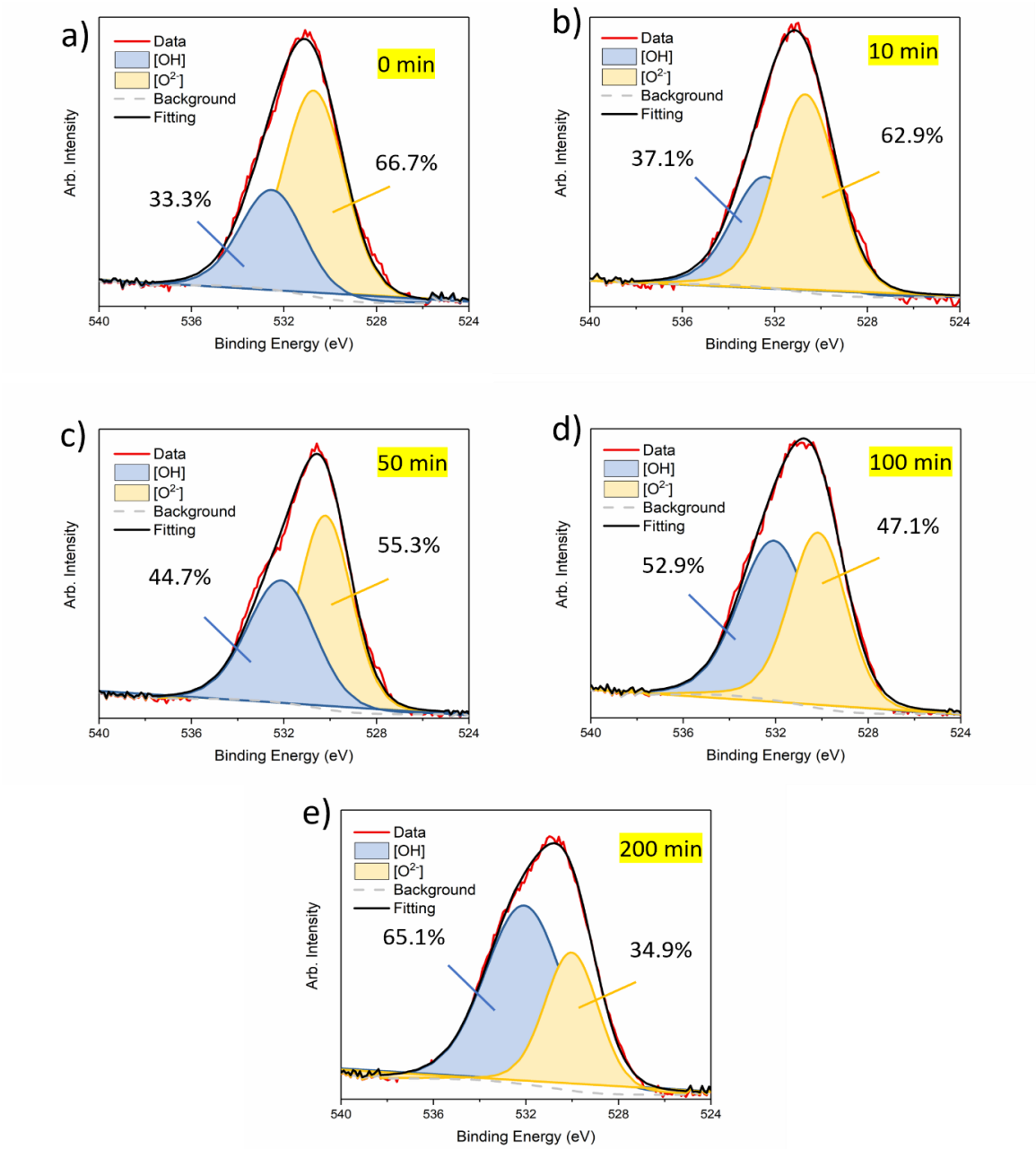


Figure 6.8 XPS profile of O 1s region at different time **a)** 0 min, **b)** 10 min, **c)** 50 min, **d)** 100 min and **e)** 200 min of the reaction. The blue shaded area is the [OH] component and the yellow shaded area is the [O^{2-}] component.

6.6.2 Operando SXRD Measurements

The operando electrochemical synchrotron XRD measurements were carried out with the specially designed three-electrode cell as described in chapter 3, section 3.2.3. The synchrotron XRD data was collected simultaneously during the chronoamperometry measurement at a constant applied potential of -1.8 V versus RHE as shown in Figure 6.7. The electrolyte concentration was diluted to 0.05 M to minimize the problems associated with the high background generated by the solution scatterings.

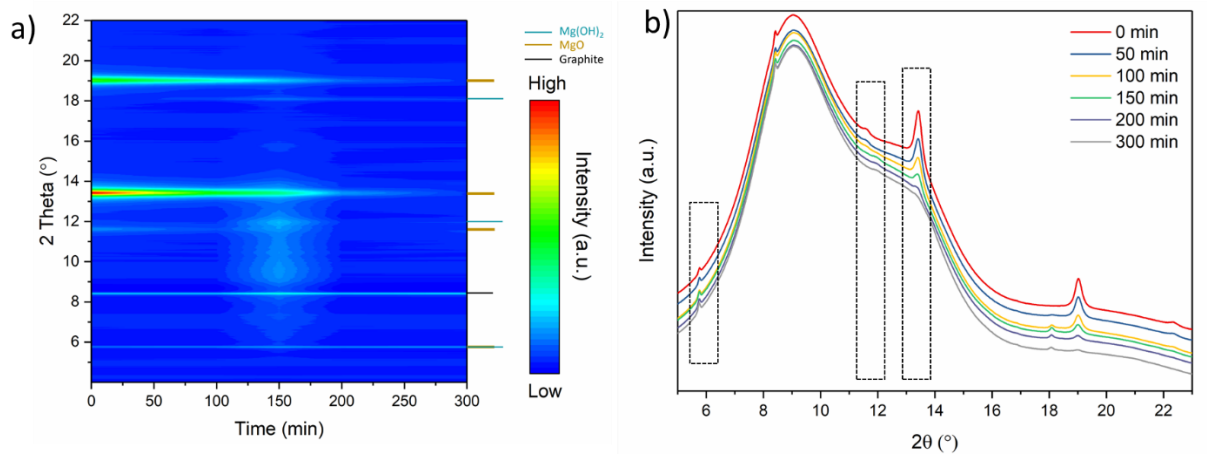


Figure 6.9 a) In-situ contour plot and **b)** SXRD patterns of the Ru-MgO (111) samples under -1.8 V versus RHE in 0.05 M H_2SO_4 with structural changing to $Mg(OH)_2$. The diffraction peaks with changing intensities over reaction time in the black dotted boxes (from left to right) were the characteristic peaks of $Mg(OH)_2$ (001), MgO (111) and MgO (200), respectively.

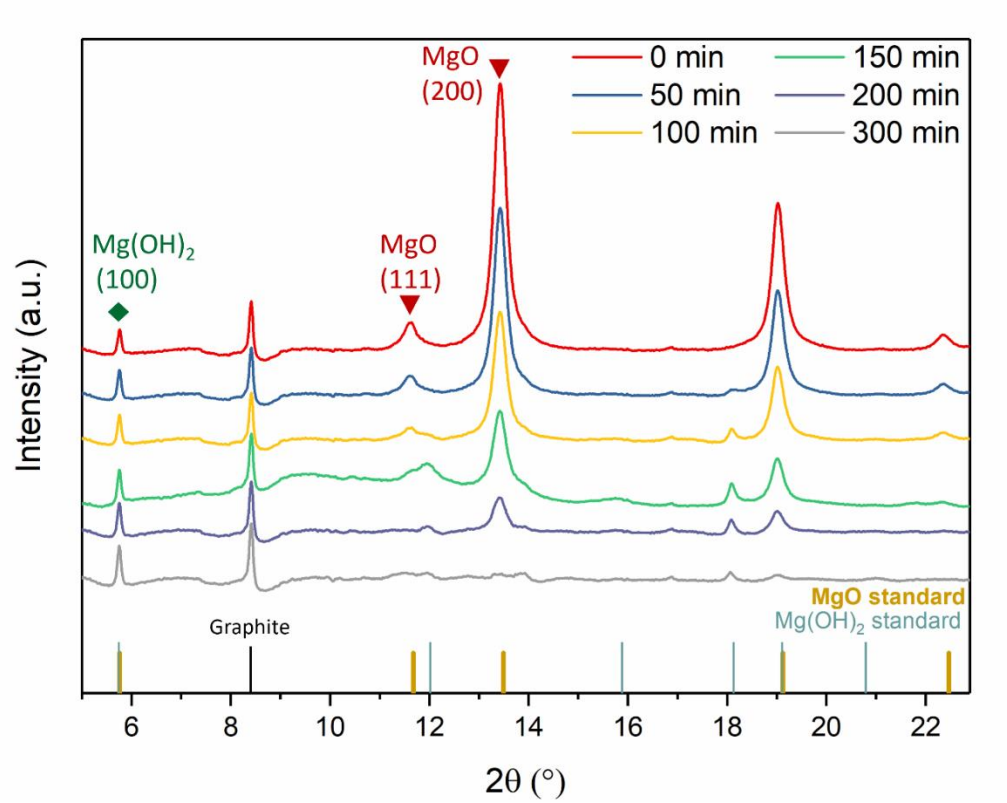


Figure 6.10 Background-subtracted operando SXRD patterns of the Ru-MgO (111) samples under -1.8 V versus RHE in 0.05 M H_2SO_4 with the structural changing to $Mg(OH)_2$. The reference diffraction patterns of MgO and $Mg(OH)_2$ are shown at the bottom for comparisons.

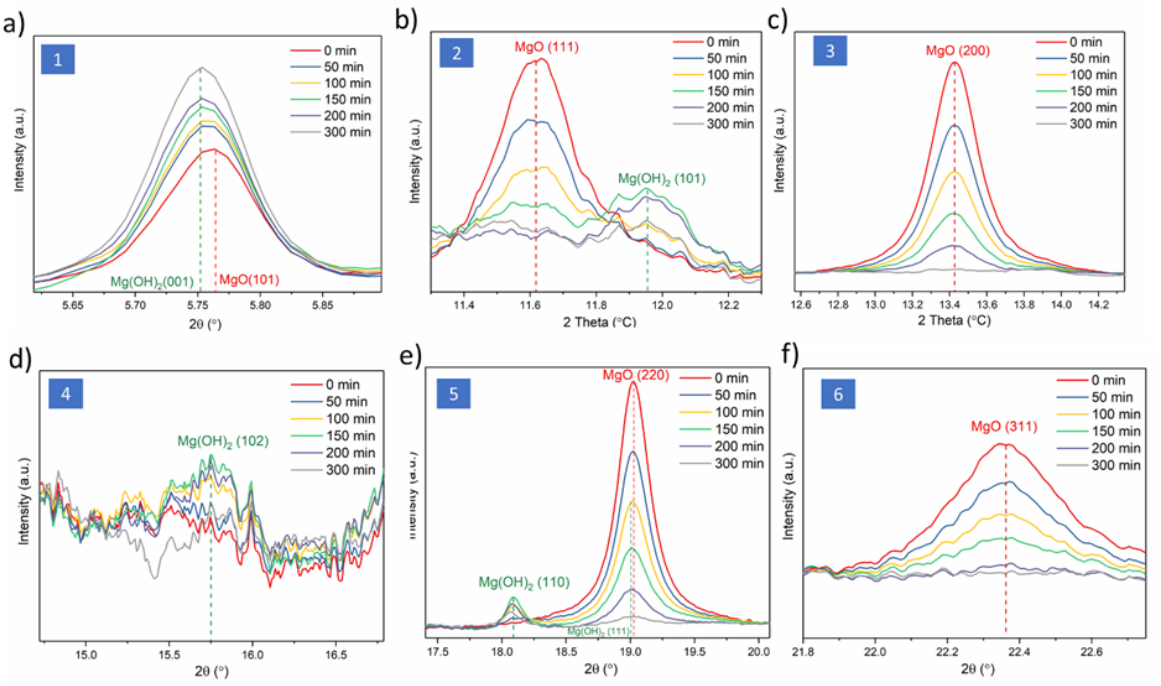


Figure 6.11 The enlarged characteristic peaks of MgO and $Mg(OH)_2$ in six different 2 theta regions.

By comparing the standard XRD diffractograms of MgO and $Mg(OH)_2$ with operando SXRD diffraction patterns in Figure 6.9 and 6.10, it shows an obvious in-situ structural change from cubic MgO to hexagonal $Mg(OH)_2$ during the HER process. As mentioned in Figure 6.7, the current density gradually increases from 36.8 to 91.8 mA cm^{-2} in the first 35 minutes, at the same time, the characteristic peaks of the cubic MgO at 11.7^o (111), 13.5^o (200), 19.0^o (220) and 22.5^o (311) are decreasing gradually in intensity as the reaction progresses. At the same time, four new diffraction peaks at 5.8^o, 12.0^o, 15.9^o and 18.1^o are forming in the SXRD patterns as shown in Figure 6.10 and 6.11, which are the characteristic peaks for the hexagonal $Mg(OH)_2$. These can be readily identified as (001), (101), (102), and (110) reflections, respectively. It is clearly indicating that the formation of the $Mg(OH)_2$ peaks is derived at the expenses of MgO peaks, signifying a structural change from cubic MgO to hexagonal $Mg(OH)_2$. The peak located at 8.3^o remains unchanged over the reaction time is corresponding to the graphite on carbon paper. Additionally, the MgO (101) and (220) peaks are in similar positions as that of $Mg(OH)_2$ (001) and (110), giving the two diffraction peaks at around 5.8^o and 19.0^o as shown in Figure 6.11. However, the peak at 5.8^o is dominated by $Mg(OH)_2$ (001) with enhanced intensity whereas MgO (220) is dominating at the peak of 19.0^o, showing a decrease intensity over reaction time.

As a result, the chronoamperometric measurements and the SXRD analysis clearly imply that the catalytic activity enhancement is greatly correlated to the structural change of the MgO supports. In order to further investigate the structural change mechanisms of the as-prepared MgO supports, the apparent intensity variations of the three characteristic peaks of $Mg(OH)_2$ and MgO in low angle ranges (see Figure 6.10) are plotted against the reaction time in Figure 6.12.

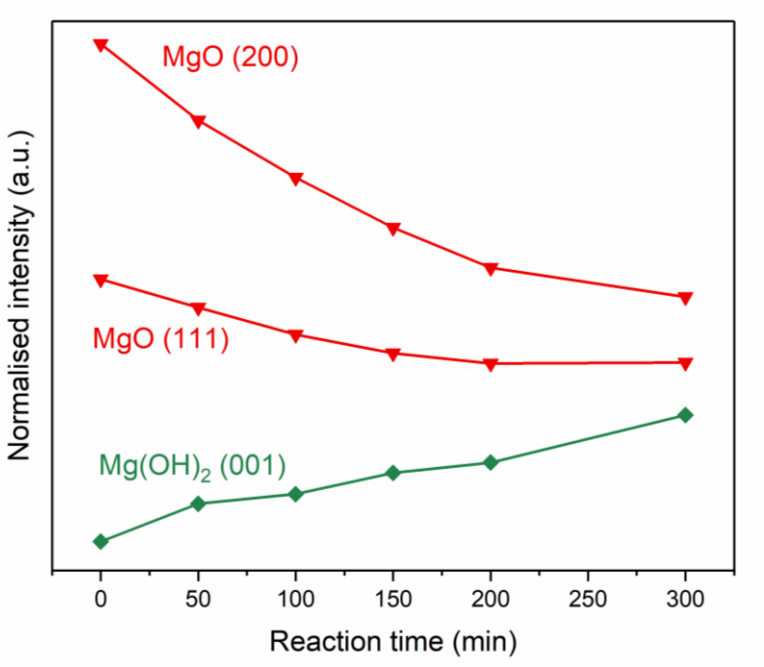


Figure 6.12 The corresponding normalised intensity variations of MgO (200), MgO (111) and $Mg(OH)_2$ (001) as the reaction progresses.

From 0 min to 300 min, the diffraction peaks for (111) at 11.7° and (200) at 13.5° of MgO are diminishing with a concomitant increase in the intensity of diffraction peak at 5.8° due to the formation of the $Mg(OH)_2$ (001) facets. As illustrated in Figure 6.13, it shows a topotactic conversion between MgO and $Mg(OH)_2$ with a crystallographic orientation relationship where the MgO (111) and MgO $[1\bar{1}0]$ are parallel to the $Mg(OH)_2$ (001) and $Mg(OH)_2$ [110] respectively.[29,33,34] It is clearly indicating that the cubic MgO unit cell expands along the MgO [111] direction with the structural transformation to hexagonal $Mg(OH)_2$ via electrochemical hydrolysis.

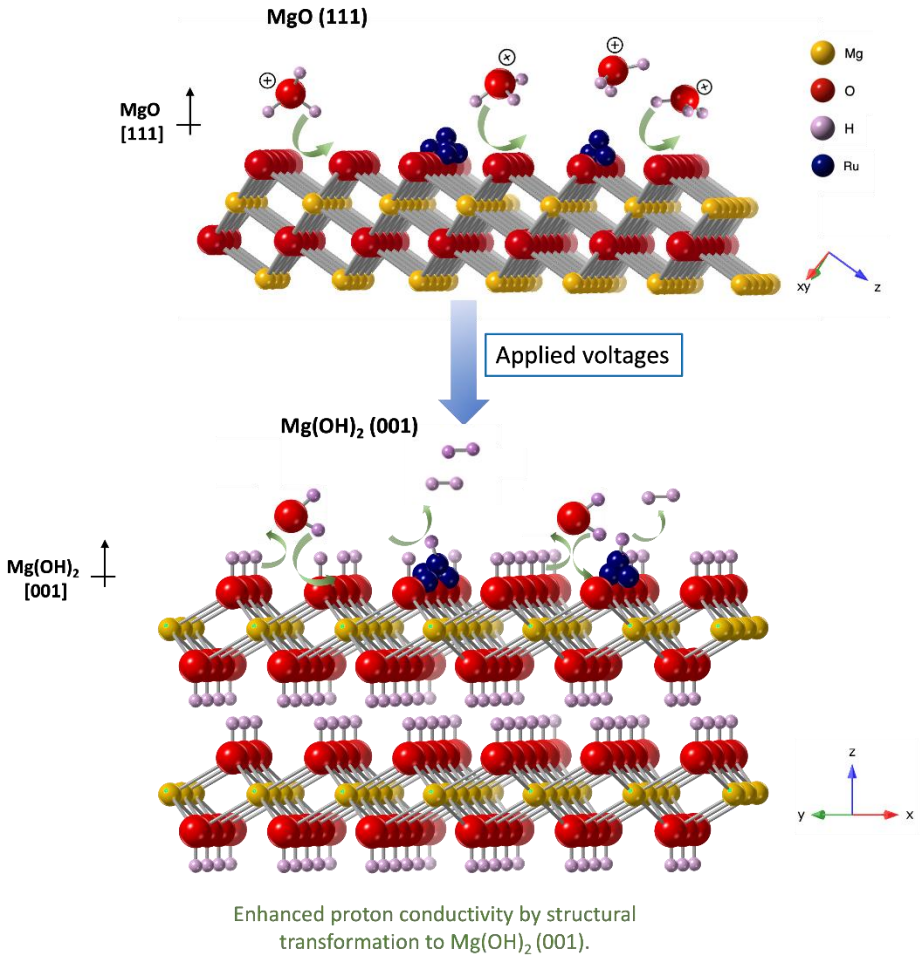


Figure 6.13 Schematic representations of the structural transformation from MgO to $Mg(OH)_2$ via electrochemical hydrolysis on MgO (111) support. The hydronium ions are reduced on the Ru clusters which are supported on the MgO or $Mg(OH)_2$.

Initially, the Ru clusters supported on MgO (111) facets provide catalytic sites to the surrounded hydronium (H_3O^+) for proton reduction. As the electrochemical reaction progresses, the MgO unit cells with preferential (111) exposed facets are expanded under applied potentials along the [111] direction via topotactic transitions, in which protons are adsorbing on the surface and penetrating through the (111) planes. This will lead to the Mg-OH bond formations in between the two Mg layers under electrochemical hydrolysis, resulting in a <001> oriented $Mg(OH)_2$ nanosheet supports. In this case, the $Mg(OH)_2$ (001) surface provides an exciting and efficient pathway for proton hopping (in the form of hydrogen bonding), which gives an enhanced proton conductivity to allow the proton diffusion and being reduced on the Ru

clusters. As a result, with the structural transformation from MgO (111) phase to $Mg(OH)_2$ (001), the surface hydroxyl groups can potentially enhance the proton conductivities and facilitate the proton reduction process, which leads to increased current densities during the electrochemical reactions.

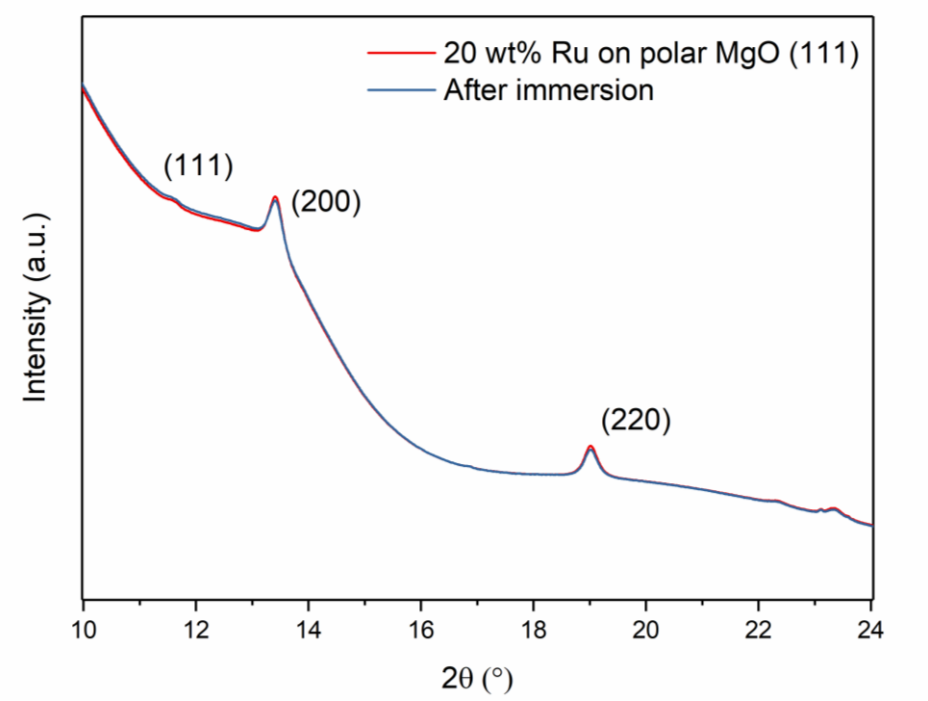


Figure 6.14 SXRD patterns of the Ru-MgO (111) before and after immersion in 0.05 M H_2SO_4 for 12 hours.

Besides, a control experiment was carried out by immersing the Ru-MgO (111) samples in the electrolyte for 12 hours without any applied potentials, and the sample was then examined by the synchrotron XRD. As shown in Figure 6.14, the diffraction patterns show no obvious difference before and after the immersion and no new diffraction peaks are formed, which confirms the stability of the Ru-MgO (111) sample in H_2SO_4 electrolyte without applied potentials. It is clearly implying that the topotactic transitions from MgO (111) to $Mg(OH)_2$ (001) are activated by the electrochemical process.

For comparison, the operando electrochemical synchrotron XRD measurements were also carried out on the Ru-MgO (110) sample under identical conditions.

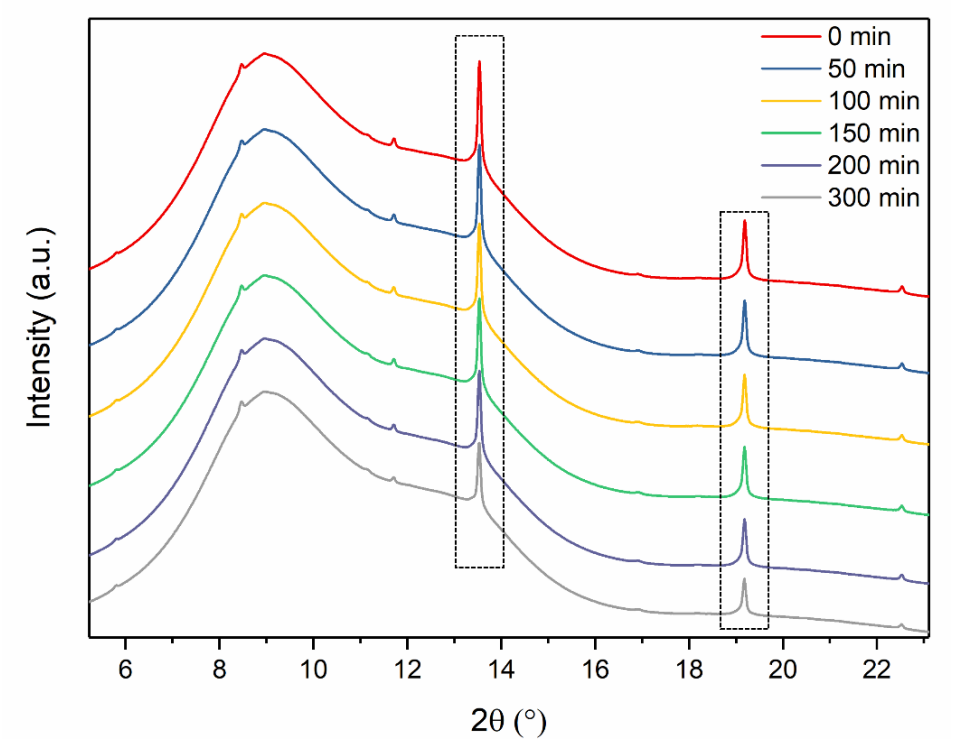


Figure 6.15 Operando SXRD patterns of the Ru-MgO (110) samples under -1.8 V versus RHE in 0.05 M H_2SO_4. The diffraction peaks in the black dotted boxes are MgO (200) and MgO (220) (from left to right).

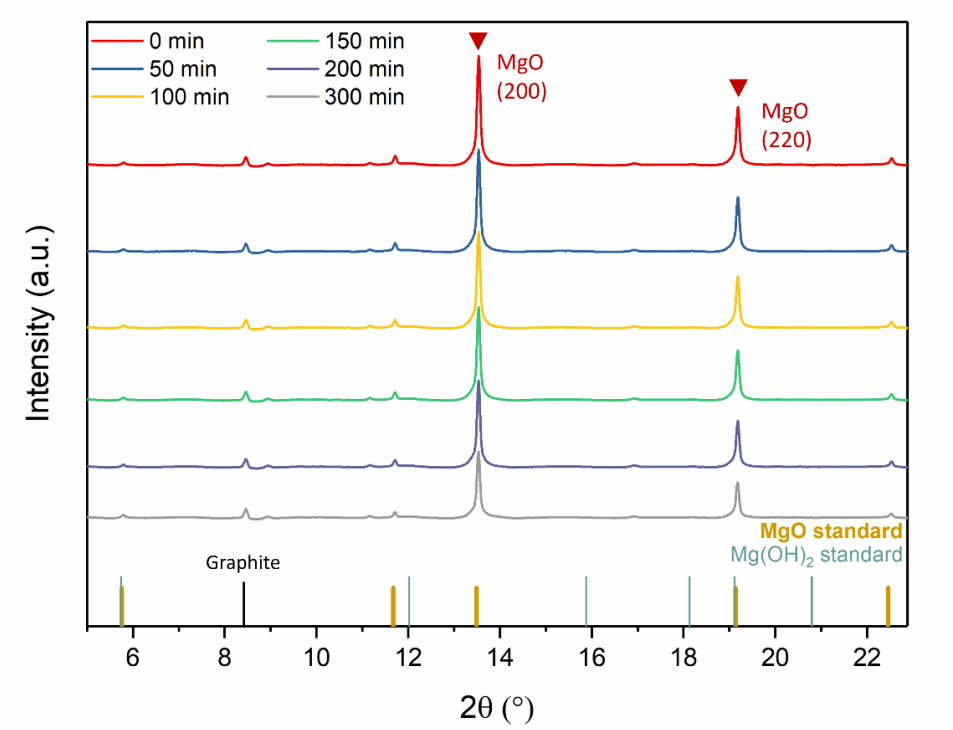


Figure 6.16 Background-subtracted operando SXRD patterns of the Ru-MgO (110) samples under -1.8 V versus RHE in 0.05 M H_2SO_4. The reference diffraction patterns of MgO and $Mg(OH)_2$ are shown at the bottom for comparisons.

As mentioned in Figure 6.6, the current densities of Ru-MgO (110) decrease gradually as the electrochemical reaction progresses because of the degradation of catalytic activities. Figure 6.15 and Figure 6.16 show the original and background-subtracted operando SXRD patterns of the Ru-MgO (110). The sharp characteristic peaks of the MgO (110) samples indicate the good crystallinity of the samples when compared with the as-prepared MgO (111) nanosheets, which is in line with the TEM imaging in Figure 6.2 that the MgO (110) samples show more compact structures. As shown in Figure 6.16, the SXRD patterns show no obvious changes over the reaction time but a small decrease in intensity of the (200) and (220) peaks as labelled. The decreased intensities may be due to the crystal collapses as a result of the applied potentials, which is causing the degradation of the catalytic activities as shown in the chronoamperometric curve of the Ru-MgO (110) samples. It is worthwhile to mention that there are no characteristic diffraction peaks correspond to the $Mg(OH)_2$ formed over the reaction time, which implies the unique topotactic transition properties of the Ru-MgO (111) reaction systems.

6.6.3 Electron Microscopy (EM) Analysis

Figures 6.17 shows the HRTEM and electron diffraction images of the as-prepared Ru NPs supported on MgO (111) nanosheets. It can be clearly observed from the HRTEM image (Figure 6.17a) that the dominant exposed facets remain to be the (111) arrangements without obvious surface reconstructions as confirmed by the Fast Fourier Transform (FFT) patterns in Figure 6.17b. The lattice spacing 0.24 nm of the MgO (111) in Figure 6.17b is in good agreement with the pure MgO (111) supports as shown in Figure 6.2a and 6.2d, which confirms the good stability of the preferential exposed (111) surface of the MgO supports during the sonochemical metal loading process. Additionally, Figure 6.17a indicates that Ru is in form of small nanoparticles of 2-5 nm and the FFT in Figure 6.17c confirms the characteristic Ru NP patterns.

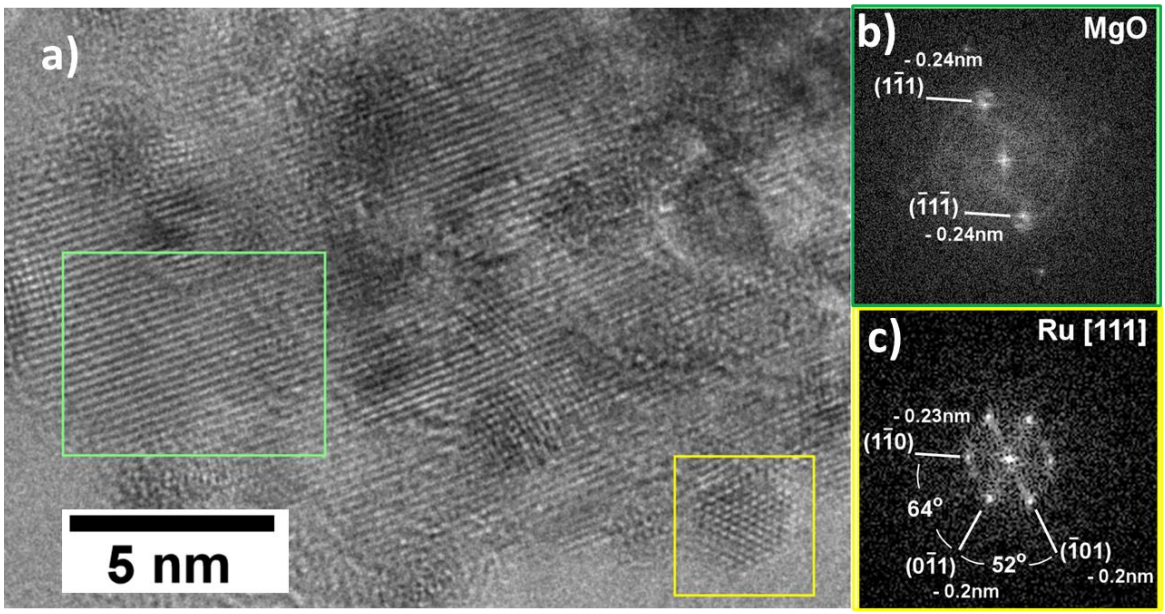


Figure 6.17 a) HRTEM of the Ru-MgO (111) samples with the corresponding FFT patterns of the faceted MgO (111) region in the green rectangle **b)** and Ru NP region in the yellow rectangle **c)**.

Having confirmed that the dominant exposed planes maintain (111) facets in the Ru-MgO (111) samples, TEM and EDX were further carried out to shed light on the dispersion of Ru NPs on the oxide supports. As shown in Figure 6.18, the HRTEM images and EDX analysis of the Ru-MgO (111) reveal even distributions of Ru species on the MgO (111) nanosheets. Additionally, due to a relatively high metal loading of 20 wt%, most of the Ru species are in the form of nanoparticles (NPs).

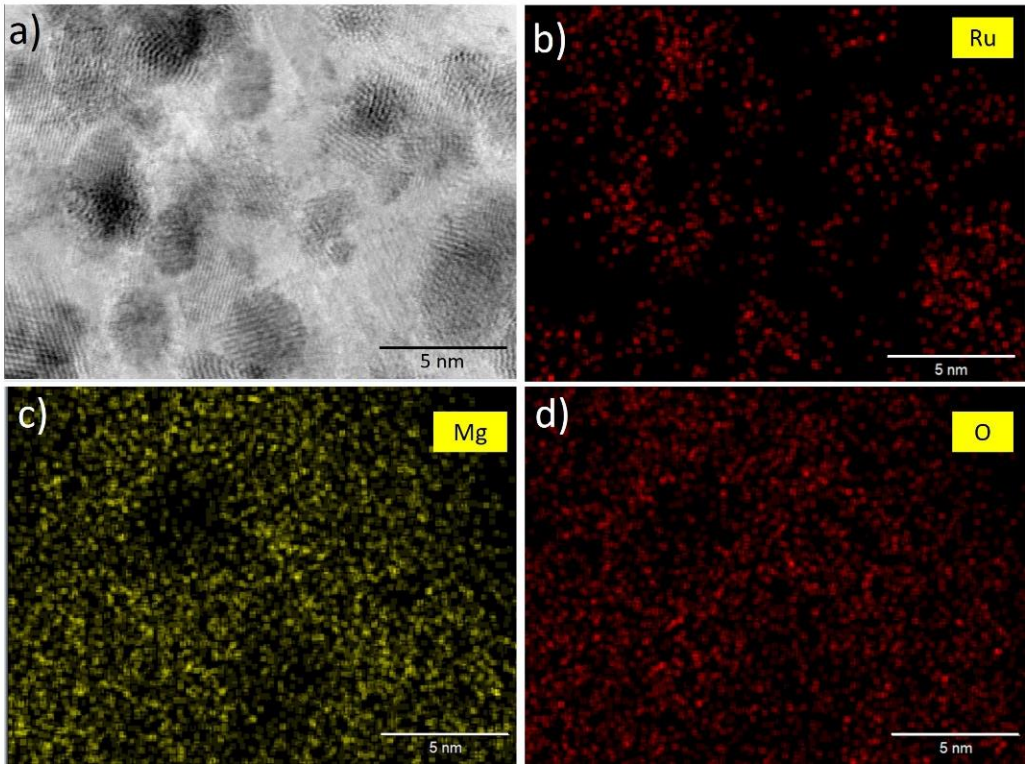


Figure 6.18 a) HRTEM of the as-prepared Ru-MgO (111) samples with the corresponding EDX analysis of **b)** Ru K-edge, **c)** Mg K-edge and **d)** O K-edge.

To further verify the structural and compositional changes of the Ru-MgO (111) samples, ex-situ TEM was employed to clarify the time-dependent phase evolutions. The electrochemical reaction was performed at -1.8 V versus RHE in 0.5 M H_2SO_4 electrolyte, and the samples were collected at 0, 10, 50 and 200 minutes for TEM imaging. As shown in Figure 6.19a, the Ru-MgO (111) samples show hexagonal nanosheet structures with smooth and flat surface. Also, the corresponding SAED (Figure 6.19e) shows the highly crystalline nature of the samples with single spot patterns. After 10 minutes, the MgO (111) supports remains hexagonal nanosheet shapes (Figure 6.19b) and the corresponding SAED (Figure 6.19f) demonstrates that the MgO is still the major phase while $Mg(OH)_2$ species start to grow during the electrochemical HER process. The heterostructures confirm the early stage of the phase transformations, which is consistent with the SXRD results (Figure 6.10) of the structural activation from MgO to $Mg(OH)_2$.

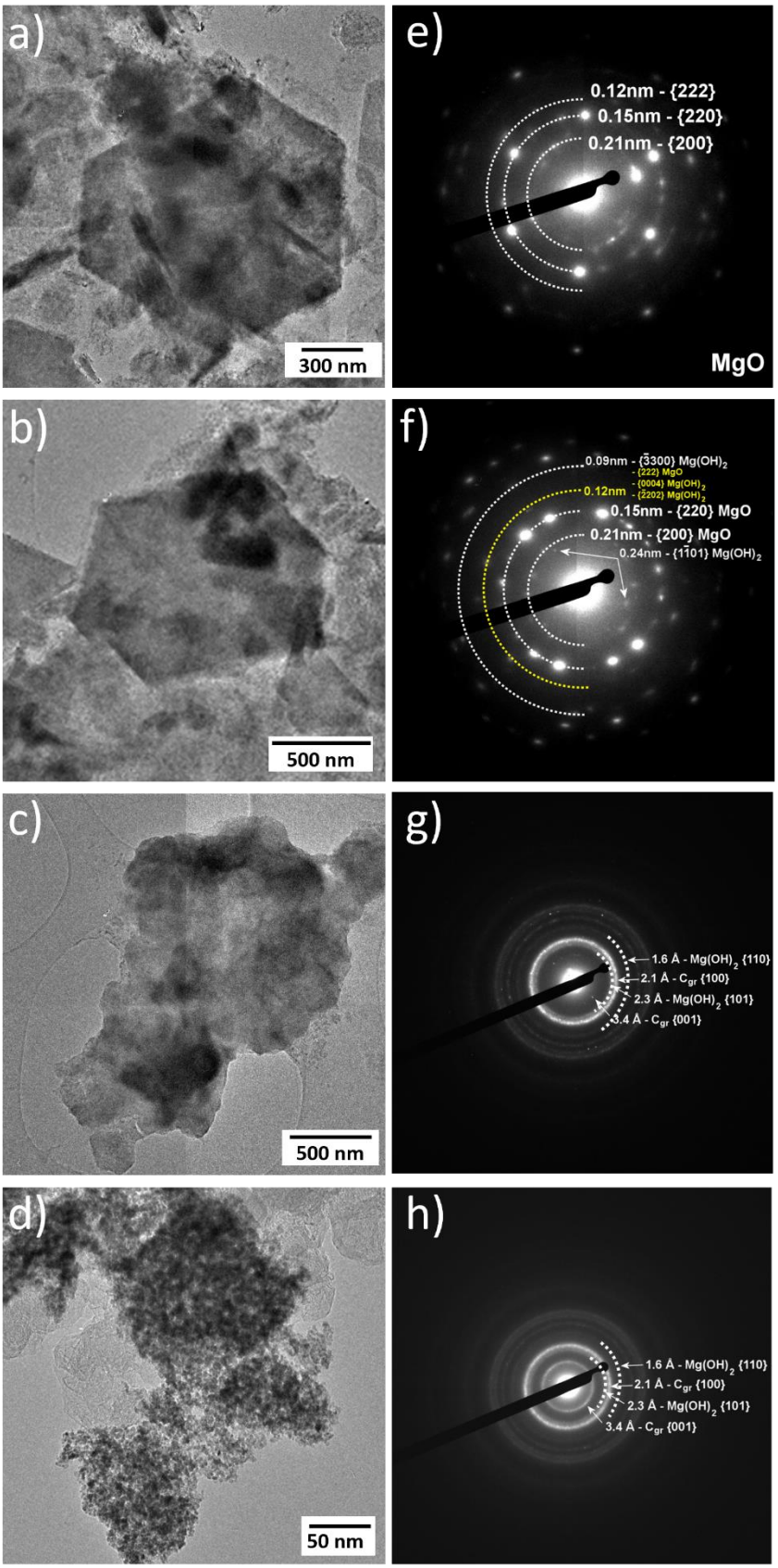


Figure 6.19 TEM images of the Ru-MgO (111) after **a)** 0 min, **b)** 10 min, **c)** 50 min and **d)** 200 min of reaction, and **e)-h)** the corresponding SAED patterns.

After 50 minutes of reaction, the Ru-MgO (111) samples become coarse and rough on the surface as shown in Figure 6.19c. The hexagonal structures start to distort, and it is on the verge of collapse. The corresponding SAED in Figure 6.19g indicates the $Mg(OH)_2$ phases increase further with most of the SAED patterns showing blurry rings rather than the scattered dots. This can be attributed to the multiple small domains in the sample.[35] The graphite rings may be caused by the contaminations from the graphite rod counter electrodes. In Figure 6.19d, the support structure finally succumbed to a ruptured state forming smaller nanoparticles after 200 minutes reaction. The structure is then dominated by the $Mg(OH)_2$ phases, which can be confirmed by the SAED patterns that only blurry rings of $Mg(OH)_2$ phases can be observed in Figure 6.19h. It can be concluded by the combinations of the SXRD and TEM results that the highly crystalline MgO particles (in the size of hundreds of nanometres) are gradually transformed into multiple small domains (tens of nanometres) with the dominating $Mg(OH)_2$ phases and diminishing MgO phases. It is worthwhile to mention that the $Mg(OH)_2$ phase is becoming the major phase from 50 minutes, which is in a good agreement with the chronoamperometric results that an electrochemical activation process is undergoing in the first 50 minutes for the structural change to $Mg(OH)_2$ and constructing the pathways for proton hopping. Thus, it is concluded that the Ru-$Mg(OH)_2$ is the actual active phase for the electrochemical hydrogen production from water splitting in this case.

6.6.4 DFT Modelling and Calculations

To understand how the polar MgO (111) surface can facilitate the structural activation to hydroxide phase as well as the subsequent proton hopping mechanism on the surface, DFT modelling was carried out. A 5 x 5 stoichiometric MgO (111) supercell was constructed, and a Ru atom was placed on the surface, which was eventually geometrically stabilised at the hollow site in between 3 surface oxygen atoms (Figure 6.20). Bader charge analysis further disseminates the electrostatic charge on Ru to be +1.3 presumably due to stabilization of

surface polarity (Table 6.4). In fact, it can be observed that the charge of the O atoms directly bind to Ru is -1.1 while those further away is -1.5 (Figure 6.20). This signifies the charge transfers between Ru and O when they are in direct contact, leading to charge quenching that relaxes the highly energetic surface. Similarly, cationic H^+ species can be favorably taken up by oxygen-terminated surface of MgO (111) for stabilization. In contrast, the charge of Ru on MgO (110) is localized to zero in the absence of the polar surface (Table 6.4).

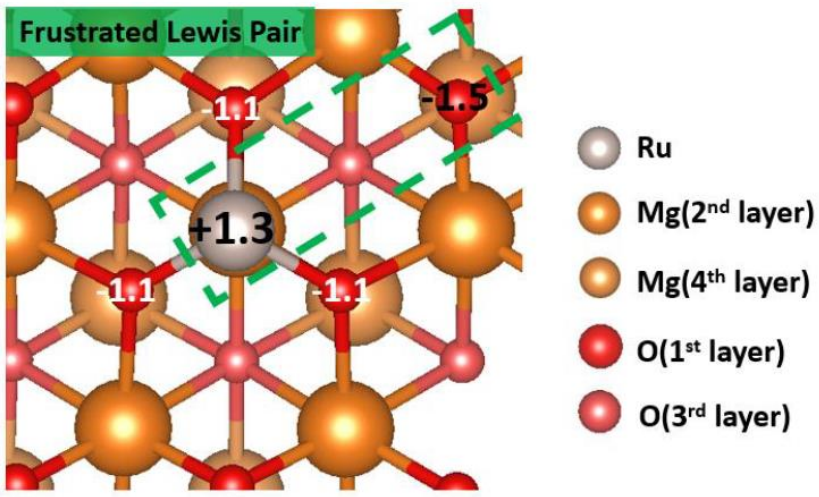


Figure 6.20. The optimised structure of Ru-MgO (111). The number on the atom represents the charge on the surface O and Ru atoms.

Table 6.4. The Bader charge calculation of Ru and O species on MgO (111) and MgO (110).

System	Ru adsorption site	q|e|		
		Ru	O bind with Ru	O no bind with Ru
Bare MgO	-	-	-	-0.971
Ru / MgO (111)	O Hollow atop Mg	+ 1.270	-1.050	-1.504
Ru/ MgO (110)	O-O Bridge atop Mg	- 0.238	-1.447	-

The dispersion of the Ru particles on the oxide support surface can be further determined by introducing another Ru atom into the system. As seen in figure 6.21, upon placing two Ru

atoms on the MgO (111) and MgO (110) respectively, it is energetically more favourable (E_{bind}) for the two Ru to disperse on MgO (111) due to high surface polarity; whereas the two Ru atoms will prefer aggregations to reduce unfavourable surface contact on MgO (110).

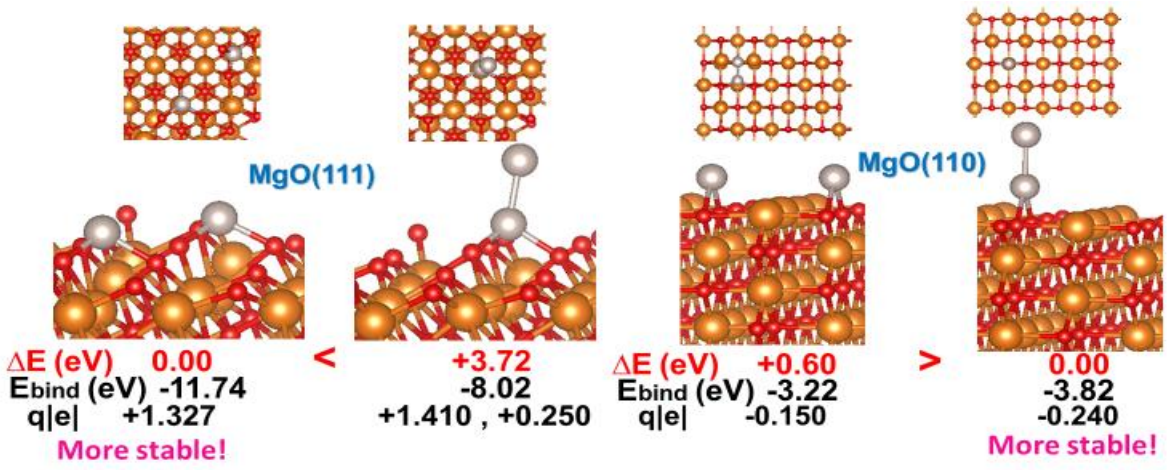


Figure 6.21 Binding energies of two separate Ru atoms and Ru_2 cluster on MgO (111) and MgO (110) supports.

Following the same logic, in H_2 atmosphere, the protonation of the MgO (111) supports leads to surface stabilization and $Mg(OH)_2$ (001) can ultimately be attained. As shown in Figure 6.22, the H_2 adsorption energy on MgO (111) (-4.0 eV) is much higher than when it is on the Ru atom (-1.03 eV), which implies a spontaneous migration from the Ru to the support upon dissociative adsorptions of H_2. The presence of Ru is crucial as it is experimentally proven no reaction will occur in the absence of Ru due to kinetic stability of MgO. In contrast, MgO (110) supports favour larger Ru cluster formations and aggregations under H_2 reduction atmosphere. Apparently, the high dispersity and high contact of Ru with the support surface properties of the as-synthesised Ru-MgO (111) renders it as a superior precursor to the hydroxide active phases. On the other hand, we have been unable to prepare the active form with Ru-$Mg(OH)_2$ directly as the precursors, presumably because the surface does not support extensive dispersions of Ru active species to form the required active interfaces.

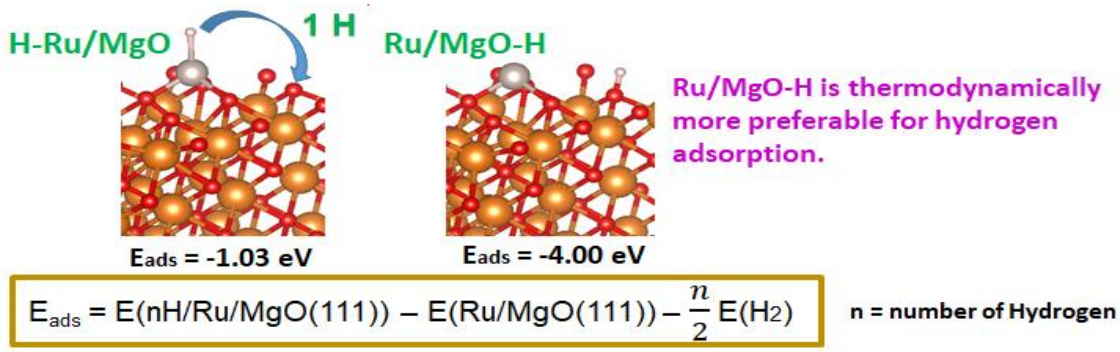


Figure 6.22 H-adsorption energies on the Ru atom supporting on MgO(111) and on the MgO(111) directly.

From these calculations, under electrochemical reaction in acidic electrolyte, it is anticipated that H^+ will favourably cover the surface to compensate the polarity of the Ru-MgO (111). It is interesting to see the extensive phase transformations from MgO (111) faceted crystals to $Mg(OH)_2$ (001) faceted particles as shown in the above electrochemical testing, in which the samples are used as HER electrocatalyst supports under a series of applied potentials. Without the applied potentials, a control experiment clearly shows the high kinetic stability of MgO against hydrolysis. Thus, it is believed that H^+ have been drawn into the internal structure of the layered MgO (111) faceted nanosheets by the applied potentials and the protonic repulsions between the protonated oxygens within the layers could facilitate the hydrolysis of the bulk phase for the phase transformations.

To probe the extent of hydroxylation on the MgO (111) surface, H atoms are added consecutively to the surface, and it is discovered that the 8-H state with one hydrogen vacancy is the most stable structure (Figure 6.23). When water molecule approaches the 8-H polar MgO (111) surface, its hydroxyl hydrogen (H_{w1}) will orient towards H-vacancy site, whereas the hydroxyl oxygen (O_w) will be attracted to the adjacent surface hydroxyl hydrogen (H_{m1}) on the hydroxylated MgO surface though hydrogen bonding (Figure 6.24). Under applied potentials, H_{w1} will be dissociated from the water molecule (at an activation energy of 0.04 eV, step (i))

and form new bond with surface O_{m1}. Meanwhile, the neighbouring O_{m2}-H_{m1} bond will be cleaved (activation energy of 0.06 eV, step (ii)) and the H_{m1} will form new bonding with the hydroxyl oxygen of the water molecule. In other words, the proton can hop across to the adjacent H-vacancy site in the presence of water. Apparently, the total activation energy of this 2-step process (0.10 eV) is smaller than that of the direct hopping (0.47 eV) as shown in Figure 6.25a, rendering the former a feasible pathway for protons to move across sites in the presence of water (Figure 6.25). This provides a solid foundation for the excellent proton conductivity of the active hydroxide phases stemmed from the structural activation of the polar magnesium oxide phases.

The two-step proton hopping process:

(i) $H_2O + O_{m1}^* \rightarrow HO + HO_{m1}^*$ $E_a = 0.04$ eV (Equation 6.1)

(ii) $HO + HO_{m2}^* \rightarrow H_2O + O_{m2}^*$ $E_a = 0.06$ eV (Equation 6.2)

* O_{m1} and O_{m2} are the surface oxygen sites of metal oxides.

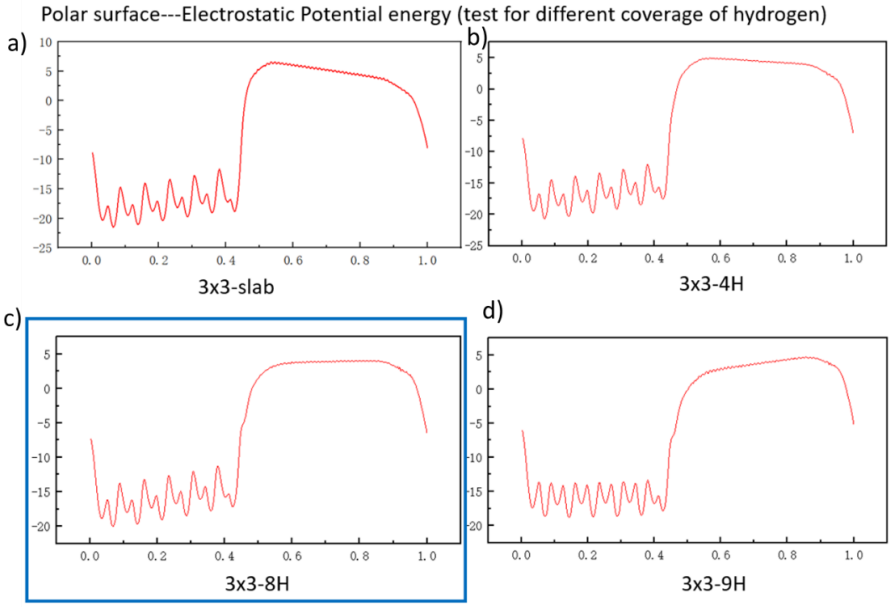


Figure 6.23 Electrostatic potential energy tests for different coverages of hydrogen atoms on MgO (111): **a)** 0-H, **b)** 4-H, **c)** 8-H, and **d)** 9-H, where x axis is the lattice position in surface normal direction (Å), and y axis is the plane average potential (eV).

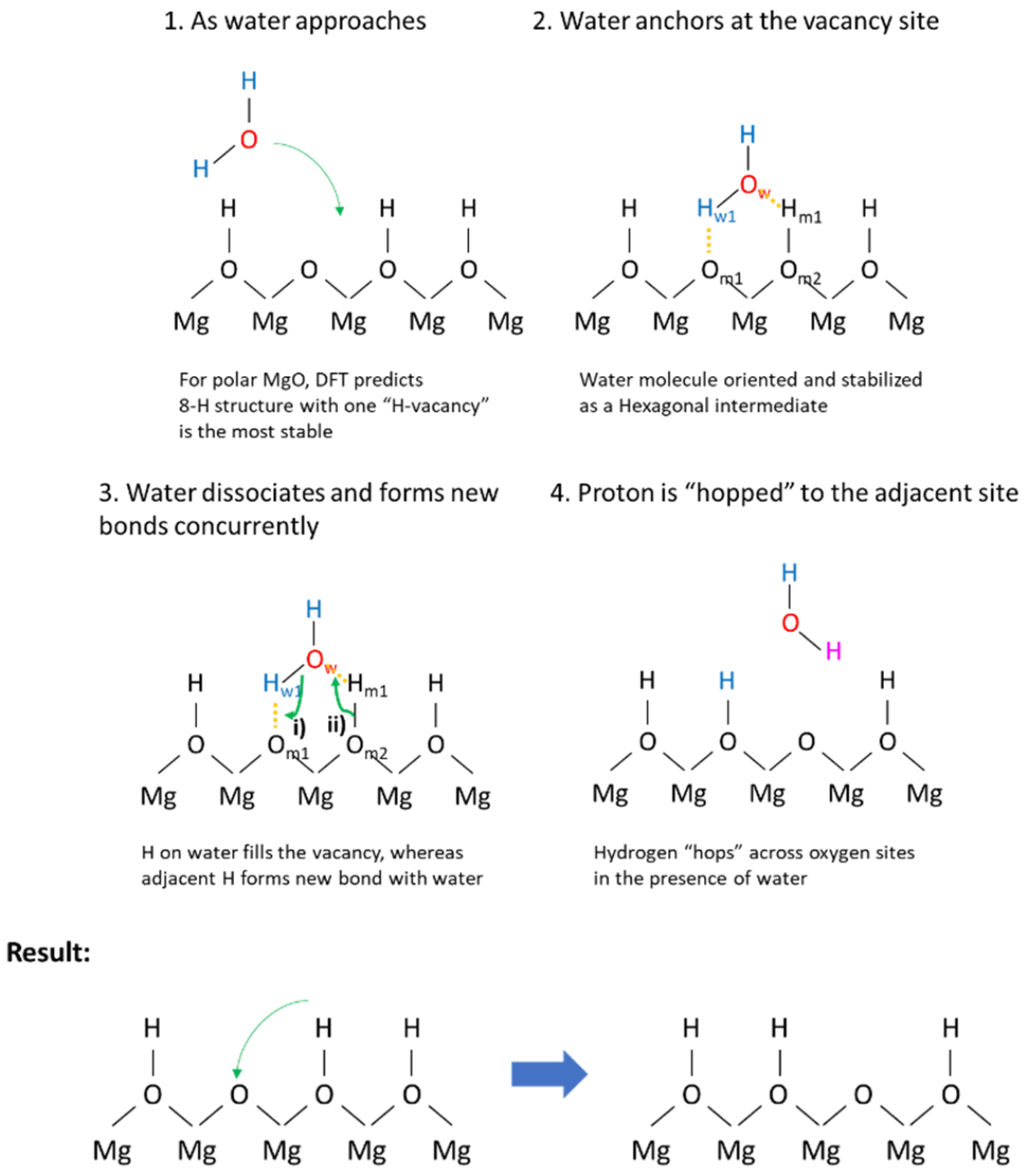


Figure 6.24 2-step proton hopping mechanism on 8-H hydroxylated surface assisted by water molecules.

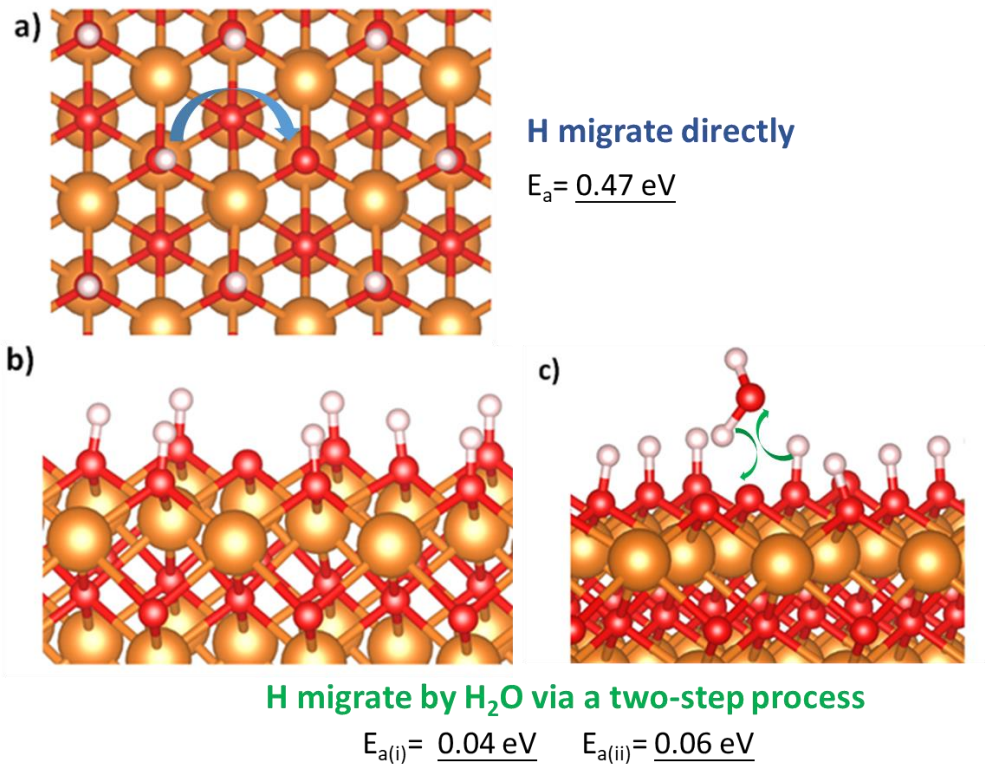


Figure 6.25 a) Direct proton migration on the hydroxylated MgO (111) surface with 8 adsorbed H atoms and 1 H vacancy (same surface feature as $Mg(OH)_2$ (001)) in top view); **b)** Side view of the 8-H hydroxylated polar MgO (111) surface and **c)** Indirect proton migration on the 8-H MgO (111) surface via H_2O at side view.

In short summary, DFT calculations have shed light on the stabilization of the surface polarity on MgO (111) provided by the cationic Ru^{2+} and H^+ species. Driven by the preferential adsorptions, protons can then hop across the surface hydroxyl sites on the $Mg(OH)_2$ (001) phase in the presence of water via a 2-step mechanism. This results in excellent proton conductivity that facilitates proton movements and improves HER activities.

6.7 Conclusions

In summary, we have successfully developed an activated magnesium hydroxide catalytic material with preferentially exposed (001) facets that offer prominent catalytic activities in hydrogen evolution reactions. The catalyst is synthesised from the electrochemical hydrolysis of polar magnesium oxide, causing an ordered topotactic transition to the hydroxide phase as

demonstrated by XPS and in-situ synchrotron XRD studies. Further calculation results elucidate that the surface hydroxyl sites are acting as Grotthuss-like channelled pathways to exert geometric control for protons to hop across, yielding a proton-conducting platform to facilitate HER. An enhancement of 149.5% in current density was found in the hydroxide catalysts when compared to the oxide counterpart before phase change, suggesting the importance of the hydroxide pathways. This study has demonstrated a novel method to synthesize ordered polar hydroxides materials that can be potentially applied in electrochemical reactions involving facile proton movements.

6.8 References

1. Mo, J. *et al.* Superior Performance of Ag over Pt for Hydrogen Evolution Reaction in Water Electrolysis under High Overpotentials. *ACS Appl. Energy Mater.* **2**, 1221–1228 (2019).
2. Li, Y. *et al.* Morphological Engineering of Winged Au@MoS2 Heterostructures for Electrocatalytic Hydrogen Evolution. *Nano Lett.* **18**, 7104–7110 (2018).
3. Luo, M. & Guo, S. Strain-controlled electrocatalysis on multimetallic nanomaterials. *Nat. Rev. Mater.* **2**, 1–14 (2017).
4. van Deelen, T. W., Hernández Mejía, C. & de Jong, K. P. Control of metal-support interactions in heterogeneous catalysts to enhance activity and selectivity. *Nat. Catal.* **2**, 955–970 (2019).
5. Guo, Y. *et al.* Low-Temperature CO2 Methanation over CeO2-Supported Ru Single Atoms, Nanoclusters, and Nanoparticles Competitively Tuned by Strong Metal-Support Interactions and H-Spillover Effect. *ACS Catal.* **8**, 6203–6215 (2018).
6. Campbell, C. T. Electronic perturbations. *Nat. Chem.* **4**, 597–598 (2012).
7. Wu, S. *et al.* Removal of Hydrogen Poisoning by Electrostatically Polar MgO Support for Low-Pressure NH 3 Synthesis at a High Rate over the Ru Catalyst. *ACS Catal.* **10**, 5614–5622 (2020).
8. Mutch, G. A. *et al.* Carbon Capture by Metal Oxides: Unleashing the Potential of the (111) Facet. *J. Am. Chem. Soc.* **140**, 4736–4742 (2018).
9. Sutradhar, N. *et al.* Controlled Synthesis of Different Morphologies of MgO and Their Use as Solid Base Catalysts. *J. Phys. Chem. C* **115**, 12308–12316 (2011).
10. Zhu, K., Hu, J., Kübel, C. & Richards, R. Efficient preparation and catalytic activity of MgO(111) nanosheets. *Angew. Chemie - Int. Ed.* **45**, 7277–7281 (2006).
11. Li, Y., Chi, S. & Tsang, E. Unusual Catalytic Properties of High-Energetic-Facet Polar Metal Oxides. *Acc. Chem. Res.* **54**, 366–378 (2021).

12. Noguera, C. Polar oxide surfaces. *J. Phys. Condens. Matter* **12**, R367–R410 (2000).

13. Wu, S. *et al.* Rapid Interchangeable Hydrogen , Hydride , and Proton Species at the Interface of Transition Metal Atom on Oxide Surface. *J. Am. Chem. Soc.* **143**, 9105–9112 (2021).

14. Li, Y. *et al.* Under-Water Superaerophobic Pine-Shaped Pt Nanoarray Electrode for Ultrahigh-Performance Hydrogen Evolution. *Adv. Funct. Mater.* **25**, 1737–1744 (2015).

15. Hansen, J. N. *et al.* Is There Anything Better than Pt for HER? *ACS Energy Lett.* **6**, 1175–1180 (2021).

16. Li, C. & Baek, J. B. Recent Advances in Noble Metal (Pt, Ru, and Ir)-Based Electrocatalysts for Efficient Hydrogen Evolution Reaction. *ACS Omega* **5**, 31–40 (2020).

17. Yang, Y. *et al.* Engineering Ruthenium-Based Electrocatalysts for Effective Hydrogen Evolution Reaction. *Nano-Micro Lett.* **13**, 1–20 (2021).

18. Yu, J. *et al.* Recent Advances and Prospective in Ruthenium-Based Materials for Electrochemical Water Splitting. *ACS Catal.* **9**, 9973–10011 (2019).

19. Du, L. *et al.* Advanced catalyst supports for PEM fuel cell cathodes. *Nano Energy* **29**, 314–322 (2016).

20. Huang, S., Ganesan, P., Park, S. & Popov, B. N. Development of a Titanium Dioxide-Supported Platinum Catalyst with Ultrahigh Stability for Polymer Electrolyte Membrane Fuel Cell Applications. *J. Am. Chem. Soc.* **131**, 13898–13899 (2009).

21. Lv, H. & Mu, S. Nano-ceramic support materials for low temperature fuel cell catalysts. *Nanoscale* **6**, 5063–5074 (2014).

22. Jiang, Z.-Z., Wang, Z.-B., Chu, Y.-Y., Gu, D.-M. & Yin, G.-P. Carbon riveted microcapsule Pt/MWCNTs-TiO2 catalyst prepared by in situ carbonized glucose with ultrahigh stability for proton exchange membrane fuel cell. *Energy Environ. Sci.* **4**, 2558–2566 (2011).

23. Wang, Y., Wilkinson, D. P. & Zhang, J. Noncarbon Support Materials for Polymer Electrolyte Membrane Fuel Cell Electrocatalysts. *Chem. Rev.* **111**, 7625–7651 (2011).

24. Marichy, C. *et al.* ALD SnO2 protective decoration enhances the durability of a Pt based electrocatalyst. *J. Mater. Chem. A* **4**, 969–975 (2016).

25. Bruix, A. *et al.* A new type of strong metal-support interaction and the production of H 2 through the transformation of water on Pt/CeO 2(111) and Pt/CeO x/TiO 2(110) catalysts. *J. Am. Chem. Soc.* **134**, 8968–8974 (2012).

26. Li, H. *et al.* The effect of microstructure and crystal defect on electrochemical performances of MgO nanobelts. *Electrochim. Acta* **123**, 103–110 (2014).

27. Chen, J., Tian, S., Lu, J. & Xiong, Y. Catalytic performance of MgO with different exposed crystal facets towards the ozonation of 4-chlorophenol. *Appl. Catal. A Gen.* **506**, 118–125 (2015).

28. T.Duffy, N.Madhusudhan & K.K.M.Lee. Mineralogy of Super-Earth Planets. in *Earth Systems and Enviromental Sciences* 149–178 (Elsevier, 2015).

29. Liu, P., Abdala, P. M., Goubert, G., Willinger, M. G. & Copéret, C. Ultrathin Single Crystalline MgO(111) Nanosheets. *Angew. Chemie - Int. Ed.* **60**, 3254–3260 (2021).

30. Wang, F., Ta, N. & Shen, W. MgO nanosheets, nanodisks, and nanofibers for the Meerwein-Ponndorf-Verley reaction. *Appl. Catal. A Gen.* **475**, 76–81 (2014).

31. Asadullah, M., Rahman, M. A., Motin, M. A. & Sultan, M. B. Preparation and adsorption studies of high specific surface area activated carbons obtained from the chemical activation of jute stick. *Adsorpt. Sci. Technol.* **24**, 761–770 (2006).

32. Larichev, Y. V, Moroz, B. L., Prosvirin, I. P., Likholobov, V. A. & Bukhtiyarov, V. I. XPS Study of Metal-Support Interaction in Ru / MgO Catalyst for Low-Temperature Ammonia Synthesis. *Chem. Sustain. Dev.* **11**, 155–160 (2003).

33. KIM, M. G., DAHMEN, U. & SEARCY, A. W. Structural Transformations in the Decomposition of Mg(OH)2 and MgCO3. *J. Am. Ceram. Soc.* **70**, 146–154 (1987).

34. Shinagawa, T., Chigane, M. & Izaki, M. Electrochemical Growth of Mg(OH)xLayered Films Stacked Parallel to the Substrates and Their Thermal Conversion to (111)-Oriented Nanoporous MgO Films. *ACS Omega* **6**, 2312–2317 (2021).

35. Williams, D. B. & Carter, C. B. *Transmission Electron Microscopy*. (Springer, Boston, MA, 2009).

Chapter 7 Conclusions and Outlook

Table of Contents

Chapter 7 Conclusions and Outlook 240
7.1 Conclusions 240
7.2 Outlook 242
7.3 Reference 243

7.1 Conclusions

This thesis explored 3 different catalytic systems for electrochemical hydrogen evolution reaction with each one of it focusing on distinct strategies to raise catalytic performance or lower the energy input.

Morphology-controlled silver nanoparticles supported on Vulcan carbon were first studied in the PEM electrolyser. In particular, Ag nanocubes showed superior catalytic performance, as determined by a current density of 3.44 A cm^{-2} at an applied potential of -2.5 V and outperformed the benchmark Pt/C catalysts by 20%. DFT calculations suggested that the hydrogen adsorption strengths on the surface of silver cubes was weaker than that of platinum. As more negative potential was applied (-2.5 V), the catalyst surface would have a high coverage of H atom to drive the change of the rate-determine step from Volmer to Tafel. Thus, the weaker Ag-H bond strength of Ag cubes NPs led to a faster hydrogen recombination rate than of the Pt/C.

The high HER activity of Ag, however, come at a cost of a high applied potential that increases the capital cost of the overall electrochemical system. From this respect, solar energy was exploited as an additional energy source to lower the power input. In order to efficiently capture the visible light, plasmonic silver and gold nanoparticles, with a broad light-absorption range, were selected and fabricated into a core-shell nanostructure. The sonochemical approach

further allowed the formation of a bimetallic atomic layer shell with precisely controlled silver to gold ratio as evidenced by atom probe tomography analysis. Catalytic results demonstrated that under visible light, this Au-Ag core-shell NPs converted solar energy to hydrogen fuel efficiently with an increase of 112.5% in current density at an optimized potential of -0.5V when compared to the light-off conditions. The hydrogen production rate of 1870 μmol g^{-1} h^{-1} for the atomic-layer Au-Ag core-shell materials at room temperature delivered a catalytic performance of 62.1% higher than that of the commercial Pt catalysts. Line-scanning STEM-EELS analysis revealed that the superb activity was due to the generation of hot electrons by LSPR when visible light was incident on the Au-Ag core-shell NPs. Specifically, gold nanoparticles facilitated plasmonic absorption of solar radiation whereas silver nanoparticles provided higher energy excited states for the LSPR-induced hot electrons to carry out proton reduction. It was further demonstrated by DDA simulation and X-ray absorption spectroscopy that the extent of HE generations induced by the LSPR electric field was sensitive to the shell chemical composition, in which the atomic-layer Au-Ag core-shell nanostructure showed the greatest concentration of HEs.

Besides altering the metal active centers to lower the cost and utilizing the plasmonic effect to promote electron transfer, modifying the catalytic support is also an effective way to enhance the electrochemical performance of HER. Specifically, the availability of active sites for proton reduction to take place as well as the mobility of protons affect the rate of reaction critically. In this thesis, the magnesium hydroxide catalytic support with preferentially exposed (001) facets was developed and found to possess excellent proton conducting properties. The unique arrangement of surface hydroxyl groups was attributed to the ordered topotactic transition from polar magnesium oxide phase to the hydroxide phase via electrochemical means as demonstrated by XPS and in-situ synchrotron XRD studies. Further calculation results suggested that the surface hydroxyl groups on the $Mg(OH)_2$ (001) facets offer a platform for

protons to hop across, creating Grotthuss-like channeled pathways to form an extensive network of hydrogen bonds. As a result of the proton conducting surface, an enhancement of 149.5% in current density was observed when compared with the oxide support without such conducting surface. This gave a comparable catalytic current density to the commercial Pt/C catalyst from -1.1 V onwards.

7.2 Outlook

The work in this thesis provides new insights into the structural design of catalytic materials as well as identifies new methodologies in lowering the energy input of the electrochemical system for HER. Generally, replacing Pt-based active centers remain the principal challenge for HER as alternative metal groups usually require higher overpotentials in order to deliver a comparable catalytic activity as Pt.[1] In addition to the metal itself, it is suggested in this thesis that the rate-determining step is also affected by the pH value and the surface species coverage.[2,3] A potential solution in identifying the right metal could be the modification of exposed facets that can in-turn tune the surface energies and affect the hydrogen adsorption strength on the metal active site. Hence, the preferential exposed facet of the metal can be controlled (by changing the morphology of nanoparticle in a macroscopic sense) to achieve a higher catalytic activity as Pt. Initial screening of the metal groups, including Pt, Ag, Au, Pd, Ir, Ru, suggests that Ag and Au can attain comparable activity as Pt at more negative potentials. A wide range of morphological structures of Ag and Au NPs can be studied to optimize the catalytic HER rates.[4–6]

Moreover, this thesis offers a novel methodology in lowering the overpotential of HER by employing solar energy to compensate part of the energy cost. By using plasmonic materials, such as Ag, Au and Cu, that can absorb a wide range of visible light, hot electrons can be generated by LSPR and subsequently promote electron transfer for the proton reduction. A potential direction to effectively utilize these coinage metals is to combine them synergistically,

through for example bimetallic/trimetallic alloys, core-shells, etc., to offer multiple functionalities at a single entity. The plasmonic metallic nanostructures also offer a new avenue in addition to traditional bandgap materials for PEC hydrogen evolution reaction.

Last but not least, graphite is usually regarded as the mainstream catalytic support for electrochemical HER due to its unparalleled electronic conductivity.[7] However, this has limited the choices of materials, as conventional low-cost (and also more resistant to industrial contaminants) metal oxide supports have low electronic conductivity. On the other hand, proton conductivity, as suggested by this thesis, turns out to be an important parameter for HER that has been neglected in the past. This thesis has investigated a novel magnesium hydroxide material that can facilitate proton hopping by a Grotthuss-like hydrogen bonding network. Alternative proton conducting materials, such as perovskites, is a potential solution where proton movements may be triggered by higher applied voltages as driving force instead of higher temperatures.[8]

7.3 References

1. Eftekhari, A. Electrocatalysts for hydrogen evolution reaction. *Int. J. Hydrogen Energy* **42**, 11053–11077 (2017).
2. Shinagawa, T., Garcia-Esparza, A. T. & Takanabe, K. Insight on Tafel slopes from a microkinetic analysis of aqueous electrocatalysis for energy conversion. *Sci. Rep.* **5**, 1–21 (2015).
3. Mo, J. *et al.* Superior Performance of Ag over Pt for Hydrogen Evolution Reaction in Water Electrolysis under High Overpotentials. *ACS Appl. Energy Mater.* **2**, 1221–1228 (2019).
4. Tran, T. D. *et al.* Gold nanoparticles as an outstanding catalyst for the hydrogen evolution reaction. *Chem. Commun.* **54**, 3363–3366 (2018).
5. Alba-Molina, D. *et al.* Tailoring the ORR and HER electrocatalytic performances of gold nanoparticles through metal-ligand interfaces. *J. Mater. Chem. A* **7**, 20425–20434 (2019).
6. Li, Z. *et al.* A silver catalyst activated by stacking faults for the hydrogen evolution reaction. *Nat. Catal.* **2**, 1107–1114 (2019).
7. Tian, W. *et al.* Porous Carbons : Structure-Oriented Design and Versatile Applications. *Adv. Funct. Mater.* **30**, 1909265 (2020).

8. Guan, D. *et al.* Screening highly active perovskites for hydrogen-evolving reaction via unifying ionic electronegativity descriptor. *Nat. Commun.* **10**, 3755 (2019).